Modeling of partial mean stress relaxation and biaxial mechanical testing of Inco718DA

Vasile-Ionut Prisacari

université PARIS-SACLAY

NNT : 2018SACLN006

Thèse de doctorat

école normale supérieure paris–saclay

Modélisation de la relaxation partielle de la contrainte moyenne et essais biaxiaux sur l'Inco718DA

Thèse de doctorat de l'Université Paris-Saclay
préparée à l'École Normale Supérieure de Cachan
(École Normale Supérieure Paris-Saclay)

École doctorale n°579 Sciences mécaniques et énergétiques, matériaux et géosciences
Spécialité de doctorat: Solides, structures et matériaux

Thèse présentée et soutenue à École Normale Supérieure de Cachan
(École Normale Supérieure Paris-Saclay), le 15 Janvier 2018, par

M. Vasile-Ionut Prisacari

Composition du Jury :

M. Sylvain Calloch Professeur des Universités - ENSTA Bretagne	(Président du jury)
M. Marc François Professeur des Universités - Univesité de Nantes	(Rapporteur)
M. Jean-Noël Périé Maître de Conférences (HDR) - IUT GMP de Toulouse	(Rapporteur)
Mme. Pascale Kanouté Ingénieur de Recherche - Onera	(Examinateur)
Mme. Sylvie Pommier Professeur des Universités - ENS Paris-Saclay	(Examinateur)
M. Rodrigue Desmorat Professeur des Universités - ENS Paris-Saclay	(Directeur de thèse)
M. Martin Poncelet Maître de Conférences - ENS Paris-Saclay	(Co-directeur de thèse)
M. Arnaud Longuet Ingénieur de Recherche - Safran Aircraft Engines Villaroche	(Encadrant industriel)

Remerciements

≪ Gutta cavat lapidem (non vi sed saepe cadendo) ≫
≪ La goutte creuse la pierre (pas par force, mais en tombant souvent) ≫

J'ai commencé mes remerciements par ce proverbe car, comme pour chaque thésard, il a fallu beaucoup de persévérance pour surmonter les problèmes, mais, surtout car c'était un processus plus longue que d'habitude et plein de "souffrance", surtout pendant la phase de rédaction, comme une goutte qui tombe sur une pierre et qui fini par la casser. Finalement c'est fait, mais je n'ai sûrement pas pu la faire tout seul.

Je voudrais donc remercier tout d'abord les membres de jury pour avoir accepté de participer à la soutenance et pour leurs questions très intéressantes, et plus particulièrement les rapporteurs, qui ont fait plein de remarques très constructives à la fois dans les rapports et sur place.

Un grand merci à Rodrigue pour tous les conseils, l'aide et pour les boosts de moral, fortement nécessaires surtout à la fin du contrat de thèse, quand se remettre sur la rédaction semblait presque impossible. Je n'oublierais jamais les discussions par téléphone avec tes gamins en bruit de fond (désolé), aux heures impossibles (tu m'as donné le feu vert pour le manuscrit un lundi à 1h de matin) ou les fameuses rencontres dans les bars parisiens pour discuter science. J'ai bien apprécié ta rigueur, ta rapidité à sortir des formules et ton optimisme quand je voyais tout en noir.

Merci Martin pour tout le temps passé ensemble, pour m'avoir introduit dans un monde assez peu connu avant la thèse, et pour m'avoir appris à aimer l'expérimental même quand les problèmes semblaient sans fin. Les discussions scientifiques passaient mieux sur du rock ou bien de la musique classique et j'ai apprécié que t'était un très bon pédagogue et des concepts très alambiqués devenaient, d'un coup, très simples.

Merci à mes encadrants Snecma (devenu entre temps Safran Aircraft Engines) pour leur support et pour avoir apporté du contexte industriel à mes études. Merci donc à Caroline et Alexandre qui ont fait partie du suivi au début et à la fin. Un grand merci à Arnaud pour son style très franc, pour avoir suivi la thèse d'un bout à l'autre et pour avoir fait partie du jury de thèse.

Merci aussi à Hugo pour son support pour le logiciel de pilotage. Un grand merci à Samir pour sa patience dans la résolution des bugs dans les logiciels, bien au-delà de ce qu'il devrait faire par défaut. Je pense que t'aurait dû voir le plus de soucis qu'on a eus à coté d'ASTREE. Merci à Rémi pour son initiative et ses solutions-miracles et à Boubou pour son aide et surtout pour ses vannes. Merci à ceux de l'équipe Eikologie sans lesquels je n'aurais pas pu réaliser une bonne partie de calculs DIC, plus particulièrement John-Eric, Florent et Ali. Merci à Pierre pour m'avoir beaucoup aidé à la fois sur le modèle, les essais et mon français. Même si les études DRX n'ont pas abouti finalement, merci à Olivier, Patrick, Mame et Benoit pour vos explications et votre aide autour de la machine. Merci également à ceux qui ont participé à ma présoutenance et qui m'ont aidé à nettement

améliorer la présentation, même si au dernier moment. La technique ne peut pas avancer sans la partie administrative donc merci Catherine pour ton aide à organiser les confs et à Charlène pour la soutenance. Merci aussi aux collègues de boulot et aux amis qui m'ont "motivé" à finir la thèse le plus rapidement possible.

Après, c'est vrai que ça devient presque un cliché au LMT de dire ça, mais une des réalisations les plus importantes du labo est le bar (hi hi). Comme il y avait un grand nombre de doctorants au labo, il y avait tout le temps quelqu'un pour un conseil, une anecdote, une blague quand la thèse n'avançait pas. Et heureusement qu'on est dans un labo de mécanique, car quand "quelqu'un" s'accroche du haut du bar à 23h00, on trouve facilement une boîte à outils pour le réparer. Sinon je pense que je ne vais pas oublier les matchs de foot vus sur le grand écran, la brioche de dimanche (merci Sylvère), le PATRAN sliding (champion 2018), le championnat de squash et bien sûr les pots de thèse qui finissait tard. Je me suis fait beaucoup d'amis, que je remercie d'autant plus pour la patience qu'ils on eue pour communiquer en français, surtout en début de thèse. Certains d'entre eux sont même venus à mon mariage (Lise et Maxime, Armel, Carole, Hash, Elena et Hortence). Comme j'ai passé pas mal de temps au LMT, je n'arriverais pas à citer tout le monde, donc merci à tous pour l'aide, les conseils et les moments sympas passés ensemble.

Je voudrais remercier aussi ma famille pour leur soutien pendant cette période. Un très grand merci à mon frère pour toute l'aide qu'il a apporté déjà pour arriver en France au M2 qui a précédé la thèse, ainsi que souvent pour des questions d'IT pointues tout au long de la thèse. Merci à ma sœur et son copain et à ma belle-sœur pour avoir beaucoup aidé dans la préparation du pot de thèse.

Finalement, un grand grand merci à la personne la plus importante de ma vie, Andreea, qui à été à mes côtés pendant cette période qui des fois semblait sans fin et qui a du sacrifier des vacances ou des weekends qu'on aurait du faire ensemble. Merci beaucoup pour ta compréhension.

Contents

Résumé étendu en français

Pour améliorer la caractérisation et le dimensionnement des disques de turbines pour les moteurs d'avion, le motoriste Safran Aircraft Engines (SAE) développe des modèles de comportement, des lois d'endommagement et des critères de fatigue plus adaptés aux chargements réels. L'Inco718DA est un super alliage à base nickel largement déployé dans la fabrication des turbines haute pression. Dans la littérature il a été montré que pour l'Inco718, un matériau qui s'adoucit cycliquement [Alexandre, 2004], l'analyse inélastique ne peut pas être basée seulement sur le cycle stabilisé du matériau [Chaboche and Cailletaud, 1986; Burlet and Cailletaud, 1986; Benallal and Marquis, 1987; Calloch and Marquis, 1997; Portier et al., 2000]. Pour obtenir une caractérisation précise, à la fois le comportement monotone (initial) et le cyclique (adouci) doit être introduit [Chaboche et al., 1991]. Ceci est un vrai défi, étant donné la transition lente entre ces deux états, plus particulièrement à des niveau de déformation faibles dans un chargement dissymétrique.

Le but principal de la thèse a été donc de développer un modèle de plasticité adapté à l'Inco718DA et capable de représenter différents chargements (monotone, cyclique symétrique et non-symétrique). La proposition puis l'identification du modèle a été possible grâce à une campagne expérimentale favorisant des tests complexes et innovants aux essais de fatigue nombreux et coûteux. Les essais ont été réalisés à la fois au LMT Cachan et dans les laboratoires d'essai de SAE. Les essais faits incluent un essai monotone avec décharges élastiques, un essai multi-niveau à R_ε=-1 et deux essais multi-niveau à R_ε=0 pour mieux caractériser la relaxation de la contrainte moyenne. Le comportement cyclique du matériau a été identifié en utilisant un écrouissage cinématique non saturant dérivé de celui développé par Desmorat [2010b] avec des éléments s'inspirant de la surface mémoire de Chaboche et al. [1979] et Delobelle et al. [1995]. Un des défis a été d'obtenir des boucles stabilisées "pointues" dans un régime de plasticité cyclique saturante, en utilisant une évolution du paramètre Γ en fonction de la déformation plastique équivalente maximale (prefacteur du terme de rappel de la loi d'écrouissage cinématique). La campagne uniaxiale, ainsi que le développement et l'identification du modèle, ont étés décrit dans le chapitre 2.

Une deuxième difficulté apparaît dans la description de la relaxation de la contrainte moyenne, phénomène complexe avec un impact considérable sur la durée de vie en fatigue. Étant donné qu'une partie des critères de rupture ne sont pas liés directement à la fatigue mais à la déformation plastique cumulée, une description précise de ces phénomènes devient cruciale pour une bonne estimation de la durée de vie des composantes.

Dans le chapitre 3, un modèle est proposé pour la caractérisation de la relaxation partielle de la contrainte moyenne. Une originalité du modèle est l'idée que la relaxation incomplète est une conséquence directe de la différence entre la charge et la décharge de la boucle d'hystérésis. En analysant les paramètres pouvant être responsables pour cette différence dans le modèle, on a trouvé des patterns indiquant qu'il y a une différence importante entre ce qui se passe entre la partie ascendante et descendante de la boucle. Pour des raisons expliquées dans le chapitre 3, section 3, Le paramètre choisi pour décrire cette différence a été le préfacteur du terme de rappel Γ, pour lequel la thermodynamique donne de la liberté. On a montré dans la section 4.1 que $\Gamma \geq 0$ est une condition suffisante pour que la dissipation intrinsèque reste positive, indépendamment du type de chargement. L'évolution du paramètre Γ a été directement calculée pour tous les cycles des essais à notre disposition et injectée directement dans le modèle.

Par rapport à d'autres lois d'écrouissage utilisées pour représenter la relaxation partielle de la contrainte moyenne [Chaboche, 1991; Chaboche et al., 2012; Gustafsson et al., 2011], notre modèle présente l'avantage d'utiliser un seul terme de rappel, mais avec une formulation plus complexe. En plus, le modèle est incrémental (écrit en taux/en vitesse dans le chapitre 3, section 5) ; il peut donc prendre en compte des chargements complexes tels qu'aléatoires ou plus simplement tels que dans les essais multi-niveaux pilotés en déformation. Un autre aspect important du modèle quand on le compare à la loi d'écrouissage multi-cinématique à seuils développée par Chaboche et al. [1991] est que la description de la contrainte moyenne $\bar{\sigma}$ en fonction de l'amplitude des déformations plastiques totales $\frac{\Delta\varepsilon}{2}$ pour un même rapport de charge R_ε est continue. Il n'y a pas de sauts successifs dans la réponse, comme ce qu'il arrive après chaque désactivation des termes de rappel dans le multi-cinématique à seuils.

Même si ce n'était pas le focus de l'étude, la dissymétrie traction-compression peut également être représentée par cette approche utilisant un paramètre Γ différent à la montée et à la descente. On a montré dans la section 3.3 qu'avec un réglage minimal des paramètres, cette dissymétrie peut être très précisément représentée.

Dans le dernier chapitre de la thèse, une campagne biaxiale vaste est présentée, avec les développements pour réaliser des essais biaxiaux pilotés en déformation. La campagne biaxiale a été réalisée sur des éprouvettes cruciformes en utilisant des capteurs LASER et des mesures de champs mono et stéréo analysées en utilisant la Corrélation d'Images Numeriques (CIN). Pour analyser la relaxation de la contrainte moyenne en biaxial un moyen de mesure et de contrôle fiable a dû être développé, adapté aux déformations plastiques élevées qui apparaissent dans la région d'intérêt de l'éprouvette. En utilisant la corrélation d'images intégrée (I-CIN) avec des fonctions de forme adaptées sur un seul élément et des calculs sur GPU, on a obtenu des fréquences de mesure de 100 Hz. En plus, avec sa précision et vitesse, I-CIN a été une technique adapté pour contrôler une machine d'essais multiaxiale hydraulique. Un résultat important obtenu quand on a réalisé des essais equi-biaxiaux pilotés en déformation a été l'observation d'une relaxation de la contrainte moyenne très faible par rapport au cas uniaxial. Ce résultat doit être pris en compte dans les études futures avec des calculs éléments finis sur l'éprouvette complète.

List of Figures

List of Tables

Introduction

Due to the increasing complexity of systems used in aeronautics, spatial, automotive industries, etc., the need for more sophisticated models to describe their behavior has grown in the past years. This implies that experiments manage to get as close as possible to the multiaxial loading states encountered in service. To improve the characterization and the design of their metallic parts, the propulsion systems manufacturer Safran Aircraft Engines (SAE) develops constitutive equations, damage laws and fatigue criteria that are more adapted to real loading.

Metallic alloys are present in a variety of engine components and depending on the temperature range in certain areas, different families are used. To list just a few, in the following some alloy families are presented for temperature ranges going from low to high [Alexandre, 2004]. Titanium alloys are used for the fan area and a part of the compressors, where the temperature is lower than 550° C (TA6V, Ti6242 or Ti17). Poly-crystalline nickel-based alloys (Waspaloy, Inco718, N18) are used for temperatures between 450° C and 700° C, such as the high-pressure compressor (disks, blades and casing) and the turbine (disks and some of the blades). The cobalt-based super-alloys are used for the combustion chamber. Mono-cristaline nickel-based super-alloys are used for blades that reach up to 1000° C towards the tip. *Fig. 1* shows some of these components for the SAE CFM56 engine, along with the high-pressure turbine disk, which is the engine part this study addresses.

The nickel-based superalloy Inco718DA is used for the manufacturing of the high-pressure turbine disks. If the fracture of a blade can be contained by the casing, the same rule doesn't apply for disks, where no fracture is allowed. This criterion makes the disks one of the most critical designed parts. A disk is subjected to temperatures ranging from 450° C to 650° C and stress levels going up to 800 MPa. In this temperature range, damage accumulation by fatigue is the main failure mechanism.

Several fatigue lifetime prediction models exist in the literature, but many of them are based on the notion of a stabilized stress-strain cycle at every point of the structure. It has been shown though for Inco718, a material which softens cyclically, that the inelastic analysis cannot be based solely on the stabilized cyclic behavior of the material [Chaboche and Cailletaud, 1986; Burlet and Cailletaud, 1986; Benallal and Marquis, 1987; Calloch and Marquis, 1997; Portier et al., 2000]. In order to have a precise characterization, both the monotonic (initial) behavior and the cyclic (softened) one should be introduced [Chaboche et al., 1991]. This is an important difficulty, given the slow transition between

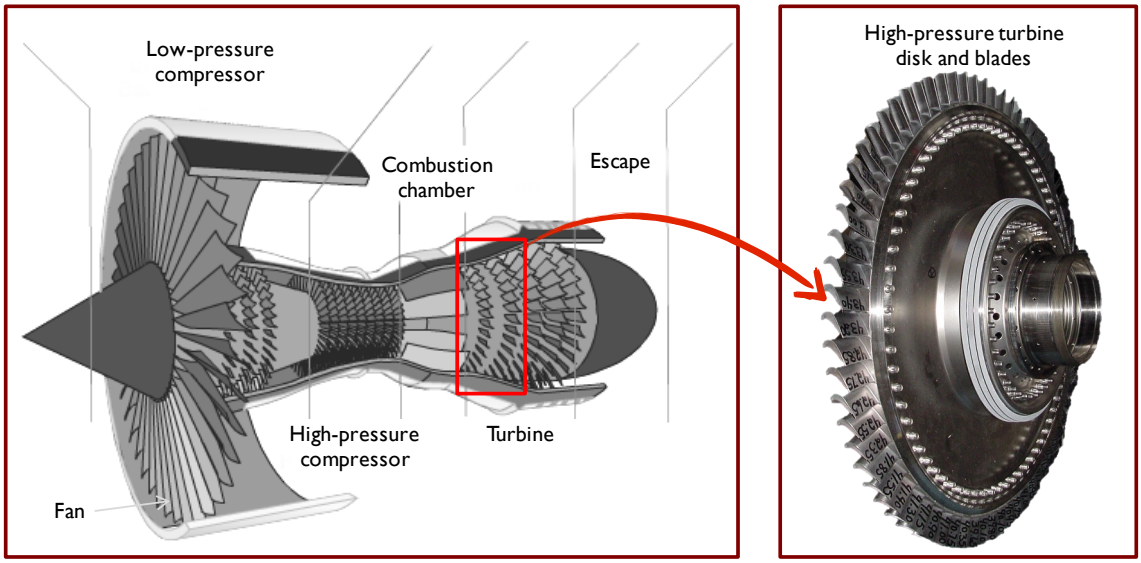

Figure 1: The SAE CFM56 engine with its high-pressure turbine disk

these two states especially at low strain levels in a non-symmetrical loading.

A second difficulty appears in the description of complex phenomena such as mean-stress relaxation [Jhansale and Topper, 1971; Chaboche et al., 2012] and ratcheting [Chaboche and Cailletaud, 1986; Burlet and Cailletaud, 1986; Chaboche, 1991], which have a considerable impact on fatigue lifetime [Lukáš and Kunz, 1989; Wehner and Fatemi, 1991; Arcari et al., 2009]. Moreover, given that some failure criteria are not related to fatigue but to the maximum accumulated plastic strain, a precise description of these phenomena becomes crucial to a good estimation of component lifetime expectancy.

The main goal of this thesis is to develop a plasticity model adapted to Inco718DA and capable of representing several loading conditions (monotonic, symmetrical and non-symmetrical cyclic loading). The identification of the model was possible thanks to a "rich" uniaxial campaign, favoring complex, innovative tests to numerous costly fatigue tests. Such tests include a monotonic test with elastic unloads, several multi-level tests with symmetric ($R_\varepsilon = -1$) and non-symmetric ($R_\varepsilon = 0$) strain ratios (the latter being used to better quantify mean stress relaxation) and a test to analyze ratcheting. The uniaxial campaign, as well as the development and identification of the model are described in chapter 2 and chapter 3, the latter focusing on the modeling of the partial mean stress relaxation.

One also aims at the model validation under multiaxial conditions close to normal engine functioning. Therefore, a biaxial testing campaign was performed using LASER sensors, mono and stereo full-field measurements using Digital Image Correlation (DIC). The latter was optimized into performing biaxial strain controlled tests using Integrated DIC on Graphical Processing Units (GPUs). The design and the results of the biaxial campaign are described in chapter 4.

Chapter 1

Bibliography

In this chapter, a literature survey is presented. The first section focuses on the material properties of Inco718DA, the alloy studied during this thesis. The understanding of its behavior is important for an accurate modeling. Second, a review of plasticity models used for metals is presented, with an accent on kinematic hardening laws. Moreover, since an important phase in model development is the validation, several experimental tests that are frequently used as identification databases are presented. Last, due to a significant evolution of experimental techniques, such as Digital Image Correlation and multiaxial machines, the experimental data recorded during a test can reach a new level of complexity. These techniques are thus presented in the last section.

Contents

1 Introduction

In view of more efficient designs of structural components, the material capability in withstanding various loading regimes is exploited further and further. Thus, in order to allow for lighter designs at ever increasing temperature and/or load levels, material scientists eagerly develop high-end superalloys with improved capabilities. However, in order to safely profit from these capabilities during the design phase, as well as to allow for an exploitation of the entire potential of already existing alloys, it is at least of the same importance to enable a precise and efficient description of the material response within the relevant loading regime [Becker and Hackenberg, 2011].

In order to be able to accurately represent the behavior of a component, several steps need to be taken. Firstly, it is necessary to understand the material, its composition, its manufacturing along with its main failure mechanisms in the different mechanical and thermal regimes, that it will have to perform. Secondly, it is important to understand the phenomena that influence the fatigue lifetime to be able to choose an adequate model. Lastly, model parameters need to be identified using the right experimental data which is not necessarily at our disposal. Following these principles, the material description is presented in the following.

2 Material properties

Inconel 718 is the most-used nickel-based alloy in the manufacturing of aeronautics turbine disks. The composition of one version of this material is given in *Fig. 1.1*. It can be noticed that there is a high percentage of chromium, which enhances its oxidation resistance, important in the temperature range it performs. Iron (Fe) and niobium (Nb) are the main components responsible for the hardening of the material. The hardening is obtained by precipitation of phases γ' and γ'' [Alexandre, 2004; Cozar and Pineau, 1973; Gao et al., 1996; Xiao et al., 2005]. Other phases are also present in inconel: the δ phase [Sun et al., 1997], NbC carbides [Fayman, 1987] and TiN nitrides. These phases play important roles at different levels. The δ phase limits high-temperature grain growth and contributes to their reinforcement [Singh et al., 2003]. The carbides and nitrides are used as germination sites for the grains during the solidification of the alloy. The carbides are also common initiation points for fatigue cracks [Connolley et al., 2003], so their presence should be limited and controlled.

Elements %	*Ni*	*C*	*Cr*	*Fe*	*Nb*	*Mo*	*Ti*	*Al*
Mini	*Base*	*0.02*	*17.00*	*15.00*	*4.75*	*2.80*	*0.75*	*0.30*
Maxi	*Base*	*0.08*	*21.00*	*21.00*	*5.50*	*3.30*	*1.15*	*0.70*

Figure 1.1: Element composition and weight percentage of Inconel 718 PQ [Alexandre, 2004]

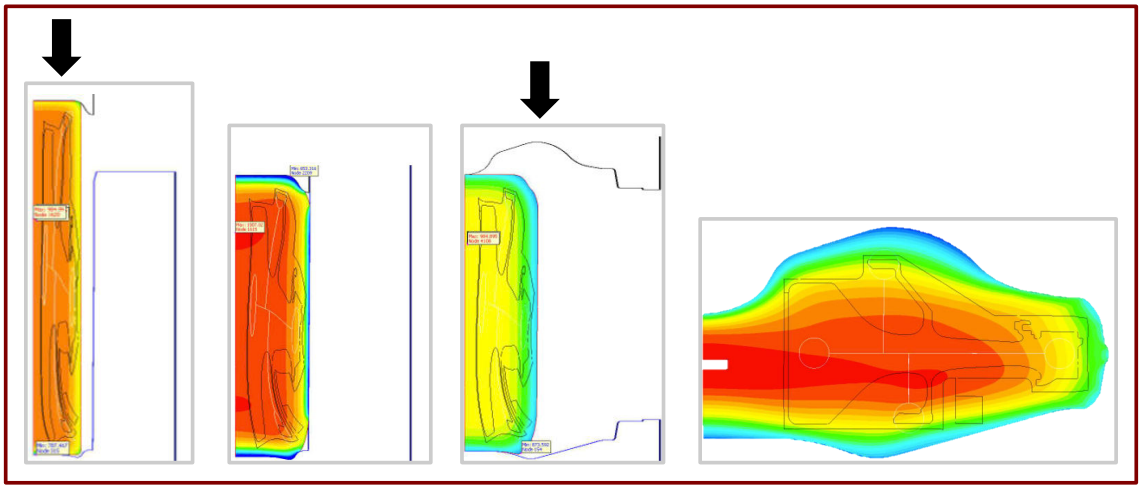

Figure 1.2: Temperature maps during the forging process for Inco718DA high-pressure turbine disks. The manufacturing steps, from left to right, are: upset forging, cooling, stamping and slow air cooling [Schwartz, 2012]

2.1 Turbine disk manufacturing

The turbine disk is obtained from a forged circular block, as shown in *Fig. 1.2* with the symmetry axis on the left hand side. Before it reaches its final shape, the block has to pass through a process of high-temperature upset forging, followed by cooling, then stamping and finally slow air cooling. Temperature gradients inside the material during such a process are important, which generates considerable heterogeneous residual stresses. Grain size, residual hardening and fiber creation are some of the main parameters contributing to the mechanical resistance of components. To ensure good properties, a disk should have a micro-structure as homogeneous and as fine as possible. Therefore, manufacturing has been studied and improved in order to obtained an acceptable behavior [Fournier and Pineau, 1977; Zhou and Baker, 1995; Alexandre, 2004; Revaud, 2013].

Another important aspect of the forging process is that it generates different grain populations in the block (*Fig. 1.3*). These populations are varied and non-uniform especially close to the edges and a little more uniform in the zone where the disk will be extracted (contour marked in red). For the current study, one such forged block was available for extracting different sized samples that we used to perform both uniaxial and biaxial experiments. By taking into account the distribution of the grain populations inside the block and the extraction zone of the disk, we performed a 3D sampling plan in order to optimize the type and number of extracted samples. The details about this plan can be found in Appendix A.

One of the more recent varieties of inconel is Inco718DA. The denomination DA or Direct Aged is an indication of the manufacturing process used for the forged block, particularly the longer air cooling time. The usage of the 718 alloy of the DA type ensures a considerable gain in terms of yield stress ($\approx$20%) with respect to its predecessor

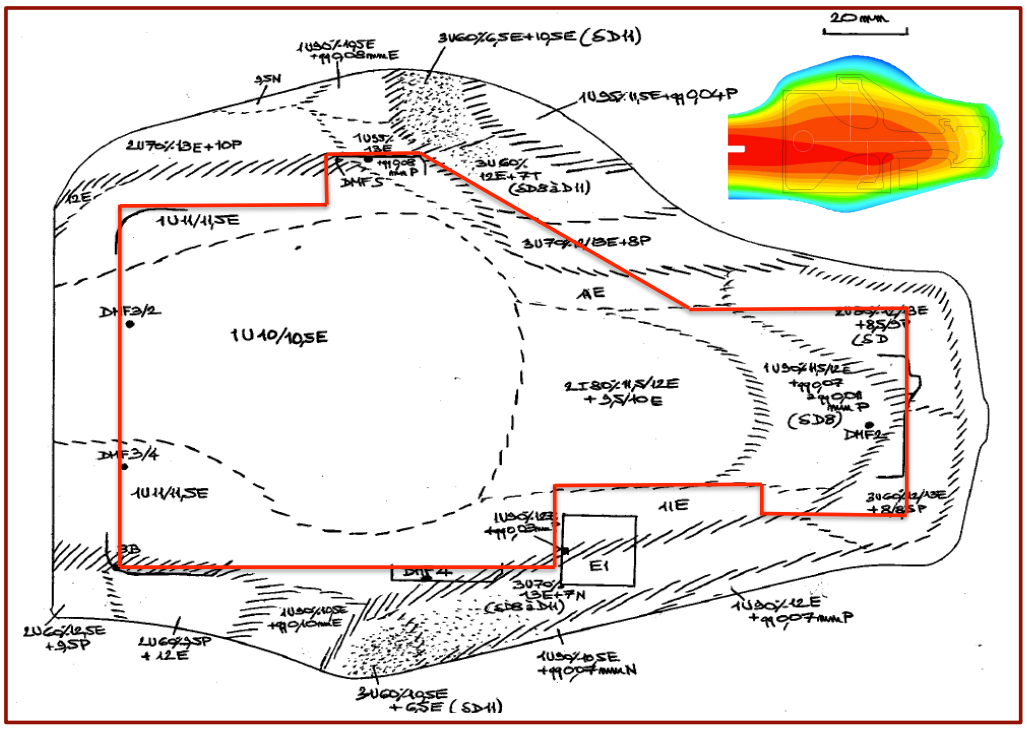

Figure 1.3: Micrographic cut of the forged block, with the extraction zone of the turbine disk marked in red

(Inco718TR), by reducing the grain size from 30 µm to 10 µm (*Fig. 1.4*a). In *Fig. 1.4b* the evolution of the yield stress (Re0.2), the maximum stress (Rm) and elongation in % (10×A) may be seen with respect to temperature for Inco718TR. The material exhibits elongations at fracture of ≈ 20% for yield limits superior to 1000 MPa. Moreover, it is important to notice that Inco718DA performs very well in the temperature range of 0° - 650°C, which explains its wide use in the high-pressure turbine disks, which operate within these limits.

2.2 Cyclic behavior of Inco718DA

During fatigue tests, Inco718DA is a material that exhibits cyclic softening [Fournier and Pineau, 1977]. If the test is stress-controlled than there will be an increase of the amplitude of plastic strains with the number of cycles. For a strain-controlled test the effect is complementary, in the sense that the stress amplitude will decline with passing cycles. In *Fig. 1.5a*, cyclic softening is shown for Inco718 for different temperatures in strain-controlled tests. In the case of Inco718, this phenomenon is due to the shear of hardening precipitates [Alexandre, 2004]. The resistance against dislocation passage through the precipitates is the source of hardening of this alloy. Once this threshold is surpassed, a lot less resistance is exerted, thus the material softens. This can also be seen in *Fig. 1.5b* where some cyclic plasticity curves are shown along with monotonic data for Inco718.

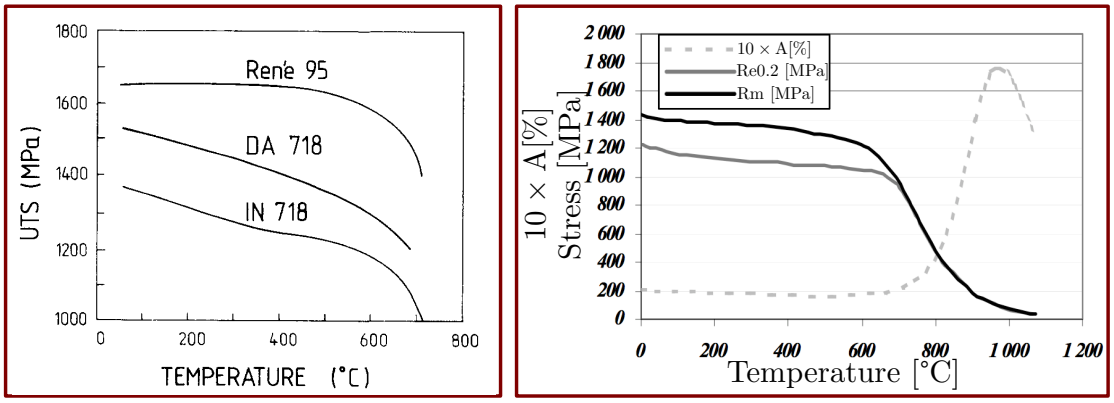

(a) (b)

Figure 1.4: Monotonic tension evolution of nickel-based alloys with respect to temperature a) Ultimate tensile strength (UTS) variation with temperature (°C) for IN 718 (Inco718TR), DA 718 (Inco718DA) and René 95 [Fayman, 1987] b) Evolution of the yield stress(Re0.2), the maximum stress (Rm) and elongation in % (10×A) with respect to temperature for Inco718TR [AMS, 2001]

The differences in the behaviors found in the graph are due to the temperature change, but also to the variability in the microstructure, given that they come from different testing campaigns performed between 1980 and 2001. Moreover, there is an important difference in the way some of the data were obtained. For the results by Clavel [1980] and Fournier [1977] the values are obtained at half-lifetime. The results of Ponnelle [2001] are obtained from incremental fatigue tests for a relatively small number of cycles (≈50) when compared to the whole lifetime span. Performing successive strain loading levels on the same sample can overrate the stress levels and, in this case, reach a hysteresis loop that is not necessarily stabilized [Alexandre, 2004]. This explains some of the scatter in the graph. Nevertheless, the main effect is visible, that there is more and more important cyclic softening as temperature grows. Moreover, if at high temperatures this behavior is expected, it can be seen that even at room temperature there is a considerable softening, which is an important aspect to model.

2.3 Mean stress relaxation and ratcheting

A phenomenon that began receiving a lot of attention these recent years due to its influence over the lifetime of aircraft engine parts is mean stress relaxation. It may occur for materials that soften cyclically, during strain-controlled tests with strain ratios $R_\varepsilon = \frac{\varepsilon_{\min}}{\varepsilon_{\max}} > -1$. As it may be seen in *Fig. 1.6*, for a loading between fixed strain limits $\varepsilon_{\max}$ and $\varepsilon_{\min}$, the mean stress $\bar{\sigma} = \frac{\sigma_{max}+\sigma_{min}}{2}$ will diminish with each cycle. Thus, depending on the plastic strain amplitude and the number of performed cycles, the sample may exhibit a partial or even total mean stress relaxation, when $\bar{\sigma} = 0$ for the stabilized cycle. This phenomenon has been studied experimentally [Jhansale and Topper, 1971;

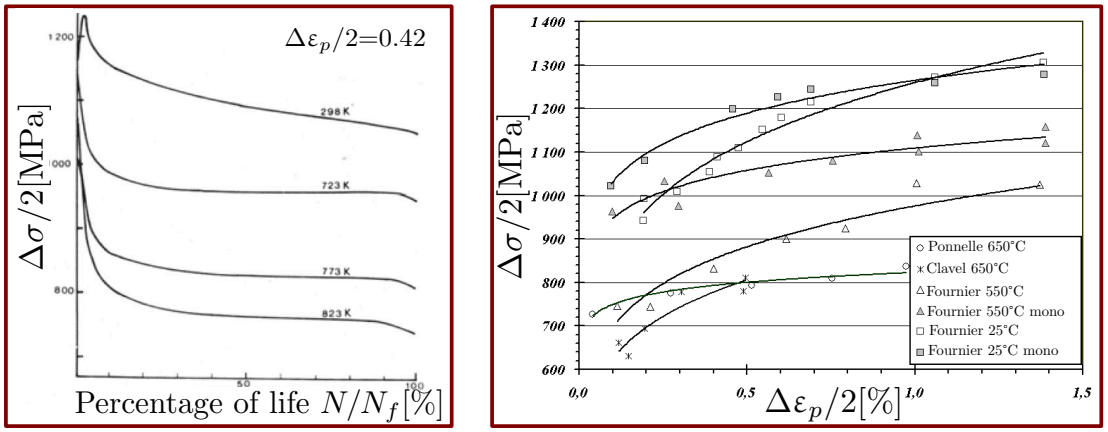

(a) (b)

Figure 1.5: Cyclic properties of Inco718DA a) Evolution of the stress amplitude ($\Delta\sigma/2$) with respect to the percentage of life for different temperatures [Fournier and Pineau, 1977] b) Cyclic plasticity curves ($\Delta\sigma/2 = f(\Delta\varepsilon_p/2)$) at different temperatures from different studies[Alexandre, 2004]

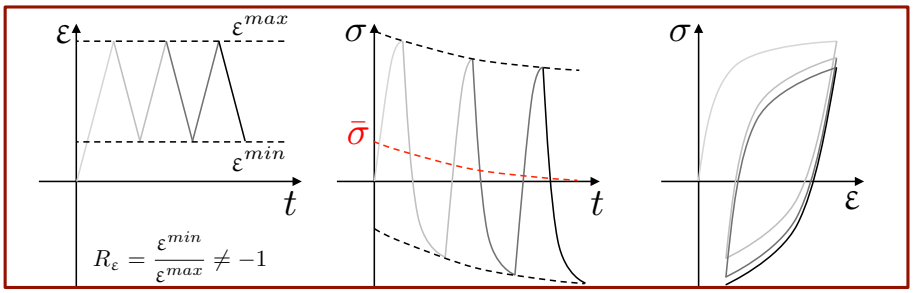

Figure 1.6: Mean stress relaxation principle

Chaboche et al., 2012] and its effect on fatigue lifetime has been analyzed [Lukáš and Kunz, 1989; Wehner and Fatemi, 1991; Arcari et al., 2009]. The phenomenon of incomplete mean stress relaxation, where even after a very large number of cycles $\bar{\sigma} \neq 0$ is an important aspect that very few models manage to represent [Chaboche, 1989b; Chaboche et al., 2012], and will be detailed in the following.

The complementary phenomenon, ratcheting, may occur in stress-controlled tests. As may be seen in *Fig. 1.7*, for a cyclic test with fixed control limits σ^{max} and σ^{min} a material can exhibit the accumulation of plastic strain at each cycle, which can diminish dramatically the fatigue lifetime. Many studies have been done on ratcheting with some interesting conclusions. Ratcheting implies the accumulations of small increments of plastic strain at each loading/unloading cycle. If the unloading is purely elastic, creep effects have been determined as being the contributors [Ruggles and Krempl, 1990]. The constitutive equations usually used to model ratcheting are those of the kinematic hardening rule. Some transient effects may occur due to cyclic hardening or softening [Kang et al., 2010], but pure ratcheting situations are considered to occur under steady conditions

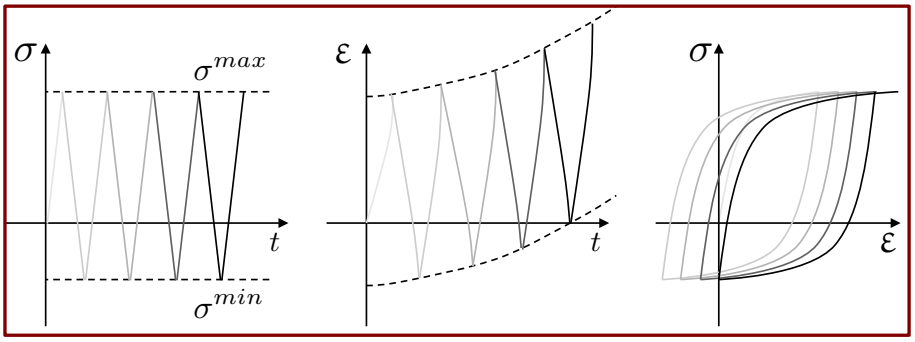

Figure 1.7: Ratcheting principle

(when cyclic isotropic hardening or softening has been saturated). In some experimental campaigns, an initial cycling is performed in order to saturate this effect [Chaboche and Cailletaud, 1986; Chaboche et al., 1991]. Multiaxial ratcheting conditions often lead to lower ratcheting than the corresponding von Mises equivalent uniaxial loading [Chaboche et al., 2012]. Many uniaxial and multiaxial experimental studies have been published [Hassan and Kyriakides, 1992; Delobelle et al., 1995; Portier et al., 2000; Aubin et al., 2003; Vincent et al., 2004; Taleb and Hauet, 2009], most of them using engineering stress control. Recent works show the importance of using true stress control [Paul et al., 2010], although the correction can be added later on for simulation purposes.

Ratcheting and mean stress relaxation have been studied for Inco 718 in France [Chaboche and Cailletaud, 1986; Burlet and Cailletaud, 1986; Chaboche, 1991; Soulé de Lafont et al., 2015] and abroad [Gustafsson et al., 2011; Becker and Hackenberg, 2011] and the solutions in terms of modeling, as well as testing decisions, will be presented in the following sections.

3 Elasto-plastic behavior of metals

3.1 General constitutive laws

According to the principles of continuum mechanics [Lemaitre and Chaboche, 1985; Lemaitre et al., 2009; Besson et al., 2010], the thermodynamics state of the continuum at a given point requires the existence of a certain number of state variables (observable) which are the temperature T and the total strain ε (when assuming small strains). These two state variables are the only ones which evolve in thermo-elasticity, plasticity, damage and fracture phenomena. In order to describe dissipative phenomena, the state at a given time also depends on the past history, thus it is important to also dispose of the values of the internal variables. Plasticity and viscoplasticity require the usage of the plastic or permanent strain ε^p, obtained using the classic strain decomposition:

$$\varepsilon = \varepsilon^e + \varepsilon^p \tag{1.1}$$

with ε^e being the elastic strain. In order to describe hardening, damage, fracture, other variables that describe the internal state of matter are required, such as the density of dislocations, the crystalline microstructure, micro-cracks distribution, etc. In Lemaitre and Chaboche [1985] they are denoted as $V_1, V_2, ..., V_K$; V_K being either a scalar or a tensorial variable. The Helmholtz specific free energy, taken as the state potential of the material, is a function of the state and internal variables and can thus be expressed as:

$$\rho\psi = \rho\psi(\boldsymbol{\varepsilon}, T, \boldsymbol{\varepsilon^e}\boldsymbol{\varepsilon^p}, p, \boldsymbol{\alpha}) \tag{1.2}$$

Given that in this study the main focus will be on hardening, the main internal variables used to describe this behavior will be presented. For the isotropic hardening, the scalar internal variable known as the accumulated plastic strain is used to describe the size of the elastic domain: $p = \int_0^t \sqrt{\frac{2}{3}\dot{\boldsymbol{\varepsilon}}^{\boldsymbol{p}}(\tau) : \dot{\boldsymbol{\varepsilon}}^{\boldsymbol{p}}(\tau)}d\tau$. For the kinematic hardening, a tensorial variable $\boldsymbol{\alpha}$ is used to describe the position of the elasticity domain. Thus, in the isothermal case, the state potential becomes:

$$\begin{aligned}\rho\psi &= \rho\psi(\boldsymbol{\varepsilon}, T, \boldsymbol{\varepsilon^p}, p, \boldsymbol{\alpha}) \\ &= \frac{1}{2}(\boldsymbol{\varepsilon} - \boldsymbol{\varepsilon^p}) : \mathbb{E} : (\boldsymbol{\varepsilon} - \boldsymbol{\varepsilon^p}) + G(p) + \frac{1}{3}C(\boldsymbol{\alpha} : \boldsymbol{\alpha})\end{aligned} \tag{1.3}$$

with $\mathbb{E}$ being the Hooke's tensor, $G(p) + \frac{1}{3}C(\boldsymbol{\alpha} : \boldsymbol{\alpha})$ the stored energy density by hardening. Using the Clausius-Duhem inequality, the thermodynamics forces associated with the internal variables can be obtained:

$$\begin{aligned}\boldsymbol{\sigma} &= \rho\frac{\partial\psi}{\partial\boldsymbol{\varepsilon}} = \mathbb{E} : (\boldsymbol{\varepsilon} - \boldsymbol{\varepsilon^p}) \\ R &= \rho\frac{\partial\psi}{\partial p} = \frac{dG}{dp} = R(p) \\ \boldsymbol{X} &= \rho\frac{\partial\psi}{\partial\boldsymbol{\alpha}} = \frac{2}{3}C\boldsymbol{\alpha}\end{aligned} \tag{1.4}$$

with $R = R(p)$ being the isotropic hardening rule. The loading or flow surface for a large variety of models is expressed with the following inequality:

$$f = (\boldsymbol{\sigma} - \mathbf{X})_{eq} - \sigma_y - R(p) \leq 0 \tag{1.5}$$

where σ_y is the yield stress and $(\boldsymbol{\sigma} - \mathbf{X})_{eq}$ is the equivalent stress, a scalar value that allows the usage of the inequality in the tensorial space. Given that it was experimentally observed that plastic flow does not depend on hydrostatic pressure, the deviatoric stress $\boldsymbol{\sigma}'$ and its invariants being chosen instead of the stress tensor itself. One of the most commonly used equivalent stress criterions is the Von Mises criterion [Mises, 1913]

which uses the J_2 invariant $J_2(\boldsymbol{\sigma}) = \sigma_{eq} = \sqrt{\frac{3}{2}\boldsymbol{\sigma}' : \boldsymbol{\sigma}'}$, but several criteria exist in the literature depending on the application [Hill, 1948; Yu, 1961; Tresca, 1864; Barlat et al., 1991; François, 2001]. Three scenarios may occur during loading-unloading conditions, depending on the value of the criterion function f and of its time derivative $\dot{f}$:

- $f < 0$: elastic behavior
- $f = 0$ and $\dot{f} = 0$: plastic flow
- $f < 0$ or $\dot{f} < 0$: elastic unloading

During plastic flow, the plastic strain rate in any point can be expressed using the flow direction, which is the unit normal vector $\mathbf{n} = \frac{\partial f}{\partial \boldsymbol{\sigma}}$, thus $\dot{\boldsymbol{\varepsilon}}^{\boldsymbol{p}} = \dot{\lambda}\mathbf{n}$. This equality, also known as the normality rule, uses a plastic multiplier rate $\dot{\lambda}$ to quantify plastic flow, which is shown to be, in many simple cases, equal to the accumulated plastic strain rate $\dot{p} = \sqrt{\frac{2}{3}\dot{\boldsymbol{\varepsilon}}^{\boldsymbol{p}} : \dot{\boldsymbol{\varepsilon}}^{\boldsymbol{p}}}$ [Lemaitre et al., 2009]. Thus, the plastic strain rate can be expressed as $\dot{\boldsymbol{\varepsilon}}^{\boldsymbol{p}} = \dot{p}\mathbf{n}$.

With the increment of plastic strain defined, the evolution of the isotropic and kinematic hardening variables R and $\boldsymbol{X}$ can also be expressed using an incremental (rate) approach. Some more common hardening laws found in the literature will be presented in the following, insisting on the kinematic hardening, given that it is the main focus of this study.

3.2 Isotropic hardening

Isotropic hardening is expressed as the uniform expansion of the loading surface. In isotropic hardening rules, this evolution of the loading surface is governed by only one scalar variable, such as the dissipated plastic work or, most commonly, the accumulated plastic strain p. The evolution of the isotropic hardening R may be seen in *Fig. 1.8* [Lemaitre and Chaboche, 1985] in the stress space, as well the stress-plastic strain curve in tension-compression.

The Prandtl-Reuss equation is a flow law used in an elasto-platic regime with isotropic hardening:

$$f = \sigma_{eq} - \sigma_y - R(p) \leq 0 \tag{1.6}$$

Several laws are used to express the evolution of the isotropic hardening, the simplest one being a linear evolution $R = Kp$, with K being the hardening slope. Given that for a considerable number of metals the monotonic macroscopic response is non-linear, a power law formulation $R = Kp^{\frac{1}{m}}$ is more adapted for modeling such a behavior. The exponential isotropic hardening rule is a popular choice and probably the most commonly used for fatigue applications, its expression being given by the evolution shown below:

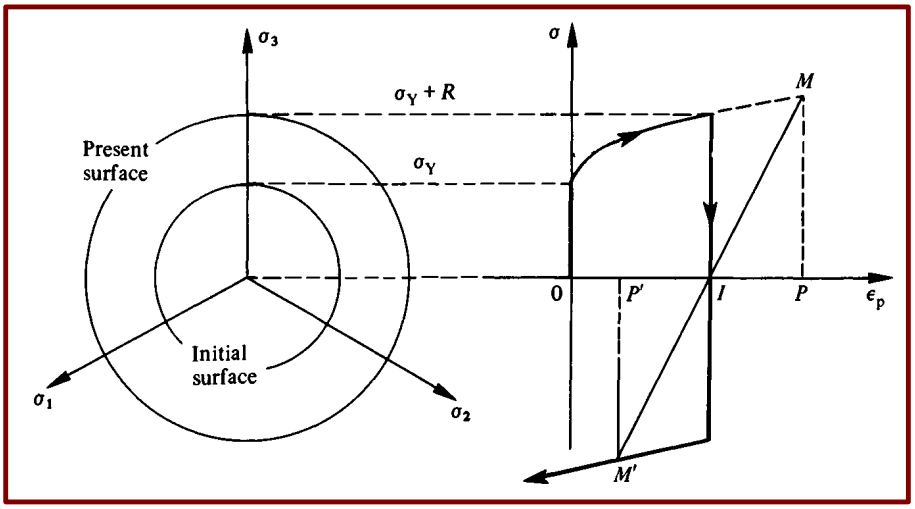

Figure 1.8: Representation of isotropic hardening in the stress space (left) and in tension-compression (right) [Lemaitre and Chaboche, 1985]

$$R = R_\infty(1 - e^{-b_R p}) \tag{1.7}$$

The evolution of the isotropic hardening variable R in this case tends towards a saturation value R_∞ when $p \to \infty$. This value can be easily identified on a monotonic curve after choosing a suitable yield stress σ_y. In order to have the description of the whole monotonic curve, the material parameter b_R is used to represent the saturation speed. In the cyclic case, the size of the elastic surface evolves during a limited number of cycles to finally reach a stabilized value. If an even more accurate description of the cyclic evolution is wanted, several isotropic hardenings can be used with different saturation speeds, in order to capture both faster and slower phenomena.

3.3 Kinematic hardening

Kinematic hardening corresponds to the translation of the loading surface. The governing hardening variable indicates the position of the loading surface, thus it is of a tensorial nature. This may be seen in *Fig. 1.9*, where the movement of the loading surface is represented in the stress space (left) and in the corresponding tension-compression modeling (right). Kinematic hardening plays an important role during un-loadings, even for large strains, and it is predominant for small strains and cyclic loadings. This is a way to successfully represent the Bauschinger effect: the yield limit under a compressive (resp. tensile) loading applied after a tensile (resp. compressive) prehardening is smaller than the reference yield limit for a compression (resp. tension) loading [Lemaitre and Chaboche, 1985; Besson et al., 2010].

There have been many different formulations of kinematic hardening models, some of which are indicated in the following. The simplest model is Prager's linear kinematic

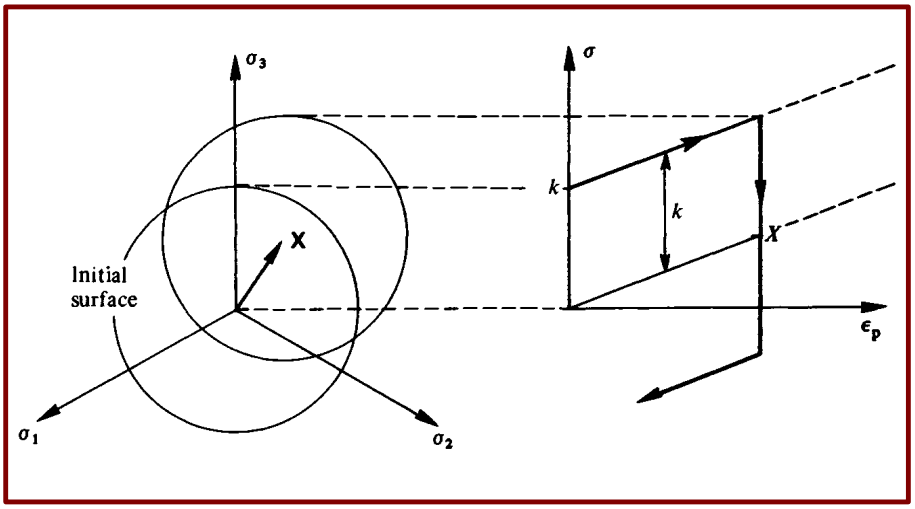

Figure 1.9: Representation of linear kinematic hardening in the stress space (left) and in tension-compression (right) [Lemaitre and Chaboche, 1985]

hardening [Prager, 1949], where the evolution of the kinematic variable $\boldsymbol{X}$ evolves linearly with respect to the evolution of the plastic strain $\boldsymbol{\varepsilon^p}$:

$$\begin{cases} \boldsymbol{X} = \frac{2}{3}C\boldsymbol{\alpha} \\ \dot{\boldsymbol{\alpha}} = \dot{\boldsymbol{\varepsilon}}^{\boldsymbol{p}} \end{cases} \quad \text{and in the isothermal case} \quad \dot{\boldsymbol{X}} = \frac{2}{3}C\dot{\boldsymbol{\varepsilon}}^{p} \tag{1.8}$$

with C being a material parameter also known as the plastic modulus, when the isotropic hardening does not evolve. Given that a linear stress-strain response, as shown in *Fig. 1.9*, is rarely observed in experiments, a better description is proposed by Frederick and Armstrong [1966], by the introduction of the back-stress term in the evolution of $\boldsymbol{X} = \frac{2}{3}C\boldsymbol{\alpha}$, which becomes in the isothermal case:

$$\begin{cases} \boldsymbol{X} = \frac{2}{3}C\boldsymbol{\alpha} \\ \dot{\boldsymbol{\alpha}} = \dot{\boldsymbol{\varepsilon}}^{\boldsymbol{p}} - \frac{3\gamma}{2C}\boldsymbol{X}\dot{p} \end{cases} \quad \text{and in the isothermal case} \quad \dot{\boldsymbol{X}} = \frac{2}{3}C\dot{\boldsymbol{\varepsilon}}^{p} - \gamma\boldsymbol{X}\dot{p} \tag{1.9}$$

γ being a material parameter also used in the Burlet-Cailletaud law [Burlet and Cailletaud, 1987], the Chaboche law [Chaboche et al., 1991] and the Ohno-Wang law [Ohno and Wang, 1993a]. The back-stress term $\gamma\boldsymbol{X}\dot{p}$, also known as the dynamic recovery term, is colinear with $\boldsymbol{X}$ and proportional to the total plastic strain rate $\dot{p}$. Thus, the evolution of $\boldsymbol{X}$, instead of being linear, is exponential for a monotonic uniaxial loading, with a saturation value of C/γ.

For a strain-controlled cyclic loading, the stabilization will occur when $X_{max} + X_{min} = 0$ [Chaboche, 2008], in terms of amplitude being:

$$\frac{\Delta X}{2} = |X_0| = \frac{C}{\gamma}tanh\left(\gamma\frac{\Delta\varepsilon^p}{2}\right) \tag{1.10}$$

In order to obtain a more accurate modeling, several kinematic hardening of the type shown in *Eq. 1.9* can be added [Chaboche et al., 1979; Chaboche and Rousselier, 1983], with significantly different constants γ_i (factors from 5 to 20 between them):

$$\boldsymbol{X} = \sum_{i=1}^{n} \boldsymbol{X}_i \quad \text{and in the isothermal case} \quad \dot{\boldsymbol{X}}_i = \frac{2}{3} C_i \dot{\varepsilon}^p - \gamma_i \boldsymbol{X}_i \dot{p} \tag{1.11}$$

thus allowing for a better description of the soft transition between elasticity and the onset of plastic flow. Even if the number of parameters used for the model seems important, Chaboche [2008] explains that the set $\{\gamma_i, C_i\}$ of superposed back-stresses should actually be seen as a series of decompositions of a simpler expression of the tensile (or cyclic) curve, such as a power law. This has been proven later by Watanabe and Atluri [1986] based on the endochronic theory of Valanis [1978].

This is actually a way to avoid, or rather to postpone, the intrinsic saturation contained in this type of model. The reason is that all of these models will eventually saturate at a value $X = X_\infty = Const$. Different possibilities to avoid such a saturation of the kinematic hardening exist: make $\gamma = \gamma(p)$ a decreasing (to zero) function of the accumulated plastic strain as in Marquis [1989], make C dependent of the plastic strain amplitude, through an index function written in the strain space, as in Delobelle et al. [1995]. None recovers the power law shape at high plastic strains.

One solution proposed by Desmorat [2010b] is to naturally gain the non-saturation of the kinematic hardening, but also define for kinematic hardening a power law counterpart to the usual exponential law.

$$\begin{cases} \boldsymbol{X} = \frac{2}{3} C \boldsymbol{\alpha} \\ \dot{\boldsymbol{\alpha}} = \dot{\boldsymbol{\varepsilon}}^{\boldsymbol{p}} - \frac{3\Gamma}{2C} X_{eq}^{M-2} \boldsymbol{X} \langle \dot{X}_{eq} \rangle_+ \end{cases} \quad \text{or (isothermal)} \quad \dot{\boldsymbol{X}} = \frac{2}{3} C \dot{\boldsymbol{\varepsilon}}^{\boldsymbol{p}} - \Gamma X_{eq}^{M-2} \boldsymbol{X} \langle \dot{X}_{eq} \rangle_+ \tag{1.12}$$

where $\langle . \rangle_+$ stands for positive part, *i.e.* $\langle \dot{X}_{eq} \rangle = \dot{X}_{eq} = \frac{\mathrm{d}}{\mathrm{d}t} (\frac{3}{2} \boldsymbol{X} : \boldsymbol{X})^{1/2}$ when positive, $\langle \dot{X}_{eq} \rangle = 0$ else. One of the main model features obtained for large values of parameter C is the possibility to represent very steep stress increase at the onset of plasticity (with no visible elasticity/plasticity slope discontinuity). Such a smooth shape of cyclic stress-strain curves, very steep just out from the elasticity domain and decreasing rapidly when yielding (but with no saturation), cannot be represented by means of a single Armstrong-Frederick law.

Another interesting aspect of this model is that both the cyclic loops $\sigma = f(\varepsilon)$ and the cyclic plasticity curve $\frac{\Delta\sigma}{2} = f(\frac{\Delta\varepsilon_p}{2})$ are non-saturating. The cyclic plasticity response (at saturated hardening) is given by:

$$\begin{cases} \frac{\Delta\sigma}{2} = k + X_{max} \\ \frac{\Delta\varepsilon_p}{2} = \frac{1}{C} \left(X_{max} + \frac{\Gamma}{2M} X_{max}^M \right) \end{cases} \tag{1.13}$$

or

$$\frac{\Delta\varepsilon_p}{2} = \left\langle \frac{\frac{\Delta\sigma}{2} - k}{C} \right\rangle_+ + \frac{1}{2}\left\langle \frac{\frac{\Delta\sigma}{2} - k}{K} \right\rangle_+^M \tag{1.14}$$

with $K = \left(\frac{MC}{\Gamma}\right)^{1/M}$ and $k = \sigma_y + R$. Given that $X_{max} \approx K\left(\frac{\Delta\varepsilon_p}{2}\right)^{1/M}$ then $\frac{\Delta\sigma}{2} = k + X_{max}$ is also of a power law type, therefore non-saturating. This feature can thus be used for complex material behavior, such as in the case of 316L stainless steel.

Other more complex phenomena such as mean stress relaxation and ratcheting have used a modification of some of the kinematic hardening models presented above in order to more accurately represent the real behavior of the material. This will be presented in detail in chapter 3, section 1. In the following, another concept used in the literature to represent more complex cyclic behavior and for certain developments during this thesis is presented.

3.4 Memory effect

A concept that was developed to represent more complex cyclic behavior and that will be used during this thesis is the memory surface of the plastic strain developed by Chaboche et al. [1979] and extended by Ohno [1982]. Such a surface is usually defined as a hypersphere in the plastic strain space, similarly to the elasticity yield surface, by a scalar isotropic variable q, which is the radius, and a tensorial kinematic variable $\boldsymbol{\xi}$, which gives the coordinate of the center of the hypersphere (*Fig. 1.10*). The equation of the hypersphere is the function $\mathcal{F} = 0$:

$$\mathcal{F} = \sqrt{\frac{2}{3}}||\boldsymbol{\varepsilon^p} - \boldsymbol{\xi}|| - q = \sqrt{\frac{2}{3}(\boldsymbol{\varepsilon^p} - \boldsymbol{\xi}) : (\boldsymbol{\varepsilon^p} - \boldsymbol{\xi})} - q \leq 0 \tag{1.15}$$

Both the normality rule ($\dot{\boldsymbol{\xi}}$ is proportional to $\boldsymbol{n}^\star = \frac{\boldsymbol{\varepsilon^p} - \boldsymbol{\xi}}{||\boldsymbol{\varepsilon^p} - \boldsymbol{\xi}||}$) and the consistency rule ($\mathcal{F} = 0$ and $\dot{\mathcal{F}} = 0$ while $\dot{\boldsymbol{\varepsilon}}^{\boldsymbol{p}} \geq 0$) are valid. Thus, the evolution laws of the two variables q and $\boldsymbol{\xi}$ are obtained :

$$\begin{aligned} \dot{q} &= \eta\mathcal{H}(\mathcal{F})\langle \boldsymbol{n} : \boldsymbol{n}^\star \rangle_+ \dot{p} \\ \dot{\boldsymbol{\xi}} &= \sqrt{\frac{3}{2}}(1-\eta)\mathcal{H}(\mathcal{F})\langle \boldsymbol{n} : \boldsymbol{n}^\star \rangle_+ \boldsymbol{n}^\star \dot{p} \end{aligned} \tag{1.16}$$

with η being a material parameter and $\mathcal{H}(\mathcal{F})$ the Heaviside function, the unit normals being defined as:

$$\boldsymbol{n} = \frac{\frac{\partial \mathcal{F}}{\partial \boldsymbol{\sigma}}}{\left|\left|\frac{\partial \mathcal{F}}{\partial \boldsymbol{\sigma}}\right|\right|} = \frac{\boldsymbol{\sigma}' - \boldsymbol{X}}{||\boldsymbol{\sigma}' - \boldsymbol{X}||} \qquad \boldsymbol{n}^\star = \frac{\frac{\partial \mathcal{F}}{\partial \boldsymbol{\varepsilon^p}}}{\left|\left|\frac{\partial \mathcal{F}}{\partial \boldsymbol{\varepsilon^p}}\right|\right|} = \frac{\boldsymbol{\varepsilon^p} - \boldsymbol{\xi}}{||\boldsymbol{\varepsilon^p} - \boldsymbol{\xi}||} \tag{1.17}$$

so that:

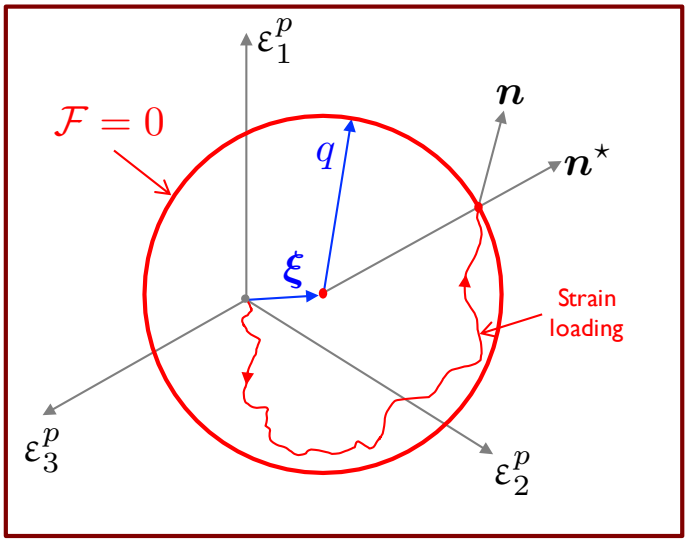

Figure 1.10: Memory surface in the pricipal strain space.

$$\dot{\boldsymbol{\varepsilon}}^{\boldsymbol{p}} = \dot{p}\,\frac{3}{2}\frac{\boldsymbol{\sigma}' - \boldsymbol{X}}{(\boldsymbol{\sigma}' - \boldsymbol{X})_{eq}} = \sqrt{\frac{3}{2}}\,\boldsymbol{n}\,\dot{p} \tag{1.18}$$

The memory effect was used by Chaboche et al. [1991] for the representation of a complex isotropic hardening. It was noticed that trying to model a complex uniaxial campaign going from large strain levels to smaller ones would fail without taking into consideration memory effect, given that cyclic softening is dependent on the applied strain range, for its rapidity, as well as for its magnitude. Thus, the amount of softening is larger for larger strain ranges and continues to play a role if the strain range is decreased. A way to circumvent this problem was to use the memory variable q in the description of the evolution of the isotropic hardening (here in the isothermal case):

$$\dot{R} = b_R(Q(q) - R)\dot{p} \tag{1.19}$$

where the function $Q(q)$, which defines the amount of cyclic softening is taken as [Chaboche et al., 1979]:

$$Q(q) = Q_M + (Q_0 - Q_M)e^{-2\mu q} \tag{1.20}$$

by introducing Q_0, Q_M and μ as material parameters. Such a model was also used by Ohno [1982]; Ohno and Kachi [1986], and under stabilized conditions $q = \frac{\Delta\varepsilon_p}{2}$. Other more sophisticated versions exist, such as in Nouailhas et al. [1982], where a part of the memory was slowly evanescent, in order to describe both monotonic and cyclic hardening of 316 SS. Even if much less popular, the memory effect was also used in the description of kinematic hardening [Delobelle et al., 1995].

3.5 Tension-compression asymmetry

A phenomenon that was encountered in Inco718DA, even though it's not very pronounced, is tension-compression asymmetry during cyclic tests. Nevertheless, many different materials exhibit this kind of behavior, porous metallic alloys, ceramics, polymers, composites or soils.

Several different models exist in the literature for representing this phenomenon, some related to plasticity criteria being presented in the following. Mohr (1900) introduced the first model using hydrostatic pressure to represent a non-symmetric behavior. The criterion is written as:

$$f = |\tau| - \sigma_n - c = 0 \tag{1.21}$$

where τ is the shear stress, σ_n the normal stress and c the cohesion of the material. Another solution is the Drucker-Prager criterion (1952), which is a linear combination between the second invariant of the deviatoric stress J_2 and the trace of the stress tensor I_1:

$$f = \sqrt{J_2} - A + BI_1 = 0 \tag{1.22}$$

where A and B are material parameters depending on the yield limits in simple tension and simple compression respectively. It was developed for soil application but is largely used for tension-compression asymmetry in plasticity.

Raghava et al. [1973] proposes a model for polymers, based on the Drucker-Prager one, then largely adapted for other materials. Also called "modified von Mises criterion" in the literature, it uses the first stress invariant and is written as:

$$f = J_2 + \frac{1}{3} I_1 (\sigma_C - \sigma_T) - \frac{1}{3} \sigma_C \sigma_T = 0 \tag{1.23}$$

Other newer models used have an even finer description of the phenomenon of tension-compression asymmetry for pressure insensitive metals [Cazacu and Barlat, 2004], sheet metals [Hu, 2005] or cast iron [Augustins, 2014].

4 Existing tests

4.1 Uniaxial tests

Mechanical tests (enriched with a thermal or a loading of a different nature) consist in obtaining basic information needed in modeling the mechanical behavior of solid materials [Lemaitre et al., 2009; Lemaitre and Chaboche, 1985]. In order to be able to make the link between the behavior of the material and the model, mechanical properties such as stresses and strains need to be correctly determined. For this reason, the "homogeneous" tests, in which the strain or stress states are uniform within the useful volume of the sample were and still are the main tests used to experimentally characterize material behavior.

The most common mechanical tests in the domain of material science are still performed in a uniaxial loading regime.

Depending on the type of behavior needed to model, a large variety of uniaxial tests exist: hardening, viscosity, damage, etc. They can be monotonic or cyclic, quasi-static or dynamic, isothermal or anisothermal or can be associated with other loading types, such as an electromagnetic field.

The most common uniaxial test is the monotonic tension or compression test. It is usually strain-controlled, at a constant strain rate $\dot{\varepsilon}$ and it allows to obtain the monotonic evolution of hardening by analyzing the stress vs strain curve. Two other complementary tests to characterize hardening and viscosity are creep and relaxation, where the sample is subjected to a constant state of stress (respectively strain) with the purpose of analyzing the time variation of strain (respectively stress). Multiple hardening-relaxation tests are also an interesting choice for obtaining hardening characteristics, as well as viscosity using only one sample.

Cyclic tests are the main type of tests used to estimate fatigue lifetime and cyclic hardening-softening behavior. They consist in subjecting the specimen to periodic load (stress or strain) and the evolution of the cyclic response is studied in terms of $\sigma(\varepsilon)$ gradually and their evolution from one cycle to the other. The main quantities used in cyclic plasticity rules are the stress amplitude $\sigma_a = \frac{\Delta\sigma}{2} = \frac{\sigma_{max}-\sigma_{min}}{2}$, the mean stress $\bar{\sigma} = \frac{\sigma_{max}+\sigma_{min}}{2}$, the strain amplitude $\frac{\Delta\varepsilon}{2}$, the plastic strain amplitude $\frac{\Delta\varepsilon_p}{2}$ and the two loading ratios $R_\sigma = \frac{\sigma_{min}}{\sigma_{max}}$ and $R_\varepsilon = \frac{\varepsilon_{\min}}{\varepsilon_{\max}}$.

The tests are usually performed in uniaxial testing machines, a classic configuration being represented schematically in *Fig. 1.11a*, along with its main elements. One of the most common uniaxial machines is the servo-hydraulic one, but more recently electromechanical machines have managed to reach comparable maximum loading levels, and are beginning to be used more and more for the stability of the signal-response loop.

For tension tests, the restriction on the samples is mainly due to machining and heating devices, thus they can be quite thin, such as the flat dog-bone sample, for which a good review can be found in [Davis, 2004]. On the other hand, compression or tension-compression samples need to be more compact, in order to avoid buckling. A typical tension sample is shown in *Fig. 1.11b*, (i). It includes the useful part, usually in the middle area, end grips and shoulders designed to minimize stress concentration. Also shown in this figure is a typical fatigue sample used in the SAE facilities (ii).

Another, less common, uniaxial test is the tensile test with unloads [Lemaitre and Dufailly, 1987]. One of the reasons to perform this type of test is to model the highly nonlinear unloading following plastic deformation seen in certain materials [Sun and Wagoner, 2011; Mendiguren et al., 2013], especially those used for metal sheets [Cleveland and Ghosh, 2002]. One example of a study on the experimental and model characterization of this phenomenon is shown in *Fig. 1.12*. Non-linear unloading behavior has been attributed to residual stress [Hill, 1956], time-dependent anelasticity [Zener, 1948], damage evolution [Halilovič et al., 2008], and piling up and relaxation of dislocation arrays [Cleveland and Ghosh, 2002]. This type of test needs to have inelastic unloadings in or-

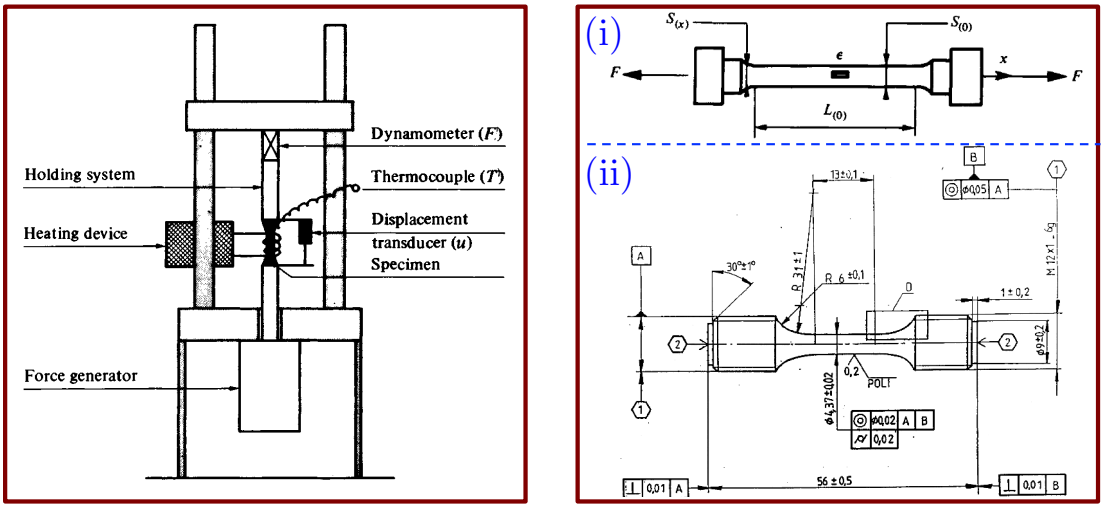

(a) (b)

Figure 1.11: a) Schematic diagram of a machine for tension-compression tests [Lemaitre and Chaboche, 1985] b) (i) Typical sample used for tension tests [Lemaitre and Chaboche, 1985], (ii) Safran Aircraft Engines fatigue sample

der to represent the necessary phenomena. On the other hand, this test can be adapted and used to obtain both the evolution of the kinematic and isotropic hardenings, if the unloads are kept elastic [Lemaitre and Desmorat, 2005]. In chapter 2, a monotonic test with elastic unloads that we performed is described, serving for this second purpose, that of identifying separately the t

4.1.1 Mean stress relaxation tests

In recent years, a large accent has been put on the comprehension and modeling of mean-stress relaxation [Landgraf and Chernenkoff, 1988; Chaboche and Jung, 1997; Zhuang and Halford, 2001; Landersheim et al., 2011; Chaboche et al., 2012]. For these types of calculations, it is of interest to be able to predict the mean stress relaxation behavior in a satisfactory way as it has an influence on the fatigue lifetime [Korth, 1991; Chaboche et al., 2012]. Experimentally, mean stress relaxation is observed when performing strain-controlled fatigue tests at a non-symmetrical strain ratio $R_\varepsilon \neq -1$ [Bonnand et al., 2011; Gustafsson et al., 2011].

A common approach after performing a significant number of fatigue tests is to analyze the results on a mean stress relaxation curve $\bar{\sigma} = f(\frac{\Delta\varepsilon}{2})$. As it may be seen in *Fig. 1.13*, the mean stress relaxation curve is normally composed of 3 zones: an elastic one, corresponding to the case where both the first loading and the cyclic loading happen in the elastic domain; an accommodated elastic zone when the material plastifies during the first loading and then cycles elastically and finally, the third zone when cyclic plastic strain may accumulate. In the transition between the accommodated elastic and the cyclic plasticity zone, phenomena leading to cyclic softening are still not fully understood. In

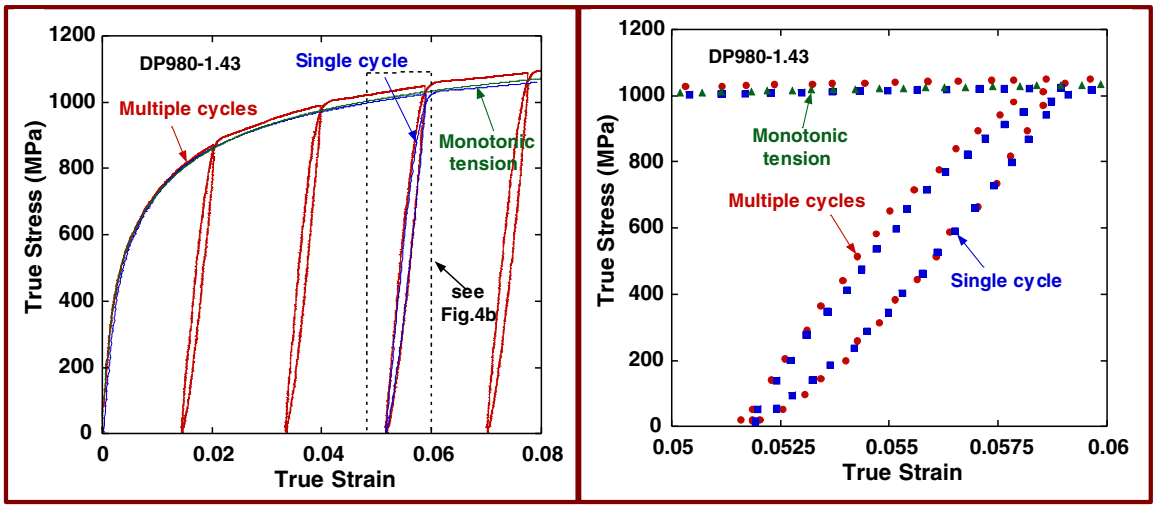

(a) (b)

Figure 1.12: The effect of repeated cycles on the loading-unloading tests [Sun and Wagoner, 2011] a) Four-cycle test vs single-cycle test b) Expanded view as indicated on (a), fourth cycle vs first cycle

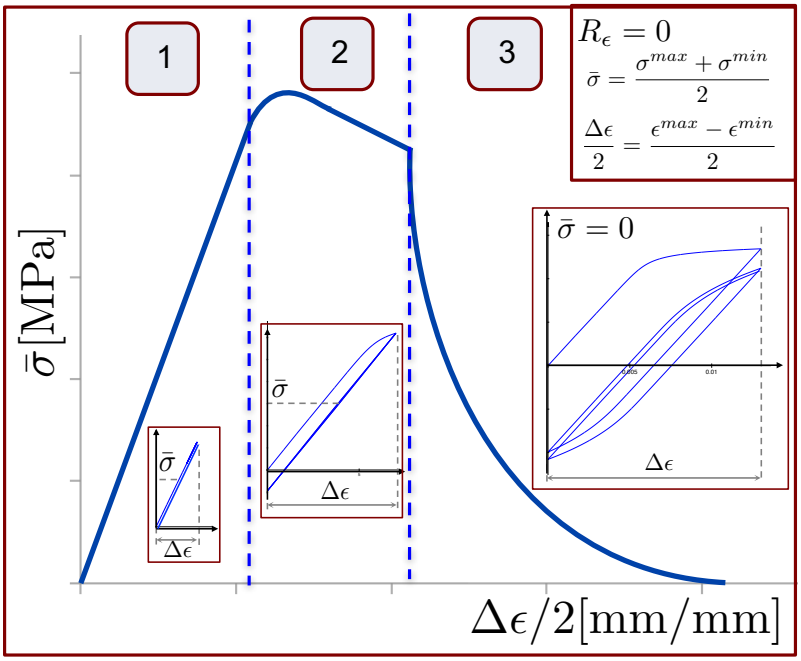

Figure 1.13: Schematic representation of a mean stress relaxation curve for $R_\varepsilon = 0$

the case of Inco718, cyclic deformation has been shown to be localized to planar slip bands, where significant shearing of γ'' particles takes place [Xiao et al., 2005]. Before the present study, a large fatigue database was available but, given that the data is obtained from samples extracted from different areas of several turbine disk blocks, there is an important scatter and it is difficult to accurately assess the true mean-stress relaxation curve. In chapter 2, an original one sample multi-level mean stress relaxation test is proposed, in order to better understand the gradual cyclic softening that leads to non-zero mean stress.

4.2 Multiaxial tests

With the raise in complexity of design and functions of engineering components, the comprehension of the uniaxial behavior of materials isn't sufficient to describe the fatigue lifetime. Modern fatigue lifetime prediction models include a multiaxial description of the behavior of materials identified based on experiments with complex loadings at different degrees of multiaxiality [Sines, 1961; McDiarmid, 1985; Papadopoulos, 1987]. Rotating parts in turbo-engines, like turbine or compressor discs, are typical examples that undergo fatigue loading and experience multiaxial stress states. Moreover, given their variable functioning in service, one must combine the understanding of low cycle fatigue (ground-to-ground cycles) and high cycle fatigue (vibratory) in regions with high biaxialities and high mean-stresses [Bonnand et al., 2011; Gaborit, 2015].

Advances in material testing equipment during last 30 years have enabled to develop multiaxial testing facilities allowing for the study of the behavior of materials and structural components by applying loads representative of the service lifetime. Many different multiaxial tests types have been used over the years, some of which being described in the following. An option was multiaxial fatigue tests in combined tension-compression, flexion and torsion [Gough and Pollard, 1935; Sines, 1961; Andrews and Ellison, 1973; Lasserre and Froustey, 1992; Kallmeyer et al., 2002; Delahay and Palinluc, 2006]. Another popular option is to use thin-walled tubes subjected to axial load combined with torsion or internal/external pressure to create biaxial stress states [Shiratori et al., 1979; Lefebvre et al., 1983; McDiarmid, 1985; Dietmann et al., 1989] and on Inco718 [Worthem et al., 1989; Bonnand et al., 2011]. The downside of this type of test is that they are difficult to obtain and are limited to positive, non-symmetrical loadings. Moreover, this type of tests is not suitable for large strain studies of anisotropic materials, because of buckling and necking instabilities which may arise before very large strains are attained [Makinde et al., 1992a]. A more easily applicable solution are the symmetrical flexion tests performed on disk samples that create a biaxial traction state [Geiger et al., 2005; Koutiri, 2011], but they only work for proportional loadings. Other studies include a triaxial cubic sample where each side is connected to an actuator [Calloch and Marquis, 1997; Calloch, 1997; Feyel et al., 1997; Calloch and Marquis, 1999]. Present PhD study was performed in the LMT lab on the ASTREE triaxial machine [Cognard et al., 1997], used as a biaxial testing rig. Its description, as well as the experimental protocol, can be found in chapter 4, subsubsection 2.1.2.

All of the aforementioned multiaxial tests have advantages and disadvantages, how-

ever, as mentioned by Demmerle and Boehler [1993], the most realistic experimental method to create a known in-plane biaxial stress state is the direct biaxial test on cruciform specimens as developed by, for example, Shiratori and Ikegami [1968], Hayhurst [1973], Kelly [1976], Makinde et al. [1992a] among others. Several reviews of the testing facilities, as well as sample types are proposed by Makinde et al. [1992a], Boehler et al. [1994], Hannon and Tiernan [2008]. In order to be able to properly identify material constitutive laws from biaxial tests data, various testing protocols and types of cruciform specimens have been proposed in the literature [Pascoe and De Villiers, 1967; Shiratori and Ikegami, 1968; Wilson and White, 1971; Makinde et al., 1992a; Demmerle and Boehler, 1993; Itoh et al., 1994; Doudard et al., 2007; Bellett et al., 2011]. The focus of these tests vary from thermal fatigue [Rezai-Aria et al., 1988; Sermage, 1998; Poncelet et al., 2010; Rupil, 2012], crack initiation and propagation [Brown and Miller, 1985; Frémy, 2012; Sadriji et al., 2016], fatigue of pressurized reservoirs [Mathieu, 2013] or other complex thermo-mechanical loadings in aeronautics and aerospace applications [Lagoda et al., 1999; Barbier, 2009; Bonnand et al., 2011; Kulawinski et al., 2011a; Gaborit, 2015].

5 Modern measurement techniques

One of the challenges in the development of multiaxial tests is knowing the local load in the Region Of Interest (ROI). Finite element calculations help identify the heterogeneity of the stress distribution in the ROI [Demmerle and Boehler, 1993; Feyel et al., 1997; Calloch and Marquis, 1999; Geiger et al., 2005] and define the transfer function between the loading applied by the machine actuators in terms of force (F_1, F_2) or displacement (U_1, U_2) and the stress and strain state in the ROI [Bonnand et al., 2011]. This estimation may be satisfying under elastic loads, but can be very complex under cyclic, eventually non-proportional plastic loading. Some authors used more complex behavior estimation methods to achieve optimized non-elastic biaxial samples. For example, Makris et al. [2010] used a numerical optimisation technique (sequential quadratic programming or SQP) coupled with a parametrically built finite element model (FEM) to concentrate and initiate damage in the ROI and achieve a uniform strain field by varying the geometrical characteristics of the cruciform specimen.

Thus, the problem of passing from local measurements to the real material behavior is not trivial and the means to obtain this state vary. An option is point-wise strain measurements that can be obtained using adapted extensometers [Makinde et al., 1992b; Sermage, 1998; Kulawinski et al., 2011b] or strain gauges, used since the 1930s, for which a good review was made by Hoffmann [1989]. They give a ”real time” value of the three plane components of the strain, but they correspond to a mean value of the studied zone. In both cases the strong assumption that the zone is homogeneous is made, otherwise there is much difficulty in interpreting these results without a complementary validation method.

An alternative that has grown in popularity in recent years for its versatility and richness in information is full-field measurements by using Digital Image Correlation (DIC)

[Sutton et al., 1983a; Hild and Roux, 2012b]. By using optical cameras directed at the samples, all three components of the strain field can be obtained by derivation from the displacement field on the surface of the ROI, information that is very important when analyzing biaxial tests [Périé et al., 2002; Poncelet et al., 2010; Rupil, 2012]. DIC can also be used to assess out of plane displacements when using two or more cameras, with the technique known as stereo digital image correlation [Geiger et al., 2005; Frémy, 2012; Mathieu and Hild, 2013; Gaborit, 2015; Pierré et al., 2017]. The principles, as well as the different types of DIC will be presented in the following.

5.1 Digital Image Correlation

Digital Image Correlation (DIC) is a technique that has as end result the full-field displacements of a loaded sample or structure based on the use of imagery. Since the first use in experimental mechanics in the early '80 [Lucas and Kanade, 1981; Sutton et al., 1983a; Chu et al., 1985], this technique has evolved considerably and is extensively used both in the academic field [Sutton et al., 2009; Hild and Roux, 2012b] and in the industrial world [Desmars et al., 2004]. As other methods such as photoelasticity [James et al., 2003] or thermoelasticity [Diaz et al., 2004], this method enables measuring without using sensors that are in contact with the sample. Therefore, the surface of the sample is not hidden, and one can use one or several cameras with several DIC algorithms in order to obtain a maximum of information during the experimental test. The displacement measurements obtained with DIC can be used for model validation, model parameter identification [Calloch et al., 2002; Avril et al., 2008; Périé et al., 2009; Grédiac and Hild, 2012], or for controlling mechanical tests [Fayolle et al., 2007, 2008; Fayolle and Hild, 2014; Le Flohic et al., 2014; Carpiuc, 2015].

The technique consists in analyzing a series of pictures in order to quantify the behavior of a surface (or of a body in the case of tomography). The minimum data required for the technique is two images. The first one corresponding to the initial state of the sample, the unloaded state, is called the reference image. The second image corresponds to a deformed state, after the sample was subjected to a mechanical loading. For the DIC computation to be accurate enough, a certain pattern has to be present on the sample (*i.e.* random and contrasting texture). The most frequent pattern, the speckle, is created by applying, for example, white and black layers of paint. Moreover, the characteristic size of the pattern has to be correlated to the physical size of the pixel and to the sought displacement. In certain cases, using paint layers to create the artificial texture is not possible (for example the tests performed at high-temperature or at a microscopic scale). In the first case, the texture can be created by abrasion or by sandblasting [Li et al., 2003]. For the DIC technique used to determine the displacement fields at the microscopic level, using SEM images, the texture can be obtained by applying nano-particles [Berfield et al., 2007] or by microlithography [Allais et al., 1994; Guery, 2014]. In some cases, the natural texture of the material may be enough to perform the computations [Bergonnier et al., 2007].

5.2 Standard DIC

If the reference image is denoted by f and the deformed image is denoted by g (Figure 1.14), the DIC algorithm permits to identify the displacement field $\underline{u}$ that will minimize the gray level differences between the two images. This relationship is written as the conservation of gray levels:

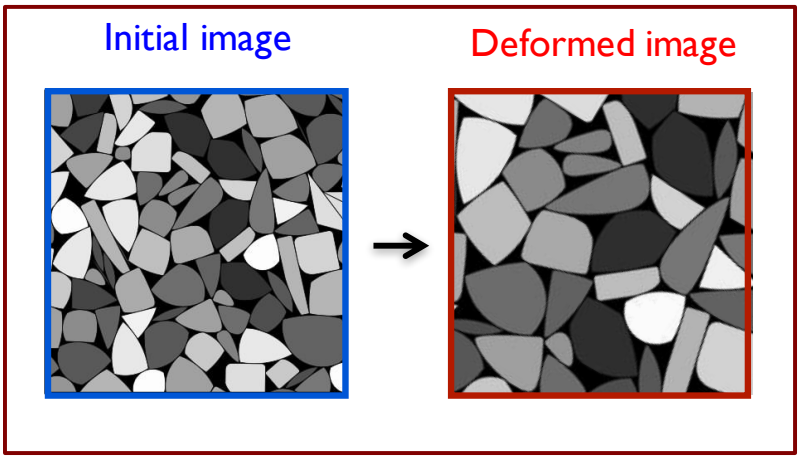

Figure 1.14: Schematic reference image (left) and deformed image (right) which constitute the minimum entry data for a DIC computation

$$f(\underline{x}) = g(\underline{x} + \underline{u}(\underline{x})) \tag{1.24}$$

A functional is written as:

$$\phi(\underline{u}) = \int_{\Omega} [g(\underline{x} + \underline{u}(\underline{x})) - f(\underline{x})]^2 d\underline{x} \tag{1.25}$$

and its minimization on the Ω domain leads to the sought $\underline{u}$. When the sought displacement is a pure translation, the previous minimization is equivalent to maximizing the Cross-Correlation Coefficient (CCC):

$$(f * g) = \int_{\Omega} f(\underline{x}) g(\underline{x} + \underline{u}(\underline{x})) d\underline{x} \tag{1.26}$$

The latter is used for a local DIC algorithm [Sutton et al., 1983b], where the region of interest (ROI) is composed of several sub-images, or zones of interest (ZOI). The local approach consists of maximizing the cross-correlation for each ZOI. Using this approach, as the name suggests, each sub-image is treated independently. For each sub-image, the output of the correlation code is the mean displacement in the middle of the ZOI. In early applications of this method, the measured quantity was a rigid body translation in the physical space [Sutton et al., 1983b] or in a Fourier space [Chen et al., 1993]. Later on, more complex degrees of freedom were taken into account, such as ZOI warping by implementing linear [Chu et al., 1985], cubic and spline [Schreier and Sutton, 2002] interpolations.

5.3 Global DIC

Opposite to the local approaches, a global DIC formulation can be considered [Broggiato, 2004; Besnard et al., 2006b]. Also called Finite-Element DIC (FE-DIC), the global DIC method applies a finite element mesh on the ROI instead of dividing it into separate sub-images. In this approach, the displacement field is treated as a continuum and, as the number of unknowns is reduced, the measurement uncertainty is diminished [Hild and Roux, 2012a]. The displacement is approximated by:

$$\underline{u}(\underline{x}) = \sum_{1}^{n} u_i \underline{\varphi_i}(\underline{x}) \tag{1.27}$$

where u_i are the unknown degrees of freedom and φ_i are the chosen shape functions. If the assumption of small displacements is considered, then $g(\underline{x}+\underline{u}(\underline{x})+\delta\underline{u}(\underline{x})) \approx g(\underline{x}+\underline{u}(\underline{x}))+\underline{\nabla g}\delta\underline{u}(\underline{x})$ and equation (1.26) becomes:

$$\phi(\underline{u}) = \iint_{\Omega} [(g(\underline{x}+\underline{u}(\underline{x})) - f(\underline{x})) + \underline{\nabla g}(\underline{x}+\underline{u}(\underline{x}))\sum_{1}^{n} \delta u_i \underline{\varphi_i}(\underline{x}))]^2 d\underline{x} \tag{1.28}$$

The minimization of the functional leads to:

$$\sum_{1}^{n} \iint_{\Omega} \underline{\varphi_i}(\underline{x})\underline{\nabla f}(\underline{x})\underline{\varphi_j}(\underline{x})\underline{\nabla f}(\underline{x}) d\underline{x}\delta u_j = \iint_{\Omega} (f(\underline{x}) - g(\underline{x}+\underline{u}(\underline{x})))\underline{\varphi_i}(\underline{x})\underline{\nabla f}(\underline{x}) d\underline{x} \tag{1.29}$$

$$\forall j \in [1, n]$$

which can be written using a matrix form:

$$[M]\delta\underline{u} = \underline{b}. \tag{1.30}$$

An iterative algorithm is then used to solve the initial non-linear least squares problem. At each iteration, a gray level interpolation is required to obtain a sub-pixel measurement resolution. This interpolation is one of the causes of the bias of this technique [Schreier et al., 2000]. Acquisition noise is also a source of non-conservation of gray levels [Besnard et al., 2006a].

A big challenge when using DIC is to find the good compromise between the measurement uncertainty and the spatial resolution [Triconnet et al., 2009; Bornert et al., 2009]. One way to reduce the uncertainty is by introducing a mechanical filter, thus eliminating the displacement that isn't mechanically admissible. This method, called global regularized DIC [Tomicevic et al., 2013], allowed the computation of displacement fields in poor contrast images [Taillandier-Thomas et al., 2014; Buljac et al., 2015]. This method has been used both in 2D [Tomičević et al., 2016] and in 3D applications [Buljac et al., 2017].

5.4 Stereo DIC

Even though biaxial tests on cross specimens are assumed to develop planar displacements, it is important to check the out-of-plane motions that can appear during the experiment. Some out of plane movements are related to the experimental protocol, such as a vertical misalignment of the actuators, others may come from design (buckling at high loading) and can be limited but never fully eliminated (ex: Poisson effect). Therefore, a 2D DIC computation can be highly influenced by out of plane movement and without any previous knowledge of its appearance the interpretation of the results can lead to erroneous conclusions. Moreover, unless telecentric lenses are used, a displacement of the sample along the camera axis will produce a false dilation effect that will create a measurement error.

In order to measure the 3D displacements or shape of 3D surfaces, a stereo-correlation technique [Sutton et al., 2009] can be used. More than one camera has to be used (with a different angle of observation) and at least two reference and two deformed images of the same ROI. To reconstruct the 3D displacement, a calibration procedure has to be performed which can vary considerably in difficulty according to the complexity of the studied sample. Most commonly, the calibration phase is performed using specific targets [Beaubier et al., 2014] but, with recent developments, the observed surface can directly be used as the calibration target [Dufour, 2015]. The Matlab code that was used for the stereo DIC computations during the current study was developed during the thesis of Dufour [2015] and has two main stages.

The first stage is the construction of the transformation matrices, which serve in the reconstruction of the 3D model from the 2D images took by the two cameras. For this, an initial guess is needed, therefore a minimum of six points with *apriori* known coordinates are selected by the user on each picture. After the reconstruction of the surface, the software modifies iteratively the position of the two cameras to minimize the global residual.

The second stage is the determination of the surface metrology. In the present work, the shape of interest is modeled using a NURBS formalism [Réthoré et al., 2007; Beaubier et al., 2014], a mathematical model to represent surfaces [Dufour et al., 2015]. Using the known transformation matrices, NURBS control points are moved away on the theoretical surface to obtain the actual shape of the sample. The shape parameters are iteratively changed to obtain a global minimum of the correlation residuals. The main advantage of such a technique is that the parametric description of the surface needs a much lower number of degrees of freedom than the FE-DIC [Piegl and Tiller, 1997]. An even more evolved technique is to recreate a NURBS profile directly from the CAD model with the advantage that the difference between the real geometry and the ideal one can be computed [Beaubier et al., 2014]. Stereo DIC isn't even limited to optical cameras, as it was successfully applied to an infrared camera coupled with an optical camera to analyze 3D thermal loadings on a 304L steel [Charbal, 2017].

5.5 Integrated DIC

All the DIC methods described previously have a computational time that is quite high due to the high number of degrees of freedom (typically in the order of $10^3 - 10^4$). For *a posteriori* image treatment this isn't a crucial issue, but when trying to use DIC in more agile applications, such as the control of a testing machine, this method falls short with the current technological conditions.

One option to achieve fast computations but with enough precision is to use an I-DIC approach (I for Integrated), in the sense that the algorithm uses sought movement as shape functions [Hild and Roux, 2006; Leclerc et al., 2009]. Through this approach, the number of degrees of freedom will be drastically reduced. Moreover, as shown by Le Flohic et al. [2014], the I-DIC algorithm can be implemented on Graphical Processing Units (GPU) [Köhn et al., 2006], which enables the parallelization of the computation, thus reaching considerably reduced computational time. Using such an optimized algorithm, Carpiuc [2015] managed to obtain a control frequency 20 Hz for Nooru-Mohamed type tests in mortar samples using a 6 degree of freedom electromechanical machine.

In the case of I-DIC, determining the displacement field consists of minimizing the functional ϕ (*Eq. 1.26*) over a set of possible displacements $\underline{u}$, where $\underline{u}$ is a linear combination of $\underline{\varphi_i}(\underline{x})$ (*Eq. 1.27*), with the assumption of small displacements. The shape functions $\underline{\varphi_i}(\underline{x})$ correspond, in the case of Le Flohic et al. [2014], to the description of rigid body motion using 3 translations T_x, T_y, T_z and three rotations R_x, R_y, R_z. Nevertheless, these shape functions should be chosen to describe the kinematics that is assumed for the studied case. As rigid body motion wasn't the main loading type for biaxial tests, the shape functions used for this thesis relied on the strain components: homogeneous strains along axis x (ε_{11}) and along axis y (ε_{22}) and homogeneous plane shear γ_{xy}.

Chapter 2

Modeling of uniaxial behavior

Inco718DA is a complex material, therefore important aspects of its behavior are still not completely explained. Phenomena like mean stress relaxation and ratcheting play an important role in determining the lifetime of engine parts, and a better understanding and representation of these aspects would permit an important reduction of the conservatism currently present in design. Efforts were made in this sense both in modeling and in experimental campaigns. The purpose of this chapter is to present the pre-existing uniaxial database and the tests performed during the thesis, along with the initial developments in the plasticity model.

Contents

1 Introduction

Many constitutive material models for the description of cyclic inelasticity have been proposed in the literature over the past few decades [Frederick and Armstrong, 1966; Mróz, 1967; Benallal and Marquis, 1987; Contesti and Cailletaud, 1989; Nouailhas, 1989; Chaboche et al., 1991; Freed and Walker, 1993; Ohno and Wang, 1993a,b; Ohno, 1998; Abdel-Karim and Ohno, 2000; Portier et al., 2000; François, 2001; Bouvet et al., 2004; Chaboche et al., 2012], with a complete review by Chaboche [2008] for a detailed discussion of some other models not mentioned here. Recent models for certain Ni-base superalloys can be found in [Manonukul et al., 2005; Mücke and Bernhardi, 2006; Shenoy et al., 2006] and for Inco718 specifically [Chaboche, 1991; Iyer and Lissenden, 2003; Gustafsson et al., 2011; Becker and Hackenberg, 2011; Bonnand et al., 2011]. Most of them do not cover an important range of modeling temperatures and some are not capable of describing monotonic, as well as cyclic behavior including softening.

Over the past four decades, extensive investigations on the fatigue lifetime of Inco718 have been made. Ever since the 1970s, Fournier and Pineau [1977] studied the uniaxial cyclic stress-strain response and the low cycle fatigue lifetime of conventionally heat-treated Inco718. Among the fatigue lifetime prediction models existing in the literature, many are still based on the notion of a stabilized stress-strain cycle at every point of the structure. It has been shown though that for Inco718, a material which softens cyclically, that the inelastic analysis cannot be based solely on the stabilized cyclic behavior of the material [Chaboche and Cailletaud, 1986; Burlet and Cailletaud, 1986]. In order to have a precise characterization, both the monotonic (initial) behavior and the cyclic (softened) one should be introduced [Chaboche et al., 1991]. This is an important difficulty, given the slow transition between these two states especially at low strain levels in non-symmetrical loading. A second difficulty appears in the description of complex phenomena such as mean-stress relaxation and ratcheting, which have a considerable impact on fatigue lifetime. Ratcheting and mean stress relaxation have been studied for Inco718 in France [Chaboche and Cailletaud, 1986; Burlet and Cailletaud, 1986; Chaboche, 1991; Soulé de Lafont et al., 2015] and abroad [Gustafsson et al., 2011; Becker and Hackenberg, 2011] with various solutions emerging.

The database proposed initially for the current study contains uniaxial HCF tests at different temperatures, loading levels and ratios, and was accumulated over the years by Safran Aircraft Engines (SAE). A typical SAE HCF fatigue test is strain-controlled at a given amplitude until 85000 cycles and, if the sample is not yet broken, the test is continued in force control until fracture. Even if the number of performed tests is important, most of them are scarce in the amount of detailed information, such as the hysteresis loops $\sigma(\varepsilon)$ or the evolution of stress during loading. A type of test that was performed not long before the launch of the thesis is a symmetric strain-controlled test using 3 loading levels and three speeds per level [Soulé de Lafont et al., 2015]. It helped in the understanding of certain phenomena occurring in the case of Inco718DA, and will be detailed in the following.

As mentioned earlier, the main goal of the thesis is the development of a plasticity model that is better adapted for Inco718DA. For each parameter of the model, it is crucial to understand the most adapted type of test for its identification. With this in mind, the existing experimental database was analyzed and it was observed that there were missing elements such as: tests giving more reliable information on the material hardening, tests that could better quantify mean stress relaxation or tests to analyze.

In order to overcome this lack of data, several testing campaigns were performed both in the LMT lab and in the testing facilities of SAE. The biaxial tests are detailed in chapter 4. In the uniaxial case, the experimental protocol, as well as the main results will be presented in the following.

2 Experimental protocol

In the beginning of the study, the first constraint was that the samples should be extracted from the same forged circular block normally used to machine one high-pressure turbine disk. In order to achieve large levels of plasticity in the region of interest (ROI) of the sample, it is needed to induce important reversed loads without causing parasite bending or buckling. Another need is that the maximum load capacity of our uniaxial testing machines should be adapted to the sought load levels.

Based on these criteria, a classic LMT uniaxial sample geometry was chosen [Lemaitre and Chaboche, 1985] (*Fig. 2.1*) with a reduced diameter of 6 mm for a 12 mm long central zone (*Fig. A.6* in Appendix A). This allows for an increase of stress to occur and for cracks to normally initiate in this central zone.

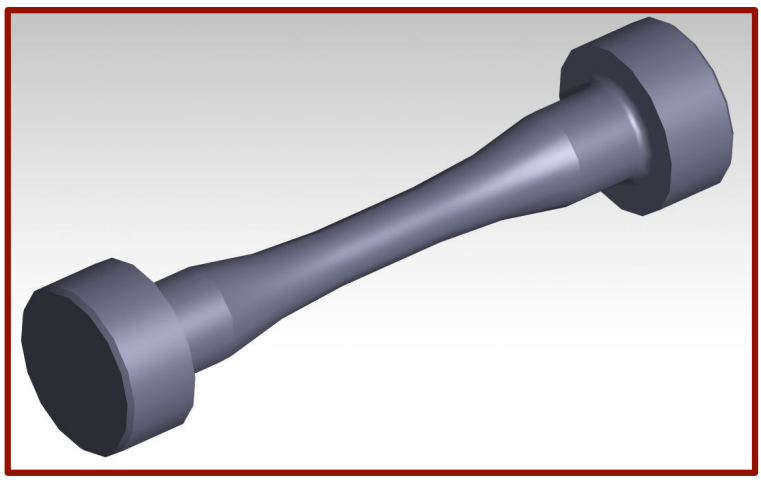

Figure 2.1: LMT uniaxial sample

The uniaxial tests were performed using a servo-hydraulic testing machine with a maximum nominal force of 50 kN. Although more powerful uniaxial machines exist in the lab, this one is sufficient, given that the critical force for monotonic failure for the chosen

sample shouldn't surpass 42 kN. Most of the tests in this campaign were strain-controlled, using a knife-edge extensometer (model 632.13F-23) with a blade distance of 10 mm and a range of ±1.50 mm (±0.15 mm/mm). The measurement uncertainty (standard deviation of the signal at zero load in force control for 100 points) was found for a typical test on our machine and for our calibration at $1.4 \cdot 10^{-6}$ [mm/mm]. Its usage is recommended in the temperature range -100°C/175°C. In order to verify how thermal fluctuations inside the sample occur during loading, the samples were equipped with a thermocouple placed on the ROI, in between the two blades (*Fig. 2.2*). Given that reversed loading will be performed, sliding wedges were used to block the extremities of the samples in place and eliminate the forming of a space between the sample and the grips.

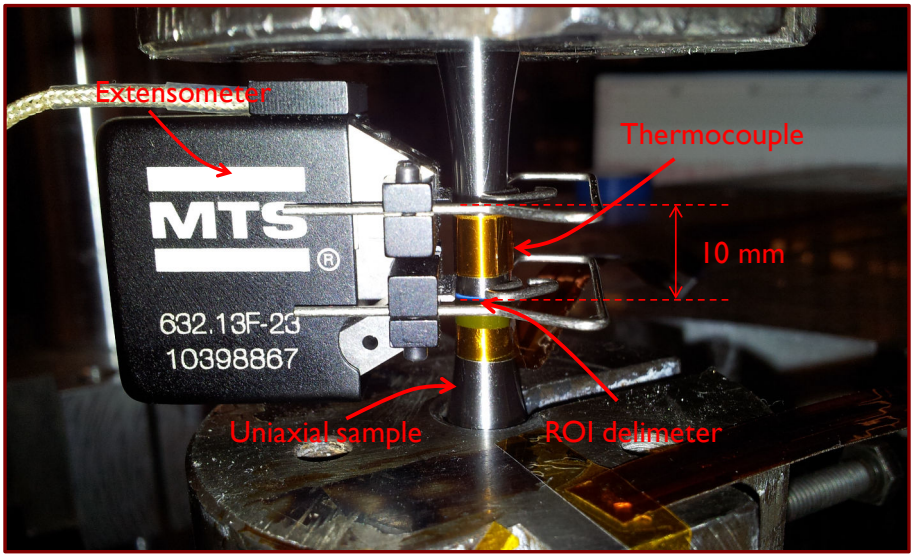

Figure 2.2: Uniaxial experimental set-up

The testing procedures were programmed in the MTS software TestSuite™ or MPE (Multi Purpose Elite), that offered a considerable number of advantages with respect to its predecessor, MPT (Multi Purpose TestWare). One important advantage of this version is the fact that variables can be attributed to certain testing parameters, such as loading level or speed, data acquisition frequency, with values that can be changed before or even during the test. Other improvements include the possibility to use visual control structures (`if` / `while` / `for`) and a finer interpretation of the evolution of the test (more complex graphs, variable monitoring, threshold detection, etc.). Some of these featured are shown in *Fig. 2.3*, where a sample of a control routine is shown in block mode. Another, more linear visualization will be shown in the following, where specific procedures will be explained.

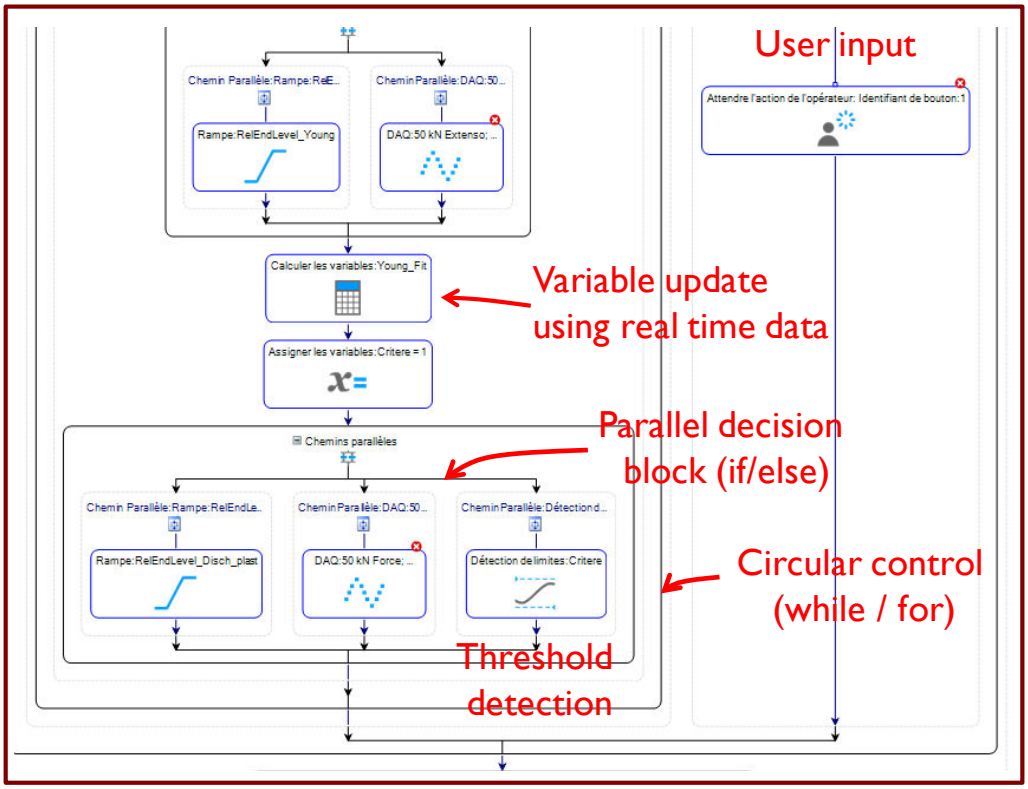

Figure 2.3: MTS software Multi Purpose Elite sample of main features

3 Cyclic tests

One of the most important aspects that needs to be taken into account by a model in the case of aircraft engine parts is the cyclic behavior. A complex cycle may be seen as a sequence of the type: take-off/flight/landing or as a complete turn of the turbine disk. Nevertheless, in the present study we will be referring to a cycle in the classic sense. A standard cyclic test thus translates as the passage from an initial state to a maximum level (either in terms of stress or strain) followed by an unloading to a minimum level and repeat this suite a certain number of times.

3.1 Multi-level cyclic tests with R_ε = -1

A stabilized cycle for a 1D strain-controlled test with strain ratio $R_\varepsilon = \frac{\varepsilon_{min}}{\varepsilon_{max}}$ = -1 may be observed in *Fig. 2.4*. One may also see on this figure the main components used in cyclic plasticity rules such as the stress amplitude $\sigma_a = \frac{\Delta\sigma}{2} = \frac{\sigma_{max}-\sigma_{min}}{2}$, the mean stress $\bar{\sigma} = \frac{\sigma_{max}+\sigma_{min}}{2}$, the strain amplitude $\frac{\Delta\varepsilon}{2}$, the plastic strain amplitude $\frac{\Delta\varepsilon_p}{2}$ and the two ratios R_σ and R_ε.

As already mentioned, prior to the launch of this study, a uniaxial cyclic test was performed and analyzed by SAE during an internship [Soulé de Lafont et al., 2015], in order

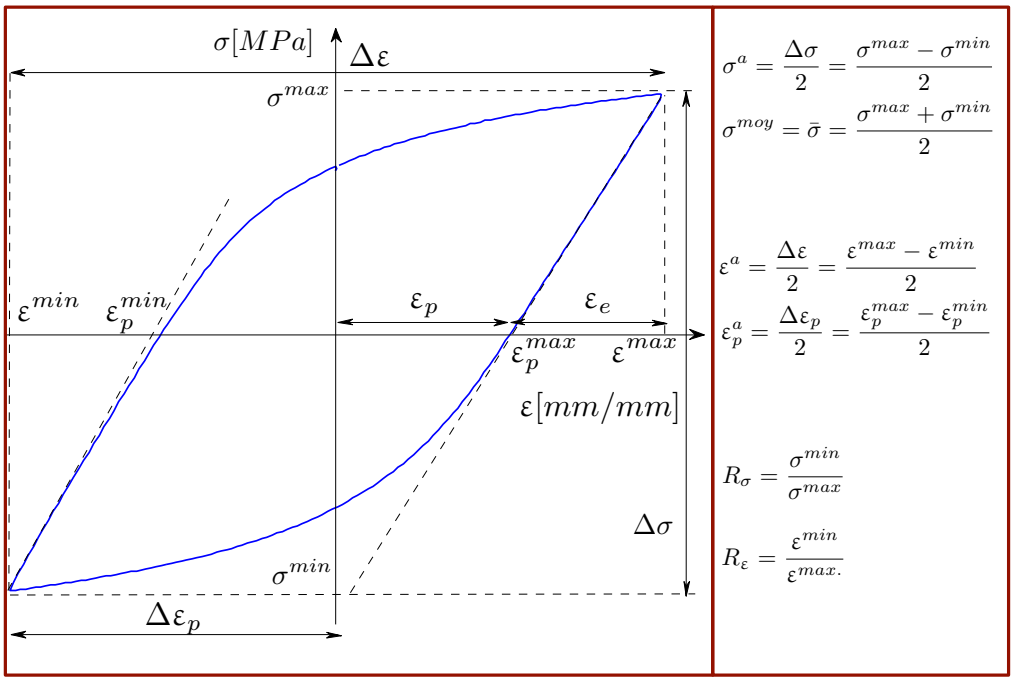

Figure 2.4: Main components used to characterize a cyclic test

to better understand the influence of loading speed on the cyclic behavior of Inco718DA. Thus, a symmetric strain-controlled cyclic test with $R_\varepsilon = -1$ was performed on one sample but for three maximum strain levels (ε_{max}=0.007, 0.009 and 0.011 mm/mm) and three loading speeds each ($\dot{\varepsilon} = 10^{-5}$, 10^{-4} and $10^{-3}s^{-1}$). This test represented the first batch of experimental data that was used for model identification, given the richness of information with respect to other available campaigns, notably $\sigma(\varepsilon)$ loops for all cycles and not only for the stabilized one.

The first test in the uniaxial campaign performed at LMT was a strain-controlled $R_\varepsilon = -1$ multi-level test. The main goals were to validate the LMT experimental protocol, verify the SAE database (by performing the same three levels) but also to enrich the test by adding two loading levels, temperature gradients measurement means and a stress relaxation test at the end. The testing parameters at the end were: $R_\varepsilon = \frac{\varepsilon_{min}}{\varepsilon_{max}} = -1$, $\varepsilon_{\max} =$ 0.005, 0.007, 0.009, 0.011 and 0.013 mm/mm and the loading speed $\dot{\varepsilon} = 10^{-3}s^{-1}$ (*Fig. 2.5*). We chose to perform 100 cycles per level in order to be able to monitor the changes between levels and so that the whole test would be reasonable in terms of total time (in this case 5 hours for the whole, test thus a mean of one hour per loading level).

This first uniaxial test was satisfactory for the following reasons:

- The measurement uncertainty of the extensometer ($1.4{\cdot}10^{-6}$) is sufficiently small for the desired strain levels.
- The experimental protocol (fixing of the sample using the sliding wedges, stability of the fixing system of the extensometer) and the design of our sample ensures a

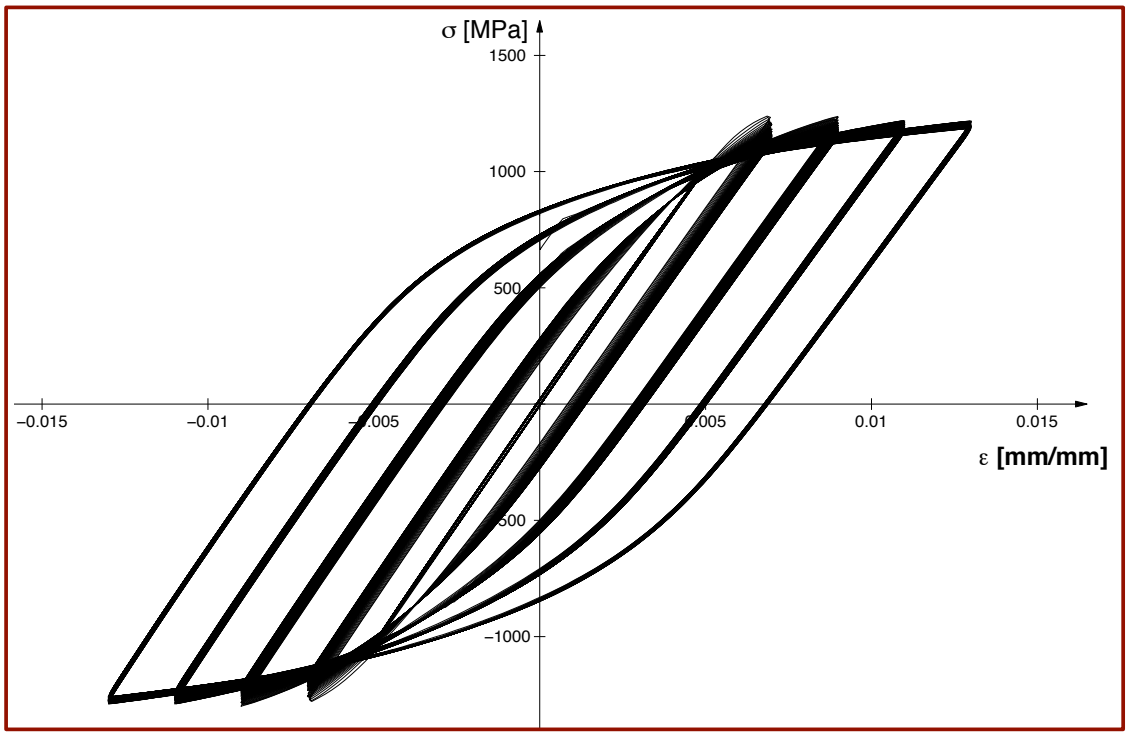

Figure 2.5: Multi-level cyclic test performed at R_ε = -1 in the LMT lab

proper control in tension-compression.

- The obtained stress levels are very similar to those obtained by SAE for the same strain-controlled levels, despite the difference in sample geometry, extensometer and testing machine.
- Even though the stress levels aren't completely stabilized after the 100 cycles, the mean difference in maximum stress levels is 0.5 MPa from one cycle to the other when considering the last 10 cycles of the second loading level ($\pm$0.007 [mm/mm]). When compared to the first 10 cycles of the same loading level, the mean difference in maximum stress levels was 5MPa, so 10 times larger. Based on this observation, we considered 100 cycles as acceptable, at least for the $R_\varepsilon = -1$ case.

Therefore, the uniaxial experimental protocol was considered viable for the other tests, even if some of the testing parameters were changed (number of cycles, strain ratio, strain levels, etc.).

3.2 Multi-level cyclic tests with R_ε = 0

A phenomenon that began receiving a lot of attention these recent years due to its influence over the lifetime of engine parts is mean stress relaxation. It may occur for materials that soften cyclically, during strain-controlled tests with strain ratios $R_\varepsilon = \frac{\varepsilon_{min}}{\varepsilon_{max}} > -1$. As

it was shown during first chapter (*Fig. 1.6*), for a loading between fixed strain limits $\varepsilon_{\max}$ and $\varepsilon_{\min}$, the mean stress $\bar{\sigma} = \frac{\sigma_{max}+\sigma_{min}}{2}$ will diminish with each cycle. Thus, depending on the plastic strain amplitude and the number of performed cycles, the sample may exhibit a partial or even total mean stress relaxation, when $\bar{\sigma} = 0$ for the stabilized cycle.

This phenomenon is usually quantified by plotting the mean stress with respect to the strain amplitude for the zones 2 and 3 described in chapter 1, as may be seen in *Fig. 2.6a*. The blue points are values obtained from stabilized cycles issued from SAE fatigue tests, with the inconvenience that there is an important lack of information such as the cyclic loops $\sigma(\varepsilon)$, the number of cycles to failure, test conditions and others. Moreover, the samples used to perform these fatigue tests were extracted from different zones of a turbine disk block, resulting in a high discrepancy. Due to these limitations, we decided to obtain the mean stress relaxation curve by performing just one original incremental test. In order for the test to be comparable to the existing SAE data, the chosen strain ratio was $R_\varepsilon = 0$.

Even if we performed only one $R_\varepsilon = 0$ test in the LMT laboratory, the control routine was written in the MTS software TestSuite™ in a versatile way, being able to use it to obtain various scenarios. The control routine is shown linearly (without visual blocks) in *Fig. 2.7*. The first part is assigning the main loading parameters such as the number of loading levels, number of cycles/loading level, the strain ratio R_ε or the ε step between levels. Afterwards, a while loop is initiated to run as many times as loading levels chosen. At the beginning of each loop, the loading limits are computed, thus obtaining ε^i_{max}, and with R_ε also ε^i_{min}. An option is to use $\approx$ iso-lifetime calculations, where the number of cycles for each loading level is computed with an upper and lower limit. In this case, the number of cycles for the first level was chosen 1600, which will be cut at the upper limit (1000) and for the others, it will be divided by two each time. Any other rule can be applied of course and if one chooses to perform the same number of cycles per loading level, it is sufficient to choose $N^{Up}_{cyc} = N^{Down}_{cyc} = N_{cyc}$. Finally, the cyclic loading level is performed and then the routine passes to the next level, so it is completely automatic. At the end, the data is exported to data files which can also be configured in terms of exit data, acquisition frequency and other. Given that the test was performed using a triangular loading with a constant strain rate $\dot{\varepsilon} = 10^{-3}s^{-1}$, the time needed to perform each cycle will grow as $\frac{\Delta\varepsilon}{2}$ grows. In order to obtain a constant number of points per cycle, the data acquisition frequency is also calculated at each new level, so there are systematically 200 data points per cycle.

The number of cycles performed for each level is different, given that we chose to perform the experiment considering approximately the same percentage of lifetime for each cycle (2%). The initial maximum strain was $\varepsilon_{\max}$ = 0.005 mm/mm which was incremented by 0.002 mm/mm until $\varepsilon_{\max}$ = 0.019 mm/mm (*Fig. 2.6b*). The last cycles from this test are also represented in black in *Fig. 2.6a*, alongside the fatigue tests.

Another constraint was for the test to take a reasonable amount of time, given that it had to be supervised because of its incremental nature. Thus, for the first level, a number of 1000 cycles were performed and for the next levels 800, 400, 200, 100 and 50 for the remaining ones. The reasoning to reduce the number of cycles for each increase in

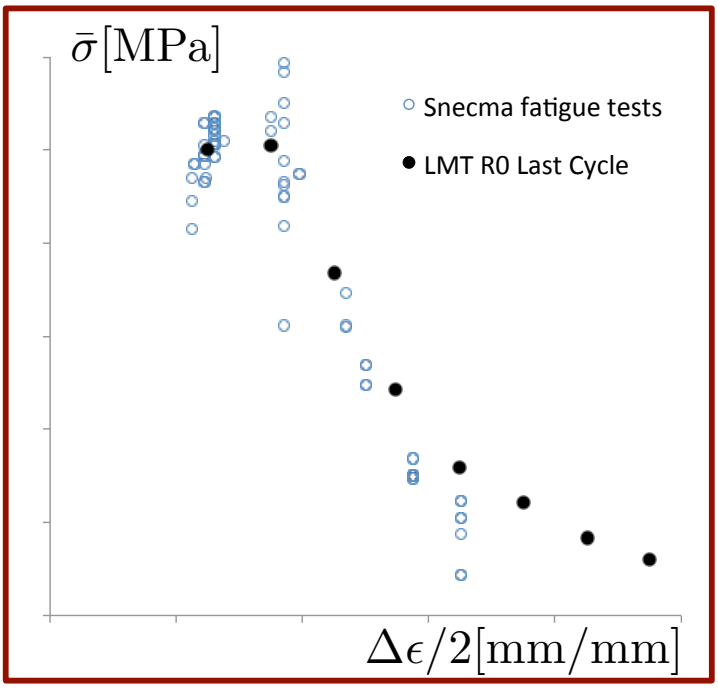

(a)

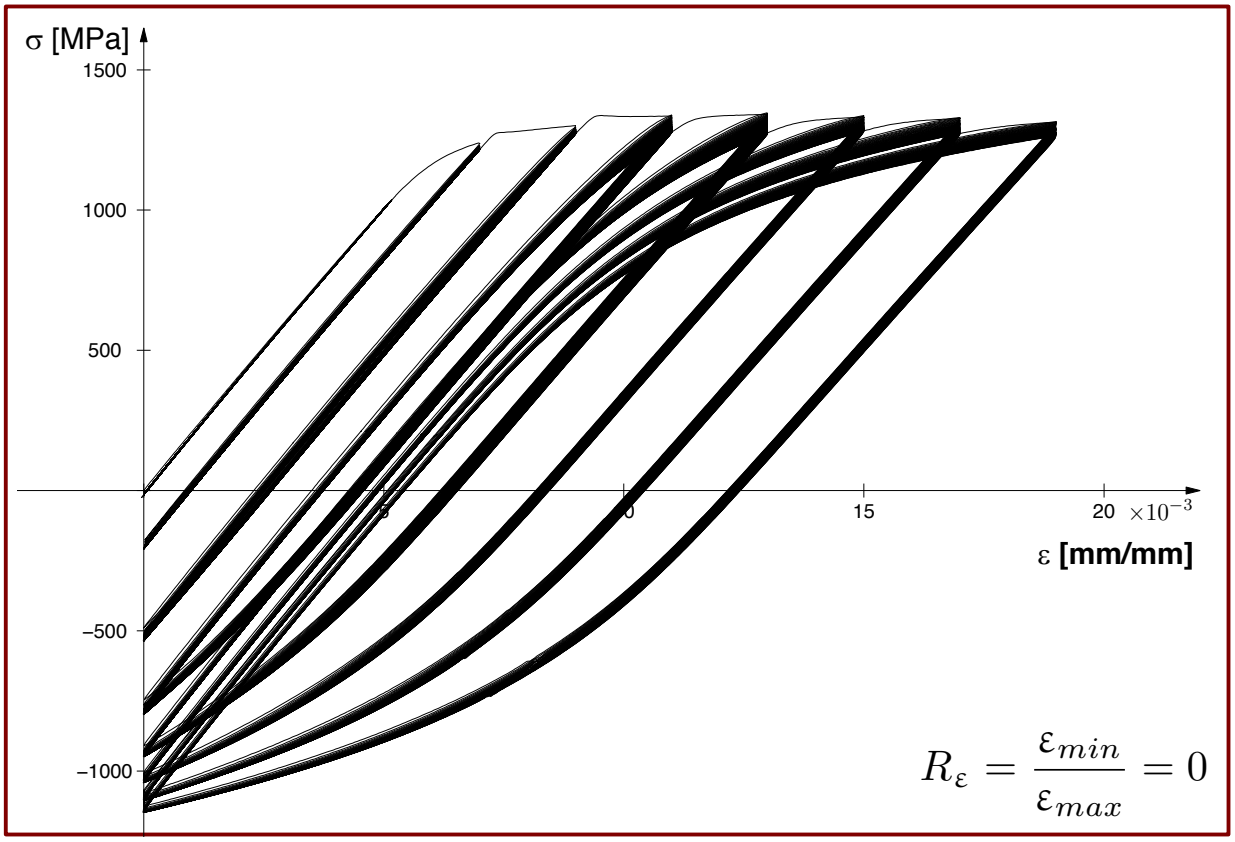

(b)

Figure 2.6: Multi-level cyclic test performed at $R_\varepsilon = 0$ in the LMT lab a) Mean stress relaxation curve b) $\sigma(\varepsilon)$ for all plastic loops

Modeling of partial mean stress relaxation and biaxial mechanical testing of Inco718DA

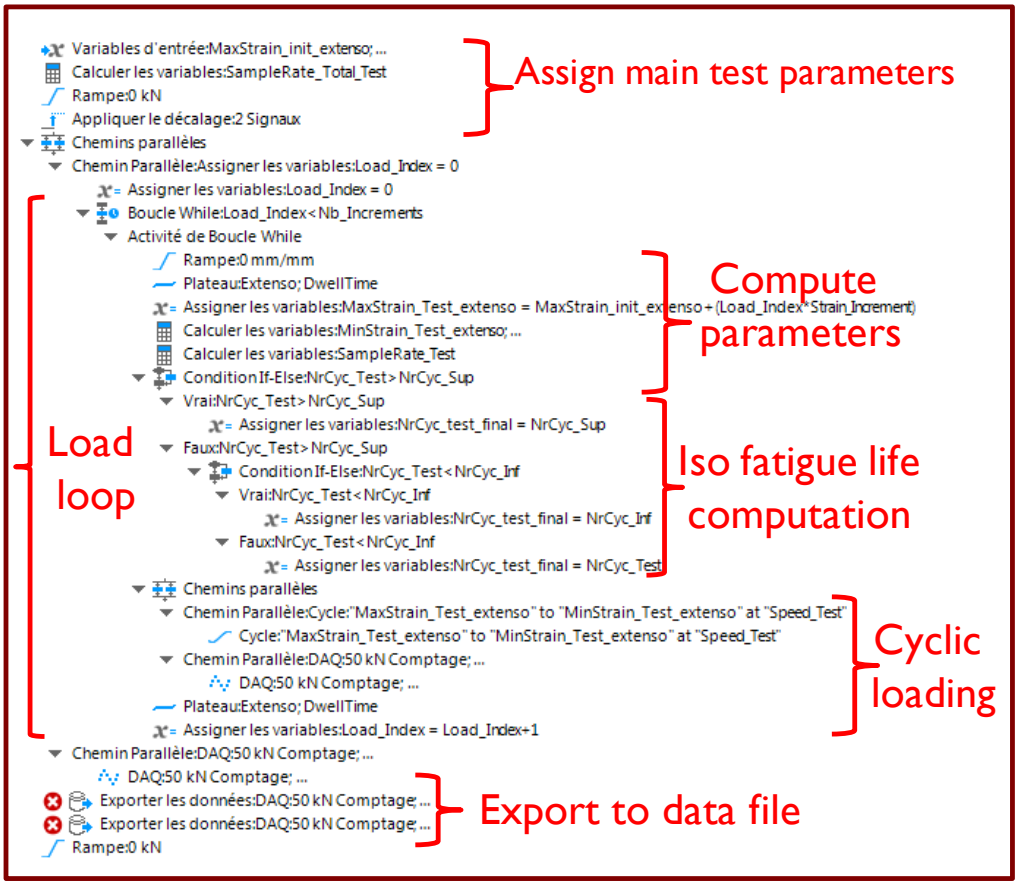

Figure 2.7: MTS software TestSuite™control routine programmed to apply cyclic loads

ε_{max} gave us the possibility to perform more levels without breaking the sample, with the inconvenience that some of the cycles weren't completely stabilized (*Fig. 2.8*). There are two effects that make the conception of such a test difficult. The first one is the fact that increasing the load level causes a reduction of the theoretical number of cycles that can be performed before fracture and the second one is that the more plastification there is per cycle the more cycles are needed to stabilize. The exception from the second rule is when the chosen ε_{max} is so large that total mean stress relaxation is reached after just a few cycles or instantaneously. The ideal scenario is to find a compromise between the two phenomena and make all levels exploitable.

In order to obtain a finer discretization of the mean stress relaxation curve but also be sure of its entire span, another similar test was performed, using the same modular procedure as for the previous test, but with different entry data. The lessons learned from the previous test were that first levels didn't need so many cycles to stabilize and for the upper levels more cycles were needed. In order to limit the total test time, a constant number of 100 cycles was performed per level. The initial maximum strain of ε_{max} = 0.005 mm/mm was chosen identical to the previous one, but the increment was smaller (0.001 mm/mm), in order to obtain a finer discretization of the mean stress relaxation

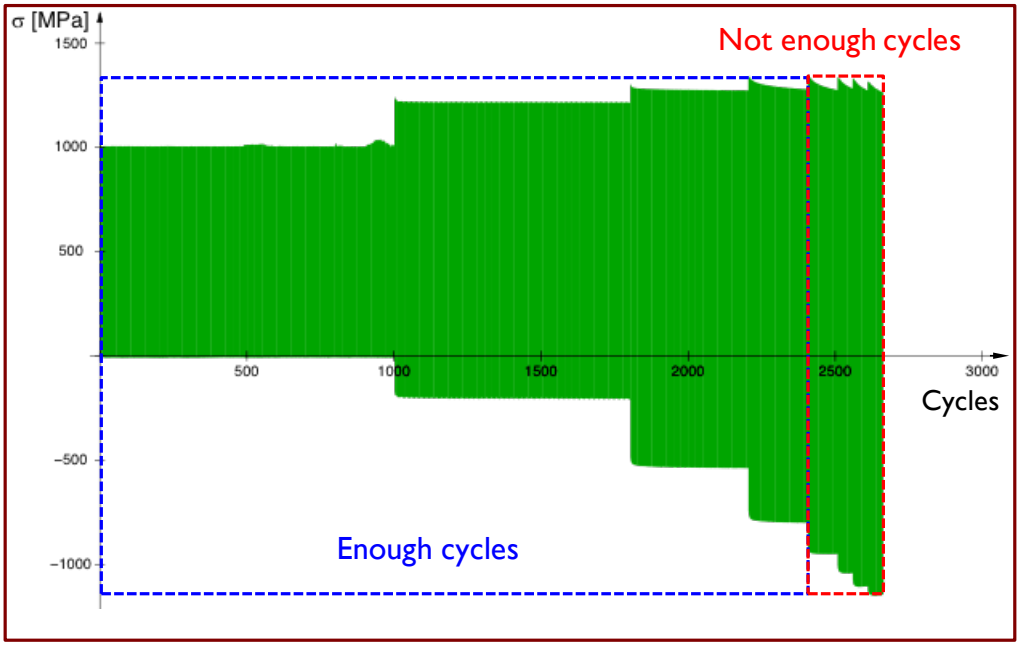

(a)

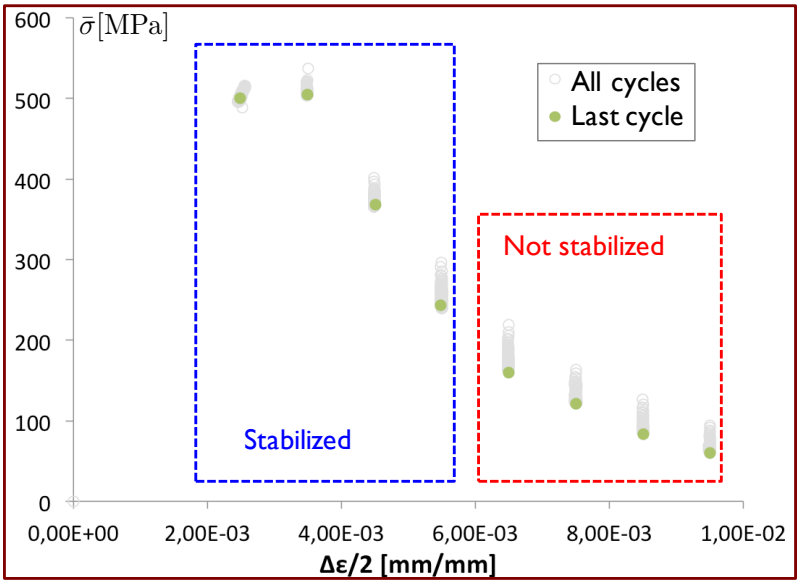

(b)

Figure 2.8: Stabilized and non-stabilized relaxation of $\bar{\sigma}$: a) Evolution of σ with respect to the number of cycles b) Mean stress relaxation curve $\bar{\sigma}(\frac{\Delta\varepsilon}{2})$

curve. Finally, the last level reached was ε_{max} = 0.025 mm/mm, so a much longer span of the curve was obtained (*Fig. 2.9b*). In *Fig. 2.9a* the mean stress relaxation curve may be observed. It is worth mentioning that having reached such large levels of maximum strain ε_{max} and, intrinsically, large levels of strain amplitudes $\frac{\Delta\varepsilon}{2}$, the mean stress relaxation curve was obtained all the way to the point in which it intersects with the abscissa. At this point we have a symmetrical stress level, given that the mean stress reaches zero, or complete mean stress relaxation. For this reason, this second test will be referred to as the complete mean stress relaxation test. Even if after only 100 cycles some of the levels aren't completely stabilized, it is the author's opinion that the beginning and end of the curve shouldn't be affected and that only the middle part might exhibit slightly lower mean stress values. Nevertheless, the main goal of these two tests was to obtain a clearer idea of the mean stress relaxation curve at $R_\varepsilon = 0$, a goal which is considered achieved. Of course, a more precise and expensive description of the phenomena may be obtained by performing complete one level fatigue tests on samples obtained from the same area of the forged block in order to obtain a more precise description of the mean stress relaxation curve.

4 Memory effect dependency of the kinematic hardening rule

The behavior of Inco718DA has certain particularities that represent important modeling challenges. One level of the R_ε=-1 multi-level test may be seen in *Fig. 2.10a*, revealing that the material softens cyclically and that there is a slight tension-compression asymmetry (both in stress levels and in the softening rate. Moreover, one can see that the cyclic loops are "sharp", in the sense that the exit out of the elastic domain is done with a high modulus. What is more interesting is that for those same sharp cycles we are already in an assumed saturated plasticity domain on the cyclic plasticity curve (*Fig. 2.10b*).

This type of behavior isn't usually taken into account by classic plasticity models. For example, the non-linear kinematic hardening rule of [Frederick and Armstrong, 1966] ($\dot{X} = \frac{2}{3}C\dot{\varepsilon}^p - \gamma X\dot{p}$ - in 1D) can represent a saturated cyclic plasticity curve with a maximum saturated stress of $\sigma = \sigma_y + R_\infty + X_\infty$ ($X_\infty = \frac{C}{\gamma}$) when the cyclic plasticity rule is saturated ($\frac{\Delta\sigma}{2} = \sigma_y + R_\infty + X_\infty \text{ th}\left(\gamma\frac{\Delta\varepsilon_p}{2}\right) \approx \sigma_y + R_\infty + X_\infty$). The inconvenience with this kinematic hardening rule is that the cycles will also be saturated, thus over-estimating stress levels (*Fig. 2.11*).

4.1 Non-saturating kinematic hardening rule

The initial kinematic hardening rule used during this study is the one developed by [Desmorat, 2010a] that uses a power-law backstress where the governing rate is no longer $\dot{p}$, as in the Armstrong-Frederick rule, but the positive part of $\dot{X}_{eq} = \frac{d}{dt}\sqrt{\frac{3}{2}\boldsymbol{X} : \boldsymbol{X}}$. The

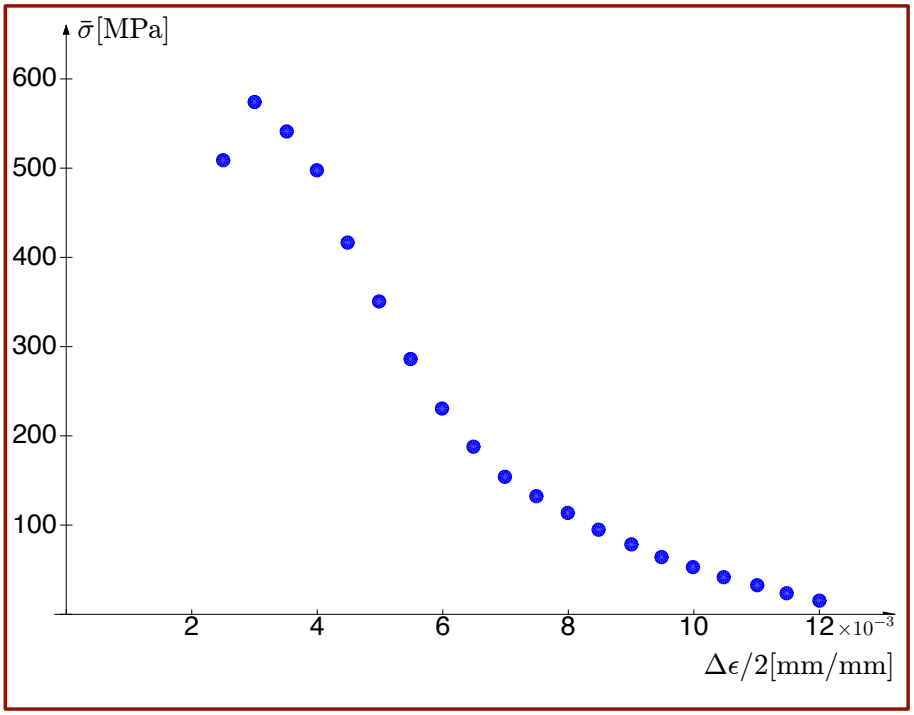

(a)

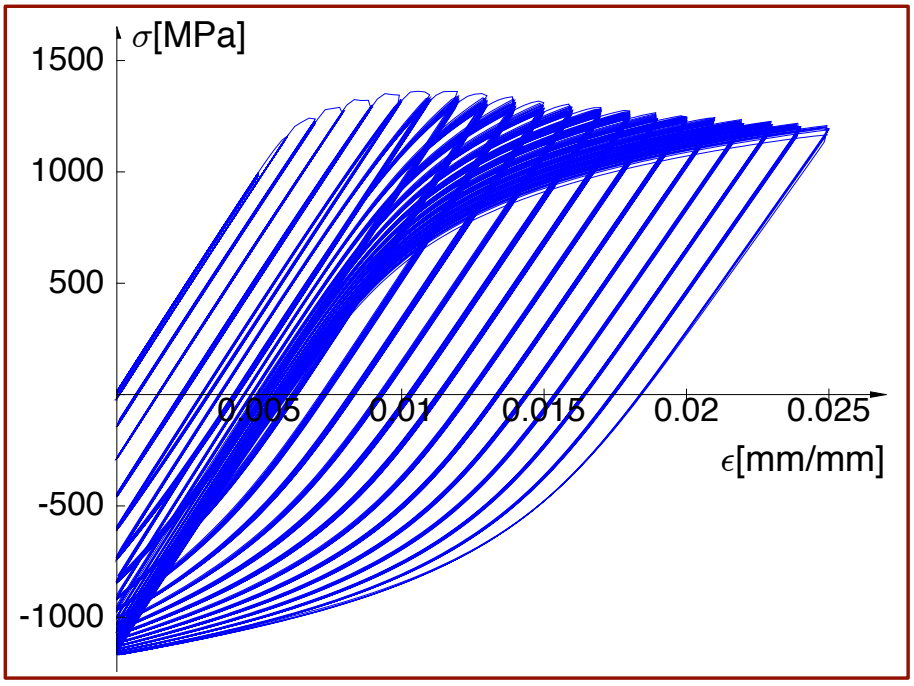

(b)

Figure 2.9: Multi-level cyclic test with $R_\varepsilon = 0$ a) Mean stress relaxation curve b) $\sigma(\varepsilon)$ for all plastic loops

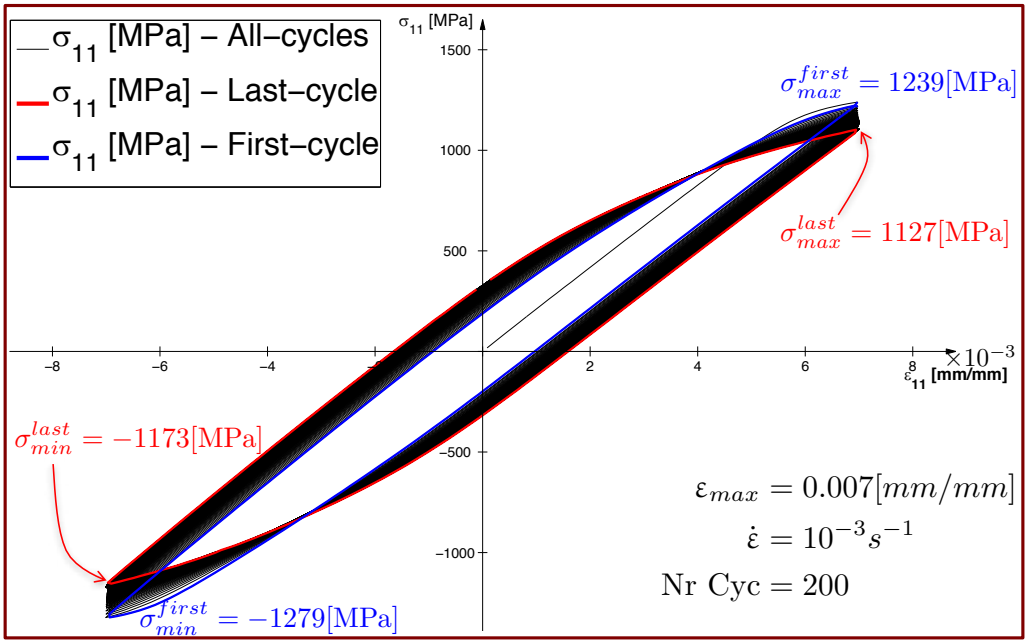

(a)

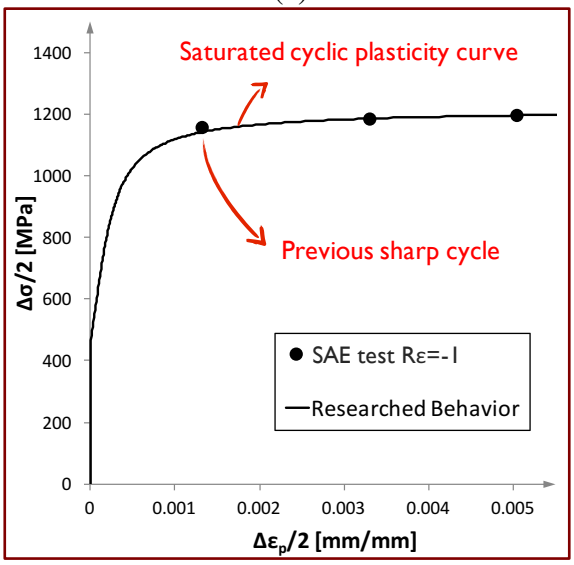

(b)

Figure 2.10: Cyclic behavior at $R_\varepsilon = -1$ for Inco718DA a) "Sharp" cyclic loops b) Saturated cyclic plasticity curve

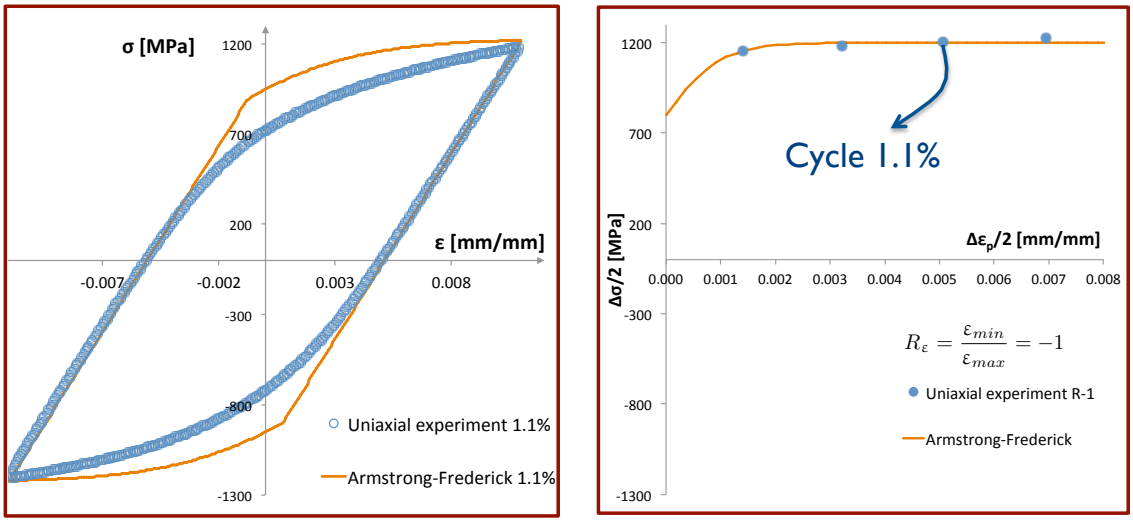

(a) (b)

Figure 2.11: Modeling the multi-level $R_\varepsilon = -1$ test performed in the LMT lab by use of the Armstrong-Frederick kinematic hardening rule a) Stabilized cycle b) Cyclic plasticity

description of $\dot{\boldsymbol{X}}$ is given in *Eq. 2.1* in the isothermal case and will be given as such in all future references.

$$\dot{\boldsymbol{X}} = \frac{2}{3} C \dot{\boldsymbol{\varepsilon}^p} - \Gamma X_{eq}^{M-2} \boldsymbol{X} \langle \dot{X}_{eq} \rangle \tag{2.1}$$

This formulation generates sharp cyclic loops but with a cyclic plasticity curve that is also non-saturating (of power-law type). The used material parameters are C, (*Fig. 2.12a*) which is given by the tangent modulus when exiting the elastic domain, the exponent M (*Fig. 2.12b*) which is given by the general shape of the loop and Γ which is given by the curvature of the loop (*Fig. 2.13*).

4.2 Memory effect principles

In order to achieve sharp cycles in a saturated cyclic plasticity domain, we have introduced into the model an approach similar to the one used by [Chaboche et al., 1979] and extended by [Ohno, 1982], which is the memory surface of the plastic strain. The principles behind the memory surface, as well as the governing evolution equations, were presented in chapter 1, subsection 3.4. In the following, some memory effect properties will be detailed, given that they will be used in different ways in the composition of the model.

The governing equations used in the description of the memory effect hypersphere

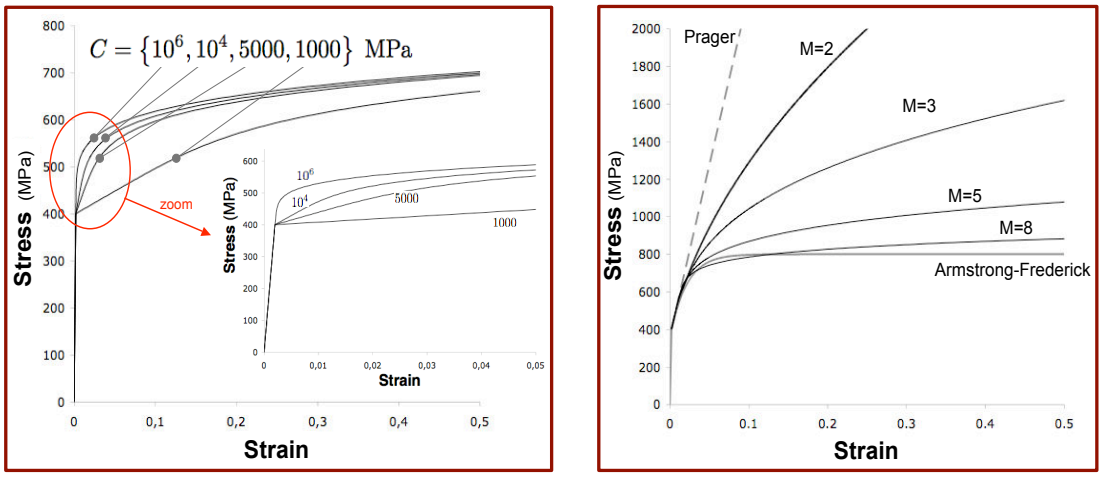

(a) (b)

Figure 2.12: Influence of the parameters of the kinematic hardening rule proposed by Desmorat [2010a] for a 316L stainless steel a) Influence of the tangent modulus C, b) Influence of the exponent M.

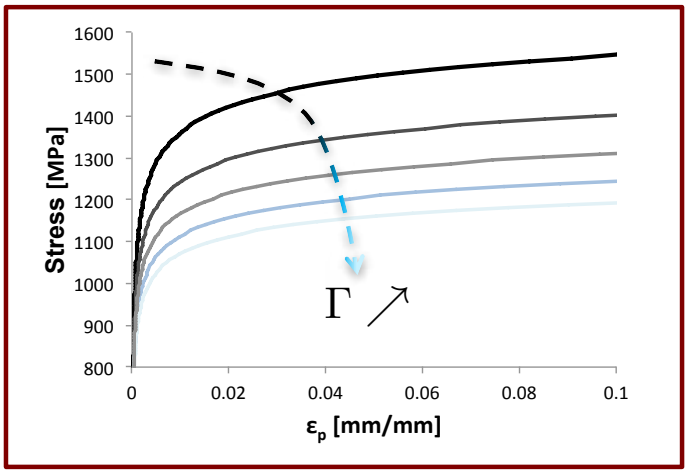

Figure 2.13: Influence of the parameter Γ of the kinematic hardening rule proposed by Desmorat [2010a].

are:

$$\begin{aligned}\mathcal{F} &= \sqrt{\frac{2}{3}}||\boldsymbol{\varepsilon^p} - \boldsymbol{\xi}|| - q \leq 0 \\ \dot{q} &= \eta \mathcal{H}(\mathcal{F}) \langle \boldsymbol{n} : \boldsymbol{n}^\star \rangle_+ \dot{p} \\ \dot{\boldsymbol{\xi}} &= \sqrt{\frac{3}{2}}(1-\eta)\mathcal{H}(\mathcal{F}) \langle \boldsymbol{n} : \boldsymbol{n}^\star \rangle_+ \boldsymbol{n}^\star \dot{p}\end{aligned} \tag{2.2}$$

with η being a material parameter, $\mathcal{H}(\mathcal{F})$ the Heaviside function, p the accumulated plastic strain, and the unit normals being defined as:

$$\boldsymbol{n} = \frac{\frac{\partial \mathcal{F}}{\partial \boldsymbol{\sigma}}}{\left|\left|\frac{\partial \mathcal{F}}{\partial \boldsymbol{\sigma}}\right|\right|} = \frac{\boldsymbol{\sigma}' - \boldsymbol{X}}{||\boldsymbol{\sigma}' - \boldsymbol{X}||} \qquad \boldsymbol{n}^\star = \frac{\frac{\partial \mathcal{F}}{\partial \boldsymbol{\varepsilon^p}}}{\left|\left|\frac{\partial \mathcal{F}}{\partial \boldsymbol{\varepsilon^p}}\right|\right|} = \frac{\boldsymbol{\varepsilon^p} - \boldsymbol{\xi}}{||\boldsymbol{\varepsilon^p} - \boldsymbol{\xi}||} \tag{2.3}$$

so that

$$\dot{\boldsymbol{\varepsilon}}^{\boldsymbol{p}} = \dot{p}\,\frac{3}{2}\frac{\boldsymbol{\sigma}' - \boldsymbol{X}}{(\boldsymbol{\sigma}' - \boldsymbol{X})_{eq}} = \sqrt{\frac{3}{2}}\,\boldsymbol{n}\,\dot{p} \tag{2.4}$$

The material parameter η serves as a weight function between the isotropic and the kinematic parts of the memory surface and, consequently, as a convergence speed. So, for high values of η the evolution is mainly isotropic (in the plastic strain space): the hypersphere is larger in size but moves very little, thus reaching the stabilized value quickly. For small values of η the evolution is mainly kinematic, so the hypersphere is moving more and growing in size less, thus needing more cycles to reach its objective. Under proportional loading, the optimal value of η (η_{opt}) in terms of precision and convergence speed is obtained with the relationship [Gaborit, 2015]:

$$\frac{\eta_{opt}}{1-\eta_{opt}} = \frac{\Delta\varepsilon^p/2}{\overline{\varepsilon}^p} \quad \text{thus} \quad \eta_{opt} = \frac{1 - R_{\varepsilon^p}}{2} = \frac{\Delta\varepsilon^p/2}{\varepsilon^p_{\max}} \tag{2.5}$$

with $R_{\varepsilon^p} = \frac{\varepsilon^p_{\min}}{\varepsilon^p_{\max}}$. The choice of the value of η will therefore be a compromise between precision and speed according to the purpose of the model. For the 1D case, the convergence values of the two variables are given by the equations below :

$$q = \max\left(\eta\varepsilon^p_{\max}, \frac{\Delta\varepsilon^p}{2}\right) \qquad \xi_{11} = \min\left((1-\eta)\varepsilon^p_{\max}, \overline{\varepsilon}^p\right) \tag{2.6}$$

The specific case $\eta = 1$, corresponding to $R_{\varepsilon^p} = -1$ is equivalent to using q as the maximum equivalent value of plastic strain over the entire loading history $\varepsilon^p_{\text{eq,max}}$:

$$\varepsilon^p_{\text{eq,max}} = \max_t\left(\sqrt{\frac{2}{3}\boldsymbol{\varepsilon^p} : \boldsymbol{\varepsilon^p}}\right) \tag{2.7}$$

The case $\eta = \frac{1}{2}$ (corresponding to $R_{\varepsilon^p} = 0$) is often used as a default value [Nouailhas et al., 1985; Hopperstad et al., 1995], although is doesn't necessarily relate to the amplitude of plastic strains.

Even though the memory effect was initially used in the description of the isotropic hardening [Chaboche et al., 1979], it has also been used previously in the literature in the definition of the kinematic hardening [Delobelle et al., 1995]. The way the memory effect is used in the current study is detailed in the following.

4.3 Memory effect like evolution for parameter Γ

An initial identification of the model parameters is achieved quite easily on an available stabilized cycle. The Young's modulus E is obtained classically by computing the slope of the elastic domain. The value of k, which is the yield stress plus the saturated isotropic hardening ($k = \sigma_y + R_\infty$), is estimated from the size of the elastic domain. By following the guidelines represented in *Fig. 2.12*, parameters M and C of the Desmorat (2010) kinematic hardening rule can be identified. For the parameter C, its minimum value can be calculated using *Eq. 2.8*. This value corresponds to a linear hardening passing through the point of maximum plastic strain.

$$C_{min} = \frac{\frac{\Delta\sigma}{2} - k}{\frac{\Delta\varepsilon^p_{\max}}{2}} \tag{2.8}$$

With E, k, M, C fixed, we can analytically compute Γ for a certain cycle (in terms of stress and plastic strain amplitudes) using the following equation, obtained by integrating the model between the symmetric limits of a typical hysteresis loop :

$$\Gamma = \frac{\frac{\Delta\varepsilon_p}{2} - \frac{\frac{\Delta\sigma}{2} - k}{C}}{\frac{1}{2}\frac{\left\langle \frac{\Delta\sigma}{2} - k \right\rangle^M}{MC}} \tag{2.9}$$

By plotting the evolution of the computed Γ points as a function of the maximum plastic strain $\varepsilon^p_{\max}$, a distribution very close to linear may be observed both in the case of Inco718DA and of TA6V [Gaborit, 2015] in *Fig. 2.14*. In order to implement this evolution into the model, the initially non-saturant kinematic hardening rule was replaced by :

$$\dot{\boldsymbol{X}} = \frac{2}{3} C \dot{\boldsymbol{\varepsilon}}^{\mathbf{p}} - \Gamma(q) X_{eq}^{M-2} \boldsymbol{X} \langle \dot{X}_{eq} \rangle_+ \tag{2.10}$$

where $q = \varepsilon^p_{\text{eq,max}}$ is the memory effect variable corresponding to $\eta = 1$. Through this method, no further material parameter is added, Γ simply being replaced by $\Gamma = \Gamma' \varepsilon^p_{\text{eq,max}}$, with non-material parameter Γ' being the slope of the linear distribution. This approach allows to keep the non-saturating cyclic loops, with their corresponding curvatures Γ, while the cyclic plasticity curve will appear as saturated, given that Γ evolves (*Fig. 2.15*).

The kinematic hardening parameters found in this identification are:

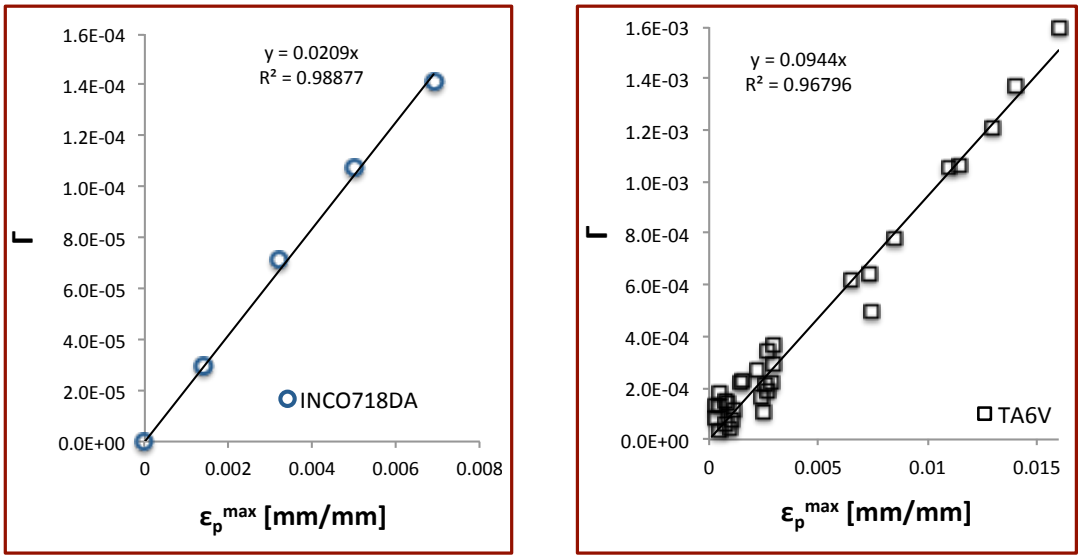

(a) (b)

Figure 2.14: Linear distribution of points $\Gamma(\varepsilon^{p}_{\max})$ a) Multi-level cyclic test with R_ε = -1 Inco718DA b) Similar distribution found for TA6V [Gaborit, 2015]

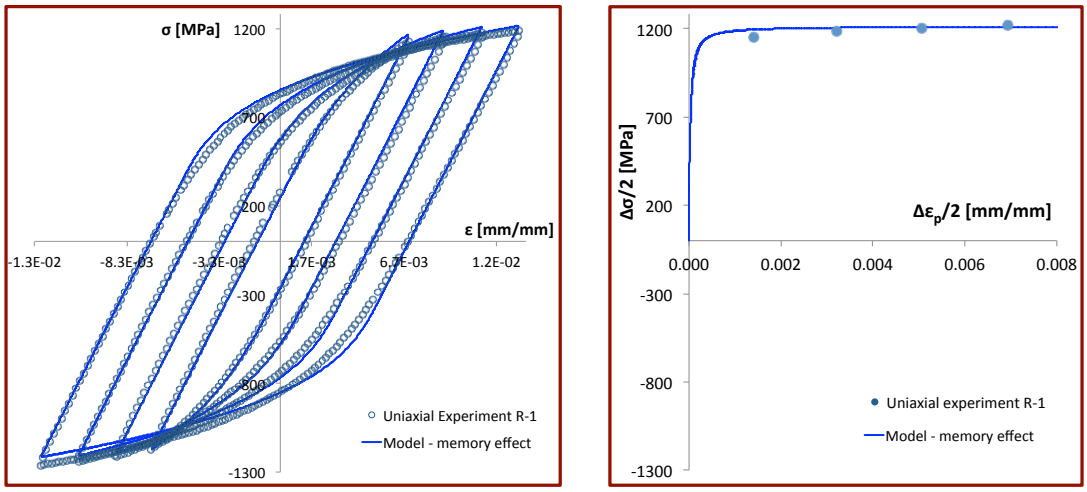

(a) (b)

Figure 2.15: Kinematic hardening rule using $\Gamma = \Gamma' \varepsilon^{p}_{\mathrm{eq,max}}$ for Inco718DA a) Sharp cyclic loops b) Saturating cyclic plasticity curve

E [GPa]	k [MPa]	M	C [MPa]	Γ' [MPa^{-2}]
206	450	3	$2{\cdot}10^6$	$2.09 \cdot 10^{-2}$

Thus, for an experimental test with $R_\varepsilon = -1$ and a symmetrical response, the behavior is quite well reproduced. Certain adjustments have to be made in order to represent the monotonic behavior, which will be presented in the following.

5 Monotonic test with elastic unloads

In order to be able to model the transition between cycles in the case of Inco718DA, its monotonic behavior has to be understood. We disposed of results such as final stresses from the literature and some tests performed at SAE. Unfortunately, the information provided by these tests was incomplete or insufficiently "rich". Thus, based on a classic method used to quantify the two types of hardening, isotropic and kinematic, we decided to perform a test using unloadings down to the replastification limit. The detection of the passage from the elastic to the plastic regime was made with respect to the principle that for Inco718DA, as for many metals, in elasticity the force/strain behavior is linear and becomes non-linear when surpassing the yield stress (classic threshold detection technique).

This type of test is a classic one, usually being used to identify the parameters of damage models by analyzing the change in the slope at every unloading [Lemaitre and Dufailly, 1987]. Nevertheless, for this type of application, a fine detection of the replastification limit is not necessary because the slope is the important information. The main reason we performed this test was to obtain the decoupled description of the isotropic hardening R and the kinematic hardening $\boldsymbol{X}$. For this, we need to plastify as little as possible so that the detection of the lowest point would be as precise as possible, and thus the unloadings as close as possible to purely elastic ones. In order to obtain reproducible results, some authors used the software Labview® coupled with the servo-hydraulic machine controller to impose the same limit at each unloading [Levieil, 2016]. For this PdD thesis, we have implemented a similar but simpler detection method using the MTS software TestSuite™ directly.

First of all, we have written the testing procedure so that it would expect three main parameters: the first strain level at which to perform an elastic unloading ε_s, the strain increment between two unloadings $\Delta\varepsilon$ and the final strain level ε_f. As shown schematically in *Fig. 2.16a*, after reaching each strain level, an unloading will be performed. In order to obtain an unloading as close to purely elastic as possible, the replastification will be precisely detected as the passage from linear to non-linear in the $\sigma(\varepsilon)$ signal. Thus, after beginning each unloading, the slope of the signal E_D is computed *Fig. 2.16b*. We were careful to use enough points for the least mean squares fit, but also not to be too close to the top (to avoid slight load inversion anomalies) or to the non-linear part. Thus, an equation of the type $\sigma = E_D\varepsilon + b_D$ is obtained for each unloading, with E being the slope of the linear fit, or in this case also the Young's modulus, and b being the intersection of

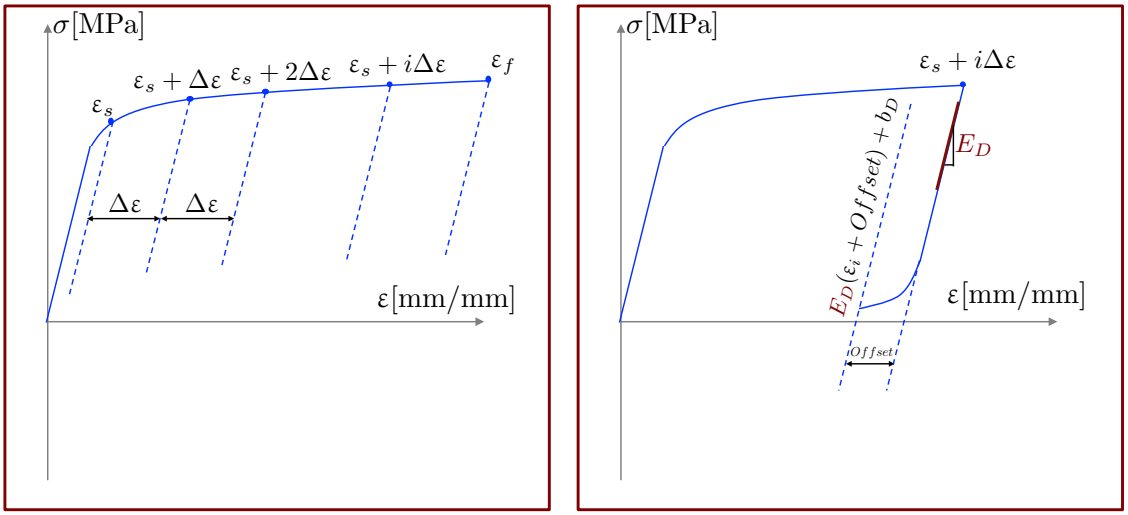

(a) (b)

Figure 2.16: Detail of the method used to perform the monotonic test with elastic unloads

the linear fit and the ordinate. In order to detect the non-linear behavior, a parallel line is used with the equation $E_D(\varepsilon + Offset) + b_D$ by applying the condition:

$$E_D(\varepsilon_i + Offset) + b_D - \sigma_i < 0 \tag{2.11}$$

Therefore, we can detect the first point i that will "stray" from these lines enough to be considered as belonging to the plastic domain. It is important to mention that the choice of this *Offset* is not trivial because if it is too large, we will plastify too much and if it is too small we can be too close to the noise of the extensometer and thus trigger the reload erratically "too soon". Rousset has shown that, for a "large" *Offset* (0.2% in his case), the plastic surface doesn't close [Rousset, 1985]. Other *Offset* values found at different authors in the literature vary between $5 \cdot 10^{-6}$ and $5 \cdot 10^{-5}$ [mm/mm] [Phillips and Lee, 1979; Rousset, 1985; Helling et al., 1986; Wu and Yeh, 1991]. With the model of extensometer that we used, for which we found an uncertainty at zero load of $1.4 \cdot 10^{-6}$ [mm/mm], we chose an *Offset* of $5 \cdot 10^{-5}$ [mm/mm], coherent with the literature [Aubin, 2001].

After detecting the plasticity threshold, the control procedure was programmed to reload to the next point of the type $\varepsilon_s + i\Delta\varepsilon$ (*Fig. 2.17*). The reason why there are 3 unloadings until zero stress level is that given the range of the extensometer ($\pm$0.1 mm/mm) and the known approximate monotonic tension limit for Inco718DA ($\approx$0.2mm/mm), the test was performed in 4 steps. After each step, the extensometer was re-positioned and set to zero, the full test being assembled by accumulating the observed final plastic strain levels for each step. Moreover, two different strain increments $\Delta\varepsilon$ were used along the test ($\Delta\varepsilon$= 0.002 mm/mm for the first and third step and $\Delta\varepsilon$= 0.004 mm/mm for the second and last step) in order to see if there was a considerable difference in the behavior.

Given the important final strain found in this monotonic test ($\approx$23%), the hypothesis

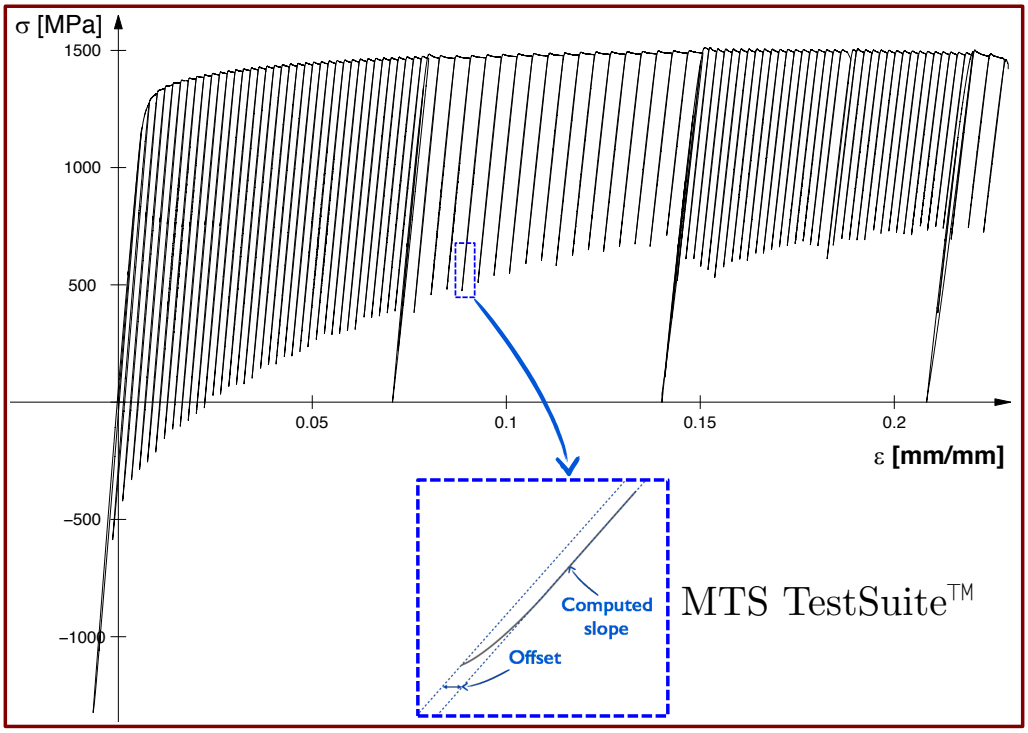

Figure 2.17: Monotonic test with elastic unloadings

of small strains isn't valid and an approach true stress vs true strain would be more appropriate. In the beginning of the thesis, this approach was considered, but in order to be consistent with the computations performed in SAE, the decision was made to work with the strain measured by the extensometer and $\sigma = \frac{F}{S_0}$ where F is the uniaxial force measured by the load cell of the testing machine and S_0 the initial theoretical surface of the uniaxial sample. Nevertheless, in the regime where we performed the cyclic tests (up to maximum 0.025 mm/mm) the true stress/true strain values are very close to the ones obtained in the small strain assumption, thus the error is negligible.

As mentioned previously, the reason we performed this monotonic test with elastic unloads was to obtain the decoupled description of the isotropic hardening R and the kinematic hardening $\boldsymbol{X}$. This identification was used in the early stages of the PhD study but a different path was chosen in the final model. Nevertheless, for academic purposes, the description of this initial identification is given in Appendix B. In the following, the identification of the monotonic behavior using only kinematic hardening will be presented.

6 The evolution of Γ in the monotonic case

Given that Inco718DA is a material that softens cyclically, we can see that the monotonic curve is above the cyclic plasticity one (*Fig. 2.18*). Thus, if we decide to use the previously identified parameters E, M, C, k, then Γ' will be different in order to change the

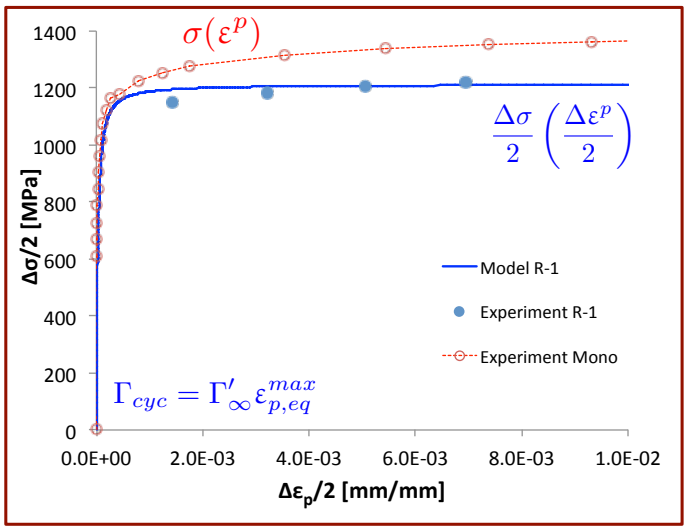

Figure 2.18: Comparison between the monotonic behavior and cyclic $R_\varepsilon = -1$ one

curvature and reach the higher stress level. By developing the model equations, a rough instantaneous value is obtained for Γ between each two successive points:

$$\Gamma_i = \frac{C\frac{\varepsilon_i^p - \varepsilon_{i-1}^p}{X_i - X_{i-1}} - 1}{X_i^{M-1}} \tag{2.12}$$

Given the noise and the precision of the method, it can be seen in *Fig. 2.19a* that the distribution doesn't follow a clear linear pattern, but a tendency may still be observed. The monotonic values used in this figure (the blue dots) are filtered, as neither using the values in the elastic part or at very large strains (larger than 0.1 mm/mm) makes sense for this computation. Nevertheless, it can be seen that by using this identification method, the distribution of Γ vs $\varepsilon^p_{\text{eq,max}}$ is no longer linear, but affine.

In order to correctly represent the monotonic behavior using this kinematic hardening rule, we need to introduce an offset term (Γ_0) in the equation so that an affine evolution can be obtained. The chosen notation for the index was ∞ (Γ'_∞) for the cyclic case (because the plastic behavior tends towards a stabilized state) and 0 (Γ'_0) for the monotonic case (because this is when the first plasticity mechanisms are triggered, starting from an initial, non-plasticized state). An important detail is that Γ is not allowed to become negative, so in the affine law a threshold is introduced, thus the Prager [1949] linear kinematic hardening is recovered for low plastic strains. Thus, the equation for computing Γ in the monotonic case is $\Gamma_{mono} = \langle \Gamma'_0 \varepsilon^p_{\text{eq,max}} + \Gamma_0 \rangle_+$, with $\langle . \rangle_+$ being the positive part (*Fig. 2.19b*). Given that our identified *Offset* is negative, we will be using the positive part of Γ in order to ensure that the dissipation is positive at all times.

The final parameters identified to describe the behavior are given below, with the already presented identifications in grey:

The final monotonic response is shown in *Fig. 2.20* alongside the cyclic plasticity

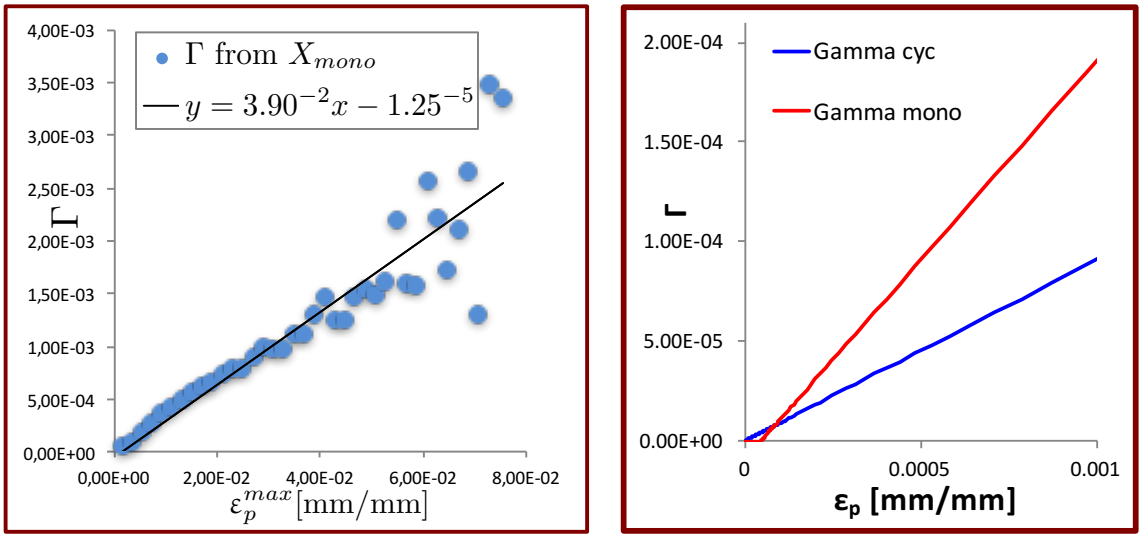

(a) (b)

Figure 2.19: Computation of the affine evolution of Γ in the monotonic case a) Linear fit of the computed Γ for the monotonic points with respect to $\varepsilon^p_{\max}$ b) Comparison between the identified evolution of Γ used in the monotonic and cyclic ($R_\varepsilon = -1$) case

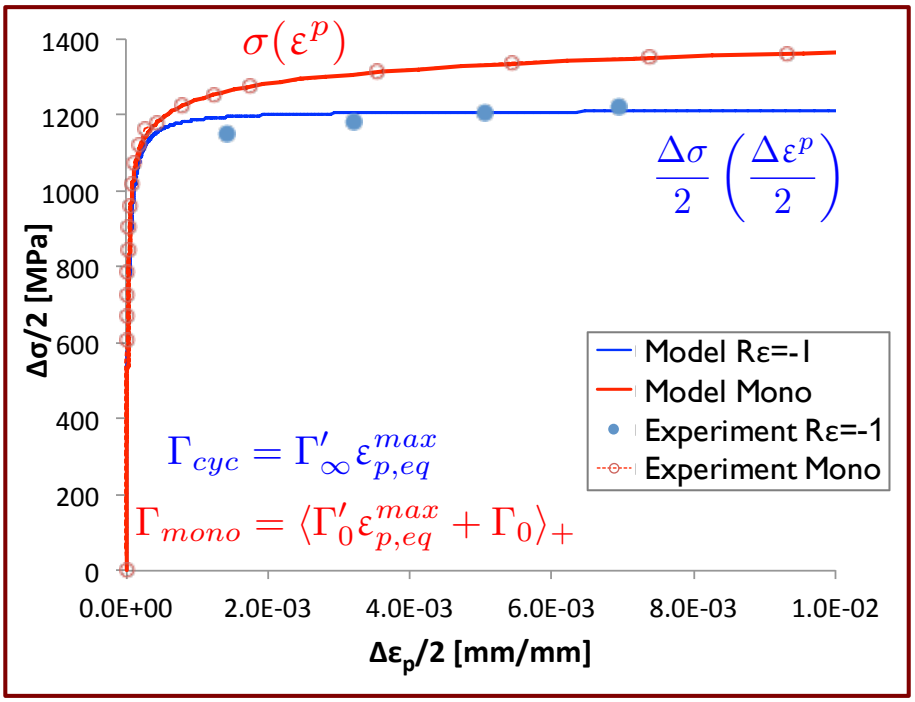

Figure 2.20: Final model in the monotonic uniaxial (Mono) and cyclic plasticity ($R_\varepsilon = -1$) case

E [GPa]	k [MPa]	M	C [MPa]	Γ'_∞ [MPa^{-2}]	Γ'_0 [MPa^{-2}]	Γ_0 [MPa^{-2}]
206	450	3	$2{\cdot}10^6$	$2.09 \cdot 10^{-2}$	$3.9 \cdot 10^{-2}$	$-1.25 \cdot 10^{-5}$

curve at R_ε=-1. It can be noticed that the monotonic behavior is precisely modeled, thanks in part to the extra degree of freedom given by Γ_0. Using this type of approach allows to accurately represent both the monotonic and the cyclic symmetrical loading by performing an independent identification of each one of the two.

7 Conclusions

In this chapter, the main uniaxial data used during the thesis were presented. An important amount of data was already available, such as HCF fatigue test results, but the amount of information for each test was quite scarce (no total number of cycles, no stress or strain evolution, no hysteresis loops). For Inco718, a material which softens cyclically, detailed analysis in the literature [Chaboche and Cailletaud, 1986; Burlet and Cailletaud, 1986] shows that the inelastic analysis cannot be based solely on the stabilized cyclic behavior of the material. In order to have a precise characterization, both the monotonic (initial) behavior and the cyclic (softened) one should be well described by a model [Chaboche et al., 1991].

In order to have a clearer understanding of the behavior of the considered material, as well as avoid the scatter coming from a vast variety of extraction zones and source forged blocks, we realized a short but "rich" uniaxial campaign both at the LMT lab and at SAE, under my supervision, as only dedicated company technicians/engineers can run the testing machines at SAE. Even though the tests were classic in terms of applied loadings, several improvements were made so that the results had a better exploitability. Some of them were related to the used machine control software MTS software TestSuite™ which allowed for the writing of a versatile procedure used both in the LMT lab and in the SAE facilities. It also had a lot of customizable features that served a great deal in the live analysis of the tests as well as their post-processing (more relevant live evolution graphs, experiment parameters treated as variables to be used in the routine, control and repeat blocks such as `while`, `for` and `if`).

In order to obtain the cyclic behavior of the material, several multi-level cyclic tests were performed at different strain ratios (R_ε=-1 and R_ε=0). The cyclic behavior was identified using a kinematic hardening law derived from the one developed by Desmorat [2010b] with elements of memory surface inspired by Chaboche et al. [1979] and Delobelle et al. [1995]. This allowed us to obtain a very good description of the stabilized cyclic response in the R_ε=-1 regime. One of the challenges was to obtain sharp stabilized loops in a saturated cyclic plasticity regime; this has been possible using parameter Γ evolving with respect to the maximum plastic strain $\varepsilon^p_{\max}$, in the back-stress of the Desmorat [2010b] model. The R_ε=0 tests were only presented from an experimental point of view, given that the details concerning this case, as well as the modeling of the incom-

plete mean stress relaxation, is the main subject of chapter 3. An accurate representation of this phenomenon is not yet possible in the formulation of the model described earlier, with the memory effect variable defined as η=1, so that $q = \varepsilon^p_{\max}$.

Using the R_ε=-1 strain-controlled test as an example, a second, load-controlled test was performed in order to quantify uniaxial ratcheting. Even though no modeling was done for this test, it is presented in Appendix C for future post-treatment.

The monotonic response of the material was analyzed by performing controlled elastic unloadings which give a finer description of the monotonic hardening evolution. An initial modeling attempt was made using both kinematic and isotropic hardening laws, described in Appendix B. Finally, the modeling of the monotonic behavior was described, to prepare the way for the complete model that will be presented in chapter 3

Chapter 3

Modeling of partial mean stress relaxation

As it was mentioned in the previous chapter, mean stress relaxation is a complex phenomenon that plays an important role in determining the lifetime of engine parts. Therefore, the plasticity model should be able to represent as accurately as possible the behavior of Inco718DA under cyclic strain loads. Moreover, the mechanisms that lead to complete or incomplete (partial) mean stress relaxation should be better understood in order to better describe these phenomena. The purpose of this chapter is to show an adaptation of the previously presented plasticity model and how it can help to represent the partial mean stress relaxation curve using parameters extracted directly from the data files.

Contents

1 Introduction

The mean stress phenomenon has been studied experimentally since the 70s [Jhansale and Topper, 1971] and its effect on fatigue lifetime has also been analyzed [Lukáš and Kunz, 1989; Wehner and Fatemi, 1991; Arcari et al., 2009; Arcari and Dowling, 2012]. Different good reviews of various kinematic hardening laws exist [Chaboche, 2008; Ohno, 1990] and some focus explicitly on ratcheting and mean stress relaxation effects [Chaboche et al., 2012]. One of the main observations related to mean stress relaxation, as detailed by [Chaboche et al., 2012], is that for low strain amplitudes (and given positive mean strain), the mean stress does not relax completely and there is a steady mean stress remaining. Increasing the strain amplitude leads to a decrease in this stabilized mean stress, until large strain ranges where both the relaxation rate increases and the mean stress reaches zero.

In recent years, a large accent has been put on the comprehension and modeling of mean-stress relaxation [Landgraf and Chernenkoff, 1988; Chaboche and Jung, 1997; Zhuang and Halford, 2001; Landersheim et al., 2011; Chaboche et al., 2012]. It has been proven that an accurate description of this phenomenon is crucial given its influence on the fatigue lifetime [Korth, 1991]. Experimentally, mean stress relaxation is observed when performing strain-controlled fatigue tests at a non-symmetrical strain ratio $R_\varepsilon \neq -1$ [Landgraf and Chernenkoff, 1988; Fang and Berkovits, 1994; Bonnand et al., 2011; Gustafsson et al., 2011]. It is an effect of the non-closing of the plastic loops because of the cyclic accumulation of plastic strain. This cyclic deformation of Inco718 has been shown to be localized to planar slip bands, where significant shearing of γ' particles takes place [Xiao et al., 2005], thus causing the cyclic softening of the material. However, the formation of the planar slip bands during the initial loading of the material is also likely to cause the initial softening of the material since it significantly lowers the resistance to subsequent plastic deformation [Gustafsson et al., 2011]. Landgraf and Chernenkoff [1988] conducted a series of tests on axial steel specimens, with the objective of evaluating the effect on fatigue lifetime of mechanical or thermal processes employed to create residual stresses. They showed a dependence of mean stress relaxation on strain amplitude and material hardness, and they postulated the existence of a strain amplitude threshold below which no relaxation is exhibited. In a study on cyclic relaxation of mean stresses in a nickel-based superalloy, Fang and Berkovits [1994] found a transition between regions of strong and weak relaxation effects around 0.5% strain amplitude. This value is of the same order as the threshold levels in the Landgraf and Chernenkoff [1988] work.

As was detailed in chapter 2 subsection 3.2, one manner in which mean stress relaxation is quantified is by analyzing the mean stress with respect to the amplitude of total strain, as may be seen in *Fig. 3.1*. The empty blue circles are values obtained from stabilized cycles issued from SAE fatigue tests and the black full circles are obtained from the

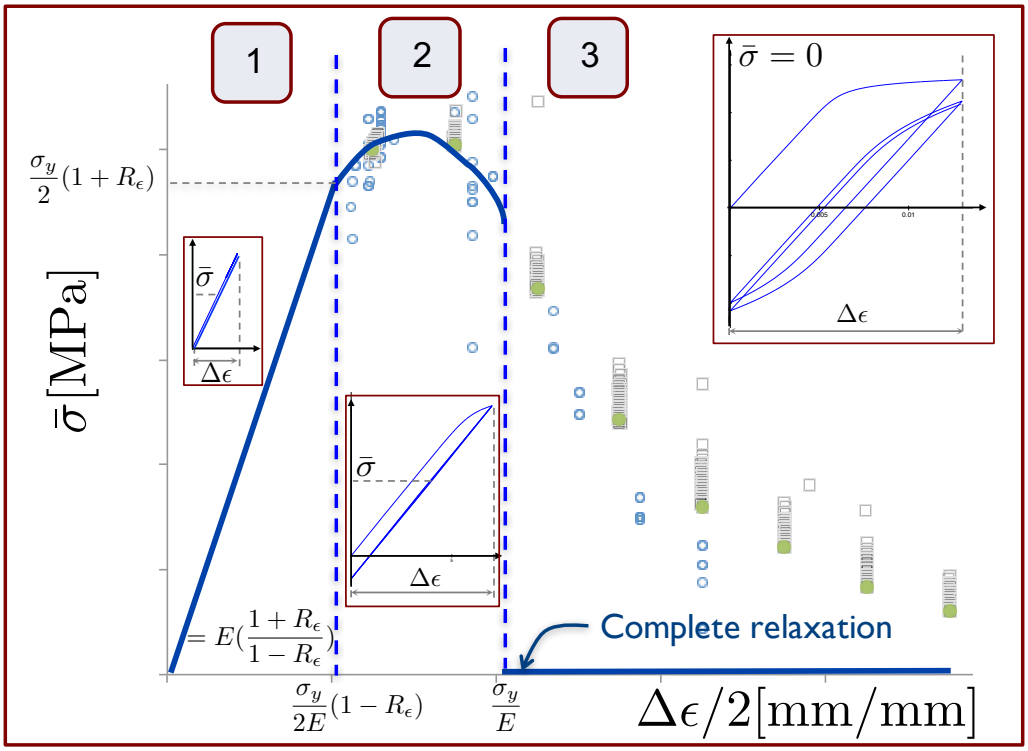

Figure 3.1: Mean stress relaxation curve

last cycles of the multi-level cyclic test with $R_\varepsilon = 0$ that we performed in the LMT lab.

As it may be seen in *Fig. 3.1*, the mean stress relaxation curve is normally composed of 3 zones. The first one, called elastic, corresponds to the case when $\varepsilon_{\max}$ is sufficiently small that both the first loading and the cyclic loading happen in the elastic domain. The slope of the first part of the curve can be computed analytically when developing the cyclic equations, thus we find Slope=$E(\frac{1+R_\varepsilon}{1-R_\varepsilon})$. The limits of this zone can also be obtained analytically, thus $\bar{\sigma}_1 = \frac{\sigma_y}{2}(1+R_\varepsilon)$ and $\left(\frac{\Delta\varepsilon}{2}\right)_1 = \frac{\sigma_y}{2E}(1-R_\varepsilon)$.

In the second zone, called accommodated elastic, the material plastifies during the first loading and then cycles elastically. The end of this zone corresponds to the moment the loading (stress range) surpasses the double of the yield stress σ_y and thus begins to plastify. Therefore, the limit value of $\frac{\Delta\varepsilon}{2}$ of this zone is $\left(\frac{\Delta\varepsilon}{2}\right)_2 = \frac{\sigma_y}{E}$. Finally, the third zone corresponds to the case when the material accumulates plastic strain both at the loading and the unloading part, resulting in mean stress relaxation.

The description of mean stress relaxation is usually done using kinematic hardening laws. For instance, linear kinematic hardening [Prager, 1949] always leads to elastic or plastic shakedown, without describing a relaxation. The model presented in chapter 2, which is based on the [Desmorat, 2010b] hardening rule, has the downside that complete mean stress relaxation will be obtained in zone 3, given a sufficient number of cycles. This effect is common to many rules derived from the non-linear kinematic hardening (NLK) (initiated by [Frederick and Armstrong, 1966]), and is due in part to the fact that

the models tend towards a symmetrical stress state, thus towards $\bar{\sigma} = 0$. This phenomenon is represented schematically by the thick blue line in *Fig. 3.1*. The fact that in the third zone the value of the mean stress is zero states that such a model, given a sufficient number of cycles, will eventually reach a symmetrical state, where $|\sigma_{min}| = \sigma_{max}$.

By superimposing several back-stresses [Chaboche et al., 1979; Chaboche and Rousselier, 1983] each of them using the Armstrong-Frederic (AF) rule but with different parameters, an improvement was made in predicting ratcheting but with little gain in the case of mean stress relaxation representation. One interesting solution in describing the partial relaxation of the mean stress was proposed by [Chaboche, 1991; Chaboche et al., 1991] by introducing a threshold in the dynamic recovery term of the NLK model, for one or several of the superimposed back-stresses. It was justified by the commonly observed existence of a limit of accommodation [Plenard and Fromont, 1988; Pelissier-Tanon et al., 1980], both in terms of mean-stress and of stress amplitude. The structure of the additional back-stress evolution equation becomes:

$$\dot{\boldsymbol{X}} = \frac{2}{3} C \dot{\varepsilon^p} - \xi \left\langle 1 - \frac{X_l}{||X||} \right\rangle_+ \boldsymbol{X} \dot{p} \tag{3.1}$$

Below the threshold, when $||X|| < X_l$, the back-stress evolves linearly because the positive part bracket is zero, thus the dynamic recovery term is null. Above this limit it is a standard AF rule, and it attains the same asymthotic value of C/γ, for $\xi = C/(C/\gamma - X_l)$. The main advantage of a model of this type is to use more than one such kinematic hardening rule in order to stop mean stress relaxation at low levels and let it go all the way at higher strains, as it occurs in reality. The same approach was formulated by [Ohno and Wang, 1993a] in a slightly different way, using the notion of a "critical state for dynamic recovery". It was shown by [Chaboche, 1994] that the two models, though different, can be adjusted to give very similar quantitative responses, both for uniaxial and multiaxial loadings. Other variations on this model were developed, mainly for ratcheting applications [Mcdowell, 1995; Ohno and Abdel-Karim, 2000; Bari and Hassan, 2001]. As was mentioned by [Chaboche et al., 2012], models that are able to capture well ratcheting effects should also have at least the potential for a correct prediction of cyclic mean stress relaxation [Chaboche and Jung, 1997; Hu et al., 1999; Zhuang and Halford, 2001; Landersheim et al., 2011].

A last class of modified models is based on multi-surface approaches, initiated by [Mróz, 1967]. Recent works by [Moosbrugger and McDowell, 1990], and [Mróz and Rodzik, 1996], showed new possibilities. Also, the use of models with discrete memory surfaces like [Chaboche, 1989a,c] offers additional flexibility [Chaboche and Jung, 1997].

In the case of Inco718, good results were obtained in [Chaboche, 1991] using only 3 thresholds. In more recent works, the NLK model is used to capture several strain ratios using 5 back-stress terms and an isotropic hardening [Chaboche et al., 2012]. Some of the results from Chaboche et al. [2012] are presented in *Fig. 3.2* which shows the prediction of the stabilized mean stress as a function of applied strain amplitude for Inco718, for different strain ratios R_ε = 0 in *Fig. 3.2a* and R_ε = 0.25, 0.50, 0.75 in *Fig. 3.2b*. The

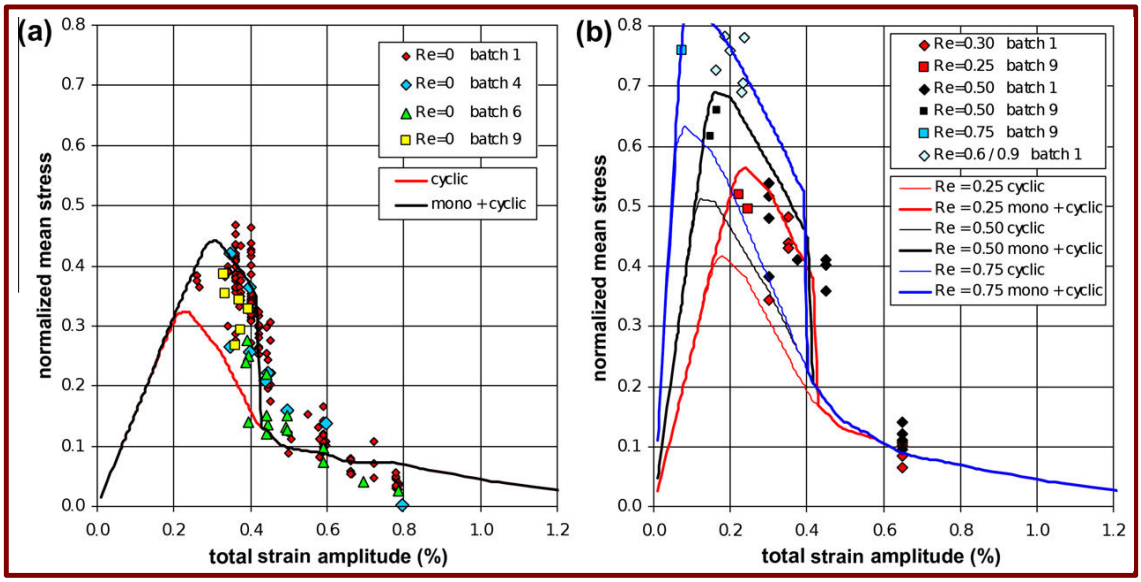

Figure 3.2: Prediction of the stabilized mean stress for Inco718 at 550 °C using a NLK model with 5 back-stress terms and an isotropic hardening as presented by Chaboche et al. [2012] (a) under $R_\varepsilon = 0$, (b) under $R_\varepsilon = 0.25, 0.50, 0.75$ strain-control

model reproduces quite well the experimentally observed facts, in particular the differences between the strain ratios for low strain ranges, and the sudden drop of the mean stress (around 0.4% strain amplitude). Nevertheless, to this authors opinion, the large scatter in the available data, especially at R_ε=0 (*Fig. 3.2a*) makes it very difficult to find the true behavior at iso-material parameters. One way to get a better understanding of the real profile of the mean-stress relaxation curve, is with the multi-level tests on one sample presented in chapter 2 subsection 3.2. The in detail post-treatment of this test will shown in this chapter of the thesis.

Other recent modeling work was done on Inco718 by [Gustafsson et al., 2011], using the Ohno-Wang multi-kinematic hardening model with three back-stresses only. It shows a good prediction of the mean stress evolution and stabilization at non-zero values for $R_\varepsilon = 0$, but only for large strain amplitudes (0.5 and 0.8%). A much more complete model was also presented recently by [Becker and Hackenberg, 2011], based on a combination of the Ohno-Wang model for kinematic hardening and the separation of the inelastic strain into a rate independent and a creep component, including cyclic behavior at high temperature. This model shows good mean stress relaxation and creep or ratchetting.

In the following, we propose an adaptation of the kinematic hardening rule presented in chapter 2, that will result in a more accurate representation of partial mean stress relaxation based on a finer analysis of the $R_\varepsilon = 0$ tests.

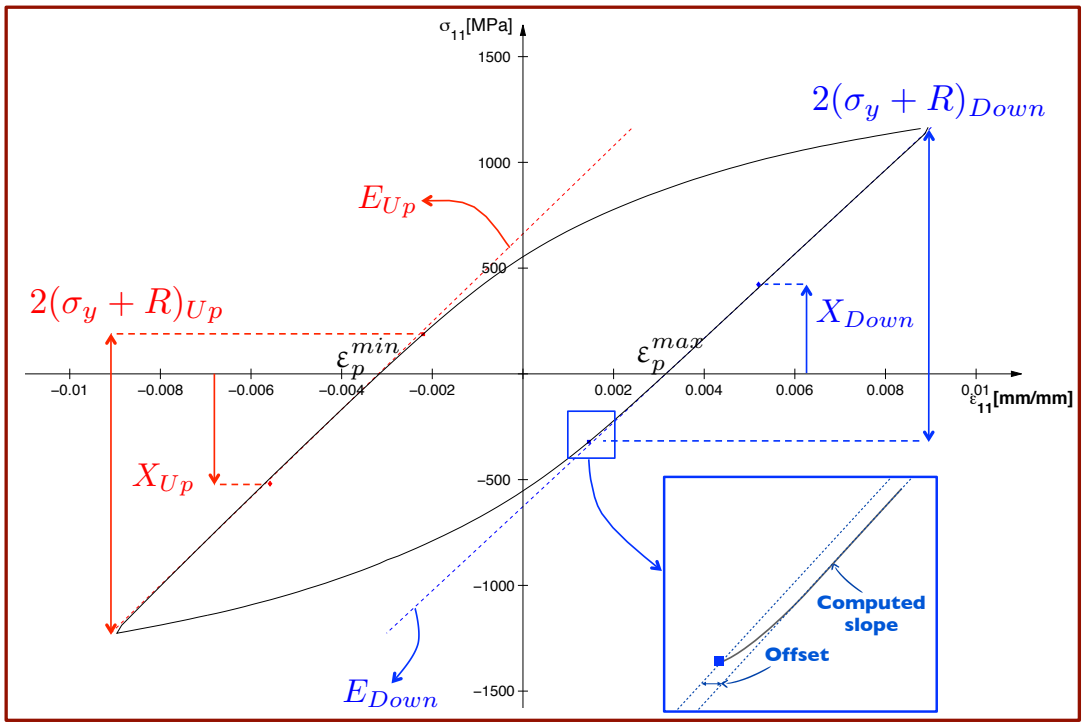

Figure 3.3: Parameter extraction from the hysteresis loops

2 Cyclic hysteresis loops analysis

In order to find a solution for the complete mean stress relaxation represented by the model in the cyclic plasticity zone, a more detailed analysis of the cyclic loops was performed (*Fig. 3.3*).

The analysis technique implies finding the elastic domain of each loop, both at the descending (parameters with the index D for Down) and the ascending (parameters with the index U for Up) parts. The technique is similar to the one used to calculate the elastic unloads in chapter 2, section 5: firstly, the equation of the initial linear zone is obtained by performing a least-squares regression on a sufficient number of data points. Given the noise of the signal when changing from loading to unloading, the first few points are ignored. Thus, for every loop we obtain two equations of the type $\sigma = E\varepsilon + b$ for the ascending and descending part, with E being the slope of the linear fit, and in this case also the Young's modulus, and b being the value given by the intersection of the linear fit with the ordinate. Secondly, the conditions:

$$\begin{aligned} \text{Descending part:} \quad & E_D(\varepsilon_i + \mathit{Offset}) + b_D - \sigma_i < 0 \\ \text{Ascending part:} \quad & E_U(\varepsilon_i - \mathit{Offset}) + b_U - \sigma_i < 0 \end{aligned} \tag{3.2}$$

are used to detect the first point i that will "stray" from these lines enough to be considered

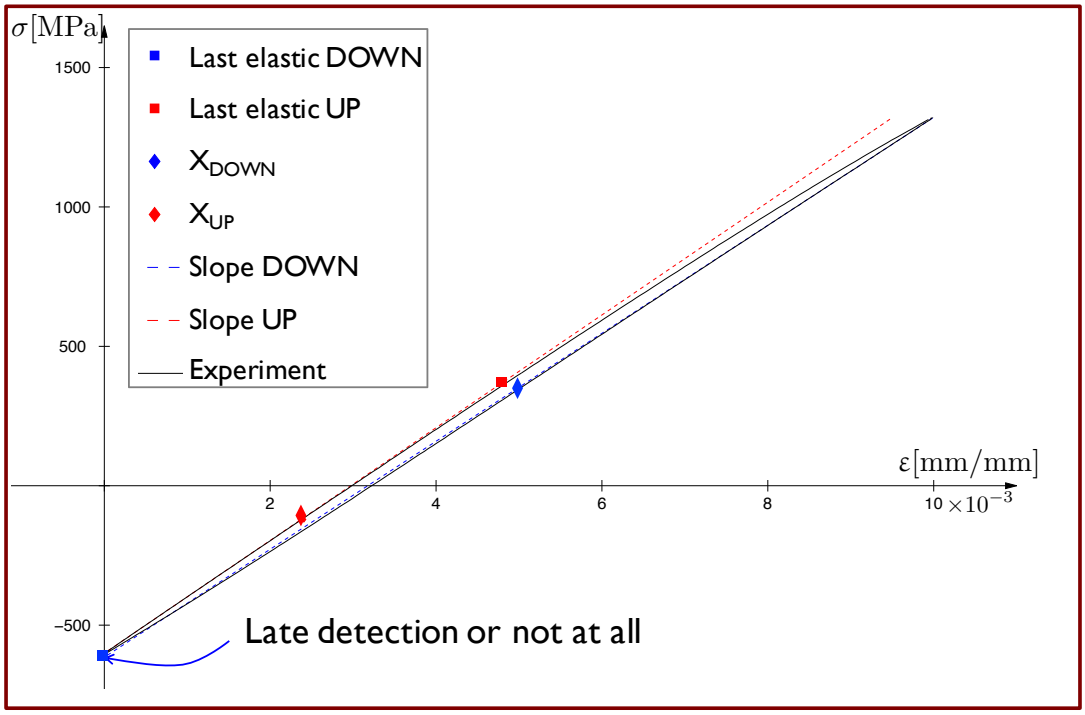

Figure 3.4: Limit of the extraction method for loops with small plastic strains

as belonging to the plastic domain, in the two parts of the loop. The offset value was chosen the same as for the monotonic test with elastic unloads, *i.e.* $Offset = 5 \cdot 10^{-5}$, in order to avoid triggering too soon (because of noise) or too late (by overrating the elastic domain).

Using this approach, the evolution of certain parameters can be obtained, such as the Young's modulus E, the size of the elastic domain, which is the double of the yield stress plus the isotropic hardening $2(\sigma_y + R)$ and the kinematic hardening X, as the position of the middle of the elastic domain.

This type of technique reaches its limit when the loops have a very small plastic zone. Given that a nonlinear zone is barely noticed, especially on the descending part on the loop in *Fig. 3.4*, no point will be detected as belonging to the plastic domain. Thus, in the results shown in the following, completely elastic or hysteresis loops with very small plastic strains have not been included, given that they are not relevant for representing some parameters such as the kinematic hardening.

2.1 R_ε=0

By applying this method to the first experimental test performed at $R_\varepsilon = 0$, we were able to obtain some interesting information concerning the material behavior. Firstly, the evolution of the Young's modulus was obtained (*Fig. 3.5a*). Even if the differences in terms of absolute size are not considerable, the graph being zoomed, the overall tendencies for

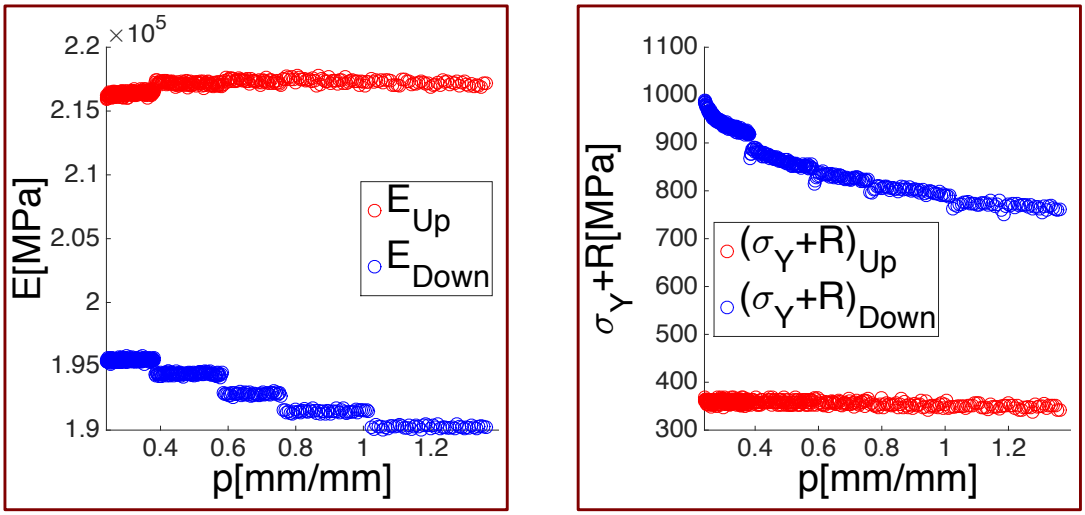

(a) (b)

Figure 3.5: Measured evolution at the ascending and descending parts of the cyclic loops for the first $R_\varepsilon = 0$ test for a) Young's modulus b) Size of the elastic domain

the ascending and descending parts are different. The Young's modulus at the ascending part tends to stay constant and at the descending part it decreases slightly.

The second analyzed variable is the size of the elastic domain, assumed to be the sum between the yield stress and the isotropic hardening $\sigma_y + R$. Similarly to what was seen on the evolution of the Young's modulus, the size of the ascending part is constant over time and at the descending part it decreases (*Fig. 3.5b*). Moreover, the gap between the two is quite important, of at least 400 MPa at all times.

Finally, the difference in the evolution of the kinematic hardening on the two parts of the loops was very important. This may be seen in *Fig. 3.6*, where we compare the kinematic hardening on the descending part (X_{Down}) and the absolute value of the kinematic hardening on the ascending part ($|X_{Up}|$).

This important difference gave us the incentive to consider a model that would represent this dual behavior. As we would see in the following, this type of approach can be responsible for the partial relaxation of the mean stress.

2.2 R_ε=-1

The loop analysis was also applied to the symmetrical strain loading case ($R_\varepsilon = -1$) and may be seen in *Fig. 3.7*. Both the evolution of the Young's modulus and of the size of the elastic domain had lower differences than in the $R_\varepsilon = 0$ case (*Fig. 3.5*). We also have more scatter in the case of these results, given that the acquisition frequency was lower for this test, leading to a less precise analysis.

Considering that the loading is symmetrical in terms of strain, an even closer behavior between the ascending and descending parts of the loops was expected. One of the reasons

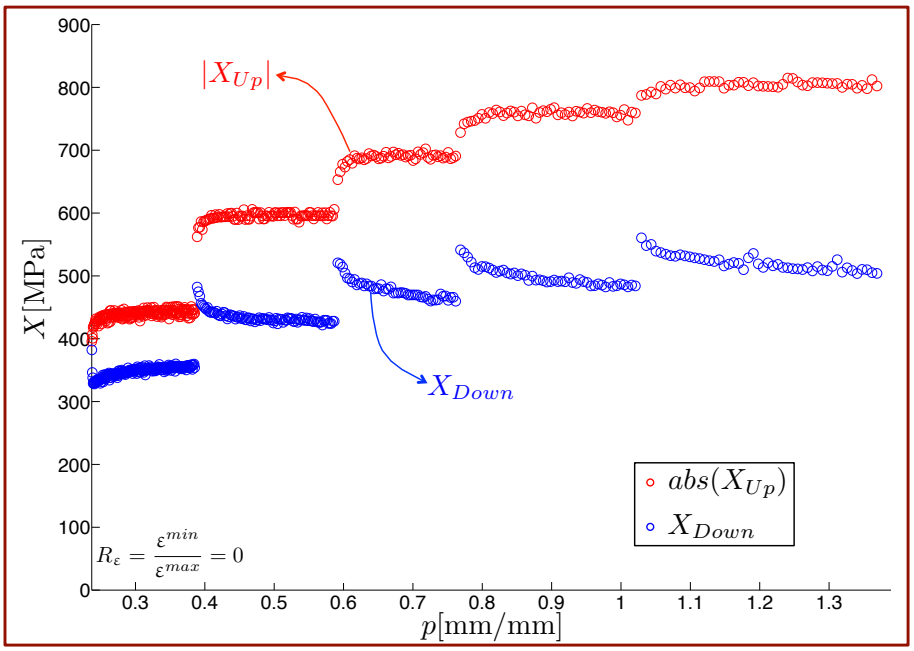

Figure 3.6: Measured kinematic hardening at the ascending and descending parts of the cyclic loops for $R_\varepsilon = 0$

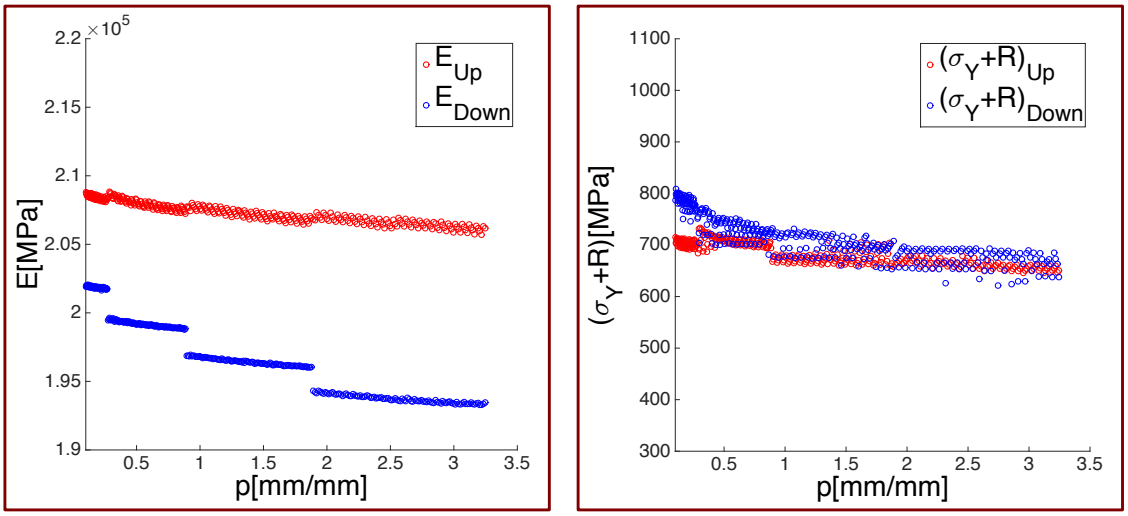

(a) (b)

Figure 3.7: Measured evolution at the ascending and descending parts of the cyclic loops for the first $R_\varepsilon = -1$ test for a) Young's modulus b) Size of the elastic domain

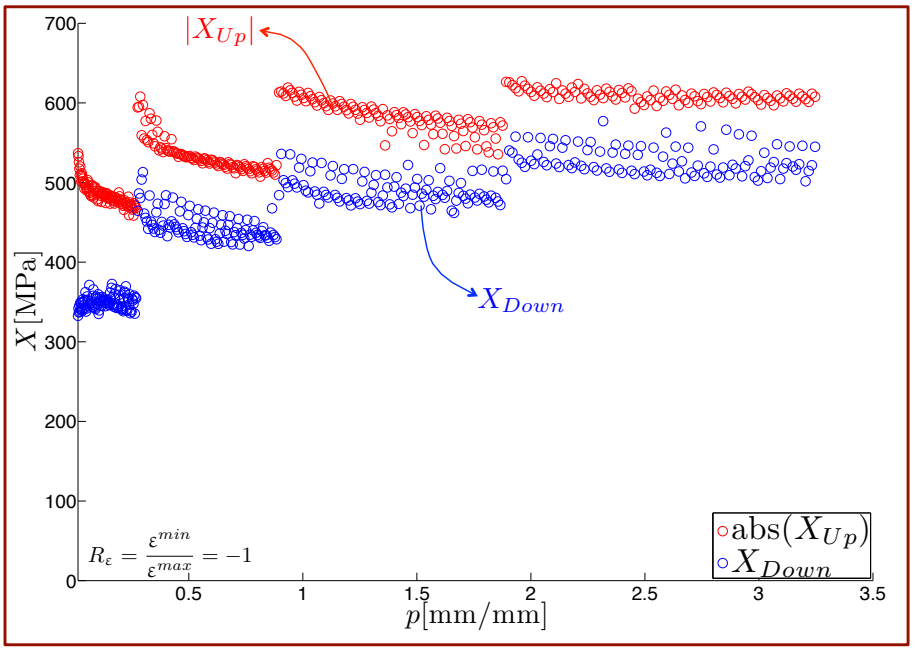

Figure 3.8: Measured kinematic hardening at the ascending and descending parts of the cyclic loops for $R_\varepsilon = -1$

behind this difference might be the fact that there is a slight asymmetry between tension and compression stress levels in our $R_\varepsilon = -1$ test, which influences the parameters, especially the kinematic hardening (*Fig. 3.8*). So far, we do not have a clear explanation for this asymmetry, but we assume it doesn't reflect the behavior of the material, but that it comes rather from the residual stresses induced during the fabrication process. Nevertheless, through the modifications of the model that will be presented in the following, such phenomena as tension-compression asymmetry can be captured.

3 Modeling of partial mean stress relaxation

As the previous analysis reveals, there is a non-negligible difference between the behavior at the ascending and the descending parts of cyclic loops. We tried to determine if these differences were responsible for certain effects in the behavior like partial mean stress relaxation at R_ε=0 and tension-compression asymmetry in symmetric strain loading.

In order to model these differences, several approaches were considered. The difference in the values of the Young's modulus E was not that important and its evolution with the accumulation of plastic strain may be treated later using damage models. Using two values for the exponent M (*Eq. 2.10*) for the ascending and descending parts would leave us with equations of different orders, thus several analytical solutions would be needed. Moreover, to get a finer tuning of this parameter, we would need to use rational numbers thus making the integration more difficult. Using a dual approach on C, the tangent mod-

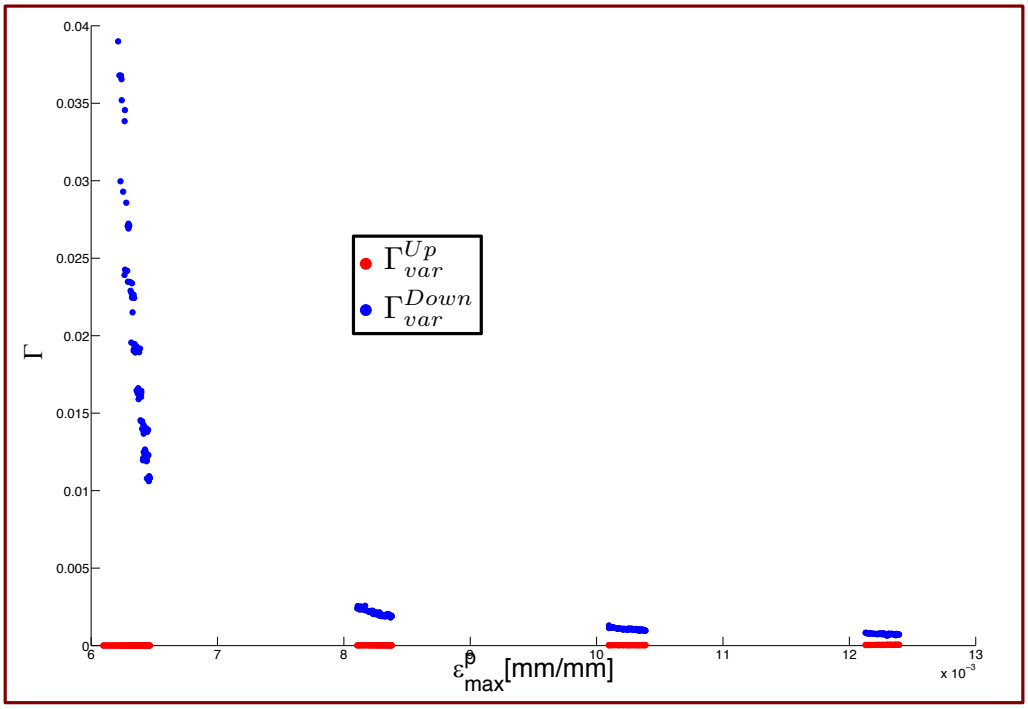

Figure 3.9: Evolution of the computed Γ_{var}^{Up} and Γ_{var}^{Down} for the first $R_\varepsilon = 0$ test, using the actual value of $\sigma_y + R$ found for each cycle

ulus, might be a valid choice but, given that it intervenes in the state laws, we need to understand its limits.

The chosen parameter to change was thus Γ for its versatility and clearer evolution patterns. In order to model separately the behavior of the ascending and the descending parts of the cycle, we identified a constant set of parameters (M, C, E) and determined the needed Γ to represent each cycle, as was detailed in chapter 2, subsection 4.3. Initially, this was performed on a trial basis, verifying that we reach the end point, in terms of σ_{max} and $\varepsilon^p_{\max}$ on the ascending part, and in terms of σ_{min} and $\varepsilon^p_{\min}$ on the descending part.

Later on, by using a modified version of *Eq. 2.9* we were able to calculate Γ_+^{Up} and Γ_-^{Down} systematically using the following equations:

$$\begin{aligned}\Gamma_+^{Up} &= \frac{M\left[C\left(\varepsilon_p^{max} - \varepsilon_p^{min}\right) - \left(\sigma_{max} - \sigma_{min} - 2\cdot k_{Up}\right)\right]}{\left(\sigma_{max} - k_{Up}\right)^M} \\ \Gamma_-^{Down} &= \frac{M\left[C\left(\varepsilon_p^{max} - \varepsilon_p^{min}\right) - \left(\sigma_{max} - \sigma_{min} - 2\cdot k_{Down}\right)\right]}{\left|\sigma_{min} + k_{Down}\right|^M}\end{aligned} \tag{3.3}$$

These equations are obtained by integrating the model between the two limits $\sigma_{max}(\varepsilon^p_{\max})$ and $\sigma_{min}(\varepsilon^p_{\min})$ and is a generalized version of *Eq. 2.9* presented in chapter 2. Using these equations, we obtain the exact Γ needed to pass through the final point of each part of the curve. The limitation of the method is that of any back-stress, which is

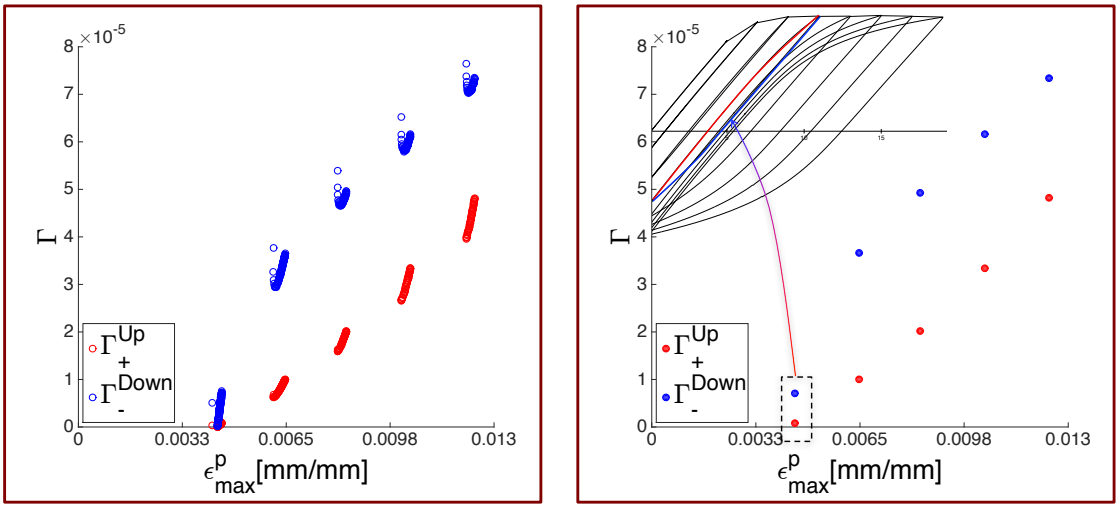

(a) (b)

Figure 3.10: Computed Γ_{+}^{UP} and Γ_{-}^{Down} for the first R_ε=0 test a) For all cycles b) Only stabilized cycles

the fact that Γ has to stay non-negative. When the computed Γ is negative (which is often the case for very small cycles depending on the chosen C) we will limit it to zero, thus resulting in a linear kinematic hardening.

Initially, we included the evolution of the size of the elastic domain $k = \sigma_y + R$ in the computation of Γ, as shown in *Fig. 3.9*. It may be noticed that there is a large gap between the evolution of Γ at the ascending part (Γ_{var}^{Up}) and at the descending part (Γ_{var}^{Down}), especially for low strain cycles, where $k = \sigma_y + R$ varies considerably. Given this difference and the lack of a clear pattern between the two, we chose a constant value k, equal to the stabilized one at the ascending part $k_{const} = k_{Up}^{stab}$=342 MPa, consistent with the standard modeling of isotropic hardening.

The results using this method will be presented in the following for the first multi-level test with $R_\varepsilon = 0$ and the multi-level test with $R_\varepsilon = -1$ we performed in the LMT lab.

3.1 Cycles at R_ε=0

Using *Eq. 3.3* and a constant set of identified parameters (M, C, E, k), the computed values of the two Γ are represented for all the cycles in *Fig. 3.10a* and only the stabilized cycles in *Fig. 3.10b*. The two dots represented in the lower left part of *Fig. 3.10b* are the values of Γ for the first stabilized cycle with a sufficiently large plastic strain to give a non negative value of Γ. This cycle is represented in the upper left corner of the σ vs ε graph, with the ascending part highlighted in red and the descending one in blue. As may be noticed in the same graph, the loading level just before the highlighted one is almost linear elastic, thus Γ is forced at zero and the plastic area will be represented by a very steep linear kinematic hardening.

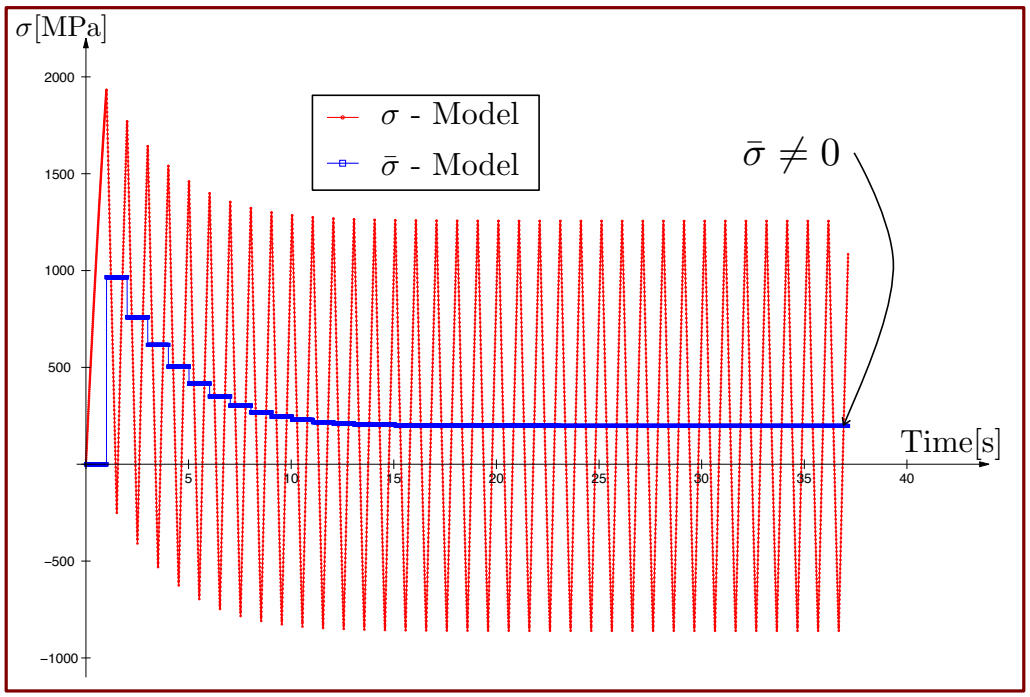

(a)

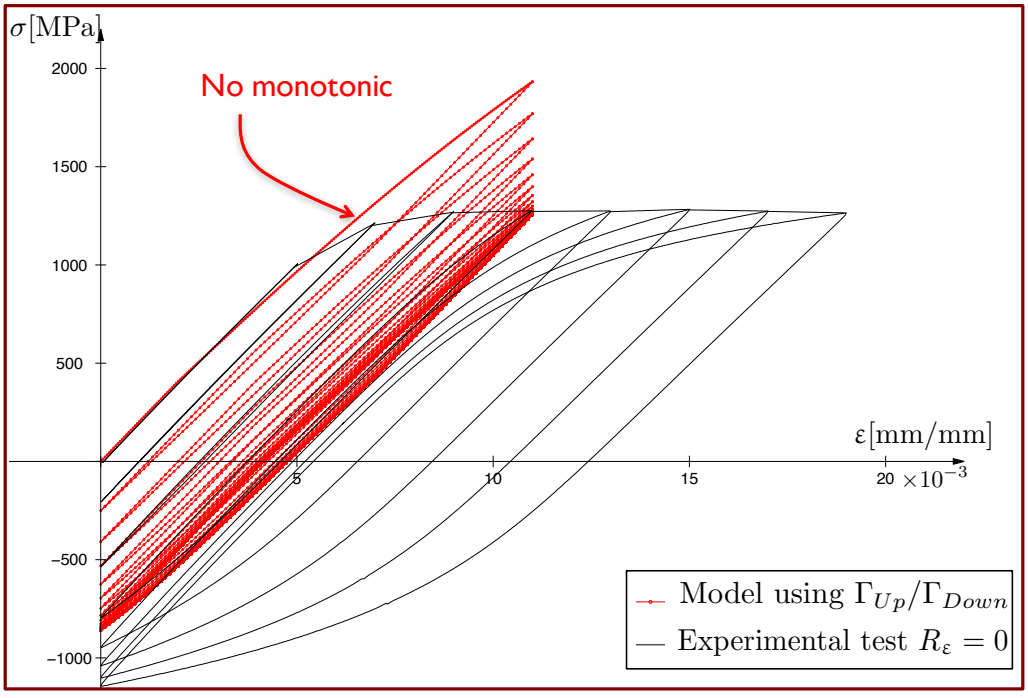

(b)

Figure 3.11: Case study for stabilized values of Γ_{+}^{UP} and Γ_{-}^{Down} for $\varepsilon_{max} = 1.1\%$ a) Cyclic stabilization b) Mean stress relaxation

Given that the values of Γ at the ascending and descending part of each stabilized cycle are different, the assumption that was made is that in this difference lies the key to the partial mean stress relaxation. Thus, we wanted to test if by imposing a set of two Γ in the description of the kinematic hardening rule at the ascending and descending of a given loading level would amount to the corresponding stabilized cycle extracted from the experiment. The first chosen set of two Γ corresponds to the cycle highlighted in *Fig. 3.10b*. As may be seen in *Fig. 3.11b*, the first and subsequent loading cycles as described by the model (red dotted line) doesn't correspond to the experimental one (black continuous line), mainly because the monotonic part was not introduced in this version of the model. Nevertheless, the loading finally saturates at the proper experimental cycle. As may be seen in *Fig. 3.11a*, not only are the cycles stabilized, but the value of the mean stress is non-zero, as opposed to the previous version of the model or to the AF model [Frederick and Armstrong, 1966]. This is an important result because it indicates that a correct combination of Γ at the ascending (Γ_{+}^{Up}) and descending part of the loop (Γ_{-}^{Down}) leads not only to the right shape of the cycle, but also to the right stabilized cycle.

After validating the method on the smallest loading level seen in *Fig. 3.10b*, the other combination of Γ_{+}^{Up} (red dots) and Γ_{-}^{Down} (blue dots) were subsequently tested. Thus, each computation ran using only the two values of Γ, from the corresponding loading level. As may be seen in *Fig. 3.12* the results are coherent in terms of stabilized cycles for all loading levels. This discovery was further developed in the following sections into an incremental (rate) model, according to the patterns found in the evolution of the two Γ.

3.2 Cycles at R_ε =-1

As mentioned previously, the multi-level experimental test performed at R_ε =-1 was studied using the same approach. Thus, the Γ parameter was computed at the descending and ascending part of each cycle (*Fig. 3.13a*).

As it can be seen in the graph, the difference between the two is less important and are directly influenced by the slight tension-compression asymmetry. Thus, using the dual Γ approach, at this time taken directly from the values of each stabilized cycle in *Fig. 3.13a*, we are directly able to model this asymmetry as shown in (*Fig. 3.13b*).

The difference between tension and compression in this case is quite small and can be ignored. Henceforth, in the R_ε = -1 case the two values of Γ will be taken equal. It is important to note though that this type of approach may be interesting for modeling materials that exhibit notable differences between tension and compression, using a different approach than those shown in chapter 1, subsection 3.5.

3.3 Unifying patterns in the evolution of Γ

First of all, our understanding of the patterns governing the cyclic loading changed when the evolutions of the computed parameter Γ were no longer considered in terms of Γ_{Up}^{+} and Γ_{Down}^{-}, but rather in terms of mean value and the amplitude of this parameter for each

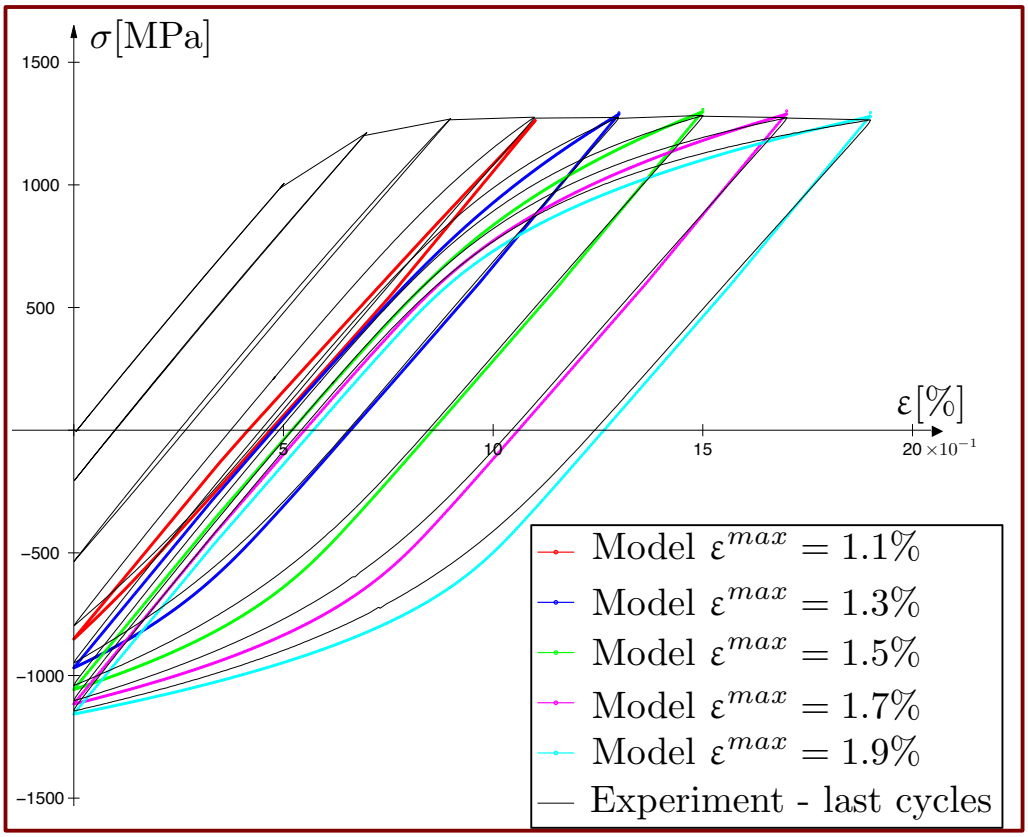

Figure 3.12: Comparison between the experiment and the model for the last cycles of each level obtained with Γ_+^{UP} and Γ_-^{Down} directly taken from *Fig. 3.10b* for each stabilized cycle, for the first multi-level R_ε=0 test performed in the LMT lab

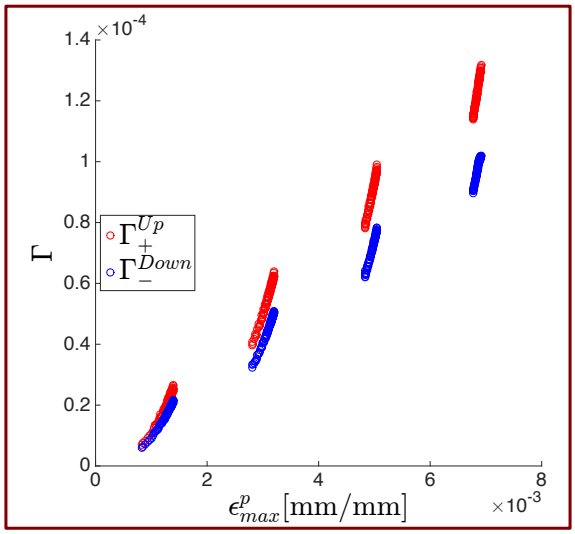

(a)

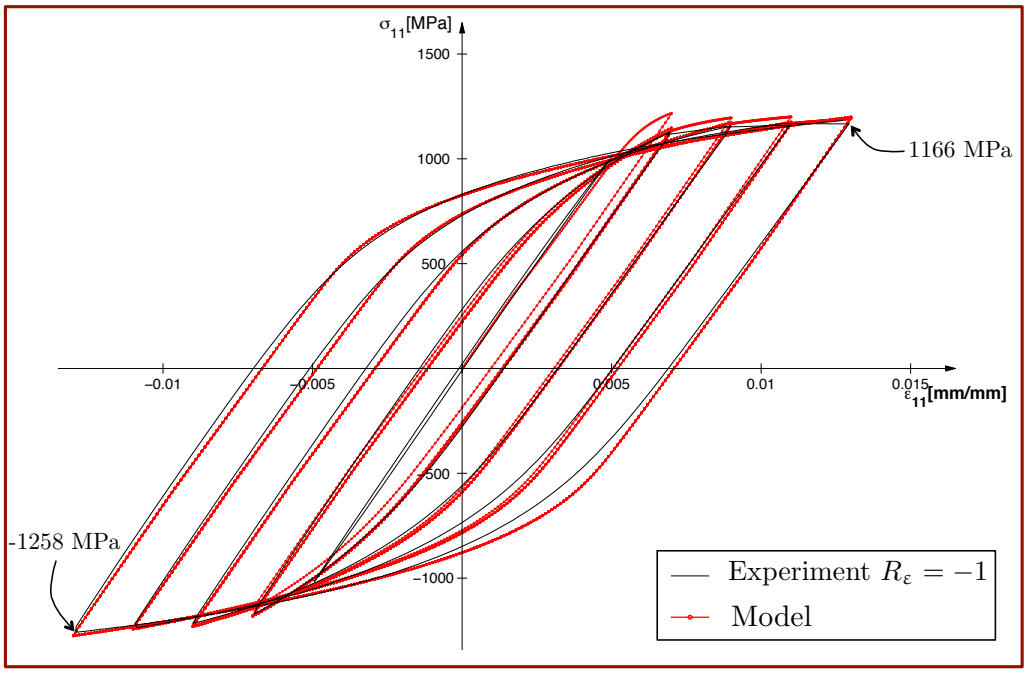

(b)

Figure 3.13: a) Computed Γ_+^{UP} and Γ_-^{Down} for the multi-level R_ε =-1 test b) Response showing the modeled asymmetry

cycle :

$$\begin{aligned} \text{Mean value of } \Gamma: \quad \bar{\Gamma} &= \frac{\Gamma^{-}_{Down} + \Gamma^{+}_{Up}}{2} \\ \text{Amplitude of } \Gamma: \quad \Gamma^{a} &= \frac{\Gamma^{-}_{Down} - \Gamma^{+}_{Up}}{2} \end{aligned} \tag{3.4}$$

When computing $\bar{\Gamma}$ and Γ^a, some interesting results arise. In *Fig. 3.14*, the distribution of Γ is shown for the first $R_\varepsilon = 0$ test in terms of Γ_+^{Up} and Γ_-^{Down} (*Fig. 3.14a*) and of $\bar{\Gamma}$ and Γ^a (*Fig. 3.14b*) for all loading levels. Some of the conclusions concerning these results are:

- In *Fig. 3.14b* it may be seen that the first computed values of Γ are obtained for a non-zero maximum plastic strain. This is due to the fact that the first cycles are either completely elastic or plastify very little. In this particular case it is important to have a sufficiently large value of the tangent modulus C, to be the least penalizing possible, as will be explained in the following.
- It may be seen that the last five levels obtain non-negative values of Γ. The observed pattern for $\bar{\Gamma}$ is an affine law. This is expected given that with all the other parameters constant (M, C, k, E) an increase in parameter $\bar{\Gamma}$ will cause the loops to be less sharp. This is what happens in reality, given that for larger strains the loops have a large plastic component, thus being flatter.
- For Γ^a, the values are close to zero in the beginning, then seem to reach a peak and then descend again for last two levels. Given the low number of levels of this test, it is difficult to conclude on this phenomenon, this being one of the reasons why the second, or complete mean stress relaxation performed at R_ε=0 (*Fig. 2.9*) has a significantly larger number of loading levels. One of the conclusions of this more complete test that will be presented in the following, is that Γ^a indeed descends until reaching zero, moment corresponding to a zero mean stress.

In order to obtain a non-negative value for Γ both at the ascending and the descending part of the loop for any given cycle, certain conditions need to be respected. As seen in *Eq. 2.10* the kinematic hardening X is composed of a linear part ($\frac{2}{3}C\dot{\boldsymbol{\varepsilon}}^{\boldsymbol{p}}$) and a non-linear back-stress part ($\Gamma X_{eq}^{M-2}\boldsymbol{X}\langle\dot{X}_{eq}\rangle_+$). Thus, in order to be able to represent a given loop, the linear part of the model should be able to pass through or beyond the extreme points of the loop. For example, *Fig. 3.15a* shows a hypothetical non-symmetrical loop. In order to pass through the point with the coordinates σ_{max} vs $\varepsilon^p_{\max}$ using only the linear part of the kinematic hardening, the tangent modulus C would have to be:

$$C_{linear} = \frac{\sigma_{max} - \sigma_{min} - 2k}{\varepsilon^p_{max} - \varepsilon^p_{min}} \tag{3.5}$$

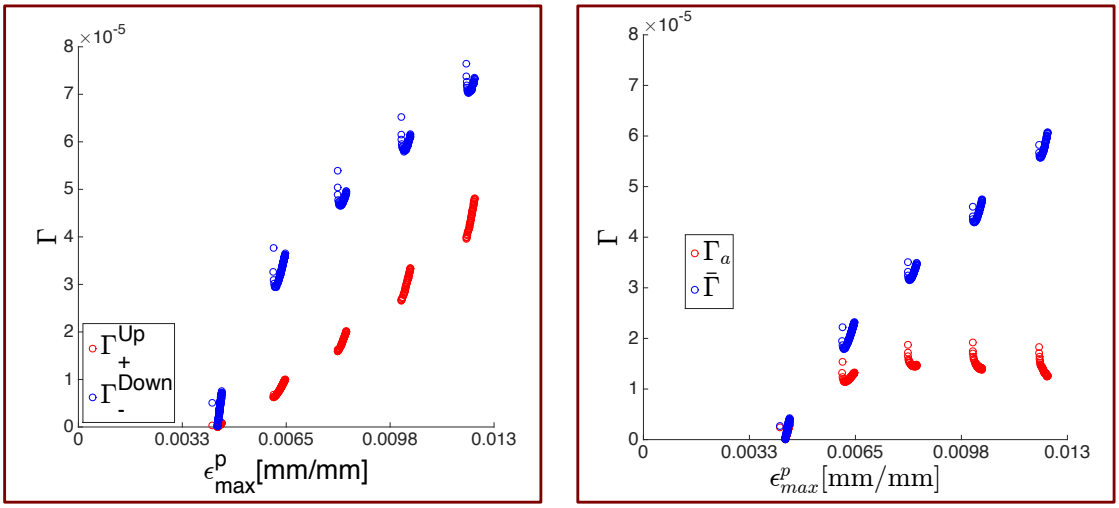

Figure 3.14: Computed Γ parameter for the first R_ε=0 test, expressed in terms of a) Γ_+^{UP} and Γ_-^{Down} b) Mean value $\bar{\Gamma}$ and amplitude Γ^a

where $2k$ is the double of the elastic domain and in the case where there is no isotropic hardening $2k = 2\sigma_y$. Thus, in order to be able to pass every time through the extreme points of a cycle, C needs to be equal or higher than C_{linear} for this same cycle. In *Fig. 3.15b*, C_{linear} is computed for every final cycle of each loading level of the first $R_\varepsilon = 0$ test, and represented with red dots with respect to $\varepsilon^p_{\max}$. The blue dots are the values of $\varepsilon_{\max}$ with respect to $\varepsilon^p_{\max}$ for the same test and serve only to graphically show the total levels.

It may be observed in *Fig. 3.15b* that the set of identified parameters is not always adapted to the studied cases. Indeed, the chosen value for $C = 2 \cdot 10^6$ MPa is greater that C_{linear} starting from the 4$^{\text{th}}$ loading level. This is because the first two levels are elastic and the third would require a much larger tangent modulus to work ($C = 2.47 \cdot 10^7$ MPa). By choosing to keep this value of C, the 3$^{\text{rd}}$ level will be slightly overrated in terms of $\frac{\Delta\varepsilon_p}{2}$ but its $\bar{\sigma}$ will still be accurate. In the final part of the chapter, some results will be shown for $C = 1 \cdot 10^7$ MPa and how this can circumvent the presented problem.

The results of the model for the complete mean stress relaxation test will be presented in detail in subsection 6.2, but one important conclusion can be drawn when looking at the distribution of Γ^a in this case. In *Fig. 3.16*, the computed Γ^a is plotted with respect to $\varepsilon^p_{\max}$ (red dots) alongside $\bar{\sigma}$. As seen for the first $R_\varepsilon = 0$ test, the first few cycles are elastic or slightly plastic, thus a non-zero value is obtained around the same maximum plastic strain $\varepsilon^p_{\max}$≈0.005mm/mm. What appears quite clearly is that for the last level, a mean stress $\bar{\sigma}$ equal to zero corresponds to Γ^a=0, thus the parameter Γ is equal at the descending and ascending parts of the loop. This means that when the cycles become symmetrical in terms of stress, then the description of the ascending and the descending parts of the loops is intrinsically obtained with a single Γ.

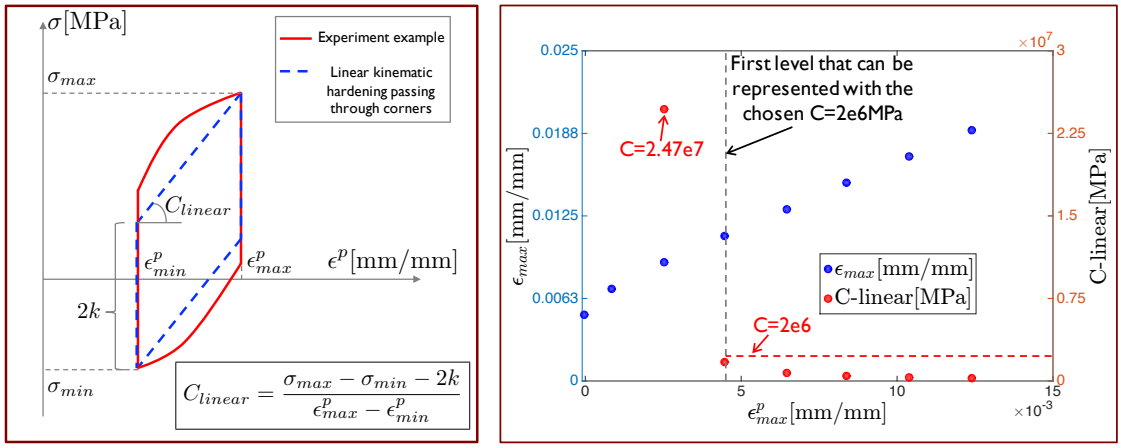

Figure 3.15: a) Method used for computing C_{linear} for a given plastic loop b) Computation of C_{linear} for the last loop of each level for the first R_ε=0 test

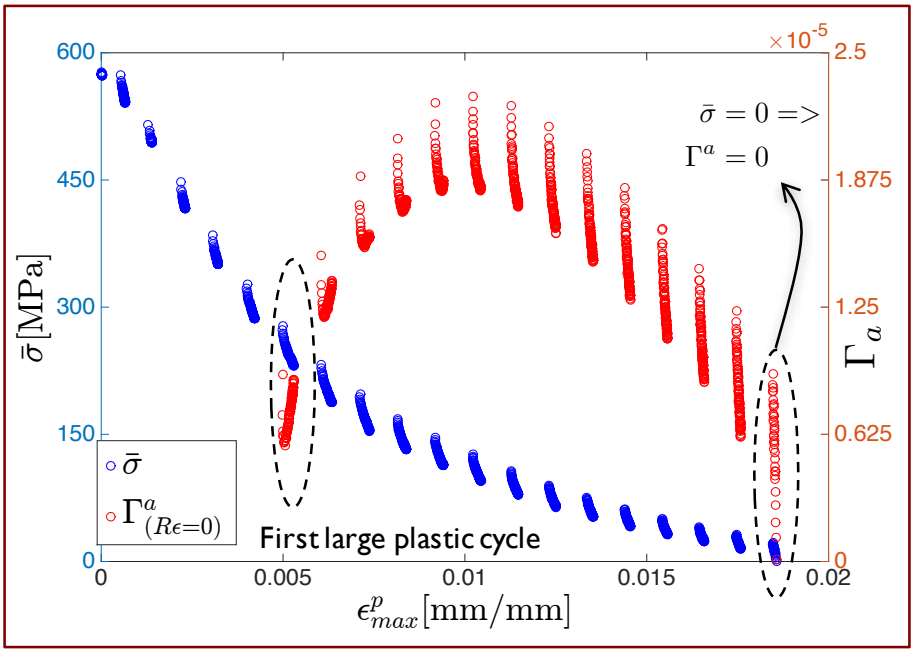

Figure 3.16: Evolution laws for Γ_a and $\bar{\sigma}$ for the second multi-level $R_\varepsilon = 0$ test (also called the complete mean stress relaxation test)

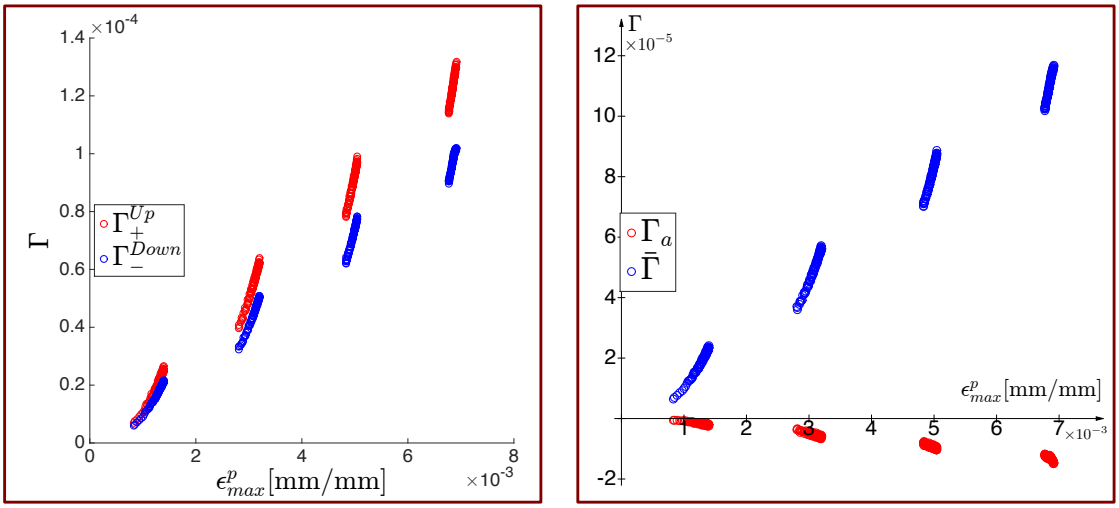

(a) (b)

Figure 3.17: Computed Γ parameter for the multi-level R_ε =-1 test expressed in terms of a) Γ_+^{Up} and Γ_-^{Down}b) Mean value $\bar{\Gamma}$ and amplitude Γ^a

In *Fig. 3.17*, the distribution of Γ is shown for the multi-level R_ε =-1 test in terms of Γ_+^{Up} and Γ_-^{Down} (*Fig. 3.17a*) and of $\bar{\Gamma}$ and Γ^a (*Fig. 3.17b*) for all loading levels. The difference between the ascending and descending part of the loops is less important than the $R_\varepsilon = 0$ case and what is interesting to see is that the values of Γ^a are negative.

The final purpose of the model is to be able to represent both the $R_\varepsilon = -1$ and the $R_\varepsilon = 0$ cases. In *Fig. 3.18* the evolutions of Γ for the two tests are compared, with the last cycles of each level being represented for $R_\varepsilon = -1$ with blue dots and for $R_\varepsilon = 0$ with red dots. In *Fig. 3.18a* the evolution of $\bar{\Gamma}$ is plotted with respect to $\varepsilon^p_{\max}$, which are very close to linear distributions with different slopes and offsets. A unified model would need to accurately represent both evolutions in their respective conditions.

In *Fig. 3.18b*, Γ^a is shown with respect to $\varepsilon^p_{\max}$. The blue dots representing the $R_\varepsilon = -1$ test are a consequence of the slight tension-compression asymmetry noticed for this test, as discussed in subsection 3.3. In the final model, this feature will not be used, given that the differences are negligible and it is not the main purpose of this model. Thus, for the $R_\varepsilon = -1$ case, the hypothesis is made that $\Gamma^a = 0$ for all loading levels, meaning that all cycles have Γ_+^{Up}=Γ_-^{Down}=$\bar{\Gamma}$.

The red dots in *Fig. 3.18b* represent the computed Γ^a for the last cycles of each level for the first $R_\varepsilon = 0$ test. The dotted line represents the author's vision of the distribution of Γ^a for this test, based on the results from this test but also on the complete mean stress relaxation test presented earlier. This evolution of Γ^a allows for the identification of three modeling zones: the first one when cycles are still elastic or slightly plastic, which will be represented through an elastic behavior or linear kinematic hardening by the model. The second zone is the one where partial mean stress relaxation occurs, and where Γ^a evolves. Finally, in the third zone, the cycles become symmetrical, meaning $\bar{\sigma} = 0$ thus $\Gamma^a = 0$.

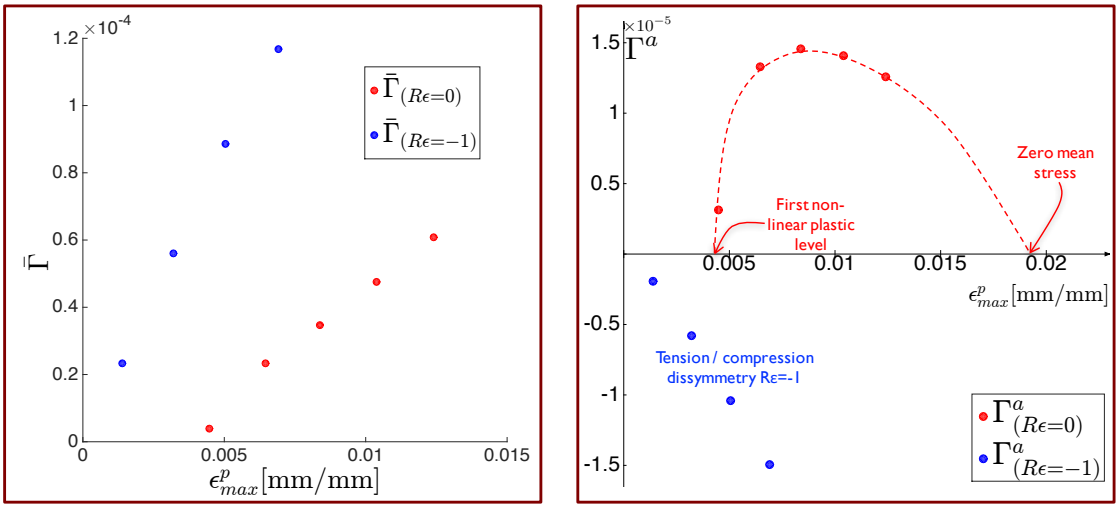

(a) (b)

Figure 3.18: Comparison between the cyclic behavior at $R_\varepsilon = -1$ (in blue) and $R_\varepsilon = 0$ (in red) a) Mean value $\bar{\Gamma}$ b) Amplitude Γ^a

It is important to note that, as shown in subsection 3.2, not all $R_\varepsilon = 0$ loading levels are stabilized, thus the estimated evolution of Γ^a is assumed to be lower in absolute value but similar in shape. High cycle fatigue tests should be performed at each loading level in order to find the exact position of the stabilized cycle. The inconvenience is that a different sample would have to be used for each level and the dispersion would be accumulated from the material properties of each sample. Until a more elaborate experimental design will be performed, the author feels that the current data at our disposal will serve well for model identification and further developments will be used to refine the parameters.

4 Proposed plasticity model with partial mean stress relaxation

As presented earlier, the partial mean stress relaxation model obtains this feature by imposing different values of the material parameter Γ at the ascending part of the loop (Γ_+^{Up}) and at the descending part (Γ_-^{Down}). For now, these values are fixed for each loading level as extracted from the experiment, in order to reach the corresponding stabilized cycle. In the last part of this chapter, the value of Γ will be computed continuously (at each time increment) based on the evolution of memory effect parameters q and ξ, resulting in an incremental (rate) model. In the following, the main constitutive equations used for the model are presented, as well as the proof of the positivity of the intrinsic dissipation.

4.1 Positivity of the intrinsic dissipation

The thermodynamic forces associated with the internal variables can be obtained from the state potential of the material:

$$\begin{aligned} \sigma &= \rho \frac{\partial \psi}{\partial \varepsilon} = \mathbb{E} : (\varepsilon - \varepsilon^p) \\ X &= \rho \frac{\partial \psi}{\partial \alpha} = \frac{2}{3} C \alpha \end{aligned} \tag{3.6}$$

The loading surface for the model is expressed with the following inequality:

$$f = (\sigma - X)_{eq} - \sigma_y - R \leq 0 \tag{3.7}$$

where σ_y is the yield stress and $(\sigma - X)_{eq}$ is the equivalent stress, a scalar value that allows the usage of the inequality in the tensorial space. The isotropic hardening R is only used as its saturation value R_∞ in the current version of the model, so that the size of the elastic domain k is constant $k_{const} = \sigma_y + R_\infty$. The equivalent stress criterion used for this model is the von Mises criterion [Mises, 1913] $\sigma_{eq} = \sqrt{\frac{3}{2}\sigma' : \sigma'}$, with σ' being the deviatoric stress.

A full plasticity model using the proposed kinematic hardening laws is a non standard model, the new springback terms not deriving from an evolution potential. One must then prove the positivity of the intrinsic dissipation $\mathscr{D} = \sigma : \dot{\varepsilon}^p - X : \dot{\alpha}$. The expression of the dissipation for the current kinematic hardening law is:

$$\mathscr{D} = (\sigma - X)_{eq} \dot{p} + \frac{3\Gamma}{2C} X_{eq}^{M-2} X : X \left\langle \dot{X}_{eq} \right\rangle_+ = \sigma_y \dot{p} + \frac{\Gamma}{C} X_{eq}^{M-2} \left\langle \dot{X}_{eq} \right\rangle_+ \tag{3.8}$$

Except for the parameter Γ, the other terms in the equation are by default positive. Thus, in order to ensure the positivity of the dissipation the parameter Γ can simply be chosen to be positive $\Gamma \geq 0$. This is an important detail and will be taken into account in the description of the model. Therefore:

$$\text{if } \Gamma \geq 0 \text{ then } \mathscr{D} \geq 0 \tag{3.9}$$

4.2 Particular plastic loading/unloading conditions

In order to precisely model both the monotonic behavior and the cyclic one, at each time we need to know in what domain we are. Thus, at any given time the model can be in one of three distinct situations, which translates in three sets of values for the material parameter Γ (*Fig. 3.19*).

The first case is the ”transition phase”, when the time derivatives of the maximum (or the minimum) value of the maximum (or the minimum) principal strain is evolving. This

condition is shown in *Fig. 3.19* in the "Yes" branch in the first decision block ($\dot{M}$ or $\dot{m} \neq 0$). The evolving quantities described in the inequality are:

$$\begin{aligned} M &= \max_t(\max_i \varepsilon_i) \\ m &= \min_t(\min_i \varepsilon_i) \end{aligned} \tag{3.10}$$

with a double maximum (resp. minimum) being used, firstly over the three principal strains (ε_i), secondly over the time history.

In the numerical scheme used for the model (represented in the following with the index *num*), this translates as the maximum (resp. minimum) value reached between 0 and the current time step t for any of the three principal strains ε_i. Therefore, either one of the two quantities M_{num} or m_{num} needs to evolve, thus either $\Delta M_{num} = M^t_{num} - M^{t-1}_{num}$ or $\Delta m_{num} = m^t_{num} - m^{t-1}_{num}$ has to be different from zero. This will occur either in the first loading or unloading (monotonic case), or when going from one loading level to the next one that is higher in either minimum or maximum strain (transition case). In this case, the parameter Γ is computed as was presented in chapter 2 section 6, by using the positive part of an affine law to describe its evolution $\Gamma = \Gamma_{mono} = \langle \Gamma'_0 \varepsilon^p_{\text{eq,max}} + \Gamma_0 \rangle_+$, the positive part being needed to force the positivity of the intrinsic dissipation, as shown in *Eq. 3.9* of the previous part.

When the maximum or minimum value of any of one of the principal strains isn't surpassed during loading (the "No" branch in the first decision block $\dot{M}$ or $\dot{m} \neq 0$) then the model will switch to a "non-monotonic phase", where the parameter Γ has to use its two different values, one for loading and the other for unloading. This can be obtained with respect to the evolution of e, which is the positive part of the maximum value of any of the principal strains:

$$e = \max_i \langle \varepsilon_i \rangle_+ \tag{3.11}$$

Thus, when the time derivative of e ($\dot{e} = \frac{de}{dt}$) is positive (the "Yes" branch in the second decision block $\dot{e} > 0$), we are on the ascending part and will use $\Gamma = \Gamma^+_{Up}$. When the strain is decreasing (the "No" branch in the second decision block $\dot{e} > 0$), then Γ will take on its value for the descending part, Γ^-_{Down}.

In the numerical scheme, in the case of strain controlled cyclic tests, the maximum and minimum strains per level are fixed, thus M and m are constant all along each loading level. The Γ parameter that we will used in the model will depend on the sign of the evolution of the strain from the previous time step $(t-1)$ to the current time step (t) or $\Delta e_{num} = e^t_{num} - e^{t-1}_{num}$.

With this type of approach, the behavior is very well represented both for the monotonic case and for the cyclic case for each level. Nevertheless, when modeling the $R_\varepsilon = -1$ multi-level strain controlled test, the parameter Γ needs to be re-adapted. In the following, a rate formulated method will be presented, that allows representing both symmetrical

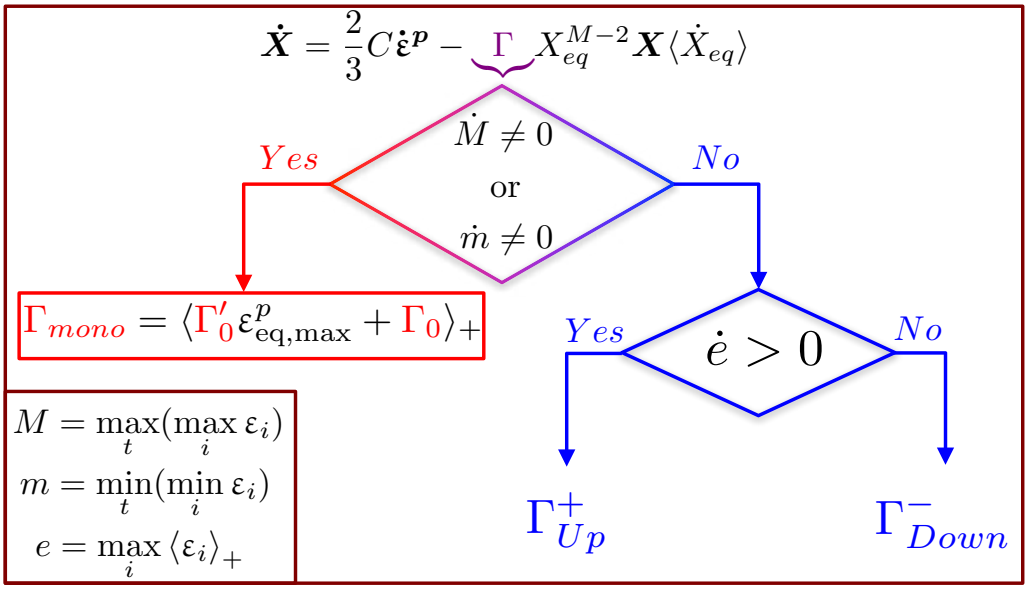

Figure 3.19: Rule for switching between monotonic and cyclic loading parameters, with ε_i being the principal strains

($R_\varepsilon = -1$) and non-symmetrical ($R_\varepsilon \neq -1$) strain controlled cyclic loading with only one, unified model.

4.3 Unified incremental (rate) model using memory effect at stabilized cycle

In order to model the evolution of Γ, both in the case of the $R_\varepsilon = 0$ and $R_\varepsilon = -1$, a generalized equation should be used that would allow to be as close as possible to the given levels and their intermediate values. This would make the model naturally converge towards a plastic loop as close as possible to the last cycle of each loading level. The solution adapted to serve this purpose was to again use the principles of memory effect, but in a different way. As explained in chapter 2 subsection 4.2, the memory surface is usually defined as a hypersphere in the plastic strain space, similarly to the elasticity yield surface, by a scalar isotropic variable q, which is the radius, and a tensorial kinematic variable $\boldsymbol{\xi}$, which gives the coordinate of the center of the hypersphere. The governing equations used in the description of the memory effect hypershpere are:

$$\begin{aligned}
\mathcal{F} &= \sqrt{\frac{2}{3}}||\boldsymbol{\varepsilon}^{\boldsymbol{p}} - \boldsymbol{\xi}|| - q \leq 0 \\
\dot{q} &= \eta\mathcal{H}(\mathcal{F})\langle\boldsymbol{n} : \boldsymbol{n}^\star\rangle_+ \dot{p} \\
\dot{\boldsymbol{\xi}} &= \sqrt{\frac{3}{2}}(1-\eta)\mathcal{H}(\mathcal{F})\langle\boldsymbol{n} : \boldsymbol{n}^\star\rangle_+ \boldsymbol{n}^\star \dot{p}
\end{aligned} \tag{3.12}$$

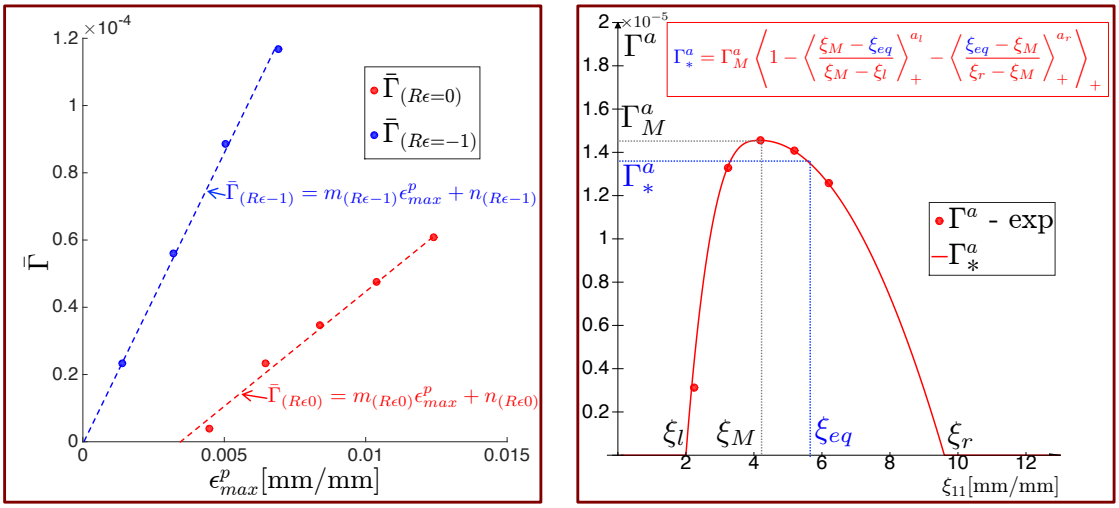

(a) (b)

Figure 3.20: Unified evolution description based on distributions for $R_\varepsilon = -1$ (in blue) and $R_\varepsilon = 0$ (in red) a) Mean value $\bar{\Gamma}$ b) Amplitude Γ^a

For this application, the memory effect will be used with the parameter η, which serves as a weight function between the isotropic and the kinematic parts of the memory surface and, consequently, as convergence speed. The values of the two memory effect variables q and ξ at convergence in the 1D case will thus be :

$$q = \max\left(\eta\varepsilon^p_{\max}, \frac{\Delta\varepsilon^p}{2}\right) \qquad \xi_{eq} = \min\left((1-\eta)\varepsilon^p_{\max}, \bar{\varepsilon^p}\right) \tag{3.13}$$

where $\xi_{eq} = \sqrt{\frac{2}{3}\boldsymbol{\xi} : \boldsymbol{\xi}}$. In such a uniaxial case $\xi_{eq} = \xi_{11}$.

Initial attempts were made with small values of η such as 0.05, 0.1 and 0.2 in order to capture a more gradual transition from the initial to the final cycle of each level. Unfortunately, for some cases this convergence speed was too slow and would cause numerical instabilities, such as mean stress relaxation reversal. The case $\eta = \frac{1}{2}$ was finally used. It is a classic choice in the literature as a default value, especially in the $R_\varepsilon = 0$ case [Nouailhas et al., 1985; Hopperstad et al., 1995]. This allows for a quick convergence and is sufficiently precise in most cases.

Firstly, the unified equation was developed for the evolution of $\bar{\Gamma}$. In *Fig. 3.20a* the evolution of $\bar{\Gamma}$ is plotted with respect to $\varepsilon^p_{\max}$ for the last cycles of each level for the first $R_\varepsilon = 0$ test in red dots and for the $R_\varepsilon = -1$ test in blue dots. The dashed lines represent the linear fit for each distribution. The slope of each line is noted m and the offset n so that we obtain the equations for the two linear distributions as follows:

$$\begin{aligned} \bar{\Gamma}_{(R_\varepsilon=-1)} &= m_{(R_\varepsilon=-1)}\varepsilon^p_{max} + n_{(R_\varepsilon=-1)} \\ \bar{\Gamma}_{(R_\varepsilon=0)} &= m_{(R_\varepsilon=0)}\varepsilon^p_{max} + n_{(R_\varepsilon=0)} \end{aligned} \tag{3.14}$$

In order to elegantly unify the two, we combined the two equations based on the fact that for $\eta = 0.5$ in the $R_\varepsilon = -1$ case $\xi_{eq} = \min\left((1-\eta)\varepsilon^p_{\max}, \bar{\varepsilon^p}\right)$ is always $\bar{\varepsilon^p}$, and for a symmetrical loading $\bar{\varepsilon^p} = 0$. Using this feature, the unified equation for computing $\bar{\Gamma}$ at any time is:

$$\bar{\Gamma}_* = \left\langle Aq + B\xi_{eq} + a + b\frac{\xi_{eq}}{q} \right\rangle_+ \tag{3.15}$$

The notation "*" was used indicate that the variable is computed at each time step following the identified equations and not fixed artificially for the whole test / load level. This convention ("*") will be used from now on in the definition of the parameter Γ to differentiate the incremental (rate) model from the manually changed model. The main parameters in the case of $\bar{\Gamma}_*$ are obtained as follows:

$$\begin{aligned} A &= m_{(R\varepsilon=-1)} \\ B &= \frac{m_{(R\varepsilon=0)} - m_{(R\varepsilon=-1)}\eta}{1-\eta} \\ a &= n_{(R\varepsilon=-1)} \\ b &= \frac{\eta}{1-\eta}\left(n_{(R\varepsilon=0)} - n_{(R\varepsilon=-1)}\right) \end{aligned} \tag{3.16}$$

In order to check the validity of the model, the equations will be developed case by case at convergence for $\eta = 0.5$:

$$\begin{aligned} &\underline{R_\varepsilon = -1} \\ &\left\{ \begin{array}{l} \xi_{eq} = 0 \\ q = \frac{\Delta\varepsilon_p}{2} = \varepsilon^p_{\max} \end{array} \right. \Bigg| \; \bar{\Gamma}_*^{(R\varepsilon=-1)} = m_{(R\varepsilon=-1)}\varepsilon^p_{\max} + n_{(R\varepsilon=-1)} \\ &\underline{R_\varepsilon = 0} \\ &\left\{ \begin{array}{l} \xi_{eq} = 0.5\varepsilon^p_{\max} \\ q = 0.5\varepsilon^p_{\max} \end{array} \right. \Bigg| \; \bar{\Gamma}_*^{(R_\varepsilon=0)} = m_{(R_\varepsilon=-1)}0.5\varepsilon^p_{\max} + \frac{m_{(R_\varepsilon=0)} - 0.5m_{(R_\varepsilon=-1)}}{\cancel{0.5}}\cancel{0.5}\varepsilon^p_{\max} \\ &+ n_{(R_\varepsilon=-1)} + \frac{\cancel{0.5}}{\cancel{0.5}}\left(n_{(R_\varepsilon=0)} - n_{(R_\varepsilon=-1)}\right)\frac{\cancel{0.5\varepsilon^p_{\max}}}{\cancel{0.5\varepsilon^p_{\max}}} \\ &= \cancel{m_{(R_\varepsilon=-1)}0.5\varepsilon^p_{\max}} + m_{(R_\varepsilon=0)}\varepsilon^p_{\max} - \cancel{m_{(R_\varepsilon=-1)}0.5\varepsilon^p_{\max}} + \cancel{n_{(R_\varepsilon=-1)}} + n_{(R_\varepsilon=0)} - \cancel{n_{(R_\varepsilon=-1)}} \\ &\Longrightarrow \bar{\Gamma}_*^{(R_\varepsilon=0)} = m_{(R_\varepsilon=0)}\varepsilon^p_{\max} + n_{(R_\varepsilon=0)} \end{aligned} \tag{3.17}$$

Therefore, the equations are verified for both cases and we should obtain a good description of the evolution of $\bar{\Gamma}$.

Secondly, the unified equation was developed for the evolution of Γ^a. In *Fig. 3.20b* the evolution of Γ^a is plotted with respect to $\xi_{11} = (1-\eta)\varepsilon^p_{\max} = 0.5\varepsilon^p_{\max}$ for the last cycles

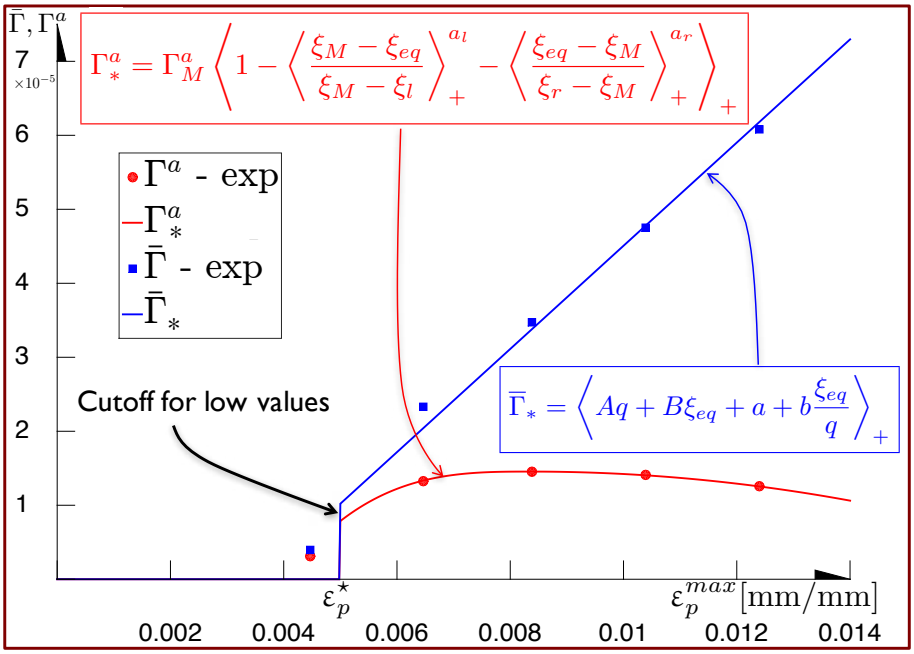

Figure 3.21: Evolution laws for Γ^a_* and $\bar{\Gamma}_*$ in the incremental model, working for both the $R_\varepsilon = 0$ (dots represented in this figure) and the $R_\varepsilon = -1$ case (not shown in this graph)

of each level for the first $R_\varepsilon = 0$ test in red dots. The red line represents the calculated distribution using the formula:

$$\Gamma^a_* = \Gamma^a_M \left\langle 1 - \left\langle \frac{\xi_M - \xi_{eq}}{\xi_M - \xi_l} \right\rangle_+^{a_l} - \left\langle \frac{\xi_{eq} - \xi_M}{\xi_r - \xi_M} \right\rangle_+^{a_r} \right\rangle_+ \tag{3.18}$$

where the point $\Gamma^a_M = f(\xi_M)$ is the maximum of the distribution; ξ_l is the intersection with the abscissa of the left branch of the curve, so the point where the first plastic cycle can be represented; ξ_r is the intersection with the abscissa of the right branch of the curve and represents the point where the first zero mean stress is obtained and beyond which cycles are symmetrical. The way the equation works is by activating each positive part at a time. If $\xi_{eq} < \xi_l$ or $\xi_{eq} > \xi_r$ the quantity inside the large positive part is negative, therefore $\Gamma^a_* = 0$. If $\xi_l < \xi_{eq} < \xi_M$ the quantity inside the left positive part is non-negative and if $\xi_M < \xi_{eq} < \xi_r$ the quantity inside the right positive part is non-negative. The exponents a_l and a_r give the degree of the polynomial for each descending branch from the peak (Γ^a_M) to zero. By default, a quadratic equation is chosen ($a_l = a_r = 2$), but it can come in handy given that it is the only other degree of freedom left besides the aforementioned parameters.

With this set of equations to describe the evolution of Γ^a_* and $\bar{\Gamma}_*$, the parameter Γ can be computed at any given time in one of its three states:

$$\begin{aligned}
\textbf{Monotonic / transition case: } & \Gamma = \Gamma_{mono} = \langle \Gamma'_0 q + \Gamma_0 \rangle_+ \\
\textbf{Non-monotonic - loading: } & \Gamma = \Gamma^+_{Up} = \langle \bar{\Gamma}_*(q,\boldsymbol{\xi}) - \Gamma^a_*(q,\boldsymbol{\xi}) \rangle_+ \\
\textbf{Non-monotonic - unloading: } & \Gamma = \Gamma^-_{Down} = \bar{\Gamma}_*(q,\boldsymbol{\xi}) + \Gamma^a_*(q,\boldsymbol{\xi})
\end{aligned} \tag{3.19}$$

With this formulation, for any q and $\boldsymbol{\xi}$ the cyclic behavior is very well described both in the $R_\varepsilon = -1$ and in the $R_\varepsilon = 0$ case. Moreover, the model is also capable of working for any given complex loading, possibly random.

One challenge that had to be overcome was the passage from $\Gamma = 0$ to a non-zero value. Given that the model is implemented on one node using an explicit python routine, the size of the loading increment is a real issue. Even when using a very small increment, small cycles can exhibit larger plastic strains than in reality, leading to a cycle that stabilizes at a smaller mean stress than in reality. Given that this issue is far more penalizing in small plasticity cycles, a cutoff was performed at a value of $\varepsilon^\star_p = 5 \cdot 10^{-3}$ mm/mm. This also avoids to have cycles with $\Gamma^{Up}_+ = 0$ for a non-zero Γ^{Down}_-, which can cause some anomalies. This is a palliative solution before a completely implicit routine will solve this issue. In *Fig. 3.21* the cutoff, as well as the evolutions of $\bar{\Gamma}$ and Γ^a are plotted with the corresponding equations for the first $R_\varepsilon = 0$ test. At the end of the study, a higher value of C was chosen, so that all 5 levels would be covered. In section 6, the final results given by the model will be presented for the monotonic and cyclic cases.

5 Summary of the proposed plasticity model

The listing below summarizes the constitutive equations of the model for the combined description of rate dependent inelasticity under monotonic and cyclic loading:

Strain partition: $\boldsymbol{\varepsilon} = \boldsymbol{\varepsilon}^{\boldsymbol{e}} + \boldsymbol{\varepsilon}^{\boldsymbol{p}}$

Isotropic elasticity: $\boldsymbol{\sigma} = \mathbb{E} : \boldsymbol{\varepsilon}^{e}$

Yield function: $f = (\boldsymbol{\sigma} - \boldsymbol{X})_{eq} - \sigma_y \leq 0$

Plastic strain rate: $\dot{\boldsymbol{\varepsilon}}^{\boldsymbol{p}} = \dot{\lambda}\frac{3}{2}\frac{\boldsymbol{\sigma}' - \boldsymbol{X}}{(\boldsymbol{\sigma} - \boldsymbol{X})_{eq}}$

Memory surface:
$$\begin{cases} \mathcal{F} = \sqrt{\frac{2}{3}}||\boldsymbol{\varepsilon}^{\boldsymbol{p}} - \boldsymbol{\xi}|| - q \leq 0 \\ \dot{q} = \eta\mathcal{H}(\mathcal{F})\langle \boldsymbol{n} : \boldsymbol{n}^{\star}\rangle_{+}\dot{p} \\ \dot{\boldsymbol{\xi}} = \sqrt{\frac{3}{2}}(1-\eta)\mathcal{H}(\mathcal{F})\langle \boldsymbol{n} : \boldsymbol{n}^{\star}\rangle_{+}\boldsymbol{n}^{\star}\dot{p} \end{cases}$$

Kinematic hardening: $\dot{\boldsymbol{X}} = \frac{2}{3}C\dot{\boldsymbol{\varepsilon}}^{\boldsymbol{p}} - \Gamma(q,\boldsymbol{\xi})X_{eq}^{M-2}\boldsymbol{X}\left\langle \dot{X}_{eq}\right\rangle_{+}$

Computation of material parameter Γ depending on the loading state :

$$\begin{cases} M = \max\limits_{t}(\max\limits_{i}\varepsilon_i) \\ m = \min\limits_{t}(\min\limits_{i}\varepsilon_i) \\ e = \max\limits_{i}\langle\varepsilon_i\rangle_{+} \end{cases} \tag{3.20}$$

if $(\dot{M} \neq 0)$ ***or*** $(\dot{m} \neq 0)$ ***then:***

| $\Gamma = \Gamma_{mono} = \langle \Gamma'_0 q + \Gamma_0\rangle_{+}$: Monotonic / transition case

else if $(\dot{e} > 0)$

| | $\Gamma = \Gamma^{+}_{Up} = \langle \bar{\Gamma}_{*}(q,\boldsymbol{\xi}) - \Gamma^{a}_{*}(q,\boldsymbol{\xi})\rangle_{+}$: Non-monotonic - loading

| ***else***

| | $\Gamma = \Gamma^{-}_{Down} = \bar{\Gamma}_{*}(q,\boldsymbol{\xi}) + \Gamma^{a}_{*}(q,\boldsymbol{\xi})$: Non-monotonic - unloading

| ***end if***

end if

Incremental (rate formulated) computation of Γ, using $\bar{\Gamma}_{*}$ and Γ^{a}_{*} :

$$\begin{cases} \bar{\Gamma}_{*} = \left\langle Aq + B\xi_{eq} + a + b\frac{\xi_{eq}}{q}\right\rangle_{+} \\ \Gamma^{a}_{*} = \Gamma^{a}_{M}\left\langle 1 - \left\langle \frac{\xi_M - \xi_{eq}}{\xi_M - \xi_l}\right\rangle_{+}^{a_l} - \left\langle \frac{\xi_{eq} - \xi_M}{\xi_r - \xi_M}\right\rangle_{+}^{a_r}\right\rangle_{+} \end{cases}$$

6 Application of the incremental model to Inco718DA

In this section, the results from the use of the incremental model will be presented for the monotonic loading, the cyclic $R_\varepsilon = 0$ and $R_\varepsilon = -1$ cases.

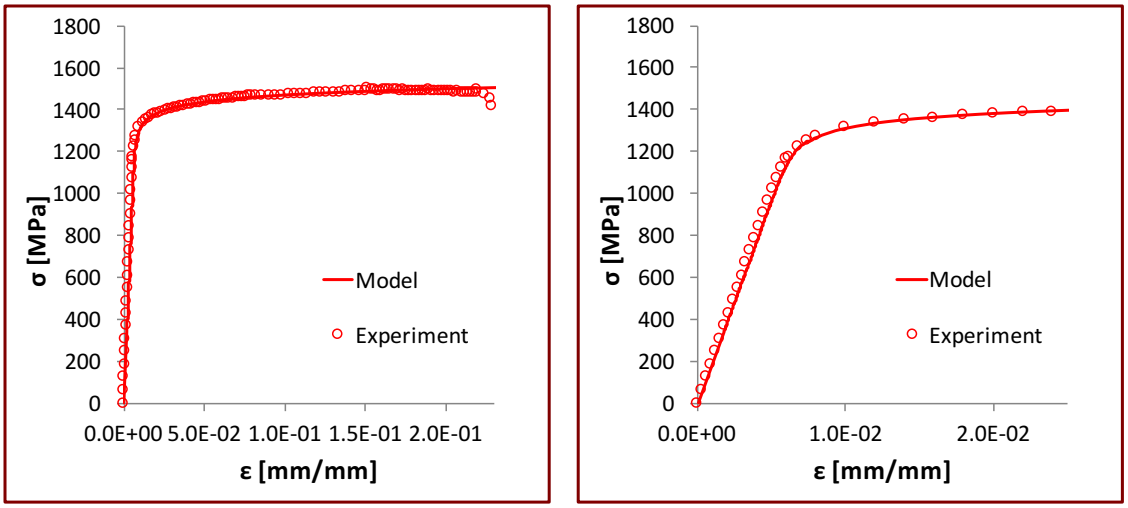

(a) (b)

Figure 3.22: Monotonic response obtained with the incremental (rate) plasticity model for a) The whole span of the test b) The domain used for the complete mean stress relaxation test

6.1 Monotonic response

One of the advantages of the described kinematic hardening law is that the monotonic behavior can be identified completely apart from the saturated cyclic behavior. During the development phase of the model, several identification options were considered, depending on the desired accuracy for each zone of the mean stress relaxation curve. Given that a well represented monotonic behavior plays an important role especially in the first two zones of the mean stress relaxation curve (*Fig. 3.1*), it is important to be able to perform a fine tuning of the model in order to capture all associated phenomena.

As was presented in chapter 2, section 6, the equation for computing Γ in the monotonic case is $\Gamma_{mono} = \langle \Gamma'_0 \varepsilon^p_{\text{eq,max}} + \Gamma_0 \rangle_+$. The need for the extra degree of freedom allowed by Γ_0 was confirmed by an instantaneous computation of Γ in the monotonic case in Appendix B. In *Fig. B.3b*, the influence of the offset Γ_0 is shown, for a fixed Γ'_0. In this example, Γ'_0 was used to accurately represent the plastic plateau and Γ_0 to reach the final, desired behavior.

The monotonic response was initially obtained with the same explicit python routine used for the cyclic loading, but it took several minutes to obtain a result with a sufficiently fine strain increment. The explicit code is especially increment sensitive in the transition between the elastic and the plastic behavior. In order to be able to easily identify the model parameters, an analytical version was obtained for the increment of plastic strain by integrating the equations of the kinematic hardening law. The resolution is described in detail in Appendix D. Therefore, by implementing this analytic version of the monotonic behavior in Microsoft Excel, the impact of the change of each parameter can be seen instantly. This is a very good tool to help a junior engineer get acquainted with the model

and how each parameter works. This could also facilitate the introduction of the model in an optimization software, in order to accurately obtain the best parameter combination.

The final monotonic response is shown in *Fig. 3.22* for the whole test (*Fig. 3.22a*) and for the domain where the cyclic tests are performed (*Fig. 3.22b*). The final parameters identified to describe the monotonic behavior are given below, with the already presented identifications in grey:

E [GPa]	k [MPa]	M	C [MPa]	Γ'_∞ [MPa^{-2}]	Γ'_0 [MPa^{-2}]	Γ_0 [MPa^{-2}]
206	342	3	$2{\cdot}10^6$	$2.09 \cdot 10^{-2}$	$3.9 \cdot 10^{-2}$	$-1.25 \cdot 10^{-5}$

6.2 $R_\varepsilon = 0$

As it was presented in the previous sections, the main interest for the proposed plasticity model in the $R_\varepsilon = 0$ case is the possibility to represent partial mean stress relaxation. This phenomenon is not captured by most kinematic hardening laws, such as the Armstrong-Frederick law, because they converge at complete mean stress relaxation. This comes mainly out of the fact that such models have the same description of the ascending and the descending part of each loop. Therefore, at each new cycle of a strain-controlled test with a strain ratio different of $R_\varepsilon = -1$, the models will relax the mean stress, even if with a small increment each time. This will always lead to a symmetrical state where $\bar{\sigma} = 0$ if a sufficient number of cycles is performed. In the plasticity model developed during this thesis, the partial mean stress relaxation lies in the measured assymetry between the ascending and the descending part of each part of the loop. This assymetry has been quantified with the parameter Γ initially in terms of Γ_+^{Up} and Γ_-^{Down}, and later on in terms of mean value $\bar{\Gamma}$ and amplitude Γ^a. This allowed the discovery of certain interesting patterns that are at the core of the incremental model.

In *Fig. 3.23* the evolutions of $\bar{\Gamma}$ and Γ^a are plotted for the second $R_\varepsilon = 0$ test with respect to $\varepsilon^p_{\max}$, for all the cycles (*Fig. 3.23a*) and only for the last cycles of each loading level (*Fig. 3.23b*). The continuous lines represent the governing equations used in the incremental model with $\varepsilon^\star_p$=0.005 mm/mm being the cutoff threshold.

The comparison between the results of the model and the experiment for the second $R_\varepsilon = 0$ test are shown in *Fig. 3.24* for the last cycles of each level. *Fig. 3.24a* shows σ with respect to ε with the model in thick blue lines and the experimental data in black lines. *Fig. 3.24b* shows $\bar{\sigma}$ with respect to $\frac{\Delta\varepsilon}{2}$ with the model in blue and the experimental data in black. The most important aspect that can be observed from these graphs is that the last cycles are coherent for the most part and thus the mean stress relaxation curve is globally well represented, especially the final part. The fact that the first two points are underrated is a direct consequence of the identified monotonic behavior. The use of a larger transverse parameter C can correct this, as it will be seen in the following for the first $R_\varepsilon = 0$ test. The issue here is, as mentioned before, the intermediate cycles between linear kinematic hardening and non-linear, relaxing, kinematic hardening. For this test, it is the loading level with $\frac{\Delta\varepsilon}{2}$ = 0.006 mm/mm which is slightly lower than

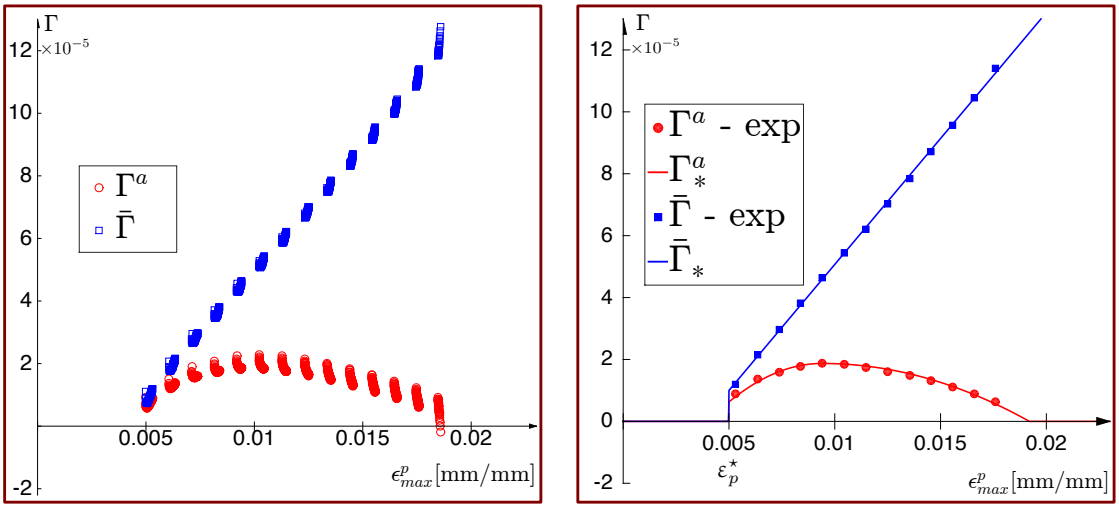

(a) (b)

Figure 3.23: Computed $\bar{\Gamma}$ and Γ^a for the second R_ε=0 test a) All cycles b) Last cycles of each loading level and their respective governing equation used in the incremental model

in the experiment in both figures. This minor issue is due to the fact the parameter Γ can switch from zero (linear kinematic hardening) to a non-zero value, causing an slight overestimation of the mean stress relaxation. This is assumed to be related to the explicit formulation of the numerical computation, and should disappear if an implicit description is used. The implicit implementation, as well as an Abaqus integration of the kinematic hardening rule, are in development in the PhD work of Estarle R. F. de Souza Campos in the ENS Cachan university [de Souza Campos et al., 2017].

Nevertheless, the impact on the global model is minimal and will hopefully be fixed in the future. Another visible aspect is that the elastic part becomes more and more distanced from reality. This change of the Young's modulus is usually captured with damage models. A perspective is to use plasticity coupled with damage to also take into account this phenomenon.

The final results that will be presented for the $R_\varepsilon = 0$ case concern the first test and mean to show the improvement brought by the usage in the model of a much higher transverse modulus. Several sensitivity tests were made and the value that was finally used is $C = 1 \cdot 10^7$ MPa. In *Fig. 3.25* the evolutions of $\bar{\Gamma}$ and Γ^a are plotted with respect to $\varepsilon^p_{\max}$. The distributions have slightly changed in shape and considerably in value. Most importantly, one of the loading levels that was cut off before can be kept. The reason for this is that in this case the point is on a stable part of the curve and not on a steep descent as for the $C = 2 \cdot 10^6$ MPa. Before, any slight change in the value of $\varepsilon^p_{\max}$ would cause an important change in the value of Γ^a and would cause instabilities in the cycle. This time, the cutoff threshold was moved to the left at a value of $\varepsilon^\star_p$=0.003 mm/mm.

With this identification, the level marked with a dotted line in *Fig. 3.25* can be represented with a non-linear kinematic hardening, which is closer to reality. The comparison

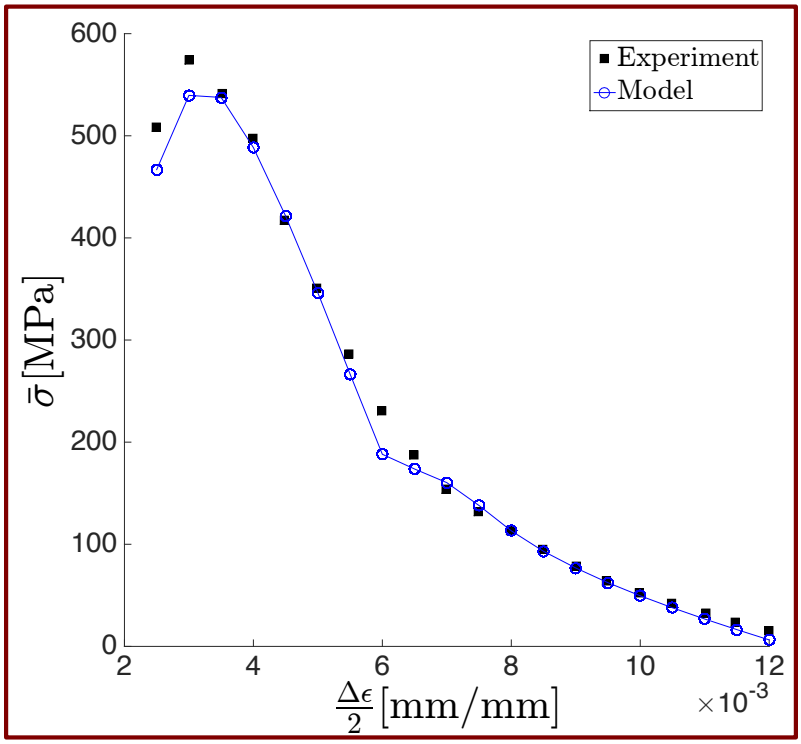

(a)

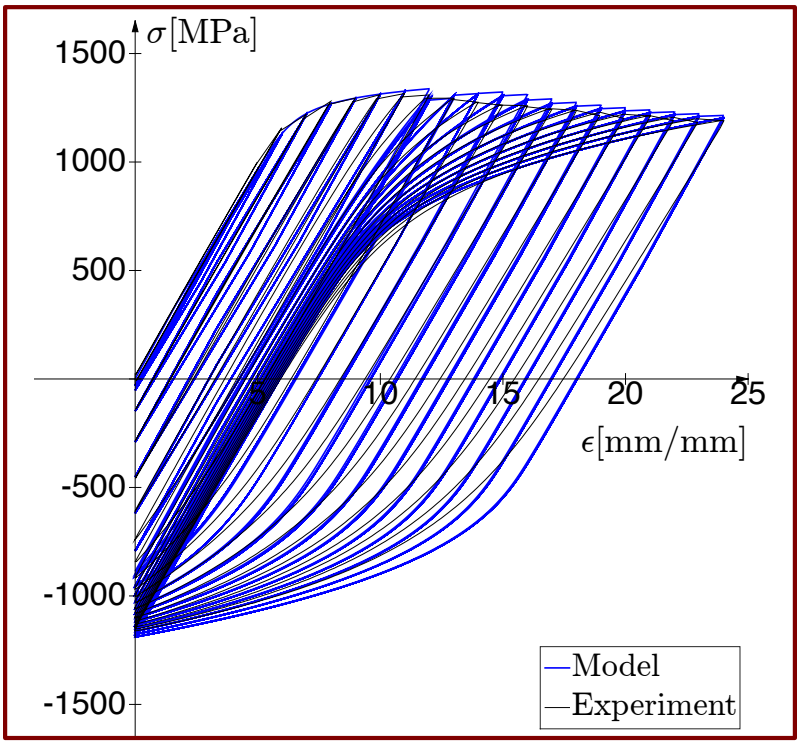

(b)

Figure 3.24: Experimental results (in black) compared to the incremental model (in blue) for the second $R_\varepsilon = 0$ test with $C = 2 \cdot 10^6$ a) Mean stress relaxation curve b) Cyclic plasticity loops

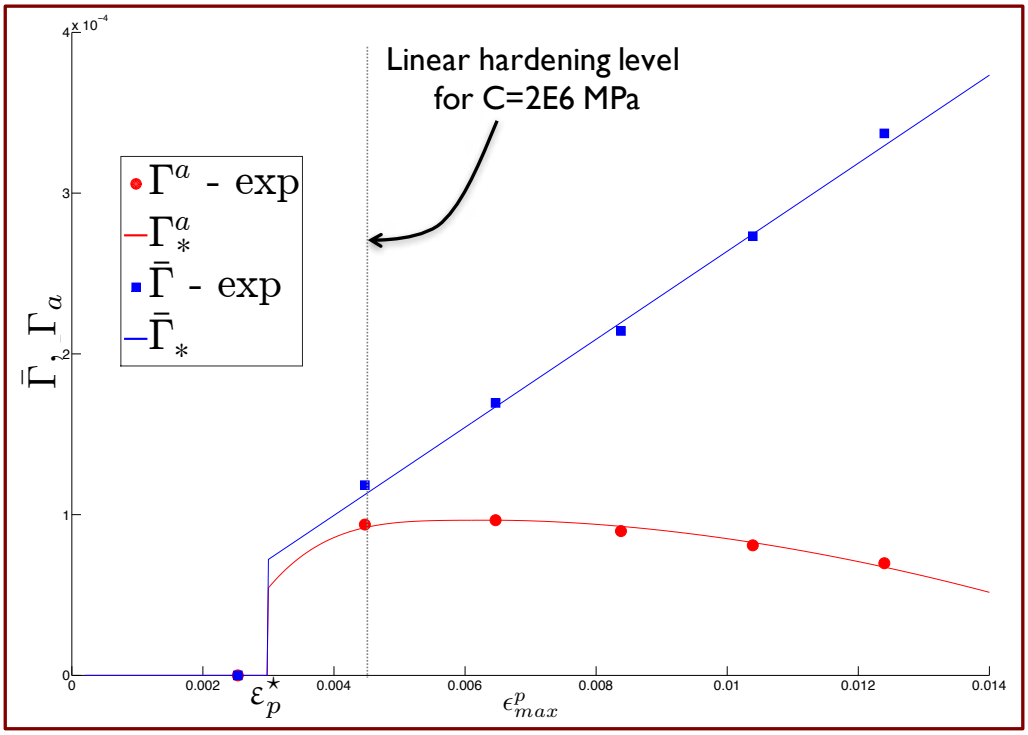

Figure 3.25: New evolution laws for Γ^a_* and $\bar{\Gamma}_*$ in the incremental model for $C = 1 \cdot 10^7$

between the results of the model and the experiment for $C = 1 \cdot 10^7$ MPa are shown in *Fig. 3.26* for the whole loading history. *Fig. 3.26a* shows σ with respect to ε with the model in thick red lines and the experimental data in black lines. *Fig. 3.26b* shows $\bar{\sigma}$ with respect to $\frac{\Delta\varepsilon}{2}$ with the model in red and the experimental data in black for the last cycles of each level. It may be seen that the forth level is very well represented. The mean stress relaxation curve is very accurate for all levels. In order to be as close as possible to the real behavior, when passing from one loading level to the other the simulation was performed continuously rather than a separate simulation per level. Thus, for the transitions between levels, the model doesn't yet capture the local hardening as in reality. Nevertheless, the stabilized cycle is obtained at the right level.

6.3 R_ε=-1

The symmetrical strain-controlled loading case $R_\varepsilon = -1$ was finally tested using the incremental model. As mentioned earlier, the slight tension-compression asymmetry can be represented by using a non-zero Γ^a, as was shown in *Fig. 3.13b*. Given that this phenomenon isn't very interesting in our case, we chose to use a symmetrical configuration, thus $\Gamma = \Gamma_+^{Up} = \Gamma_-^{Down} = \bar{\Gamma}$. Using the evolution of $\bar{\Gamma}$ described in *Fig. 3.20a* the results shown in *Fig. 3.27* are obtained.

These results are more than satisfactory and prove that the incremental model is adapted to model both the $R_\varepsilon = 0$ and the $R_\varepsilon = -1$ cases using one unified formulation.

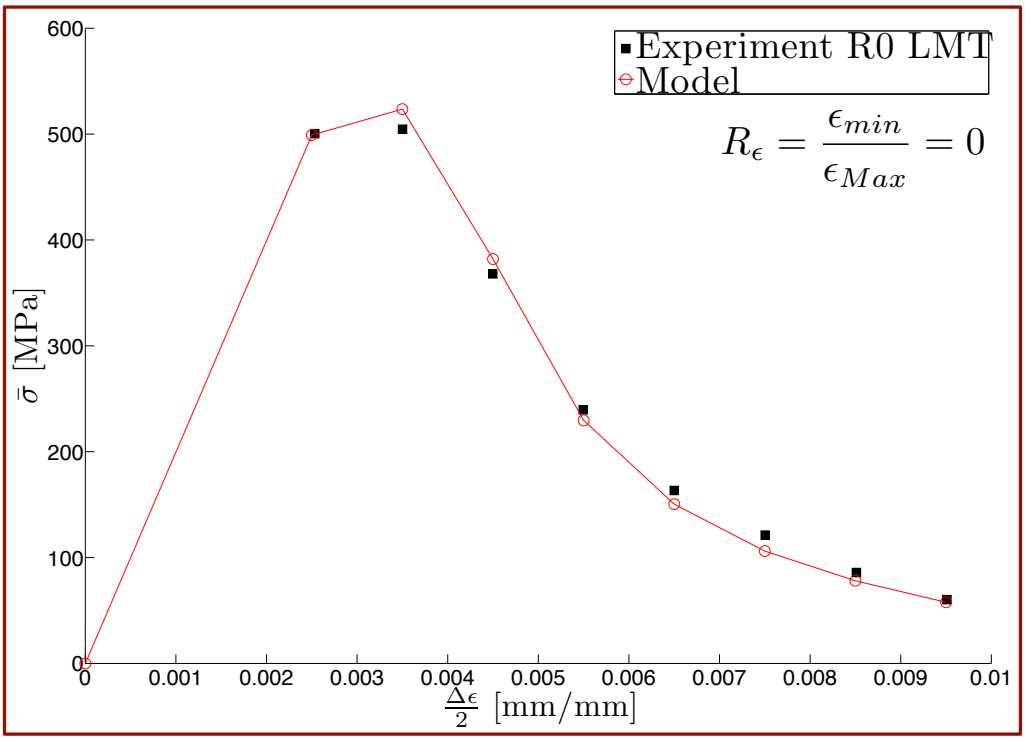

(a)

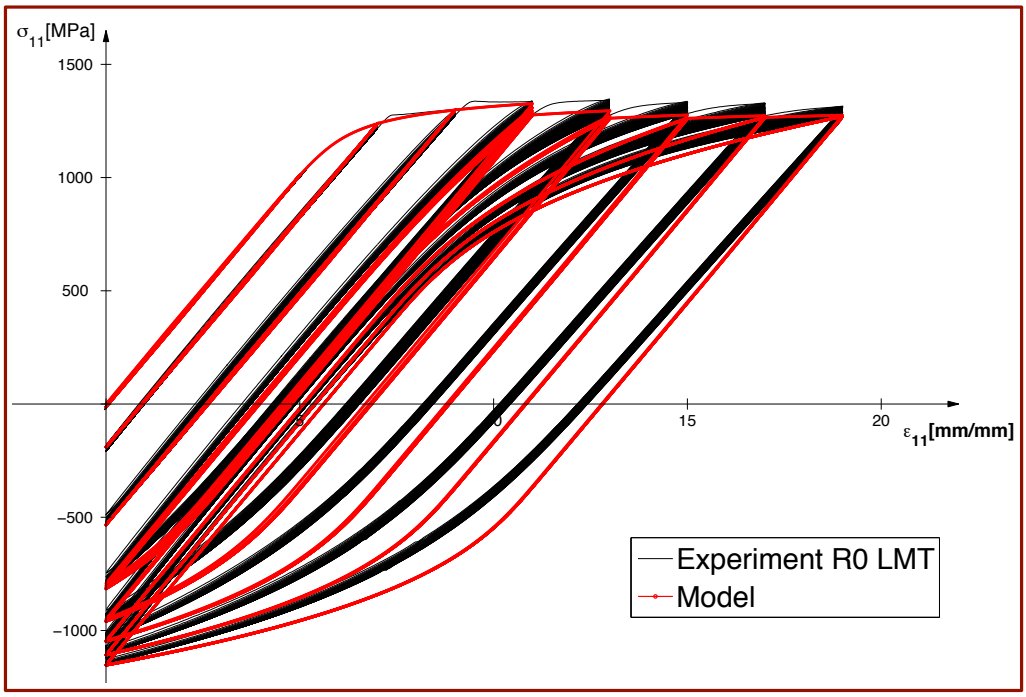

(b)

Figure 3.26: Experimental results (in black) compared to the incremental model (in red) for the first $R_\varepsilon = 0$ test with $C = 1 \cdot 10^7$ MPa a) Mean stress relaxation curve b) Cyclic plasticity loops

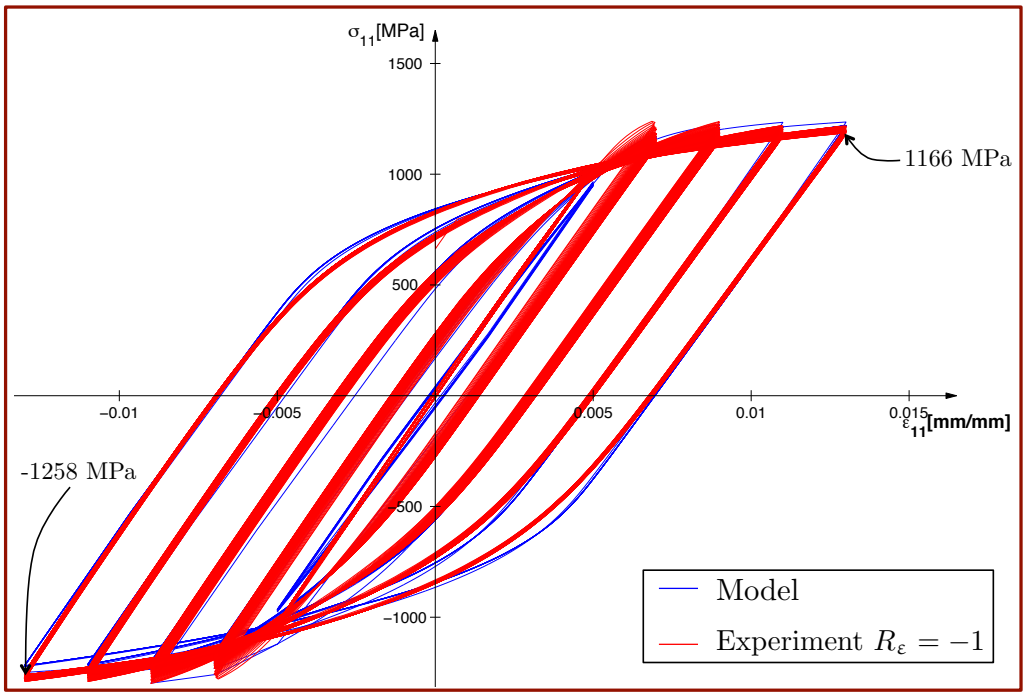

Figure 3.27: Experimental results (in red) compared to proposed plasticity model (in blue) for $R_\varepsilon = -1$

7 Conclusions

In this chapter, a detailed description of the final version of the model is made. The main feature of this model is that it provides a good description the partial mean stress relaxation in the cyclic plasticity zone of the $\bar{\sigma}(\frac{\Delta\varepsilon}{2})$ curve. When compared to confirmed kinematic hardening laws that model non-zero mean stress relaxation [Chaboche, 1991; Chaboche et al., 2012] our model presents the advantage of using only one backstress, even if its description is more complex. Moreover, the model is incremental, so it can take into account complex loadings such as gradually increasing maximum strain tests.

One of the more original parts of the creation of the model is the idea that partial mean stress relaxation is a direct consequence of the difference between loading and the unloading part of the hysteresis loop. By analyzing the parameters that could be responsible for this difference such as the Young's modulus, the size of the elastic domain k or the kinematic hardening parameters M, C, Γ, etc., we were able to find patterns that would indicate that there was indeed a considerable difference between what happens at the ascending and at the descending part of the loop. For reasons explained in section 3, the chosen parameter we used to describe this difference was Γ. Its evolution was directly computed for all the cycles of the available tests and some interesting patterns arose when looking at Γ in terms of mean value $\bar{\Gamma}$ and amplitude Γ^a obtained for the two parts (loading and unloading).

One important conclusion when analyzing the R_ε=0 tests was that the complete relax-

ation of the mean stress was linked to Γ^a becoming zero. In other words, when the two parts have the same description, the cycle becomes symmetrical. It is an interesting data to find, and we used it directly in our model to obtain a smooth evolution of the mean stress relaxation curve. When compared to confirmed non-linear kinematic hardening with thresholds model developed by Chaboche et al. [1991], the number of used parameters is lower in our model and the description has no subsequent jumps in the response, as it happens with each deactivation of back-stresses for the NLK hardening with thresholds.

Even if it was not the focus of this study, an interesting aspect that can also be represented with this dual Γ approach is the small, but observed, asymmetry between tension and compression. It was shown in subsection 3.3 how by a minimal tuning of the parameters this asymmetry can be very accurately represented. In the last chapter of the thesis, a vast biaxial campaign will be presented, along with developments to make I-DIC strain-controlled tests.

Chapter 4

Biaxial tests

In the current chapter, the cyclic tests performed on biaxial cross-shaped samples are presented. The purpose of these tests is to provide a database used to validate plasticity models under multiaxial conditions and especially the one presented in the previous two chapters. First, the choice of the sample and the experimental protocol are presented. Second, the principles and feasibility of the integrated digital image correlation strain control will be explained. Last, the results of the experimental campaign will be shown and interpreted.

Contents

1 Introduction

The main goal of this study is the development of a plasticity model adapted to the behavior of Inco718DA under multiaxial loading conditions. In order to identify the model, cyclic biaxial tests need to be performed at large cyclic plastic strains.

The biaxial tests were performed in the triaxial testing machine ASTREE from LMT Cachan [Calloch, 1997; Cognard et al., 1997; Calloch and Marquis, 1999; Frémy, 2012]. In order to be able to properly identify material constitutive laws from biaxial tests data, various testing protocols and types of cruciform specimens have been used in this machine varying from thermal fatigue [Sermage, 1998; Poncelet et al., 2010; Rupil, 2012], crack initiation and propagation [Frémy, 2012; Tomicevic, 2015; Sadriji et al., 2016], fatigue of pressurized reservoirs [Mathieu, 2013] or other complex thermo-mechanical loadings in aeronautics and aerospace applications [Barbier, 2009; Gaborit, 2015].

One of the measurement and control techniques classically used is the strain gauge for its precision and simplicity. Unfortunately, the important strains developed in the sample are likely to surpass the measurement range and there is also a high risk of gauge debonding. Biaxial extensometers [Makinde et al., 1992b; Sermage, 1998; Kulawinski et al., 2011b] also offer reliable strain measurements, but their inconvenience is that they assess only a mean value for a much more important zone than that of a strain gauge. In both cases, certain heterogeneities might be missed. Another important aspect is the detection of unexpected cracks, which is assumed to occur in the center of the sample. The strain gauge method covers the region of interest (ROI), rendering it non-exploitable, while the biaxial extensometer solution is possible but unpractical.

An alternative is to perform full-field measurements by using Digital Image Correlation [Sutton et al., 1983a]. Since the first use in experimental mechanics in the early '80 [Lucas and Kanade, 1981; Sutton et al., 1983a; Chu et al., 1985], this technique has evolved considerably and is extensively used both in the academic field [Sutton et al., 2009; Hild and Roux, 2012b] and in the industrial world [Desmars et al., 2004]. With this approach, the surface of the sample is not hidden, and one can use several cameras with several DIC algorithms in order to obtain a maximum of information during the experimental test. The displacement measurements obtained with DIC can be used for model validation, model parameter identification [Calloch et al., 2002; Avril et al., 2008; Grédiac and Hild, 2012], or for controlling mechanical tests [Fayolle et al., 2007; Fayolle and Hild, 2014; Le Flohic et al., 2014; Carpiuc, 2015].

In the following, some of the improvements that had to be made in the lab in order to perform the biaxial campaign will be presented (sample geometry choice, testing machine, new grips, instrumentation, strain-control technique) as well as the biaxial tests results.

2 Experimental protocol

2.1 Mechanical loading

2.1.1 Biaxial sample geometry

In the beginning of the study, the first constraint was that the samples would be extracted from a forged circular block, normally used to machine one high-pressure turbine disk. The forged block is a revolution piece with a section that would fit a sample of maximum 255 mm in length (*Fig. A.4*). Micrographic cuts were regularly analyzed in the forged blocks, so we also knew the grain size in this area, which was in the order of 10 µm. Thus, to obtain a suitable enough sample, we would need a rough minimum volume of interest of $10\times10\times10$ grains. In order to achieve large levels of plasticity in this ROI, we would need to induce important loads and obtain pure strain or stress states (plane strain or plane stress). Thus, parasite bending or buckling would have to be at a minimum or zero.

Based on this consideration, two cross-shaped specimen geometries were initially considered, one LMT version developed during several studies [Sermage, 1998; Barbier, 2009], and another developed by Safran Aircraft Engines (SAE) for a biaxial study at ENI Tarbes [Selva et al., 2017]. Both geometries have been used prior to this work ([Barbier, 2009; Rupil, 2012; Gaborit, 2015] for the LMT one, [Selva et al., 2017] for the SAE one), which validates their design for loadings close to the aimed ones. A comparison between the two geometries was carried out in order to choose the better adapted one for our study. Our main need was to perform cyclic, high amplitude, strain-controlled tests. For this, we ideally needed a sample that would exhibit a homogeneous strain field in the region of interest during tests. A heterogeneous stress field would be acceptable in the case of elasticity, but in the present case of elasto-plasticity, it would not be straightforward at all, if not impossible to accurately analyze. The gauge zone was uniform in the case of the SAE sample, but not for the LMT one, given that the latter has a spherical calotte fillet in the middle, leading to a meniscus shape, and thus a nonconstant thickness. Secondly, high strain amplitudes needed to be obtained in the central zone in order to have plastic hysteresis loops to compare to the uniaxial case. Since no high bicompressive stress states have been applied during the previous studies, rough Abaqus simulations were performed on both sample types using the same material properties. The material behavior chosen in Abaqus was an isotropic and elasto-plastic one, and besides the Young's modulus and Poisson's coefficient, stress vs plastic strain data extracted from the uniaxial monotonic behavior of Inco718DA were used as interpolation points, combined with a von Mises equivalent stress. As can be seen in *Fig. 4.1*, the region of high stresses is, as expected, much more restricted for the LMT specimen. It is also more rigid (*Fig. 4.2*), and even going from zero to the full range of the machine would cause very little plastic strains. Moreover, one must keep in mind that this is the value only in the central point, so it is actually the maximum for σ and ε^p for the LMT sample given its geometry, and a mean value over the ROI would be even smaller.

Given the fracture shape of the ROI in the case of some compression tests for the SAE

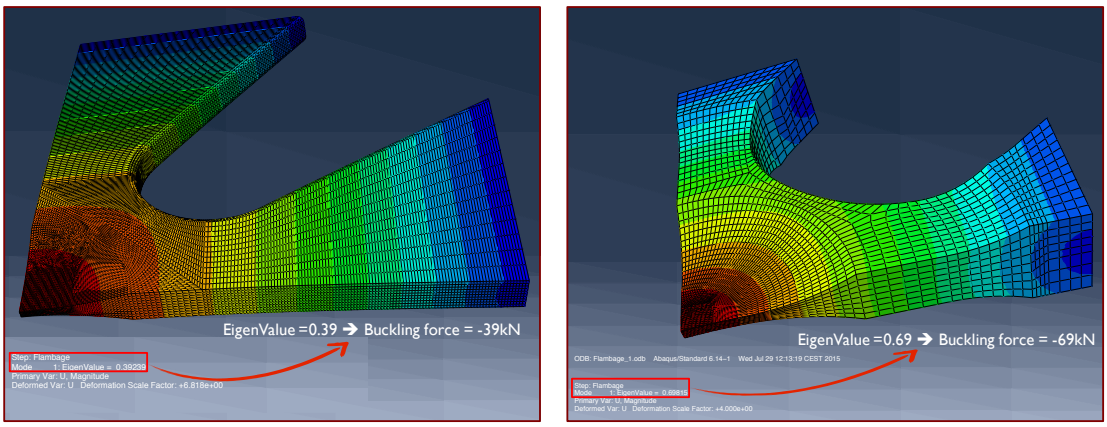

(a) (b)

Figure 4.1: Comparison between the behavior of the two samples in Abaqus buckling simulation a) LMT sample b) SAE sample

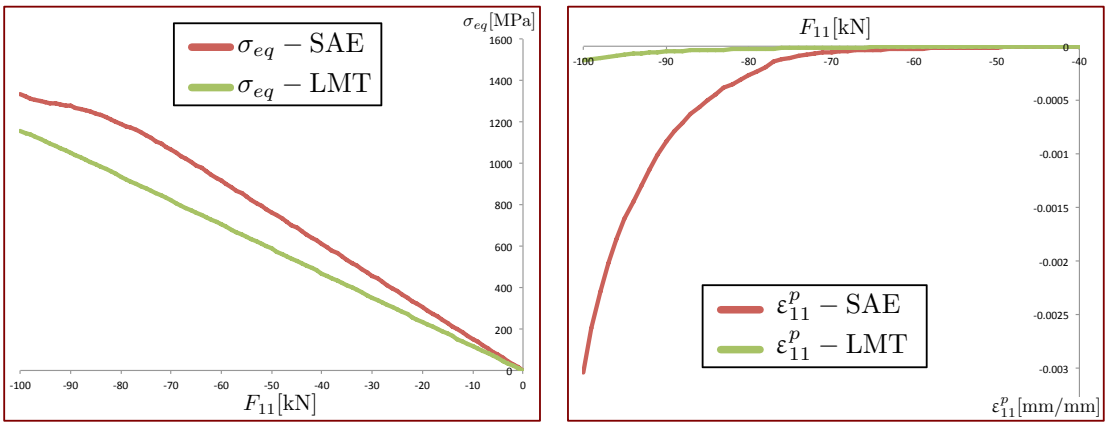

(a) (b)

Figure 4.2: Comparison between the behavior of the two samples in monotonic compression a) σ_{eq} vs F_{11} b) ε^p_{11} vs F_{11}

geometry, buckling simulations were also performed in Abaqus. Although restricted to the global instability type (local buckling may also occur as shown in the following), and highly dependent on the boundary condition choice (here an equi-biaxial compression force), it still provides a qualitative indication that the SAE sample behaves better under compression. Displayed on *Fig. 4.1*, the appearance of buckling for each specimen geometry shows that the SAE one allows a higher compressive stress without buckling. This phenomenon will be studied more in detail during experiments, when stereo-correlation will be used to assess the out-of-plane motions and establish the buckling limit.

Given all the criteria mentioned earlier, the SAE geometry was chosen. The sample has three orthogonal symmetry planes and the dimensions $200 \times 200 \times 9.6$ mm (*Fig. A.8*). The disk sample extraction plan is detailed in Appendix A. As it may be seen in *Fig. 4.3*, the x, y and z axes correspond to the radial, tangential and out-of-plane directions respectively.

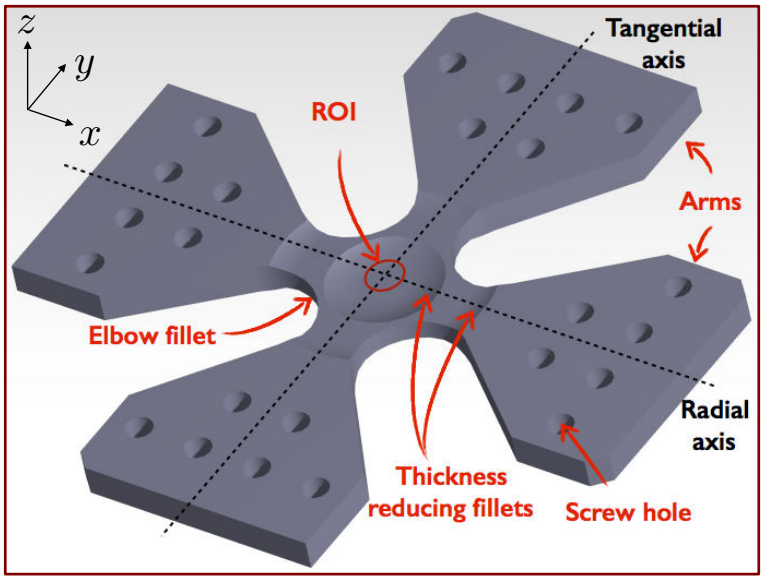

Figure 4.3: Biaxial sample used during the experimental campaigns

The thickness of the sample is 9.6 mm at arm level and is reduced down to 1 mm in the center via two successive fillets (intermediate thickness of 6.16 mm). The central zone is circular, with a 12 mm diameter and it represents our region of interest (ROI). One of the reasons why this geometry was chosen, was the constant thickness of the gauge zone, which allows (but does not ensure) a uniform strain field in the ROI. Therefore, it is very important that the thickness of the central zone, as well as its position with respect to the mean plane (xy) is respected during the machining phase.

During the reception of a first batch of samples (XA1...4) a machining error was noticed for XA4, which had the center shifted by 1 mm. Thus, this sample was considered too far beyond the demanded geometrical tolerances and has been used in an initial phase of the study as a 'tuning sample'. It was used to make certain adjustments to the machine such as setting the PID, verifying the testing procedure and the experimental protocol.

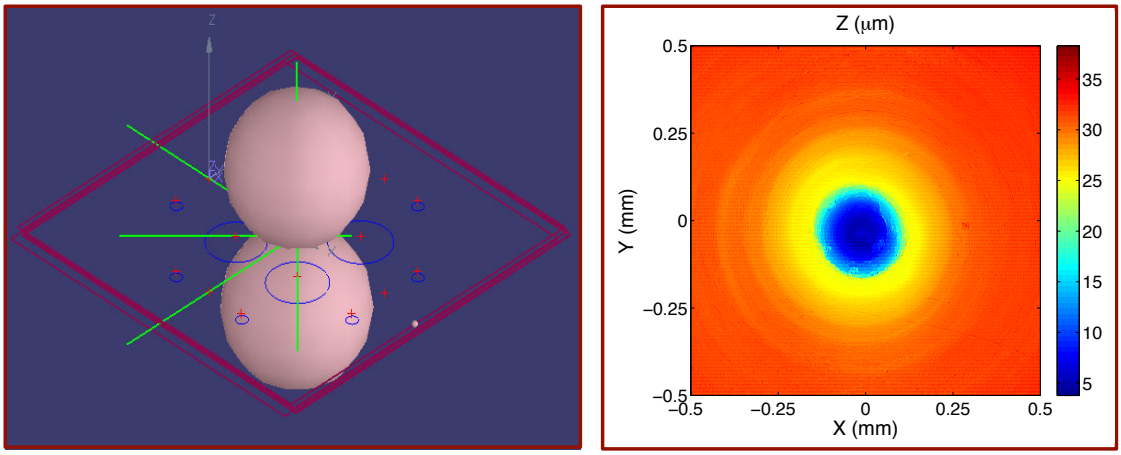

(a) (b)

Figure 4.4: Geometry measurements of the biaxial sample a) Coordinate Measuring Machine schema b) White light interferometry

Given the innovative tests that were envisioned and performed, three other samples were machined, with the same geometry and out of a material with similar properties as the Inco718DA (XT1...3). They were created in order to avoid accidentally destroying or damaging the real samples which were very expensive and scarce.

In order to ensure the quality of the sample surface, a general precision of 0.2 mm was demanded, with stricter restriction on the ROI (0.1 mm for the coaxiality of the center with respect to the group of screw holes and 0.02 mm for the position of each face with respect to the surface of the arms). Moreover, geometry measurements were made using a Coordinate Measuring Machine (CMM) on all the samples, and surface quality measurements on one specimen using white light interferometry (*Fig. 4.4*), showing the samples to be withing tolerances or slightly out of range in some cases. The CMM measurements were performed using a machine with an estimated uncertainty of 10 µm for each measurement point. This step is obviously tremendously important since the accurate knowledge of the real thickness is necessary to calculate the applied stresses. Among all possible geometrical defects, we focused mainly on those in the central area, in terms of thickness and position. For the thickness, we measured the distance between the external planes determined by 10 points on each of the two sides of the sample, in the central zone. In order to verify if the ROI wasn't shifted vertically (on the z axis), the mean plane was generated using the two faces of the sample at the arm level.

The position of the center of the sample in plane xy was computed using three distinct references. The first one is the group of screw holes, which also serve as a reference in the machining plan. The second one is given by the two surfaces of the thickness reducing tori that surround the central zone. They were approximated to spherical surfaces, given that the CMM software doesn't allow the palping of a torus. The center of the sample is thus given by the intersection between the line unifying the centers of the two spheres and the mediane plane. The last reference is given by the four "elbow fillets" between the arms of

the sample (*Fig. 4.3*). By treating each of these fillets as a cylindrical surface, we obtain a quadrilateral by projecting the axis of each one of the cylinders on the median plane. The intersection of the diagonals of this quadrilateral gives the center of the reduced thickness region. Given that the first method is used as the reference in the machining plan, the results from the two others are compared to this one.

Tol(mm)	⏥Up 0.05	⏥Down 0.05	C.Fillets 0.1	C.Tori 0.1	Th.ROI 0.04	Dist.Up 0.02	Dist.Down 0.02
XA1	0.0547	0.0542	0.0823	0.0752	1.0228	0.4718	0.5511
XA2	0.0308	0.0317	0.0722	0.0928	1.0775	0.5099	0.5678
XA3	0.0268	0.0572	0.5092	0.1762	0.9988	0.6270	0.3718

Table 4.1: Coordinate Measuring Machine (CMM) results

In *Tab. 2.1.1*, the quantities obtained from CMM measurements may be seen: the flatness of the central zone (for the upper plane ⏥Up and for the lower plane ⏥Down); the difference between the position of the center computed with the reference screw holes and the fillets (C.Fillets) and the two torus surfaces (C.Tori); the thickness of the central zone (Th.ROI); the distance between the mean plane and the central surfaces (Dist.Up and Dist.Down, with the obvious relationship Th.ROI = Dist.Up + Dist.Down). The values are consistent with the imposed tolerances in certain cases, but for the values in red and orange they slightly surpass them. The error in the thickness of the central zone goes up to 7%. What also has to be taken into account is the fact that the measurement of the position of the center with the two methods involve precision palping (small sized central zone, fillets, etc.), thus needing to be performed with caution. For the rest of the samples we received (XB1, XB2, XC4), machined after complaints were made to the company, CMM measurements were performed by an exterior firm, and the results were within the specified bounds.

The white light interferometry measurements were performed in the LURPA laboratory of ENS Cachan on one sample. One sees in *Fig. 4.4b* that there is a defect of 30 µm in local flatness. Given that the first batch of samples was machined using the same procedure, we can assume the same order of magnitude in the size of the defects of each sample. This is the result of a turning process used to obtain the central area, which can result in either a hole or a peak, both withing acceptable bounds.

2.1.2 Multiaxial testing machine ASTREE

In order to obtain biaxial tests with plastic cyclic loops, important forces must be applied to the chosen sample geometry. As one may see in *Fig. 4.2*, considerable plastic strains begin to appear in the equi-biaxial case, for loads superior to 80 kN in the monotonic case (given the chosen behavior, the tension case is symmetrical). The choice was thus made for the biaxial tests to be performed in the triaxial testing machine ASTREE from LMT Cachan [Calloch, 1997; Cognard et al., 1997; Calloch and Marquis, 1999; Frémy, 2012].

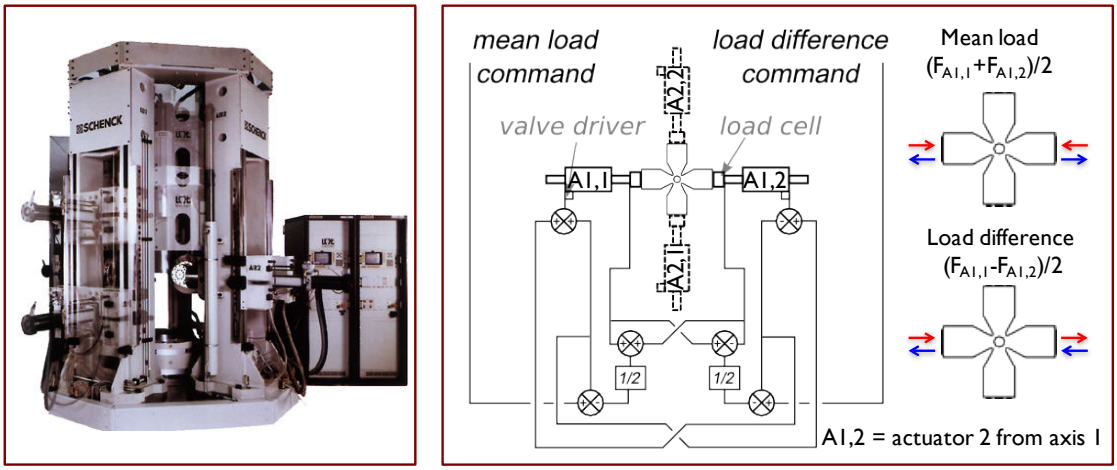

(a) (b)

Figure 4.5: Triaxial testing machine ASTREE a) Photo b) Modal control ($F_{A1,1}$ and $F_{A1,2}$ are the loads corresponding to the two actuators of axis 1)

Among the six servo-hydraulic actuators that the machine is equipped with, the four horizontal ones are used (*Fig. 4.5a*). They have a load capacity of 100 kN and a 250 mm displacement range. The system can be translated vertically to accommodate complex instrumentation and different test scenarii. The machine is equipped with a versatile digital controller (Instron 8800) and is controlled from one main computer using the corresponding interface software (Consol 8.2). The actuators may be controlled either independently or in pairs. The latter, also called "modal control", permits a vast array of linear or non-linear combinations between the available input signals (forces, displacements or other external channels). The most common application, as seen in (*Fig. 4.5b*), is to impose a given mean load amplitude ($F_{Ai,1}$+$F_{Ai,2}$)/2 and a zero load difference ($F_{Ai,1}$-$F_{Ai,2}$)/2 along an axis i (composed of two actuators 1 and 2). This allows to maintain the center of the sample motionless (if we suppose the behavior to be symmetrical), which is very useful in practice, when analyzing a region of interest of reduced size.

For the biaxial tests performed on cross-shaped samples [Hannon and Tiernan, 2008], the most common scenario in the laboratory was to use the horizontal actuators for the mechanical loading and the vertical ones for fixing the measurement means [Sermage, 1998; Doudard et al., 2007; Périé et al., 2002; Poncelet et al., 2010; Rupil, 2012; Mathieu and Hild, 2013; Tomicevic, 2015; Gaborit, 2015]. The vast majority of tests were force controlled for accuracy and safety purposes (more accurate than displacement, more secure than the strain gauge). Indeed the build-in displacement measurement setup is based on LVDTs, which are placed very far from the region of interest and are influenced by the thermal fluctuations of the actuators.

The machine is equipped with a PID controller on each of its axes. As is common for classic hydraulic machines, the command is calculated using the control error (the difference between the setpoint and the measured response), its integral and its derivative. The controller attempts to minimize the error over time by adjusting a control variable

Load PID	Modal 1A	Modal 1B	Modal 2A	Modal 2B
Proportional [dB]	-10	0	-10	0
Integral	5.1	10	5.1	5.3
Derivative	0	3	0	0

Table 4.2: Values for the load PID used for the biaxial tests in ASTREE

(such as the position of a control valve) to a new value determined by a weighted sum:

$$u(t) = K_p e(t) + K_i \int_0^t e(\tau)d\tau + K_d \frac{de(t)}{dt} \tag{4.1}$$

where K_p, K_i and K_d denote the coefficients for the proportional, integral, and derivative terms, respectively (more commonly denoted P, I, and D). These variables thus allow us to set the contribution of each effect. The PID is adjusted in similar conditions (stiffness, temperature, load, etc.) as for the test to be performed, and its validity range depends on the precision we seek at the input features (amplitude and frequency in the case of a sinusoidal signal) that we impose.

In order to tune the PID for the load cell, different aspects were studied such as necessary load amplitudes, frequencies and cyclic test types (sinusoidal and triangle). Square signals were also tried out in order to test that the system is sufficiently stable. In the modal control of ASTREE, commands are usually given in terms of average load (Modal B), which is the load amplitude imposed to a certain axis, and in terms of load difference (Modal A), which is usually zero, because we normally don't want any macroscopic shear of the arms to occur. Thus, the notation "Modal 1B" represents the load amplitude for axis 1, in modal control. The final values chosen for the PID are shown in *Tab. 2.1.2*.

The control of ASTREE is currently performed using two software packages. The first one, Consol, permits the configuration of all acquisition and control channels. Basic quasi-static and cyclic (sinusoidal, triangle, square) loading cases, as well as real time graphs of up to four variables can be programmed using Consol. It's very practical for tasks such as PID tuning or sensor calibration (LVDT, load cell, LASER) before the tests. The second software, called Wavematrix, was developed by Instron for other multi-actuator platforms and adapted for the triaxial case of ASTREE (*Fig. 4.6*). It allows writing more complex procedures containing more diverse functions (*e.g.*amplitude/phase control, event triggers, block repetition, relative command and precise camera trigger). Also, the graphical user interface is color coded and scaled to the range of each channel, thus making it easier to verify that no mistakes were made in the writing of each procedure.

2.1.3 New grips for biaxial tests

In order to be able to perform the biaxial tests on the chosen sample geometry, we designed and tested new grips for the ASTREE machine. The main reason behind this is the fact that the previously used grips wouldn't allow the mounting of such a sample, which

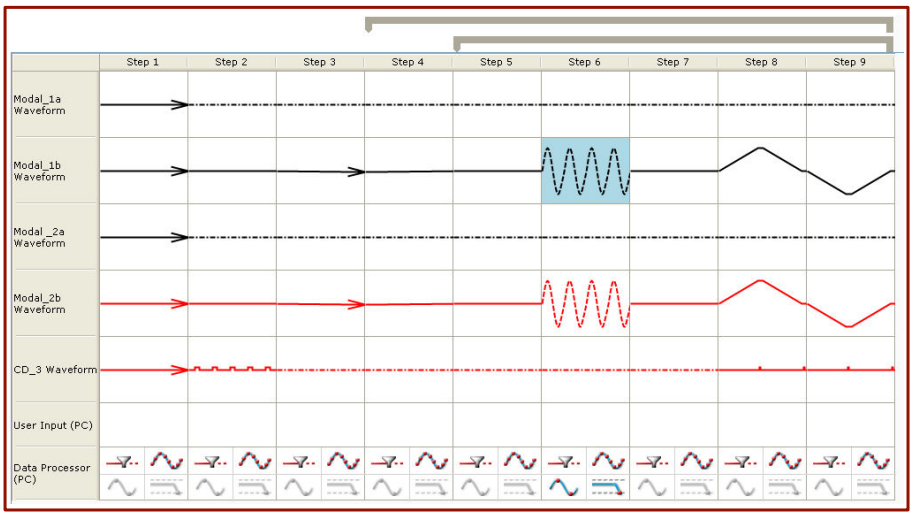

Figure 4.6: Typical procedure written in the control software Wavematrix

is shorter and thicker than the ones tested prior to this study. The old grips couldn't get so close to each other for the samples to be mounted, and the extra thickness meant that the mean plane of the sample would no longer be aligned to that of the hydraulic actuators. The new design corrects these inconveniences and presents other advantages as well, especially greater flexural stiffness, but at the cost of a more restrictive clamping procedure [Poncelet et al., 2014]. The design and some of the features of these new grips are presented in Appendix E. The sample chosen for the biaxial machine has the central part identical to the one used in ENI Tarbes, and the arms were modified so that they could be mounted in the new grips (*Fig. 4.3*).

The experimental setup also contains two LASER sensors (Keyence LK-G407), which give the "real-time" relative displacements between two opposite grips. These sensors are used because of the lack of precision in the machine's LVDT sensors, which are far from the ROI and are prone to errors due to elasticity and thermal fluctuations in the actuators. They also served as a way to detect eventual slipping of the upper part of the grip with respect to the lower part, given that the sensors are mounted on the lower parts.

Before launching the biaxial tests, a first stage of adjustments and verification was needed. This was performed on the calibration sample, XA4. The alignment of the axes is done using a linear spirit level, thanks to a vertical degree of freedom for each of the grips, given by the cylindrical centering pin in its slotted hole.

The tightening during the validation of the new grips was performed on samples 5 mm thick and 274 mm large. The vertical contact was ensured by using textured jaws that are fixed on the two parts of each grip. The sample is tightened using 8 M8 vertical screws to ensure contact and 5 M12 horizontal screws to keep the mobile and fixed parts of the grips together. In order to tighten the cross-shaped sample used for current study (which is shorter and thicker at arm level than usual biaxial samples used in ASTREE), different, thinner jaws were machined so that the mean plane of the sample stays aligned with the

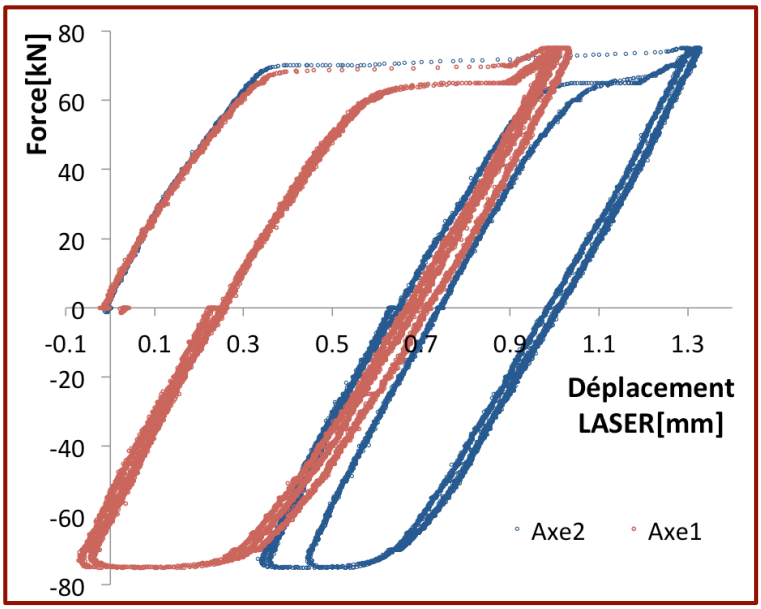

Figure 4.7: Slipping detected using LASER sensors, before passing to the dynamometric key

mean plane of the actuators. The vertical tightening was initially made using 6 M8 screws and an Allen key, but slipping was noticed given the high load levels and surface hardness of Inco718DA (*Fig. 4.7*). It was then decided to use 10 M8 screws, in order to create a more important contact pressure. Moreover, the screws were henceforth tightened using a dynamometric key, which ensured a more important and constant torque per screw type (35 Nm for the M8 screws and 50 Nm for the M12 ones). Another important aspect was the order in which the tightening was made. If either one of the two connection zones (jaw/sample and mobile part/fixed part) were to be too tightly fixed at first, than the other wouldn't have enough freedom to assure good contact and slipping might occur at high load levels. In order to overcome this problem, an incremental strategy was used, incremental in the sense that all the screws assuring a contact zone weren't fully tightened at first but little by little and in a precise order. In short the strategy was to assure partial contact between the fixed and mobile part by tightening two M12 screws, then one line of M8 screws, then untighten the two initial M12 so that good contact can be ensured with the sample by tightening all the M8 screws. Finally, the 5 M12 screws are tightened to ensure contact between the parts. The detailed strategy is available in [Poncelet et al., 2014] and if performed in the correct order, very little or no slipping appeared during our tests.

During one of the verification tests, an imposed load limit was accidentally triggered and the machine became unstable and performed high frequency, high amplitude, non equi-biaxial loadings on the XA4 sample. After 10 seconds, the sample suffered important self-heating in the ROI followed by fracture (*Fig. 4.8*). This allowed us to better understand how machine limits worked and that stopping the functioning of one axis at a

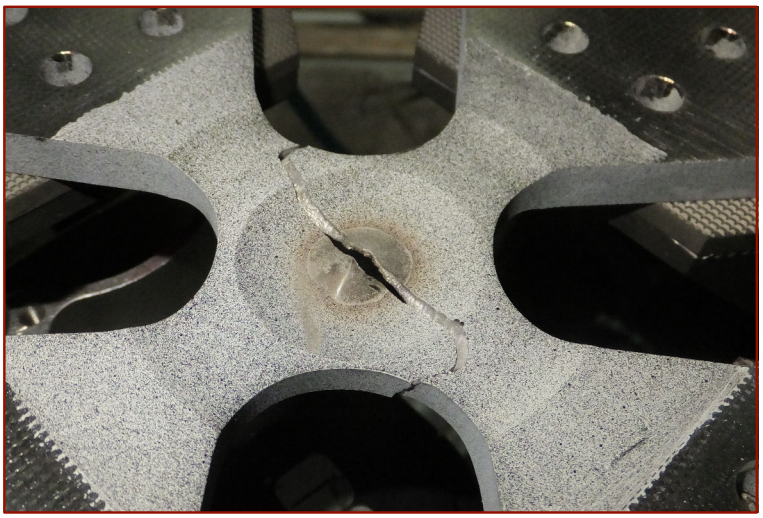

Figure 4.8: Accidental fracture of the calibration sample XA4

time just introduced more instability in the system, and did not protect the sample. Thereafter we used a limit trigger action called "System stop", which transfers to displacement control on both axes and waits for user decision. Thus, we can choose how to return to a safe state for the sample and continue testing.

2.2 Instrumentation

The instrumentation inside ASTREE has evolved considerably during past years, thus optimizing the experimental campaigns by performing fewer but "richer" tests. During the thesis, different configurations were used and will be detailed for each test. For most tests, the default measuring techniques will be presented in the following. As mentioned earlier, the four horizontal actuators apply the loads along the two horizontal axes (*Fig. 4.9*). In order to obtain full-field measurements using Digital Image Correlation (DIC) [Sutton et al., 1983a], two cameras are mounted perpendicular to the horizontal plane, one facing the upper side (Cam_1^{Up}) and the other one facing the lower side (Cam_2^{Down}). The camera model is Dalsa Falcon 2, with a maximum 4:3 resolution of 2432×1728 pix, 8 or 10 bit depth and a pixel size of 6 µm. This camera allows the setting of an area of interest (AI) and multiple regions of interest (ROI) that can be taken during a single shot. The size and offset of the AI and ROI can be set using serial commands, and are very practical for fine centering and when important acquisition rates are needed (*Fig. 4.10*). The cameras have a maximum frame rate of 168 Hz at full frame but can go up to 450 Hz for smaller areas of interest. This high resolution vs frame rate is one of the reasons this model was chosen to be used for the control of the machine using DIC.

The cameras are equipped with ×0.5 telecentric lenses and observe zones of 800×800 pix in the center of each face (*i.e.* 9.6×9.6 mm). Given that the ROI is supposed to be in a homogeneous strain zone (inside the circle of thickness 1 mm), we needed to

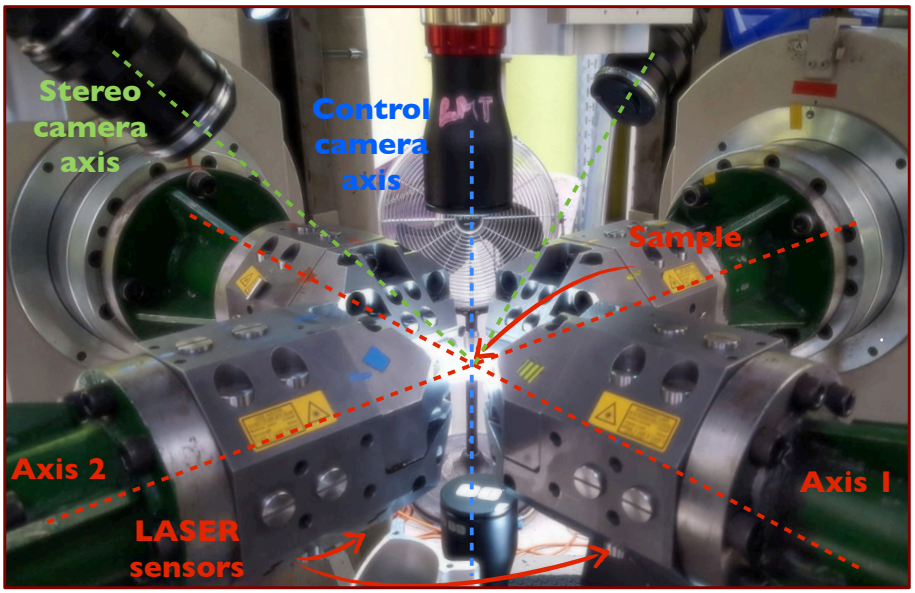

Figure 4.9: Instrumentation in ASTREE during biaxial tests

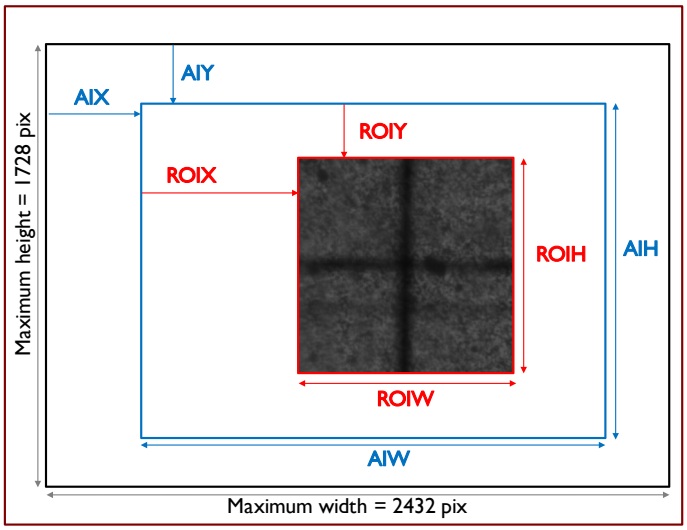

Figure 4.10: Properties adjustments for the area of interest (AI) and the region of interest (ROI) of Dalsa cameras

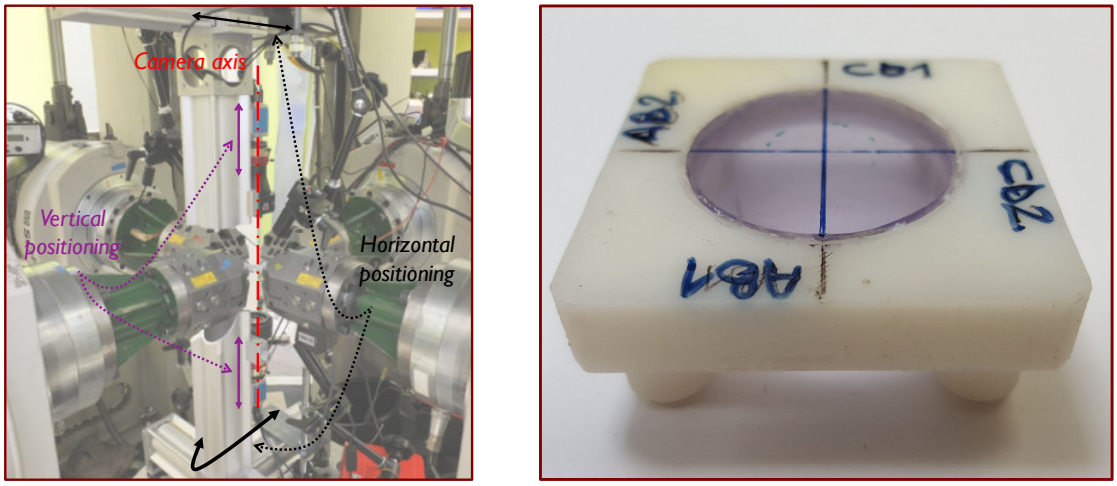

(a) (b)

Figure 4.11: Camera calibration during biaxial tests a) Degrees of freedom cameras b) Centering device

make sure that the frame is well positioned. Thus, a centering device was designed and manufactured out of PVC using a 3D printer (*Fig. 4.11b*). The device has four supports that snugly fit in the elbow fillets. It is composed of an opaque frame in the middle of which a translucent part is attached, with a cross marking to precisely see if the center of the photo corresponds to the center of the piece (*Fig. 4.10*) [1].

The two Dalsa cameras were adjusted using the following protocol: the focus is set with a fully open diaphragm (minimum depth of field), afterwards a compromise is made between a minimum exposure time and a maximum opening of the diaphragm. In order to center the cameras, a Newport X95 rails system was used, which are attached to the upper and lower inactive actuators (*Fig. 4.11a*). The cameras, as well as the vertical rails, are fixed on joints that slide when not fully tightened, which allows moving vertically and horizontally respectively.

After noticing some problems in the 2D displacement fields, when large compression loading was applied, two other cameras were introduced in the experimental protocol in order to perform stereo-DIC. The cameras are AVT MANTA G-145B (1392×1040 pix, pix size = 6.45 µm, 12 bits), equipped with F1.4 35-mm Zeiss lenses. They observe a zone of 800×800 pix which includes most of the sample, including the visible part of the arms. This way, we can better assess global and local displacements both in plane but especially out-of-plane. The initial calibration between the left and right images is performed with the help of a calibration target, which is a V-shaped prism with a known black and white chessboard pattern (*Fig. 4.12*). These squares allow us to precisely select the same points in the images taken with the left and right cameras, and thus obtain the transformation

[1] A more complex centering instrument is in development in order to be more versatile (adaptable for different sample types) and to clamp the sample from the sides so that it doesn't fall when placed on the bottom side

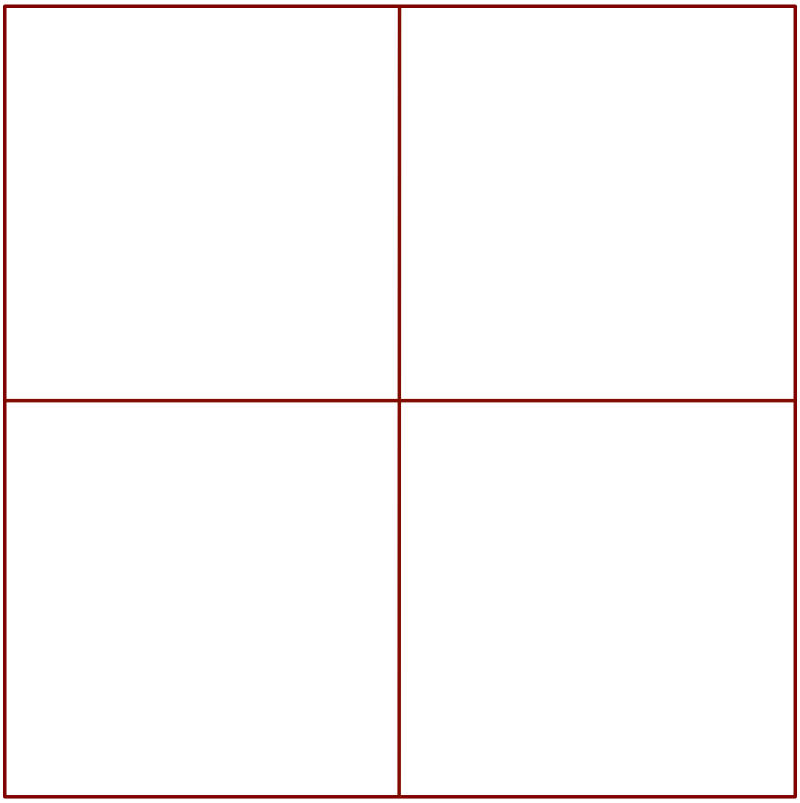

Figure 4.12: Photos of the calibration target used for the stereo-DIC analysis taken with the left and right cameras

matrix more precisely.

For the lighting of the ROI, two LED spot lights (EFFI-Sharp-FF-000-1) were used on each side. This ensures a uniform, constant light, thus eliminating fluctuations that might appear due to environmental changes in luminosity. The LED spots are far-field, thus allowing their positioning to be further from the sample, making it more accessible during the tightening phase.

2.3 I-DIC control technique

One of the main experimental objectives of the thesis was to perform strain-controlled biaxial tests, in order to study biaxial mean stress relaxation. In order to achieve this, the control of the machine using Digital Image Correlation (DIC) was developed. Several challenges had to be overcome to achieve this goal. The first was to test if the behavior of the sample in the ROI was sufficiently homogeneous so that a machine control using a mean strain was relevant. Second, the data to be used for the control from photos would have to be recovered, treated and then transmitted to the testing machine, all this in a sufficiently low time to allow cyclic loading. Last, the DIC signal would have to be sufficiently stable and with a low enough uncertainty for the type of strain increments needed

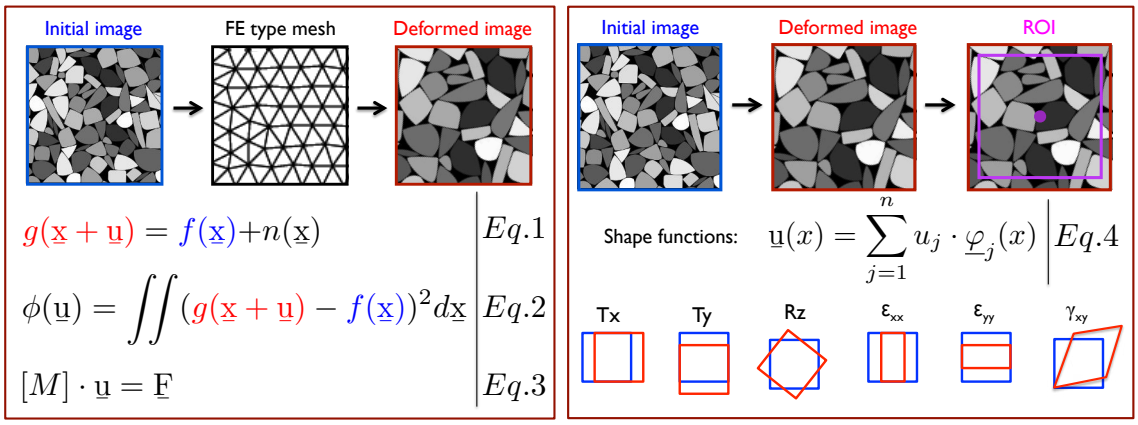

(a) (b)

Figure 4.13: Principle of digital image correlation a) Global DIC b) Integrated DIC

in our test. The different available types of DIC techniques were presented extensively in chapter 1 subsection 5.1. In the following, the principles of DIC will be briefly presented, followed by the validation of the method and finally its implementation.

2.3.1 DIC principles

The principle behind digital image correlation resides in analyzing the gray level of an initial image f versus that of a deformed image g and minimizing the difference between the two by conserving the optical flow (*Fig. 4.13a*, *Eq.* 2). One of the ways to achieve this is to discretize the ROI according to the Finite Element formalism [Besnard et al., 2006b], thus with data at the nodes that are interpolated over the whole element (*Fig. 4.13a*). The solution displacement field u is found by solving iteratively the linearized version (*Fig. 4.13a*, *Eq.* 3) of the minimization of the previous equation. Basically, $[M]$ represents the sensitivity of the initial image to the researched degrees of freedom and F the difference between the two images. The size of $[M]$ and F is proportional to the number of nodes times the number of degrees of freedom per node (usually equal to 2, corresponding to the displacements in the two directions). This method, also called the global approach, gives a high spatial resolution result of the structure, but is quite slow given the important number of unknowns (typically in the order of $10^3 - 10^4$).

Another option is to use a ROI of the same size, but with only one "super element" having only one node, and to enrich the shape function base in order to allow a more realistic description of its kinematics (*Fig. 4.13b*). The researched kinematics is therefore "integrated" into the shape function base (*Fig. 4.13a*, *Eq.* 4), thus the name Integrated Digital Image Correlation (I-DIC). Through this approach, the number of degrees of freedom will be drastically reduced. In our case, we may consider sufficient the following 6 shape functions: translations along axis x (T_x) and y (T_y), in-plane rotation around axis z (R_z), homogeneous strains ε_{11} and ε_{22} along axis x and y and homogeneous plane shear γ_{xy}. Even if this approach isn't as detailed at the global scale as the previous one, its main

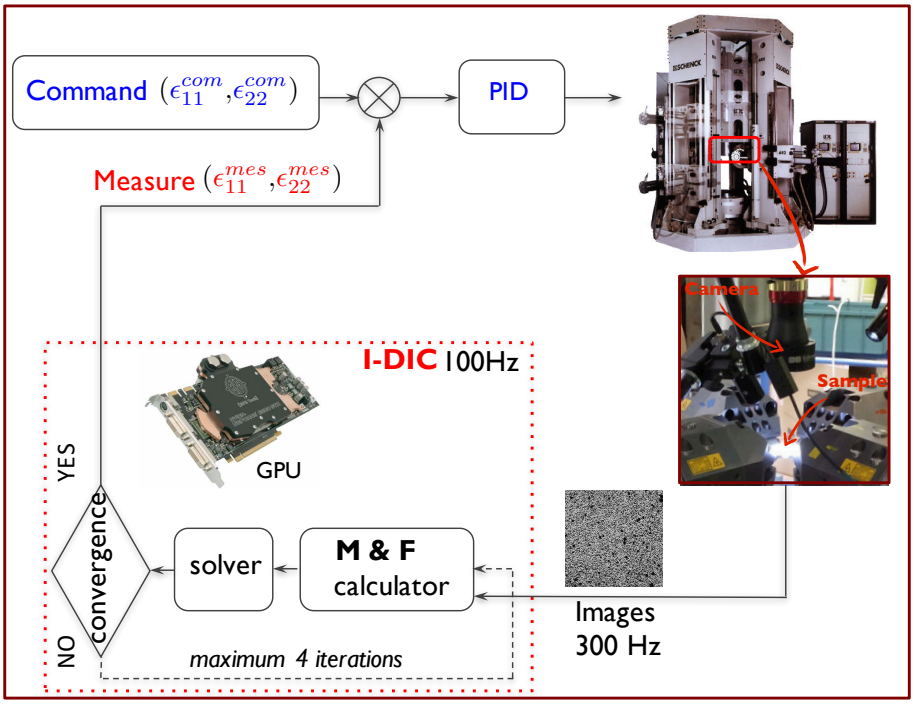

Figure 4.14: Control loop of the biaxial machine using I-DIC

advantage is exactly this speed/precision compromise that allows its use for the control of a testing machine.

By using the principle of I-DIC, we aim at controlling the machine directly in terms of strain (ε_{11} and ε_{22}). To do this, photos of the ROI are taken at 300Hz and analyzed with I-DIC using graphical processing units (GPUs) to reduce the computational time to around 0.01 s, *i.e.* $\approx$ 100 Hz measurement frequency. Finally, the measured values of the two strains are the input for a correction of the command, computed through the PID, as any other classic external measurement (*Fig. 4.14*). Among the images used for the control (taken at a very high frequency and erased from the RAM after use), some will be saved to be analyzed afterwards, using the global DIC technique, in order to check for crack initiation or to allow other post-treatments such as localization and damage.

2.3.2 Validity of the mean value for biaxial strain control

In order to test the applicability of the I-DIC control method, elastic force-controlled experimental tests were performed for typical loading scenarios: equibiaxial, uniaxial, non-proportional. The post-treatment was performed using the global DIC software with triangular elements, LMT Correli RT3 [Tomicevic et al., 2013], to obtain a rich field and verify if a more coarse method (I-DIC) is suitable.

The evolution of loads was performed in steps (sequences of ramp/hold), thus each photo (corresponding to each point on the graph in *Fig. 4.16a*) is taken after a period of constant load, in order to minimize the uncertainty coming from the testing machine. The

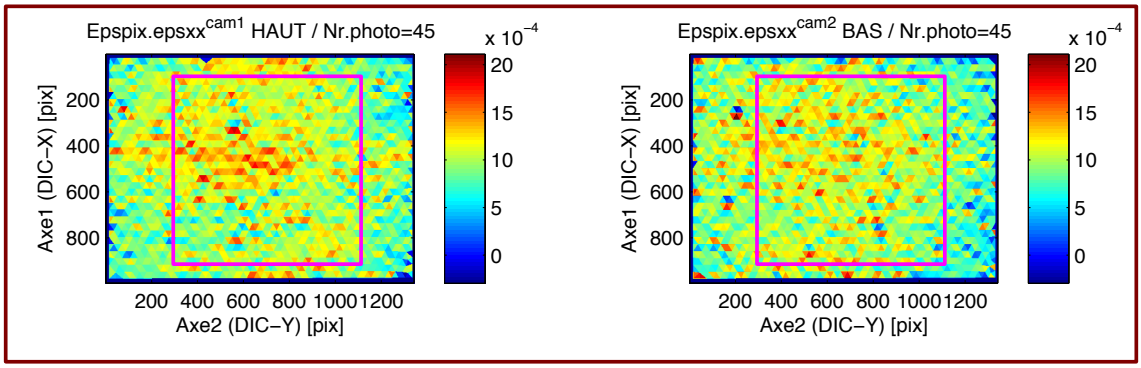

Figure 4.15: Strain maps of ε_{11} using an ROI of 800×800 (purple square) given by the upper (left) and lower (right) cameras

figure also shows the strain maps in direction 1 (ε_{11}) for the photos taken by camera 1 (upper face) and camera 2 (lower face).

Firstly, it needs to be mentioned that the global DIC computation was performed using very small triangular elements (30 pix in size) and without mechanical regularization. This explains the fact that there may be local spikes coming from speckle quality or optical problems. Other contributors for the slight differences between the DIC elements are the geometry of the sample and the loading fluctuations. Nevertheless, the global response of the structure is overall homogeneous in the ROI (represented by the purple square),

Secondly, no important difference is observed for the two faces for ε_{11} (*Fig. 4.16a*), with the values from the upper side in blue and the lower side in red. Therefore, in this elastic case, no flexion appears and the response of only one camera could be sufficient for the analysis. Nevertheless, in more extreme loading conditions or during long cyclic campaigns the possible difference in response between the two faces would offer important information about the behavior of the sample.

Thirdly, we compared the mean strains, which were computed using an optical gauge the size of the ROI, to the theoretical strain field. In order to obtain the theoretical strain magnitudes, elastic simulations were performed with Abaqus on an eighth of a sample (given its symmetry planes). *Fig. 4.16a* shows the loading for axis 1 (blue) and for axis 2 (red). Moreover, when comparing the experimental response with that of the Abaqus simulation (*Fig. 4.16b*), the results are very similar. The evolutions of strains are linear, which shows that the measurement result is (as expected) proportional to the efforts and the measurement uncertainty is quite small (lower than 10^{-4}). One of the reasons for the difference in the results might be the fact that, for the used sample, 3D measurements performed with a coordinate-measuring machine revealed that the theoretical mean plane was shifted by approximately 20%. Nevertheless, the fact that the results are coherent even for such small variations of efforts is a good sign for the applicability of the I-DIC control method.

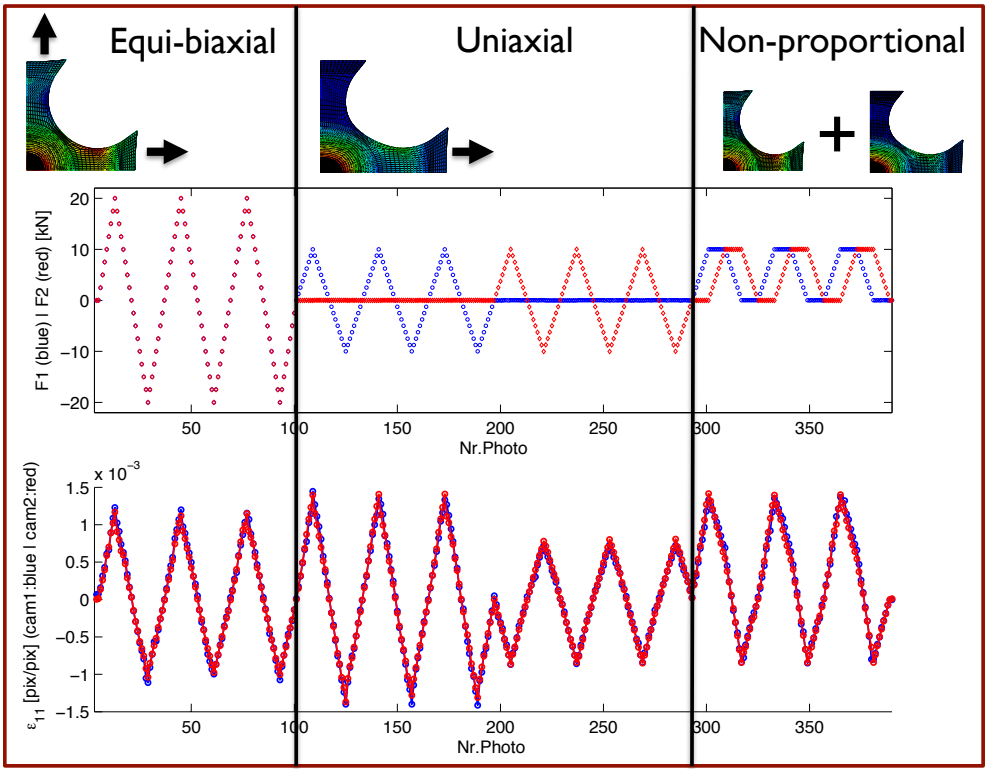

(a)

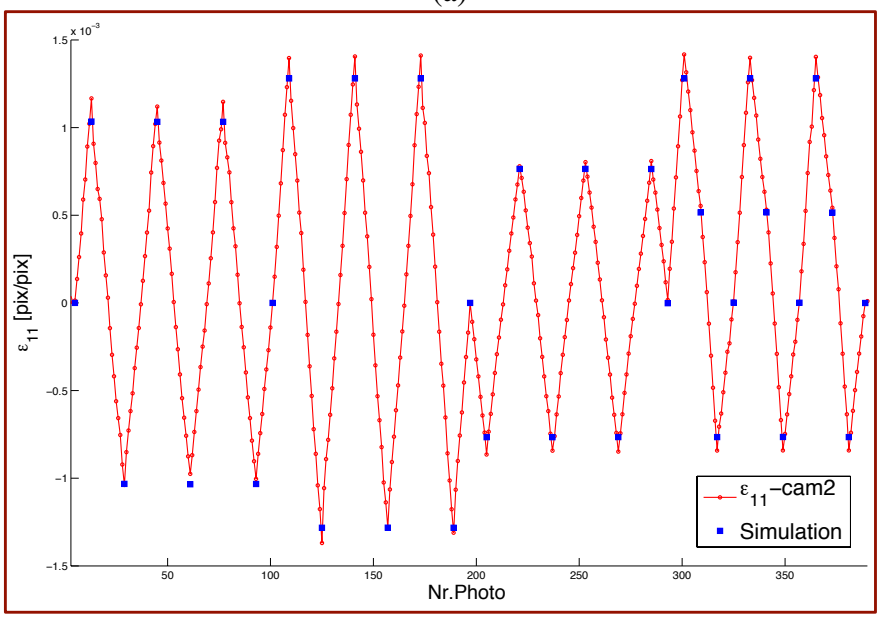

(b)

Figure 4.16: Results of elastic tests (ε_{11}) a) DIC optical gauge results (down) showing ε_{11} on the upper side (blue) and on the lower side (red) b) Comparison between the DIC results for the camera on the lower side (red) and the Abaqus simulations (blue)

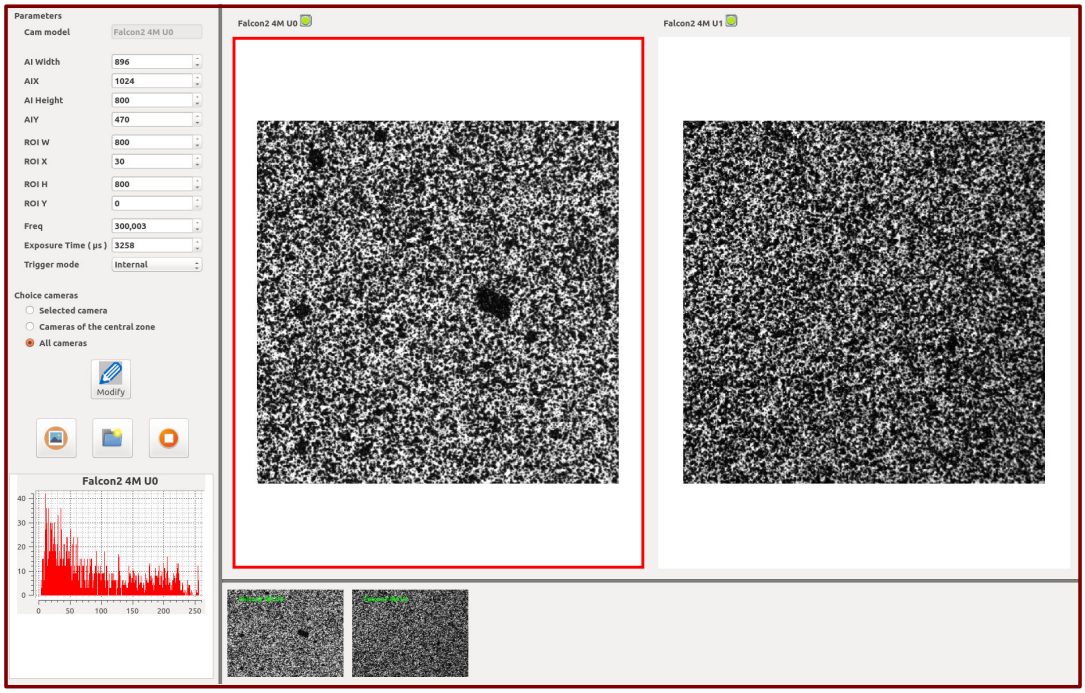

Figure 4.17: *Vision* software that controls camera acquisition

2.3.3 Technical specifications for the ”on-the-fly” I-DIC control

Having validated the applicability of the method by using an ”averaged” global DIC, we passed to the implementation of the integrated method. A C++ and Cuda code was developed in order to perform the GPU computations. It is based on a software described by Le Flohic et al. [2014] and improved by Carpiuc [2015], which was used for a six actuator testing machine in the LMT-Cachan, the hexapod [Nierenberger et al., 2012]. This software was adapted for our needs (shape function base, viewed variables) and optimized in order to achieve the necessary speeds. It will be referred in the following as *ASTREE-IDIC*.

In the present version, the image acquisition is decoupled from the I-DIC computation system by use of a shared memory inter-process communication. To this aim, a second software, named *Vision*, was developed by Samir Amrouche, an IT developer working in the lab. The *Vision* software ensures the communication with the control cameras. It allows to start/stop the camera acquisition, to set the image parameters (AI, ROI, exposure time, acquisition frequency) and to have live views of the images and their grey level histograms (*Fig. 4.17*). Given that the control cameras run at a very high speed on internal trigger mode (freerun), we can not use an exterior voltage trigger as is normally done in the case of other cameras during biaxial tests. One of the advantages of having a home grown software was the possibility to add a custom trigger function in the code with the following parameters: time between two saved images, time to take photos, time to pause acquisition between photo sessions and total acquisition time. For example, when

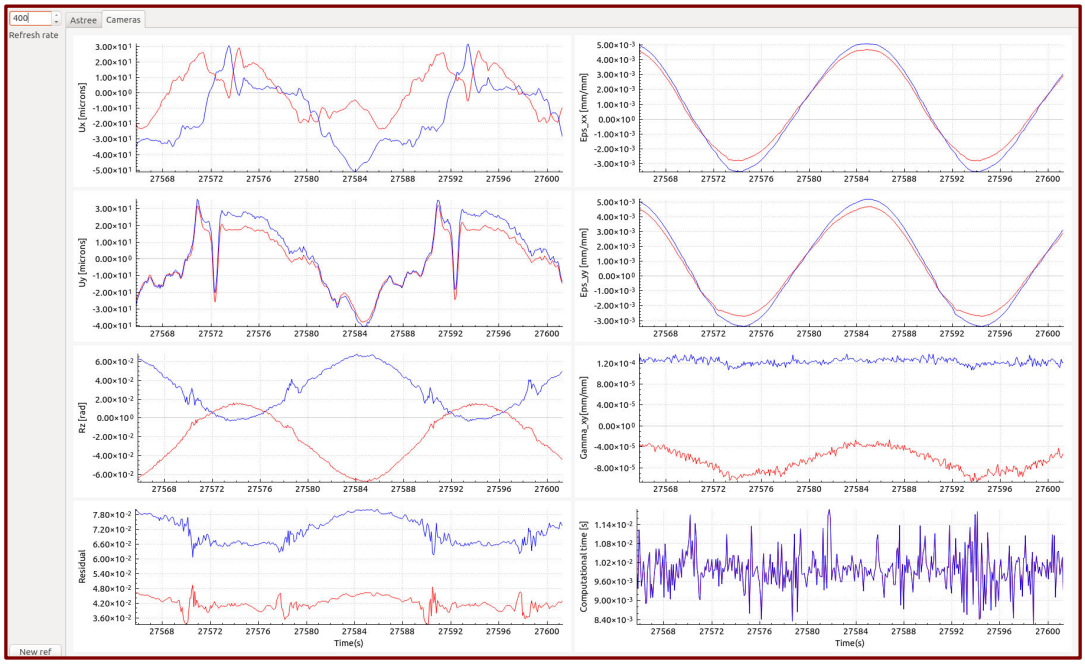

Figure 4.18: Graphical user interface of the *ASTREE-IDIC* software

performing 501 load cycles we wanted to save 20 photos/cycle for 6 cycles (cycles 1, 101, 201, 301, 401, 501). Thus, among the photos taken at a very high frequency (*e.g.*300 Hz) we would save a photo each second during 20 s (the time to complete a whole cycle at 0.05 Hz), pause for 1980 s and then repeat this for a total time of 10020 s (the total time needed to perform the 501 cycles).

Both *Vision* and *ASTREE-IDIC* are implemented on the same PC (Intel® Core™ i7 CPU at 3.3Ghz, 12Go DDR3 RAM, Nvidia GTX690 GPU, Linux Ubuntu 14.04 OS). *ASTREE-IDIC* is written in the C++ and CUDA languages on the programming platform Metil [Leclerc, 2007], and uses multithread and parallelized techniques in order to optimize the computational time. The graphical interface and the I-DIC calculation are the main tasks performed on separate threads. Moreover, the I-DIC computations are separated on several threads, each thread corresponding to a camera, and is performed on a different GPU. The GUI of *ASTREE-IDIC* (*Fig. 4.18*) was created using QtDesigner and allows to monitor the experimental test and to set different parameters like the number of points to visualize and setting the current photo as a new reference image.

2.3.4 Control loop time optimization and control security

One of the main challenges that had to be overcome for a reasonably fast I-DIC control was the small time needed for the source-delay-measure cycle. In order to achieve this cycle, one important part was sending the results from the computer to the testing machine. This process has to be sufficiently precise but also fast, both in terms of frequency and delay. Given that the machine controller can only receive analogical signals, we had

to find a solution involving a digital to analog converter. A first try was using an available oscilloscope connected by USB. Even if it was acceptable in terms of frequency and resolution, the oscilloscope has only one analogical exit and the sending delay was about 200 ms (*Tab. 4.3*). In order to reduce this delay, we looked for solutions that were using a different, much faster connection. After many discussions and research, we found a DAC board (Access PCI-DA12-8) that can send 8 synchronized analog signals at a 12bits resolution with a very small delay due to its PCI connection. The only inconvenience found while installing the board on the computer, is that the board isn't compatible with our motherboard under the current operating system (Linux x64bits), which is necessary for the GPU calculation. One way to circumvent this issue was to use an extra computer, with a compatible configuration, just to send the data. The digital data was thus sent to this intermediate machine using a socket protocol through Ethernet cable. Even with this solution, less satisfactory than directly plugging the card in the DIC computer, the time to send the data to the machine is estimated to be around 1 ms.

Solution	Advantages	Disadvantages
	• Frequency = 70 MHz • Resolution = 16 bits • Easy coding	• Only one analog output • Important send time (≈200 ms) - USB
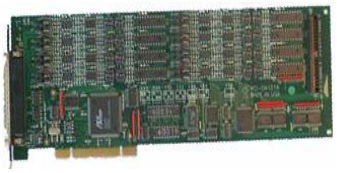	• 8 synchronized DACs • Resolution = 12 bits • Fast send time - PCI (≈50ns $\Longrightarrow$ maximum frequency of 20kHz)	• Not compatible with our motherboard $\Longrightarrow$ Using an intermediate PC

Table 4.3: Digital to analog converter choice between 1) Oscilloscope 2) DAC Board

The DAC board is controlled through a C++ script using typical I/O functions. Its 8 synchronized analog outputs are connected through coaxial cables to the analog inputs of the testing machine controller. These channels will be used to send the I-DIC computation signals, such as displacements, strains but also the residual values. Each channel needed to be finely tuned in order to get the precise exit tension. Given that the board has a 12bits precision (2^{12} = 4096 increments), the range for each channel needed to be well chosen: small enough for the noise to be sufficiently low, but large enough to stay in the estimated strain/displacement bounds of each test type. For most tests, the strain range was set ± 1 %. In order to lose as little precision as possible, the strain value (in %) is transformed into an integer value and then sent to the DAC board. From here on, the digital data it transformed into electrical tension, on each calibrated channel, and sent to the machine controller, using the highest available tension range (-10V..+10V) so that the

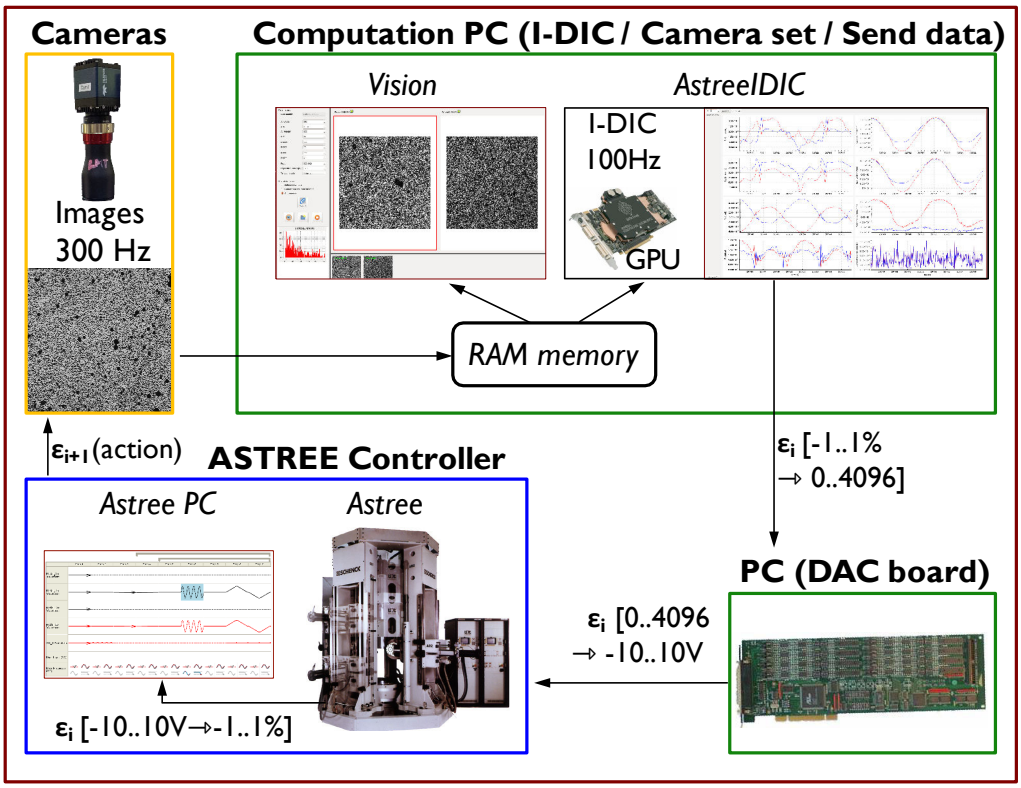

Figure 4.19: ASTREE control loop components

signal is sufficiently high with respect to the static noise. Each analog input channel of the machine is then recovered in the control PC, and the last transformation converts back to the ± 1 % range (*Fig. 4.19*).

Having found a fast and reliable solution to send the data to the testing machine, we needed to see if the whole loop was fast enough. This is very important when wanting to perform cyclic tests at a sufficiently high frequency. The initial target was a frequency of 0.05 Hz, given that it was the strain rate equivalent of the uniaxial tests. In *Tab. 4.4* the main processes involved in the control loop are listed.

Control loop running at 100 Hz	**Time [ms]**
Time for I-DIC computation with 4 iterations	5
Mean time for one I-DIC iteration	2
Time to take one photo	3
Time to transfer one photo	2
Time to send data $\Longrightarrow$ DAC board $\Longrightarrow$ ASTREE	1
Time for complete control loop	**10**

Table 4.4: Time of each process of the control loop

In order to test the influence the number of iterations has on the precision and speed of

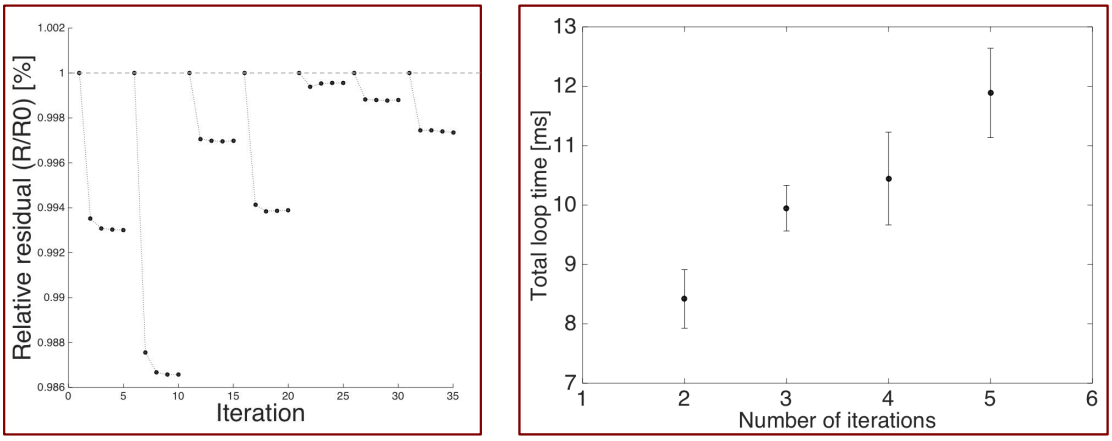

(a) (b)

Figure 4.20: Study on the influence of the number of iterations used in the I-DIC computation a) Relative residual obtained using 5 iterations per computation b) Total control loop time using different fixed number of iterations

the I-DIC computation, elastic sinusoidal cycles were performed at large enough loading levels ($F_1 = F_2 = \pm 20$ kN which is equivalent to $\varepsilon_{11} = \varepsilon_{22} \approx \pm 0.1\%$). The time needed to perform an iteration is ≈2 ms, but it is the first iteration that is by far the longest overall. Nevertheless, such a low computational time is possible mainly because the result of the previously analyzed photo is used as an initial guess for the next one. After the first iteration, the following ones are not only faster but also contribute to a much lesser extent to the gain in precision. This aspect can be seen in *Fig. 4.20a*, where the relative residual, which is the residual at the current iteration (R) over the residual at the first iteration (R0), is noticed to be close to stabilized after only two iterations. I-DIC computations were performed using different fixed number of iterations in order to test the impact on the total loop time. This can be seen in *Fig. 4.20b*, where the mean value and the standard deviation is plotted for the total loop time, over a population of 1000 computations, for each fixed number of iterations. The total times evolves from ≈8 ms (for the computations with 2 iterations) to ≈12 ms (for the computations with 5 iterations). Given that a computation using four iterations amounts to a reasonable total loop time of ≈10 ms, it has been chosen to use a fixed number of four iterations all time, in order ensure robustness.

Several safety measures have been introduced in the control loop, in order to avoid an unstable or accidental behavior of the machine. One such measure was to use as initial guess the result from the undeformed image, in the computation following a spike in the residual (as opposed to the usual scenario which is to use the previous image). Such a one-time event, which could be due to a physical event, camera acquisition bug, computation error, an insect flying in front of the lens etc., would cause a chain reaction resulting in the lack of convergence in subsequent correlation if the initial guess wouldn't be changed. In order to avoid that such temporary spikes in the signal (usually unrelated to the behavior of the ROI) wouldn't disrupt the control, a condition was imposed that if the high levels

in the residual last less than 3 consecutive photos (≈30 ms), then it isn't even sent to the machine, considering that it is one of the aforementioned situations. If the phenomenon persists for more than 3 successive photos, then it is decided that the behavior is really physical and needs to be taken into account, thus the signal is sent to the machine.

A similar safety measure was introduced to compensate for eventual lags in the transmission of data from the computer to the DAC. Thus, if data isn't received by the socket for more than 2 s, then it was decided that the strain lag would become too dangerous and the machine will be put in displacement control until the problem is fixed. In both cases, the machine will be stopped, given that a limit was imposed on the residual, limit which would trigged either because the value is actually too large (the first case) or because we would artificially send a value of the residual surpassing this limit if the data doesn't arrive to the DAC for an amount of time considered dangerous.

Apart from these important security considerations, one must retain from *Tab. 4.4* that each process inside the control loop has a reasonable time, and that we manage to get the control loop running at 100 Hz, with none of the processes being an important bottleneck.

2.3.5 Measurement uncertainty

Another important aspect of the I-DIC control is its reliability, in the sense that control fields are sufficiently uniform for the mean value to be valid. In order to test the stability of the mean strain, optical gauges of different sizes were analyzed on the global DIC treatment of the available images. Given the resolution of the photos (800×800 pix), 3 square, centered, optical gauges were considered, with the sizes of 700, 200 and 100 pix. The results from these gauges are compared to those from the I-DIC computations and shown in *Fig. 4.21* for a typical cycle, in terms of ε_{11}. The difference between the three optical gauges (700 - in blue, 200 - in red and 100 - in green) is quite small, even though their sizes vary considerably. The mean difference between the minimum and maximum values obtained with the three gauges sizes along the studied loading cycle is $15 \cdot 10^{-3}[\%]$. It needs to be mentioned that the strain amplitude of the imposed sinusoidal loading is important (0.8%) and thus the error with respect to this value is of 1.9%.

Another test was to check the evolution of the uncertainty when changing gauge size. The uncertainty is computed as the standard deviation for the strain (ε_{11}) recorded on 10 photos taken at zero load. During this time, the machine was turned on, so the machine control noise is already included in the uncertainty. For the 800×800 configuration, the found value varied from one camera to another, but never surpassed $1 \cdot 10^{-3}[\%]$. Moreover, when analyzing the mean value between the upper and the lower camera, the uncertainty passes at $0.6 \cdot 10^{-3}[\%]$. The choice was made to use a mean value between the responses of the upper and lower faces of the sample for controlling the machine, in order to avoid flexion effects, with the added advantage of reduced uncertainty. This uncertainty obtained for the average between the two cameras ($0.6 \cdot 10^{-3}[\%]$) will be considered as base value for the I-DIC computation in the following.

In *Fig. 4.22*, the uncertainty is computed for different size optical gauges, as well as the I-DIC case. For the sake of comparison, the dashed line represents the uncertainty

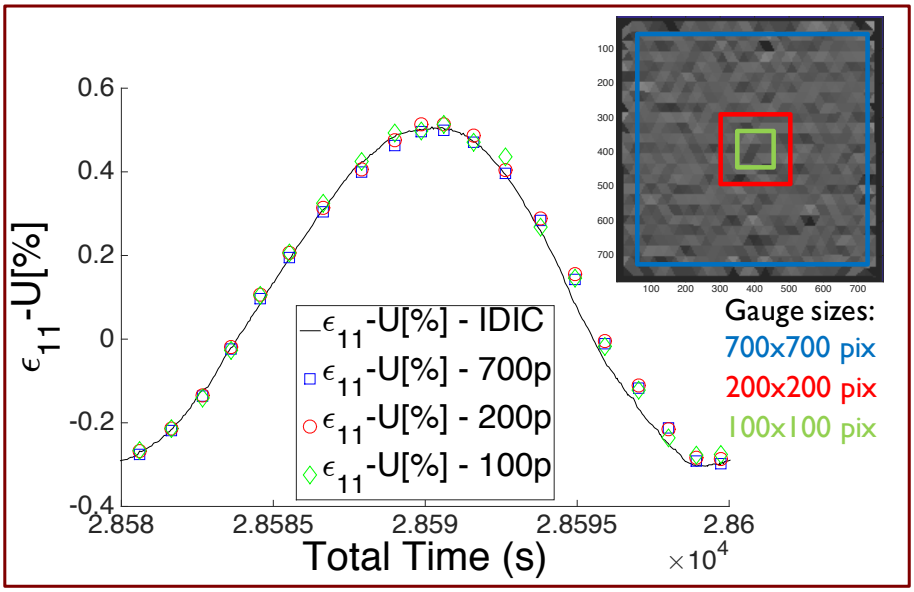

Figure 4.21: Comparison between the strain in direction 1 obtained using I-DIC and the optical strain gauges of different sizes

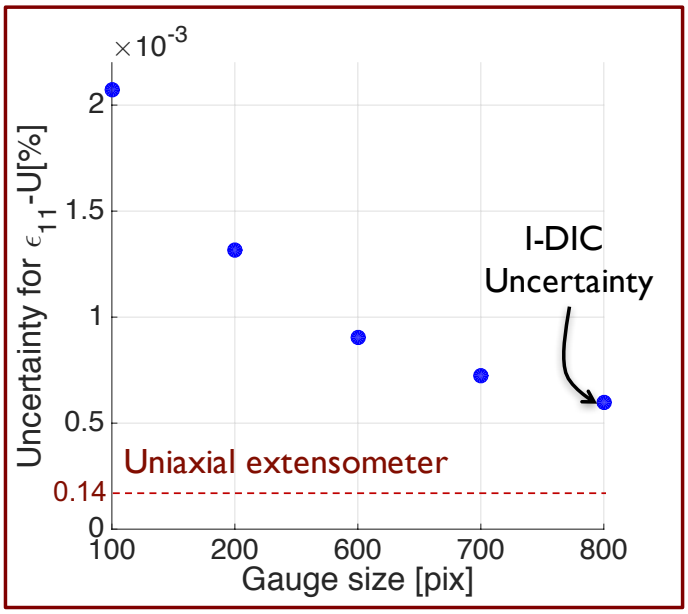

Figure 4.22: Comparison between the uncertainty in direction 1 (ε_{11}) obtained using I-DIC and the optical strain gauges of different sizes

obtained for the *uniaxial* extensometer used to perform the uniaxial tests, which has a gauge zone (10 mm) equivalent to the 800 × 800 I-DIC with the ×0.5 lens and chosen cameras. It may be noticed, as expected, that the uncertainty is higher as the size of the optical gauge is smaller. Nevertheless, the value is sufficiently small for the control, thus allowing further acceleration of the method. Given that we had already obtained a

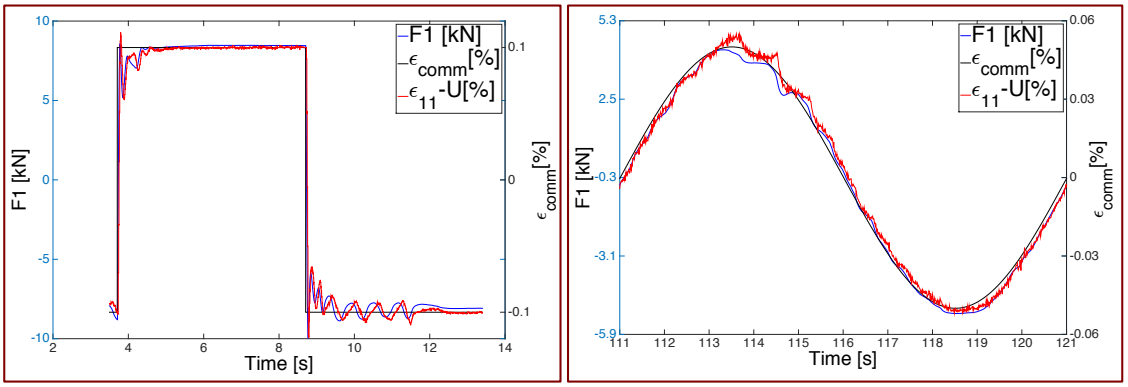

(a) (b)

Figure 4.23: Uniaxial strain control PID using the strain signal from only the upper camera (ε_{11}^{U}) a) Square loading b) Sinusoidal loading

100 Hz strain-control loop, which was sufficient for the envisioned testing frequency, we decided to use the 800×800 configuration for both its smaller uncertainty level as well as a safety measure. This way, the signal would be more stable in case some unexpected local anomalies occurred.

2.3.6 I-DIC control tuning

The next challenge was tuning the PID so that the machine strain control would be reactive but also stable enough. Thus, a tuning sample was used, XT4, on which several tests were made (sinusoidal, triangular and square) using different strain amplitudes and loading frequencies. We started at a baseline close to that of the force PID (P = -10 / I = 0 / D = 0) and on only one axis (Axis 1). It is worth mentioning that P is given in decibels (dB), thus is on a logarithmic scale, whereas the other two parameters have a linear scale. The signal that we first used to control the machine was ε_{11}^{U}, which is the I-DIC strain value for the upper face (U for Up). We saw that the system would become very unstable, just seconds after passing in strain control mode, without yet giving any strain level change. The PID was too reactive and the lag between the command and the response would trigger this unstable reaction. The value of P was gradually reduced until we managed to control the machine using a slow ramp, but upon reaching a certain strain level we would again become unstable. It must be noted that this behavior is unexpected in the framework of the theory of linear system control, and thus may reveal non-linearities or other violations of the theoretical assumptions in the complete real control loop. This forced us to make an important compromise on the value of P, so that instability wouldn't occur. Therefore, the final value chosen for the PID was (P = -24 / I = 3 / D = 0).

The contribution of the integral would partially compensate in terms of correction speed, giving a slight overshoot when performing a square loading (*Fig. 4.23a*), which is particularly challenging for DIC measurement (potential blur, initiation value far from the converged one). Even so, the square loading serves only as a guarantee to the stability of

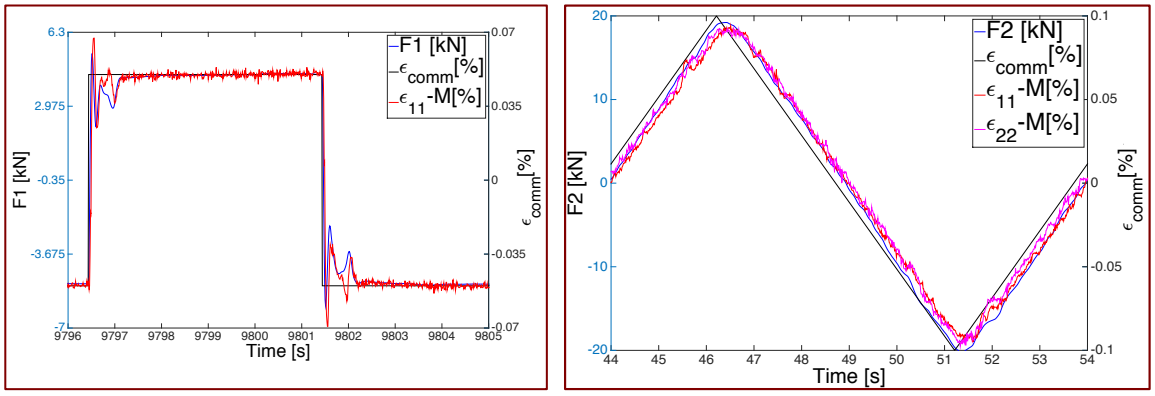

(a) (b)

Figure 4.24: Passage to the strain control using the mean strain value between the upper and the lower camera (ε_{ii}-M) a) Uniaxial square loading b) Triangular biaxial loading

the system, given that the tests needed to be performed are much slower. Thus, it can be seen in (*Fig. 4.23b*) that for a sinusoidal load, the less reactive PID is not a real problem at this strain amplitude and frequency.

In order to correct some of the parasitic factors that may influence the behavior of the sample (flexural movements, camera noise, asymmetric strains), the values of the strains in the two directions used to control the machine were replaced with ε_{11}^{M} and ε_{22}^{M} which are the mean values between the strains from the upper and lower face, ε_{ii}^{M} = -ε_{ii}^{U}+ε_{ii}^{D})/2. As mentioned before, the flexion effects will be less impacting and the uncertainty will be reduced from $1 \cdot 10^{-3}$[%] (when using only the upper camera) to $0.6 \cdot 10^{-3}$[%](when using the mean value). Thus, the signal becomes less noisy and the tests will be cleaner (*Fig. 4.24a*).

The same PID was then set for signal ε_{22}^{M}, and the first biaxial strain-controlled tuning tests were performed. As it can be seen in the triangular loading featured in *Fig. 4.24b*, the signals for ε_{11}^{M} and ε_{22}^{M} are less noisy and follow quite well the command, even with a less reactive PID, for a frequency of 0.1 Hz.

Lastly, it is worth noting that for these tuning loads, the amplitudes were about 10 times smaller than what they will be during the real biaxial tests, so the noise will be very small with respect to the final strain amplitudes. Other details concerning the strain control will be presented in the results section, for each type of test.

3 Biaxial tests results

Several biaxial campaigns were performed, with the purpose of providing rich data for the plasticity model under development. A total of 6 biaxial samples were tested and another 4 were used for calibration during the experiment development phases. Each test was unique in terms of loading type and included more than one level (both in the case of force-controlled and of strain-controlled tests). The test types were decided as

development progressed, both in the case of the plasticity model and of the strain control of the machine.

As presented in detail in Appendix A, the names of the biaxial samples are in the form of two letters and a number. The first letter, X, corresponds to the fact that it is a biaxial sample, the next one to the block of 4 samples it came from (A, B, C or D) and the number gives its vertical position inside the circular forged block out of which the samples were extracted (1-highest, 4-lowest). Apart from the samples tested in order to asses the behavior of Inco718DA, others were machined to be used for calibration and tuning before the actual tests. They were also made of inconel, but before being subdued to the thermo-mechanical processes that improve its properties. Three such samples were manufactured, being named XT1..3, with T for tuning. Thus, we were able to work on these samples, quite similar to the real ones. This allowed us to know what to expect and to eliminate potential problems. The tests will be presented in the following, insisting on the important aspects of each of them.

3.1 First force controlled test XA3

The first biaxial test was performed soon after the uniaxial campaign in order to test the behavior of the sample at higher load amplitudes that those performed at ENI Tarbes [Selva et al., 2017]. The loading levels were initially chosen the same as the levels of the force-controlled uniaxial test (presented in Appendix C), in terms of equivalent stress (σ_{eq}). This equivalence was made by imposing in Abaqus a material behavior based on interpolations of given points $\sigma = f(\varepsilon_p)$ extracted from the uniaxial monotonic curve. A more elaborate cyclic computation should be performed in order to better estimate this biaxial-uniaxial equivalence.

The test is equi-biaxial, so F1 should be equal to F2 at any given time. The found loading levels were: the mean values $\bar{F} = 0, 1.5, 3, 4.5, 6$ kN and an amplitude $\frac{\Delta F}{2} =$ 75 kN. The loading was sinusoidal, using the same frequency as in the uniaxial case ($5 \cdot 10^{-2}$ Hz) for the same number of cycles (300/level). Each level is represented in *Fig. 4.25a* by 6 symbolic cycles. After each series of 50 cycles, 4 images were taken (maximum/ zero/ minimum/ zero load). This was done in order to monitor the evolution of the test and also for post-treatment. For this test, two PCO Pixelfly cameras were used (depth of 14 bits, maximum resolution of 1392×1040 pix and pixel size of 6.5µm) equipped with $\times$ 0.5 telecentric lenses.

Given that the sample didn't break after these first 5 levels, we continued increasing the mean load $\bar{F}$ by a step of 5 kN and kept the same load amplitude. Thus, we obtained 3 more levels: with $\bar{F} = 10, 15, 20$ kN and $\frac{\Delta F}{2} = 75$ kN. After this, the maximum value of the force was maintained, given that 95% of the machine capacity ($F_{max} = 95$ kN) was reached. The force amplitude was increased, which gave us a command of $\bar{F} = 15$ kN and $\frac{\Delta F}{2} = 80$ kN. After 240 cycles at the last level, the sample broke, but the crack wasn't detected after the first block of 50 cycles from the last loading level.

An aspect that was noticed during this test was that the strain map is quite different for

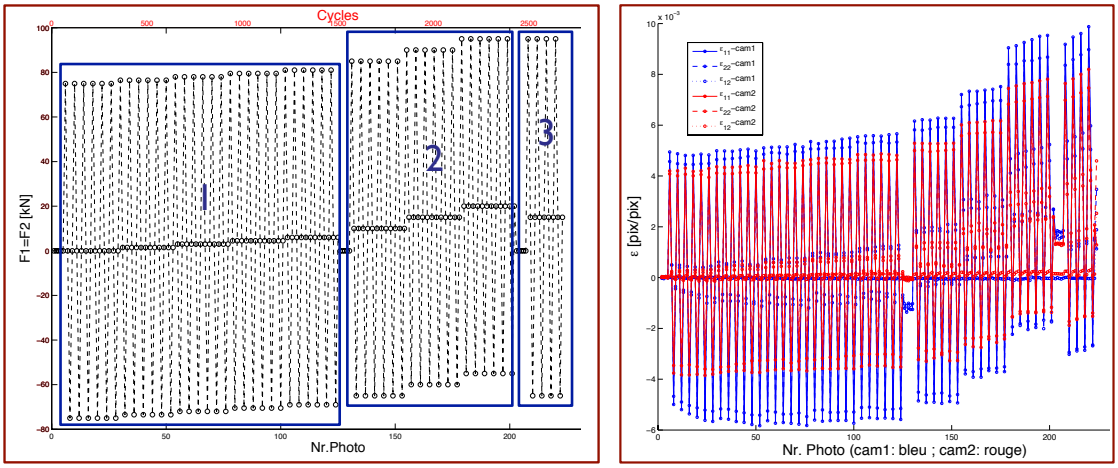

(a) (b)

Figure 4.25: First equi-biaxial force controlled test XA3 a) Loading scheme b) Evolution of the strain components ($\varepsilon_{11}, \varepsilon_{12}$ and ε_{22}) on the two sides of the sample obtained with a global DIC algorithm for an optical gauge of 400×400 pix

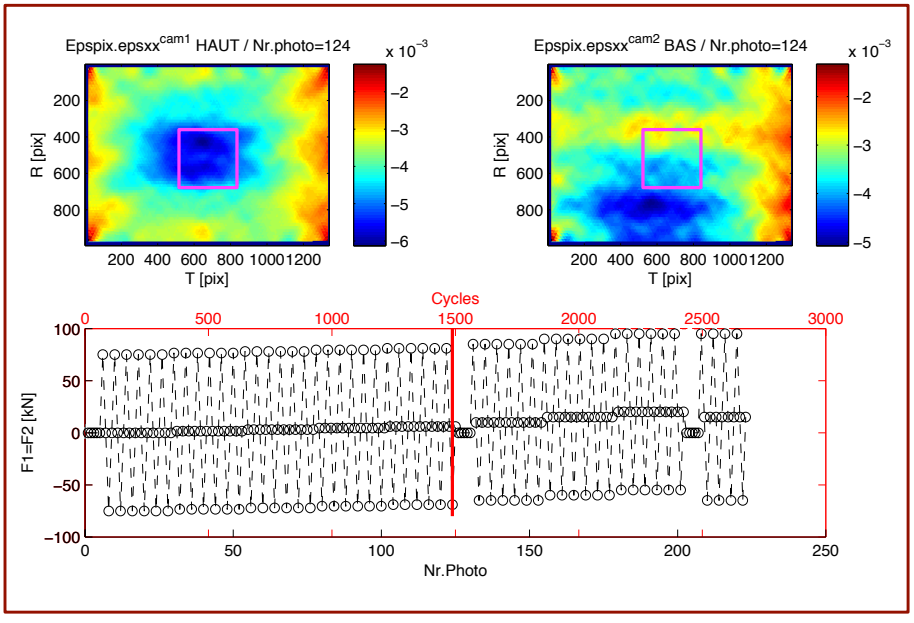

Figure 4.26: Local instability phenomenon observed in strain maps at high compression loading

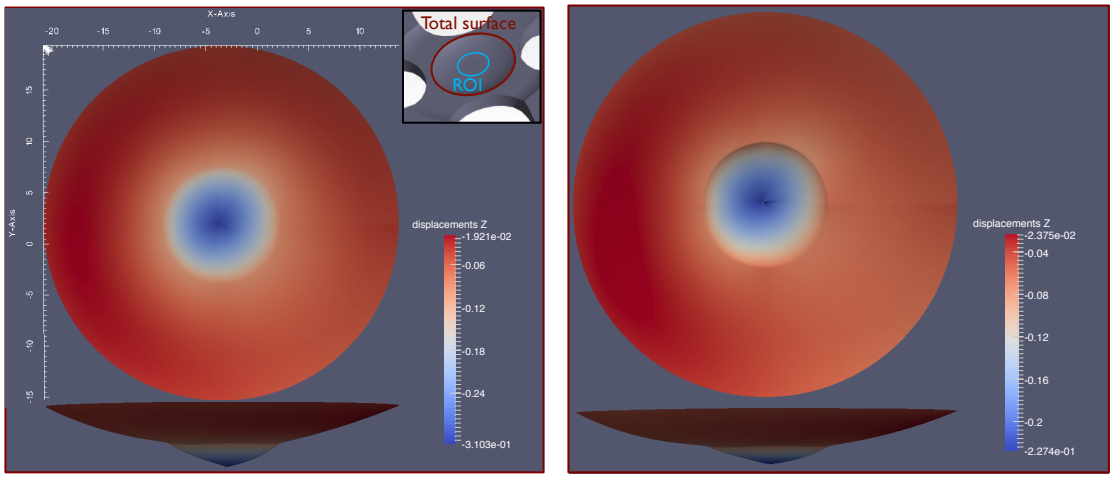

(a) (b)

Figure 4.27: Out-of-plane displacement U_z in mm during buckling (visual scale of 1:5), detected on biaxial sample XT2: a) First maximum compressive loading (-80 kN) b) Zero loading after three cycles

the upper face when compared to the lower one. This generates a difference in the mean strain (*Fig. 4.25b*) made on an optical gauge of 400×400 pix ≈ 2.6×2.6mm (represented in purple in *Fig. 4.26*). By placing a dial indicator on the central surface of the sample during the test, a relative out-of-plane movement of Δh = 40 µm per cycle was observed. Even if this value is smaller than what was found in stereo measurements on the following test, it was the first sign that buckling might occur for large enough compression stresses in the central zone. The next tests we performed had the purpose of seeing how far we could go in compression before local instability occurred.

3.2 Buckling detecting tests XT2 and XA2

In order to better understand the way the buckling phenomenon occurs in the center of the biaxial samples, multi-level tests were performed. The purpose was to quantify the out-of-plane movements and determine for which loading levels it would occur. As it was unclear in the beginning of the study that the heterogeneity seen in the 2D DIC maps of the previous test (XA3) was indeed local buckling, a first quasi-static loading was performed on sample XT2.

Thus, the sample was equi-biaxially loaded in tension up to 80 kN, followed by a loading in compression down to -80 kN. Photos are taken of the sample with the two Manta cameras presented in subsection 2.2 every 5 kN, in order to precisely find when the first instabilities occur, by using stereo-DIC. Down to -60kN, the measured value of the out-of-plane displacement (U_z) stays in reasonable bounds with respect to the surrounding, more rigid area. A value of 0.05 mm relative U_z displacement is thus found for the central area. With the next levels, we see a considerable increase, reaching a maximum value of

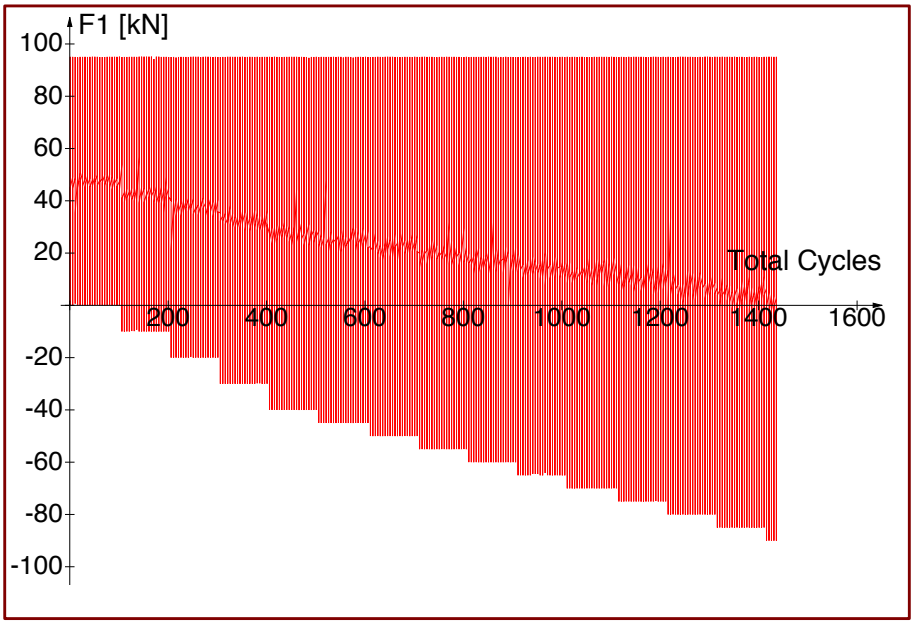

Figure 4.28: F1 versus Total cycles for the buckling detecting test XA2

≈-0.31 mm at -80 kN (*Fig. 4.27a*). After only 3 cycles, this value reaches a maximum of ≈-0.36 mm at -80 kN. Moreover, a large part of this strain is plastic, given that at the last unloading ($F_1 = F_2 = 0$ kN) the out-of-plane displacement U_z has a value of ≈-0.27 mm. We may conclude that there is a threshold in compression that will result in buckling far too important to consider that the behavior in the ROI remains sufficiently homogeneous. Moreover, this value represents ≈30% of the thickness of the sample, so it is imperative to find the safe load range. This is not trivial, because on the one hand each geometry is slightly different, and certain eccentricities would exacerbate the phenomenon and, on the other hand, we would like to obtain important plasticity levels in the center of the sample, which can be obtained going closer to this limit. Given that during cyclic tests an accumulation of plastic strain may be encountered, buckling might appear for a certain load amplitude only after a number of cycles was performed.

In order to better understand the phenomenon, a second equi-biaxial force-controlled test was performed, this time on the testing sample XA2. As the purpose was to find the largest force span before buckling would occur, the maximum applied force in both directions was chosen at 95% of the capacity of the machine in tension (95 kN). The minimum force was gradually decreased, begining from 0 down to -90 kN in steps of 10 kN at first, then later 5 kN, for a total of 15 levels (*Fig. 4.28*). For each level, 101 cycles were performed, except for the last level ($F_1 = F_2$=+95..-90 kN), when 21 cycles were achieved before fracture occurred, for a total number of 1416 cycles. The switch from a step of 10 kN to 5 kN was made at -40 kN, when we assumed the risk of buckling to increase considerably.

Starting with this test and until the end of the biaxial campaign, the equipment de-

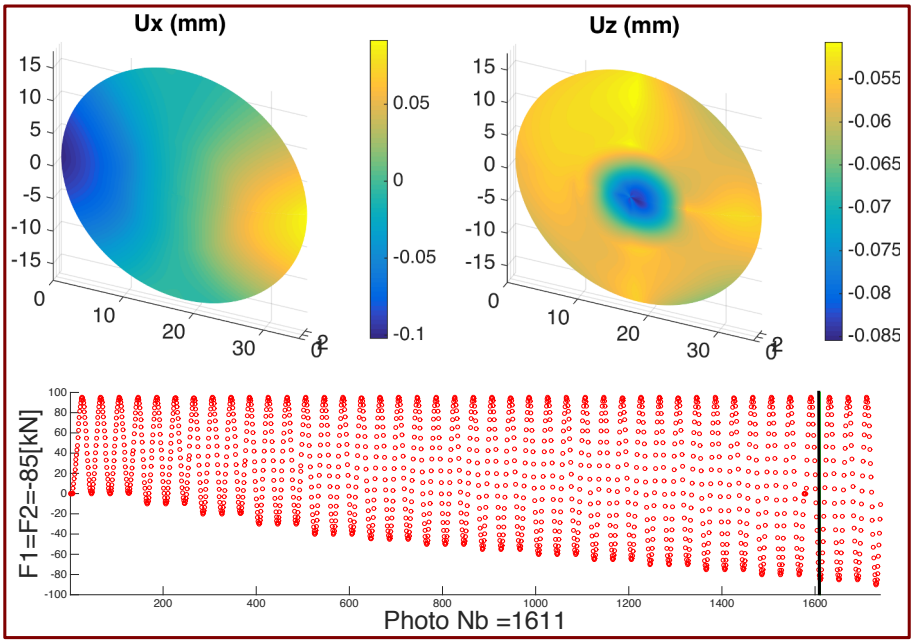

Figure 4.29: First visible out-of-plane movement on sample XA2 at F_1 =-85 kN

scribed in subsection 2.2 was used (Dalsa cameras for the central zone and Manta cameras for the stereo images). With the Manta cameras being triggered using the analog output of ASTREE, 3 cycles per level (1,51,101) were captured with a number of 40 photos per cycle. Each photo is represented as a red circle in the bottom part of *Fig. 4.29*. The minimum and maximum levels were mainly analyzed in order to detect obvious changes in behavior. Given that XA2 was the sample with the thickest central area and small mean plane shift (*Tab. 2.1.1*), its behavior was very stable. Only in the last two levels more important out-of-plane movement was observed, as may be seen in the upper-right part of *Fig. 4.29*. The maximum value of Uz is reached at -90 kN in the last loading level and has an absolute value of $Uz \approx 0.15$ mm but a relative value of only $\Delta Uz = 0.04$ mm with respect to the rest of the thickness reducing fillet zone. This results shows that machining defects (thickness, mean plane shift) can have an important impact on the behavior of the sample, affecting if and how buckling occurs. Unfortunately, the exact moment when the ROI stops being sufficiently homogeneous for the I-DIC computations to be valid is difficult to assess accurately using the stereo analysis of only one face.

Another measurement technique used during this test was the two Dalsa cameras observing a zone of 800×800 pix. on each side of the sample. Starting with this sample, the I-DIC computations ran during the test at a frequency of ≈100 Hz. Thus, the values of ε_{xx} (or ε_{11}) and ε_{yy} (or ε_{22}) were transmitted to the machine control software (Wavematrix) and stored for each data point we decided to save (≈400 points per cycle). The values were marked U (Up) for the upper face and D (Down) for the lower face (*e.g.* ε_{11}^{U} is the strain along axis x measured on the upper side of the sample). The cameras were set on internal trigger, with a frequency of 300 Hz, to ensure a flow of information as close

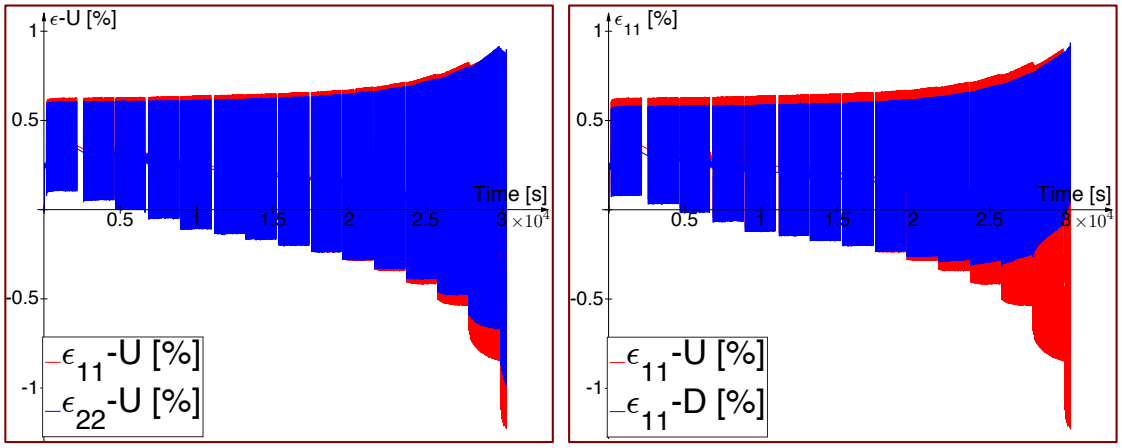

(a) (b)

Figure 4.30: Strain vs Time curves for the sample XA2 a) ε_{11} and ε_{22} I-DIC results for the upper face b) ε_{11} I-DIC results for the upper and lower faces

to "real-time" as possible before the new I-DIC computation can be performed. Out of these photos, stored initially in the RAM memory, some were saved in order to be analyzed *a posteriori*. The trigger for these photos was synchronized as close as possible to the trigger for the stereo cameras. The timing of a loading step (cyclic or quasi-static) is very precise, but the passage between steps has a lag of 2∼3 seconds. Before such a manual trigger sequence is initiated (on mouse click) a user input button was placed in Wavematrix in order not to miss setting off the signal and to systematically follow the same procedure. Even if the two triggers are not perfectly synchronized, the delay should stay constant and sufficient points per sinusoidal cycles guaranties an accurate detection of peaks.

When analyzing the I-DIC computations, some interesting results emerge. First of all, as we may see *Fig. 4.30a*, the response of the structure is quite consistent in the two directions for the most part of the loading history. The evolution of the strains has very little differences up until the last four levels, when the two seem to drift more and more. This difference is all the more noticeable in *Fig. 4.30b*, when comparing what happens on the upper and lower faces. It can be seen that, due to buckling, the upper face exhibits increasing compression strains, whereas the lower face begins going in the opposite direction, even reaching a positive mean strain at $F_1 = F_2$=-90 kN during the last loading levels. This phenomenon is similar to what happens during bending tests, when one side is in tension and the other in compression. This proves that once we pass a certain threshold, the percentage of strain due to buckling becomes more important than that due to the actual load, thus rendering the results unexploitable. Therefore, the divergence between the I-DIC strains in compression could serve as a viable indicator of bucking occurring.

What is important to see is that through this measuring method we obtain strain data for every point and thus plastic force-strain curves can be analyzed (*Fig. 4.31a*). As

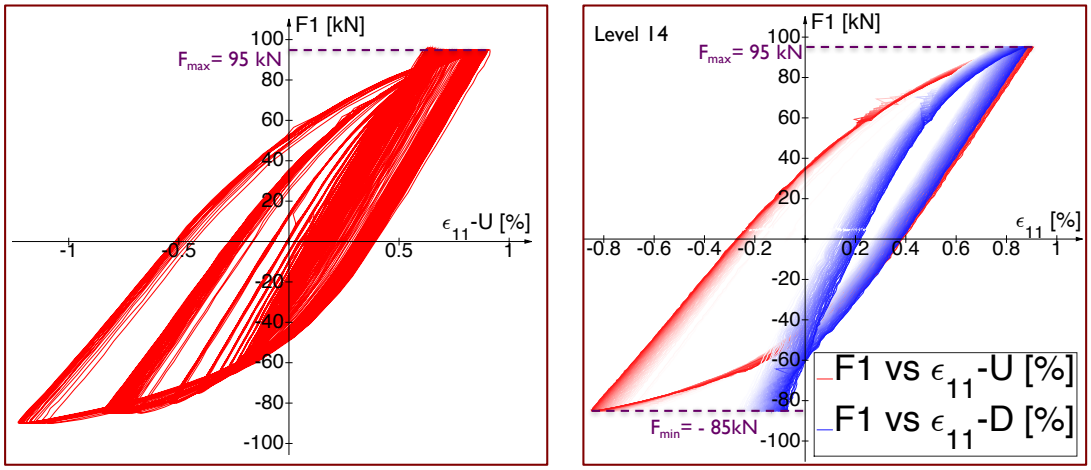

(a) (b)

Figure 4.31: F_1 vs ε_{11} curves for XA2 a) All cycles b) Buckling shown by comparing results from the upper (ε_{11}^U) and lower (ε_{11}^D) faces

mentioned previously, the curves extracted from the final levels, when buckling occurs, can't be considered valid, as the mean is made on a very heterogeneous field and the difference between the response from the two faces clearly shows it (*Fig. 4.31b*). The very large opening of the hysteresis loops is mostly due to buckling and not in plane plastic strains.

The difference noticed between the strain levels exhibited on the two sides of the sample during the acceptable levels (1 to 11) occurred since the first level (*Fig. 4.32a*), when the two force-strain curves slightly diverged. This could be due to a number of reasons such as slight flexion, sample geometry or imperfect centering. In tension, this shift seems to remain about the same all through the test (*Fig. 4.32b*), whereas in compression we notice the influence of the instability, at first just slightly and at the end obviously.

It can be seen in *Fig. 4.32b* that some of the acceptable levels offer hysteresis force-strain loops with some plasticity (non-linearity). Thus, this test has shown that we can obtain plastic force-strain curves below the buckling threshold, which was its initial purpose.

3.3 First equi-biaxial strain-controlled test XB1

The first strain-controlled experiment we performed was an equi-biaxial test with 10 levels, with 101 cycles per level. The purpose of the test was on the one hand to validate the control method for high strain levels, and on the other hand to study the behavior of the sample when going more and more into compression. The levels were computed based on the results given by the previous test (on sample XA2), trying to stay within the safe bounds where buckling wouldn't occur. As mentioned in subsection subsubsection 2.3.6, the chosen control signal was the mean value given by the upper and lower cameras in

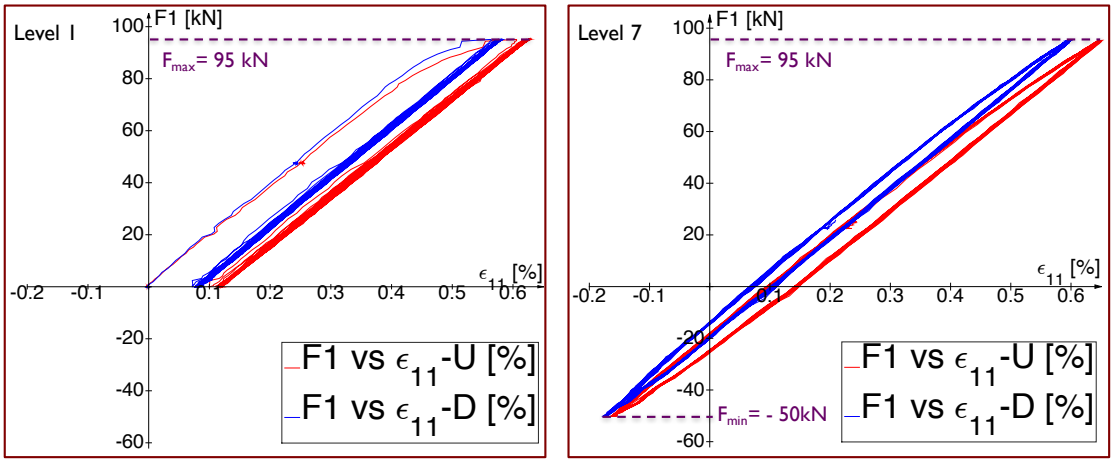

(a) (b)

Figure 4.32: F_1 vs ε_{11} curves for XA2 from the upper (ε_{11}^U) and lower (ε_{11}^D) faces a) Level 1 b) Level 7

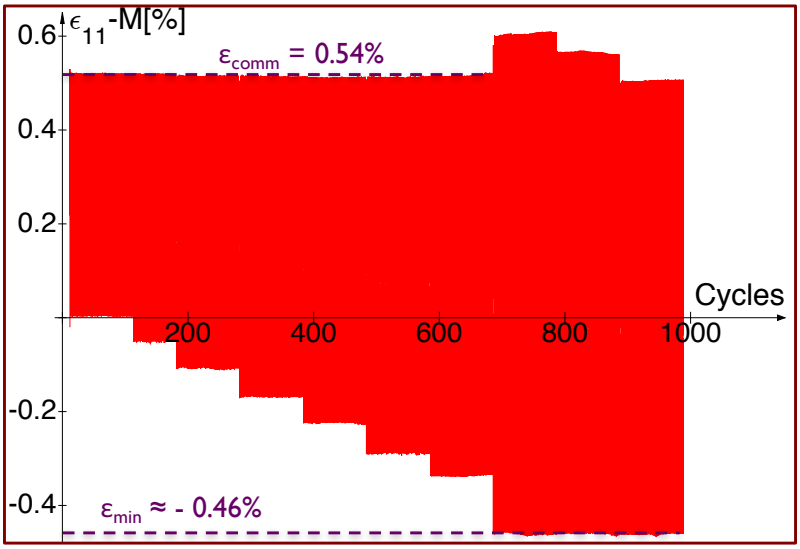

Figure 4.33: ε_{11}^M vs time for the first equi-biaxial strain-controlled test on sample XB1

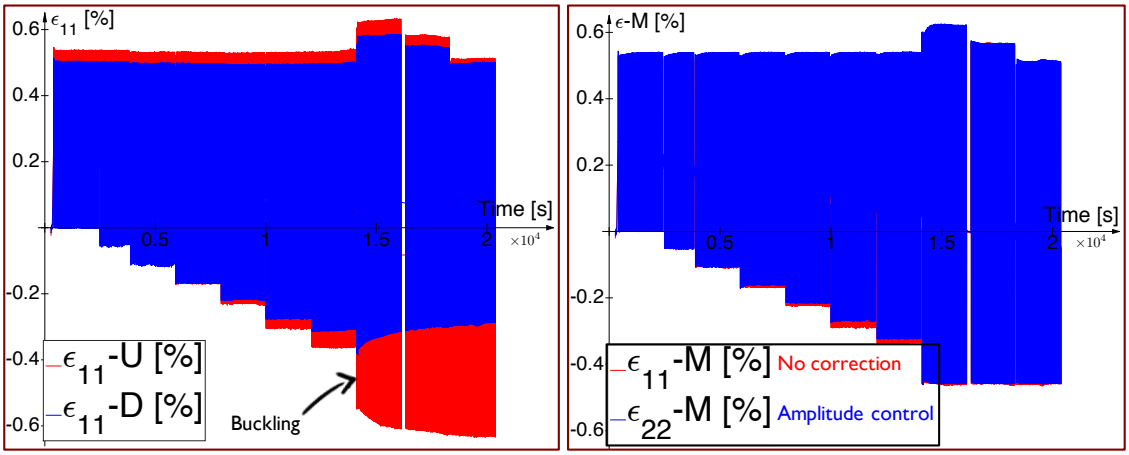

(a) (b)

Figure 4.34: ε vs time for the first equi-biaxial strain-controlled test on sample XB1 a) Difference between strain on upper (U) and lower (D) faces b) Difference between the two directions

each direction, $\varepsilon_{ii}^{M} = (\varepsilon_{ii}^{U}+\varepsilon_{ii}^{D})/2)$. As in the previous test, the maximum mean strain ($\varepsilon_{11}^{M} = \varepsilon_{22}^{M}$) was chosen close to the theoretical limit strain inflicted by the machine. In this case, for the first 7 levels, the maximum strain level was chosen $\varepsilon_{11}^{max} = \varepsilon_{22}^{max} = 0.54\%$ (*Fig. 4.33*). The minimum strain level started from 0% and was incremented down to -0.32% in steps of 0.054%. For the last three levels, after having realized that a minimum strain of -0.46% already generated some buckling effects, there was no point in going beyond. So, for the last three levels, the minimum strain was $\varepsilon_{11}^{min} = \varepsilon_{22}^{min} = -0.46\%$, and the maximum one was decreased in steps, to see how it would influence the behavior ($\varepsilon_{11}^{max} = \varepsilon_{22}^{max} = 0.62/0.57/0.51\%$). The loading frequency was 0.05 Hz, which is equivalent to that used in the uniaxial strain-controlled tests.

The response of the structure was quite uniform. As can be seen in *Fig. 4.33*, the command strain is almost reached and there are no important fluctuations in the control. The fact that the exact value of the command isn't reached is due to the less reactive PID, but also to the high levels needed to be reached and the 10 ms lag for the complete control loop to happen. Even if the value of ε_{11}^{M} is reached consistently in the same manner, it can be seen in *Fig. 4.34a* that in the last three cycles, when buckling occurs in compression, ε_{11}^{U} and ε_{22}^{D} begin to diverge in order for the mean value to be constant. Once again, these loading levels are unexploitable, given that the I-DIC computation performs a mean over a very heterogeneous zone. Given that this first test was suppose to validate/invalidate different aspects of the method, for the control of axis 1 only the PID was responsible, whereas for axis 2 a correction method called "amplitude control" was also used (*Fig. 4.34b*). This correction serves the purpose of compensating a PID incapable of reaching the setpoint. It calculates the difference between setpoint and measured response over the course of a number of cycles and then begins slowly modifying the command so that it is finally reached. It can be seen in *Fig. 4.34b* that ε_{22}^{M} slowly grows in the begining of each

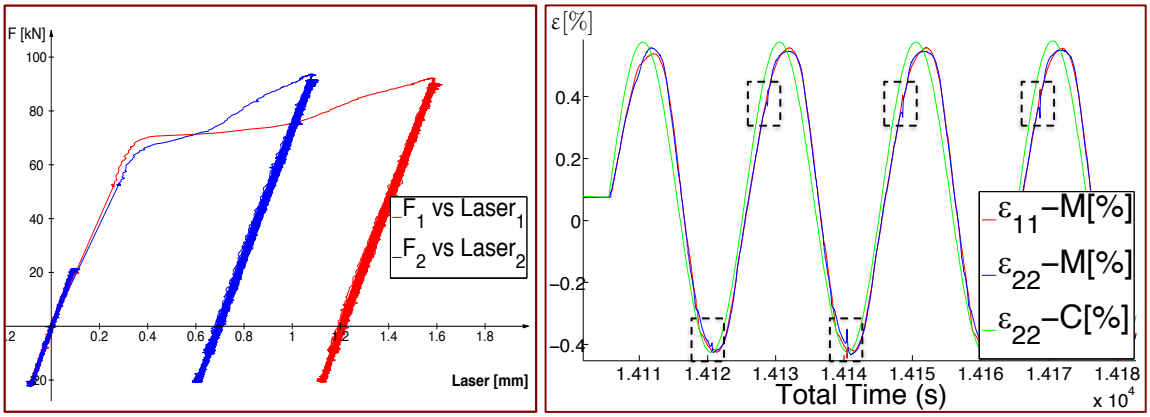

(a) (b)

Figure 4.35: Slipping occurring during two instances of the XB1 test a) First load up to 0.5% b) Beginning of level 8

new level, which is the direct effect of amplitude control. This feature is very useful in high cycle fatigue tests, where several tens of initially imperfect (and smaller amplitude) cycles don't play such an important role. If the PID can't be set as sufficiently reactive due to different causes, this correction could offer a solution if enough cycles were to be performed. In our case, that of behavior tests, such fluctuations could be detrimental in understanding the true phenomena occurring in the material.

Another problem that was encountered in the first tests was the slipping of the grips. An important slip occurred on both axes during the first loading, up to the maximum strain $\varepsilon_{11}^{max} = \varepsilon_{22}^{max} = 0.54\%$ (*Fig. 4.35a*). Even though the relative displacements of the grips during this initial slip, as given by the LASER sensors, were in the order of 0.5 to 1 mm, the displacements encountered in the ROI were a lot smaller, thus the sample wasn't shifted too much from its initial position to cause the I-DIC residual displacements to spike. Moreover, this had little influence over the strains in the ROI, given it is mainly rigid body motion that occurs. This is also the case when an important change is made in the minimum and maximum strain levels, during level 8 (*Fig. 4.35b*). It can be seen that even though displacements may have important sudden fluctuations, the strain signal isn't affected too much, and the strain control manages to remain sufficiently stable.

As mentioned in the beginning of the chapter, the main purpose of the biaxial experimental campaign is to perform plastic strain-controlled tests. With the limits in load levels imposed by the machine capacity and the geometry of the sample that results in buckling problems for high compression, it was important to find out if the loading conditions were proper to obtain exploitable plastic cycles. It can be seen in *Fig. 4.36a* that some plastic loops were obtained during this test. For the last three levels, after buckling occurs, the response is very different on the two sides of the sample, and the mean value, although reached by the PID, is no longer valid (*Fig. 4.36b*). It can also be seen that there are no important drifts in the maximum/minimum strain levels, given that 100 cycles are represented in these figures. Thus, the strain signal given by the I-DIC computations is

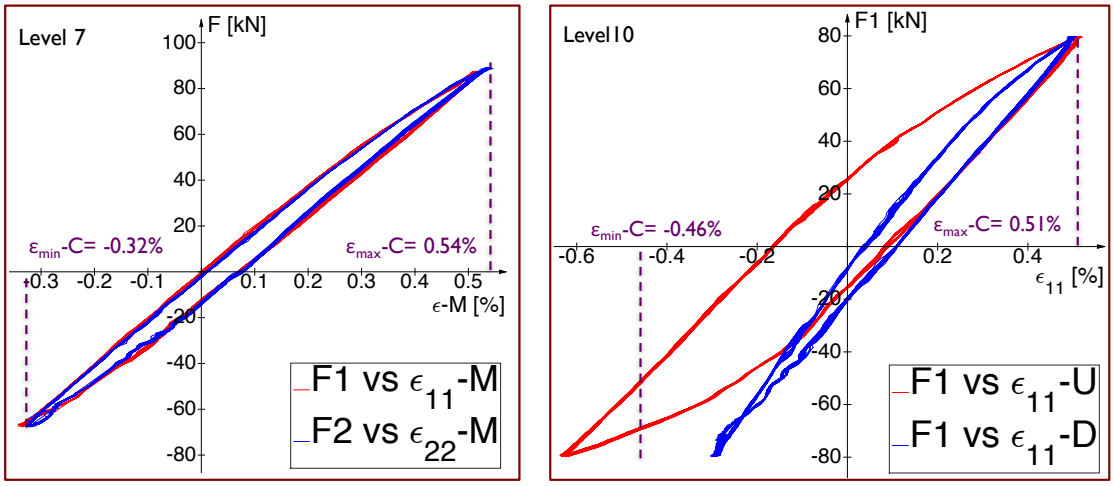

(a) (b)

Figure 4.36: Force vs strain curves for the XB1 test a) Level 7 plastic curves without buckling b) Level 10 unexploitable curves due to buckling

sufficiently stable and consistent to be used for even longer biaxial campaigns.

Another important aspect of the study was analyzing the mean strain relaxation phenomenon in the biaxial case. It is more difficult to assess the stress state in the ROI, given the complex geometry of the sample, but some remarks may be made concerning the force levels. As can be seen in *Fig. 4.37*, the force in the two directions during the exploitable cycles (1..7) don't exhibit important variations during each level. It is thus necessary to perform more cycles during these plastic levels in order to see if the force remains constant over a longer period of time. One important reason behind this effect is that the ROI is confined in a much thicker, elastic region, that barely deforms during our tests. This should have a considerable effect on the potential for relaxation of the applied loads, given that the local stress in the ROI isn't well known. When compared to the uniaxial case, where necking occurs and the plastic strain directly impacts the stress in the loading direction, a stress relaxation can be more directly linked to a load reduction. For this biaxial case, a more complex finite-element structural computation would be necessary in order to fully quantify the stress relaxation in the ROI. This is one of the aspects that will be treated in the PhD work of Estarle R. F. de Souza Campos [de Souza Campos et al., 2017], where Abaqus computations will be performed on our sample, using a UMAT with the model presented in chapter 3.

3.4 Non-equi-biaxial strain-controlled tests XA1 and XC4

The equi-biaxial strain-controlled tests performed previously have shown that we are able to obtain valid plastic loops, although with quite small macroscopic plastic strains. A maximum strain amplitude of $\Delta\varepsilon_{11} = \Delta\varepsilon_{22} = 0.4\%$ has been reached with no buckling occurring in compression. Other options needed to be explored in order to obtain larger

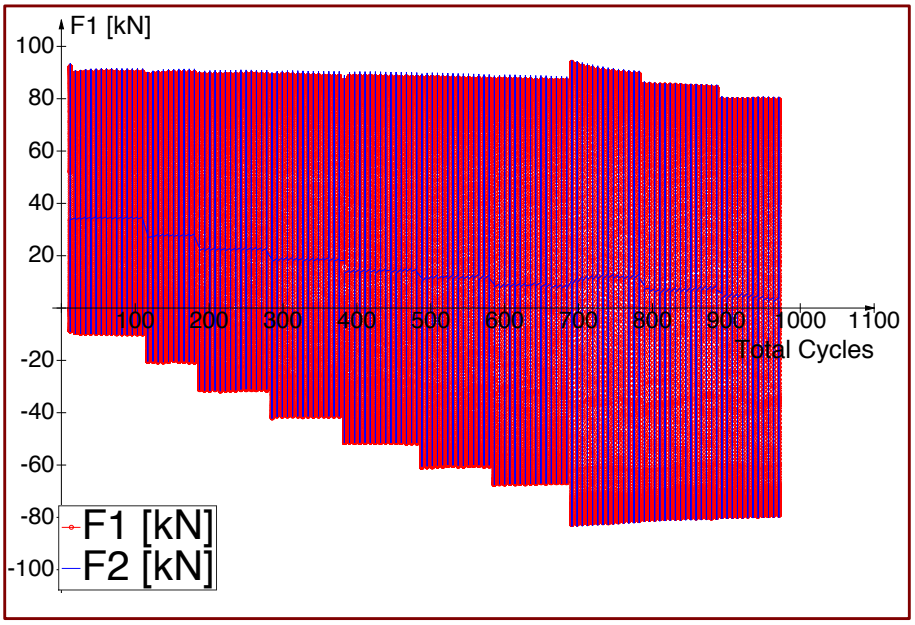

Figure 4.37: Force vs time for the first equi-biaxial strain-controlled test on sample XB1

plastic strains in the ROI without causing instabilities. In order to better understand the behavior in the central zone of the sample, uniaxial elastic simulations were performed using ABAQUS on an eight of the sample, given its symmetry axes. After applying a unit force in one direction ($F_{\parallel}$ = 1 kN) and a zero force in the perpendicular direction ($F_{\perp}$ = 0 kN) we extract the strains and stresses on the surface in the central point ($\varepsilon_{\parallel}^{1kN}, \varepsilon_{\perp}^{1kN}, \sigma_{\parallel}^{1kN}, \sigma_{\perp}^{1kN}$). Using these values, we can calculate the elastic stresses and strains obtained by any combination of forces with the following equations:

$$\begin{cases} \varepsilon_{\parallel} = \varepsilon_{\parallel}^{1kN} F_{\parallel} + \varepsilon_{\perp}^{1kN} F_{\perp} \\ \varepsilon_{\perp} = \varepsilon_{\parallel}^{1kN} F_{\perp} + \varepsilon_{\perp}^{1kN} F_{\parallel} \\ \sigma_{\parallel} = \sigma_{\parallel}^{1kN} F_{\parallel} + \sigma_{\perp}^{1kN} F_{\perp} \\ \sigma_{\perp} = \sigma_{\parallel}^{1kN} F_{\perp} + \sigma_{\perp}^{1kN} F_{\parallel} \end{cases} \tag{4.2}$$

A choice was made for direction 1 to be the one we would like to obtain higher strains for, so in the following the $\parallel$ and $\perp$ directions will be 1 and 2 respectively. Using the force ratio $\left(RF_{21} = \frac{F2}{F1}\right)$, the strain ratio $\left(R\varepsilon_{21} = \frac{\varepsilon_{22}}{\varepsilon_{11}}\right)$ and the stress ratio $\left(R\sigma_{21} = \frac{\sigma_{22}}{\sigma_{11}}\right)$, *Eq. 4.2* was developed to find:

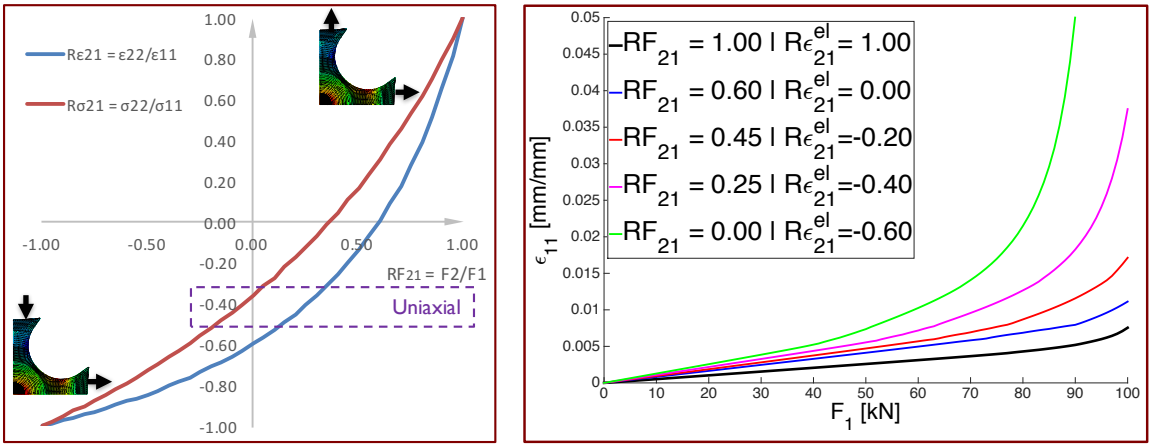

(a) (b)

Figure 4.38: Study of the influence of different force ratios a) $R\varepsilon_{21}$ and $R\sigma_{21}$ vs RF_{21} b) Abaqus simulations results for the whole testing machine force range

$$R\varepsilon_{21} = \frac{\varepsilon_{11}^{1kN} + \varepsilon_{22}^{1kN} RF_{21}}{\varepsilon_{11}^{1kN} RF_{21} + \varepsilon_{22}^{1kN}}$$
$$R\sigma_{21} = \frac{\sigma_{11}^{1kN} + \sigma_{22}^{1kN} RF_{21}}{\sigma_{11}^{1kN} RF_{21} + \sigma_{22}^{1kN}} \tag{4.3}$$

Using *Eq. 4.3*, the strain and stress ratios ($R\varepsilon_{21}$ and $R\sigma_{21}$) were computed for the entire range of the force ratio $RF_{21} = -1..1$. In *Fig. 4.38a* the evolutions of $R\varepsilon_{21}$ and $R\sigma_{21}$ are plotted with respect to RF_{21}. It can be seen that the extremes (-1 and 1) are the same for the three ratios, but the evolutions are quite different. When analyzing the possible strain ratios to consider, we eliminated the range $R\varepsilon_{21} = -0.3.. - 0.5$ given that in between these limits the system is in a uniaxial state (ν = 0.3..0.5) and thus results for this case can be obtained through typical uniaxial tests. For $R\varepsilon_{21}$ too close to -1, the strain maps would become too heterogeneous in the ROI, thus the I-DIC computation would no longer be relevant. For $R\varepsilon_{21}$ too close to 1, the maximum possible strains are still not large enough. In order to better understand the behavior of the structure, extensive simulations were carried out in Abaqus using different ratios RF_{21}, given that controlling a structure using local strain states is not trivial. Some of these results are shown in *Fig. 4.38b*, where it can be seen that the lower RF_{21} is, the larger the potential strain gets in direction 1. Following these guidelines, two values were chosen for the strain ratio, to be performed on the samples XA1 and XC4.

For sample XA1, $R\varepsilon_{21}$ was chosen equal to -0.6 which corresponds, during elastic loading, to a force ratio RF_{21} = 0. The ratio between maximum and minimum strain ($R\varepsilon = \frac{\varepsilon^{min}}{\varepsilon^{max}}$) was, in both directions, equal to 0 ($R\varepsilon_{11} = R\varepsilon_{22} = 0$). A total number of 6 levels were performed, with 401 cycles per level at a loading frequency of 0.1 Hz. The maximum command strain in direction 1 began at ≈0.76%, and was increased by a step

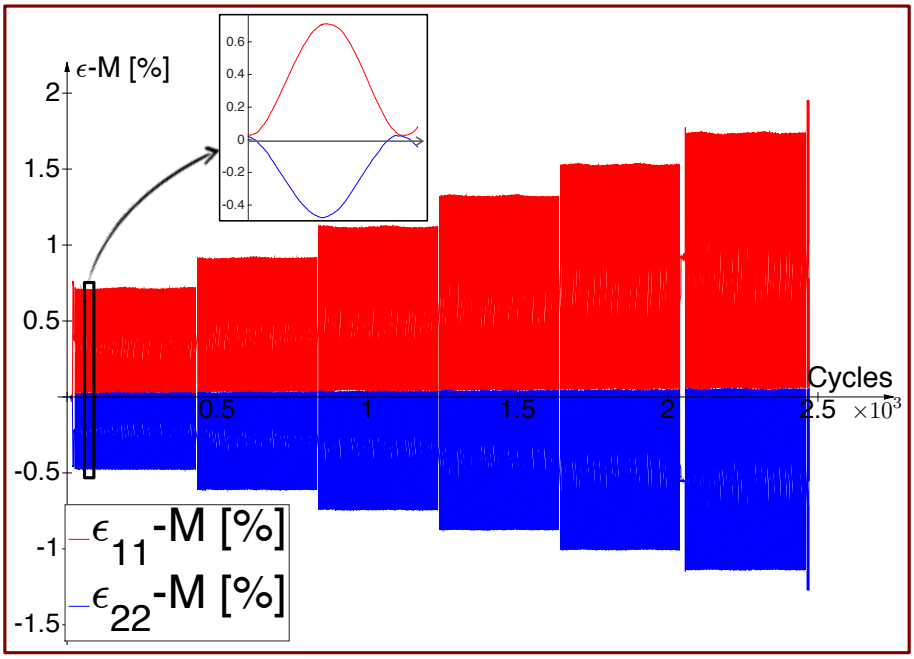

Figure 4.39: Strain vs total cycles in the first non equi-biaxial test XA1 ($R\varepsilon_{21}$ = -0.6)

of ≈0.22% at every level, thus obtaining ε_{11}^{max}-C ≈ 0.76 / 0.97 / 1.19 / 1.41 / 1.62 and 1.84% (*Fig. 4.39*).

The less reactive PID, but also the material behavior, made it that the zero strain value, which was the maximum command in direction 2 and the minimum command in direction 1 (ε_{11}^{min}-C=ε_{22}^{max}-C=0%), wasn't exactly reached, although results were consistent throughout the 401 cycles of each level (*Fig. 4.40a*). The maximum values are reached in direction 1, as computed, so the principle behind the non equi-biaxial test was validated. Unfortunately, as can be seen in *Fig. 4.40b*, the results do not have the usual shape of plastic hysteresis curves. Instead of the sharp loops encountered in the uniaxial case that got wider with strain/stress amplitudes (larger plastic strains), the F_1 vs ε_{11}-M curves seem to go from equally open and blunt at the extremes (*Fig. 4.40a*), to a shape that resembles the number 8 (*Fig. 4.40b*), where the zone that should have the largest opening has almost none at all. This phenomenon will have to be further examined in order to make a clearer conclusion.

For sample XC4, $R\varepsilon_{21}$ was chosen equal to zero, so a theoretically uniaxial strain state. This corresponds, during elastic loading, to a force ratio $RF_{21} = 0.6$. A total number of 6 levels were performed, with 501 cycles per level at a loading frequency of 0.1 Hz. The maximum command strain in direction 1, ε_{11}^{max}, was a constant ≈0.65% for all levels, and the minimum, ε_{11}^{min} started at 0% and was decreased by a step of 0.11% at every level, thus resulting in ε_{11}^{min}-C ≈ 0 / -0.11 / -0.22 / -0.33 / -0.44 and -0.55% (*Fig. 4.41*).

For this test we can see that the PID is indeed struggling to keep the value of the strain on the second axis at zero (*Fig. 4.42*). It has to be taken into account that the material "naturally" tends towards a state different from zero in the opposite direction of loading,

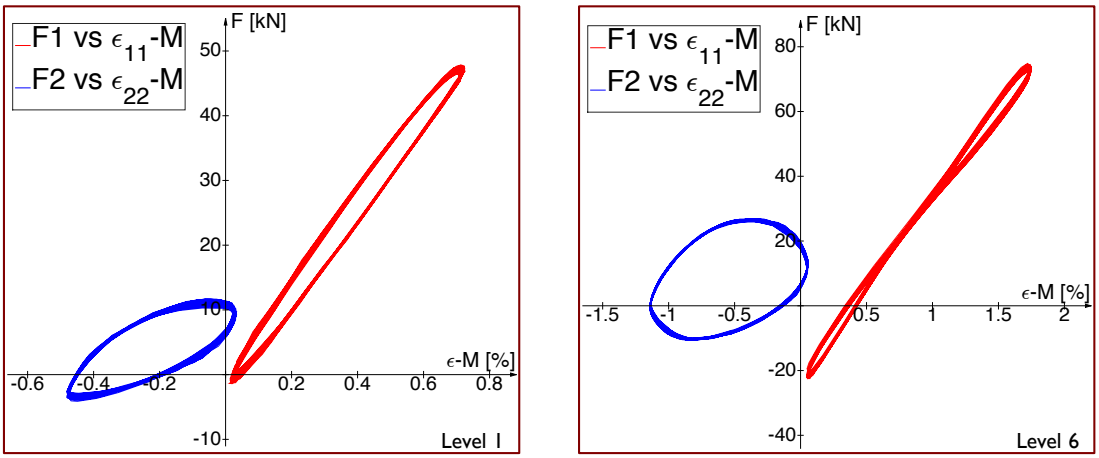

(a) (b)

Figure 4.40: Force vs strain curves of the XA1 test for a) Level 1 b) Level 6

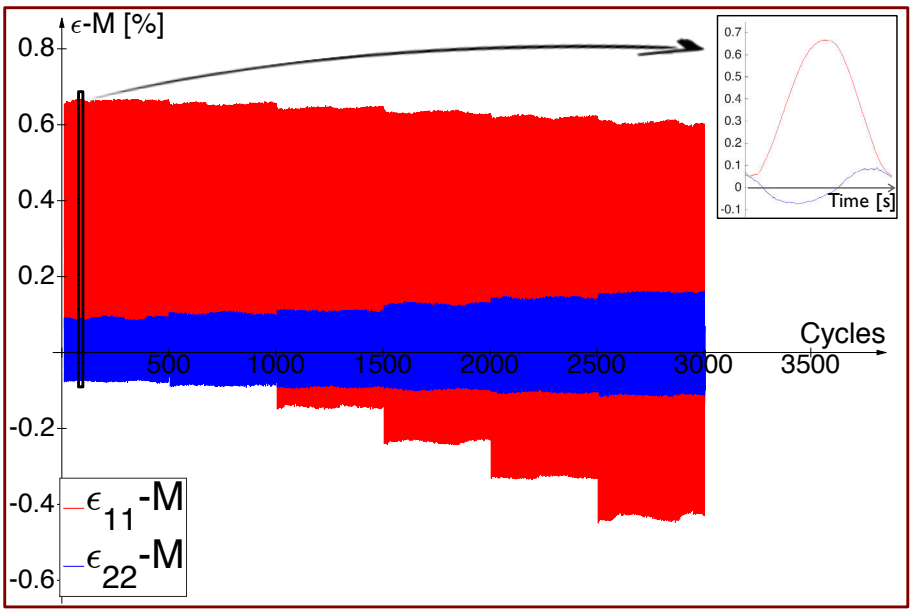

Figure 4.41: Strain vs total cycles for non equi-biaxial test XC4 ($R\varepsilon_{21} = 0$)

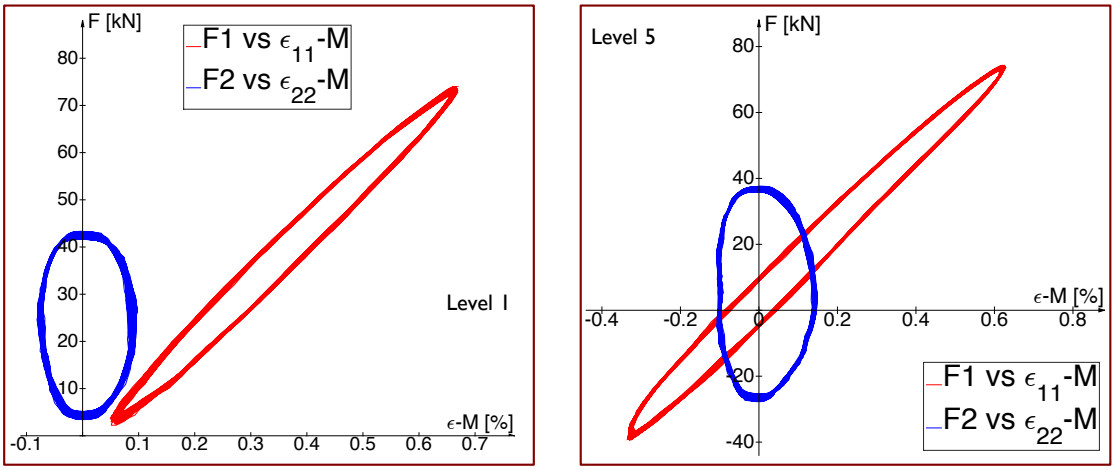

(a) (b)

Figure 4.42: Force vs strain curves of the XC4 test for a) Level 1 b) Level 5

due to the Poisson's effect. Nevertheless, a much more reactive PID would be needed in the future, at least for the second axis, for the response to be closer to the command. Such a PID is not trivial to set, given that this problem occurs even in force control, which uses a signal much more reliable (higher refresh rate and smaller delay), for highly non-equi-biaxial loading states. Moreover, the decrease noticed in the maximum strain level seen in red in *Fig. 4.41* is also a result of the influence one direction has over the other, causing the response to be less and less accurate even for the first axis. The loops in direction 1 still do not resemble the uniaxial ones, although the phenomenon seen in the previous test doesn't seem to reappear. They don't, however, get a lot larger, but seem to have the same permanent strains throughout all levels.

3.5 Stabilized equi-biaxial strain-controlled test XB2

In order to verify if the results found in the case of sample XB1 do not evolve differently over the course of more than 101 cycles, a test was performed on sample XB2, with 3 levels, 501 cycles per level (*Fig. 4.43*). The loading levels were chosen among those performed in the XB1 test, in order to be able to see if the results are consistent. Thus, the maximum strain command for all three levels was ε_{11}^{max}-C=ε_{22}^{max}-C=0.54% and the minimum was gradually decreased, resulting in ε_{11}^{min}-C=ε_{22}^{min}-C=-0.11/-0.27/-0.32%. These bounds were chosen large enough to plastify, but without buckling appearing in the center of the sample. For these first three levels, the loading frequency was, as in the case of sample XB1, 0.05 Hz.

Given that this test is considered valid in its entirety (no buckling occurred), an in detail analysis was performed on some of the images taken by the control cameras and saved during the test. The strain maps were quite homogeneous on both sides of the sample even in high compression levels. In *Fig. 4.45*, the strain maps in direction 1 are

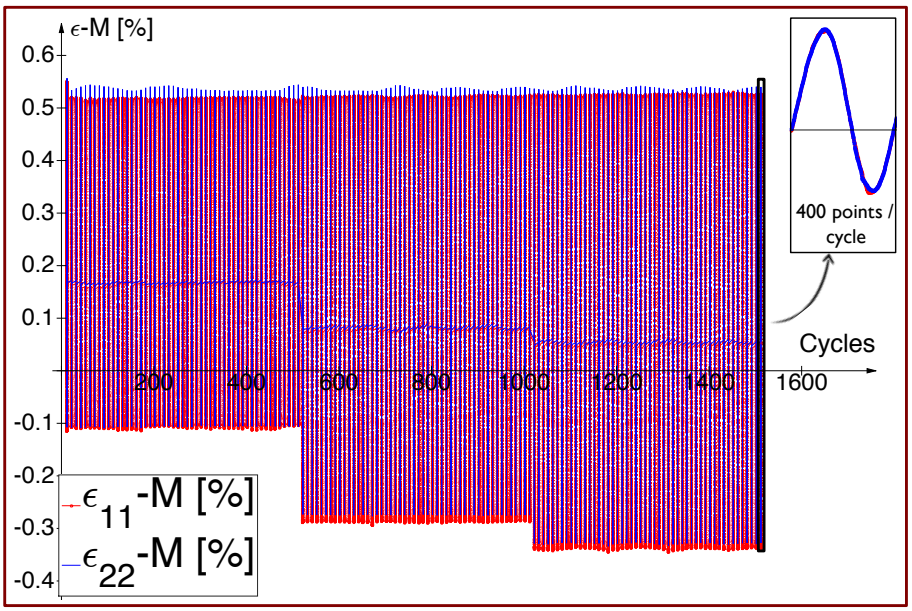

Figure 4.43: Strain vs total cycles for the equi-biaxial strain-controlled test XB2

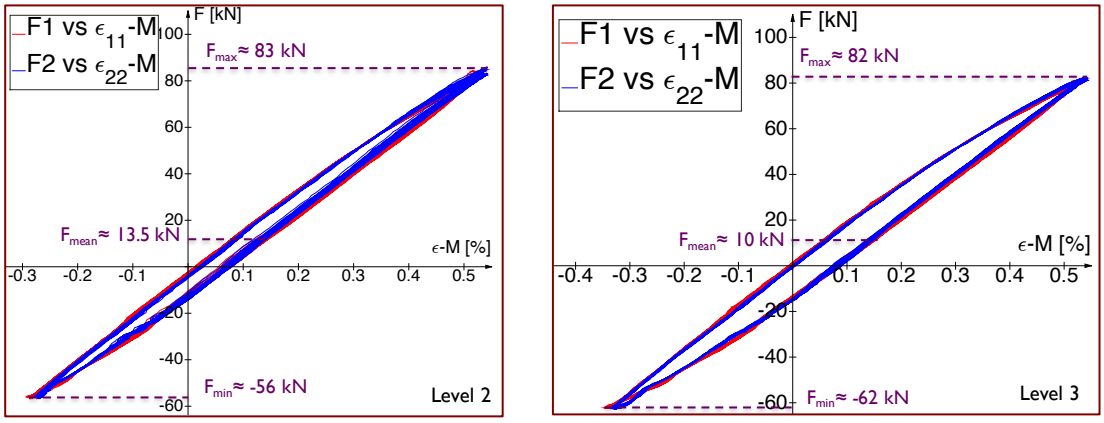

(a) (b)

Figure 4.44: Force vs strain curves of the XB2 test for a) Level 2 b) Level 3

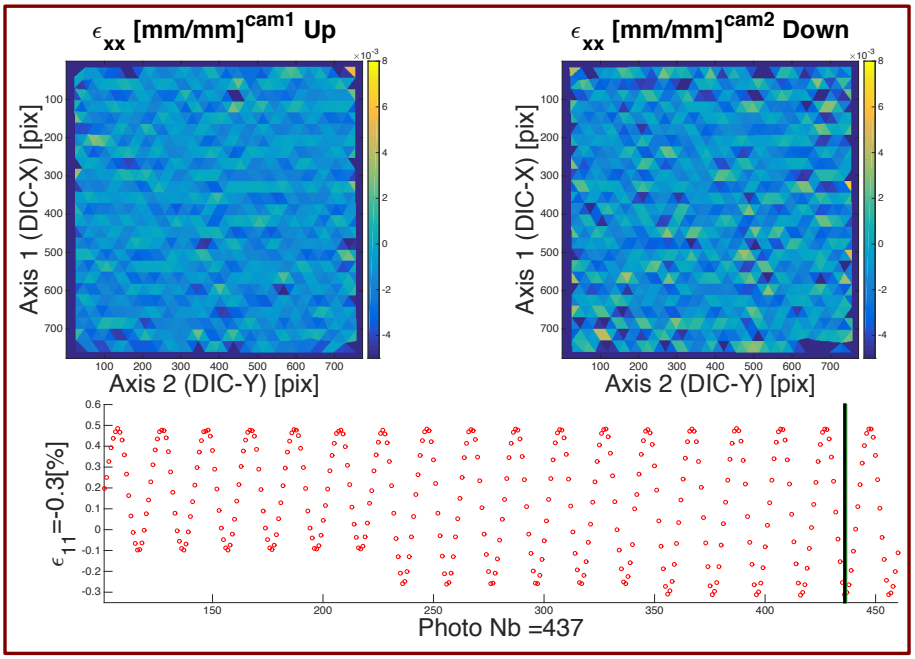

Figure 4.45: Homogeneous strain maps for the equi-biaxial strain-controlled test XB2

shown for the two sides of the sample (Up and Down). The photos are taken in a moment when the minimum strain is reached (ε_{11}-M =ε_{22}-M=-0.32%) and there are no visible signs of buckling.

As in the previous test, very little difference was encountered in the evolution of F_1 and F_2 during a loading level, even though the opening in the hysteris loops shows they are clearly plastic. Thus, no mean force relaxation occurs during these 501 cycle periods (*Fig. 4.44*). In order to go even further, the bounds of the last level were kept but the loading frequency was changed to 0.1%, so twice as fast as before in order to reach 4001 cycles in a reasonable amount of time (*Fig. 4.46*). We noticed that the less reactive PID had some trouble in reaching the upper limit, although not the lower one. Even so, very little evolution was noticed in the force levels, in the order of 3$\sim$4 kN.

These results make the comparison with the uniaxial strain-controlled results difficult, given that in the uniaxial case, important mean stress relaxation was noticed. As mentioned earlier, the stress relaxation in the ROI is masked in the biaxial case by the elastic thick region surrounding it. To overcome this issue, a more complex FE plastic computation needs to be made in order to fully asses the stress state in the ROI.

4 Conclusion

For analyzing complex phenomena like mean stress relaxation, a reliable measurement and control method has to be developed for the high plastic strains occurring in the region of interest of the sample. Classic measuring techniques, such as strain gauges and

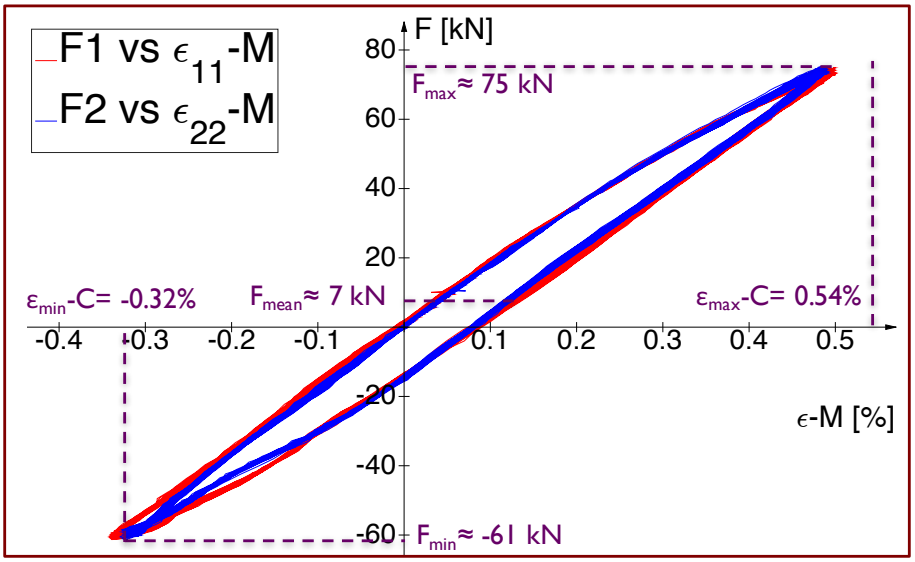

Figure 4.46: Force vs strain curves for the XB2 test for ε_{max}-C $= 0.5\%$ and ε_{min}-C $= -0.3\%$, 4001 cycles at 0.1 Hz

extensometers are difficult —if not impossible— to use in order to perform biaxial strain-controlled cyclic tests because of the high levels of plasticity and their aforementioned inconveniences. Global DIC is too slow to control a testing machine in our testing scenarios, thus integrated DIC (I-DIC) was used. By using adequate shape functions on one element and GPU computations, we were able to obtain measurement frequencies of 100 Hz with a accumulated response delay of 10 ms. With the current technology, there isn't much place for improvement in terms of speed and delay. With more powerful GPUs, the treatment time would improve negligibly with the current code. The main time loss is related to the transfer of the images. Even if they are only transferred in the computer RAM, it's still a considerably sized matrix. One lead would be direct camera treatment, such as FGPA cameras, where images wouldn't need to be transferred to a computer. Nevertheless, for low cycle fatigue tests at 0.1 Hz, this method performed very well.

First elastic tests have revealed that the results are coherent with the Abaqus simulations and that the strain maps are sufficiently uniform to validate the use of a mean value (I-DIC). After an initial "on the fly" monitoring of I-DIC obtained strains, results were coherent in the two directions and on the two sides of the sample up to a certain point, when the structure exhibits buckling. This phenomenon was extensively studied using Abaqus simulations and stereo-DIC measurements, in order to determine the safe loading domain.

The presented biaxial DIC strain-controlled tests were carried out using the mean value from the upper and lower cameras as a control signal. The loading levels and purpose of all biaxial tests are summarized in *Tab. 4.5*. The symbols mean: $\times$ - sample suffered complete fracture during the test, ✓ - sample unbroken after test. The color red

	Sample	Test details
×	XA3	First force-controlled equi-biaxial test, that shows buckling occurring (9 levels |300 cycles/level |$\Delta F/2$ = 75..80 kN |$\bar{F}$ = 0..20 kN)
×	XA2	Force-controlled equi-biaxial test performed to find buckling limits (16 levels |101 cycles/level |F_{max} = 95 kN |F_{min} = 0..-90 kN)
✓	XB1	First strain-controlled test performed (Equi-biaxial) (10 levels |101 cycles/level |ε_{11}^{max} = 0.58% |ε_{11}^{min} = 0..-0.43%)
✓	XB2	First fully viable strain-controlled test performed (Equi-biaxial) (3 levels |501 cycles/level |ε_{11}^{max} = 0.50% |ε_{11}^{min} = -0.1/-0.25/-0.3%)
×	XA1	Non equi-biaxial strain-controlled test ($R\varepsilon_{21} = \varepsilon_{22}/\varepsilon_{11}$=-0.6 |$RF_{21}\approx$0) (7 levels \|401 cycles/level \|ε_{11}^{max} = 0.70..1.9% |ε_{11}^{min} = 0%)
×	XC4	Non equi-biaxial strain-controlled test ($R\varepsilon_{21} = \varepsilon_{22}/\varepsilon_{11}$=0 |$RF_{21}\approx$0.6) (6 levels \|501 cycles/level \|ε_{11}^{max} = 0.70% |ε_{11}^{min} = 0/-0.1..-0.5%)
×	XA4	Poorly machined, thus used as first tuning sample (accidental fracture)
×	XT1	Tuning samples, in different states of damage, used for: centering /
✓	XT2,XT4	PID adjustments / camera trigger / strain control / testing *ASTREE-IDIC*

Table 4.5: Summary of the biaxial campaign on cross-shaped specimens

means that an accident occured and the sample broke, whereas the color green means the sample served its desired purpose.

As was shown in the previous sections, the I-DIC measurements are sufficiently precise to be used as a reliable ”real-time” sensor for biaxial tests with a sufficiently homogeneous ROI. Moreover, with its precision and speed, I-DIC proved to be a suitable technique for controlling a biaxial hydraulic machine. It worked very well for the equi-biaxial strain control, up to very high levels of strain, superior to gauge capability. In the more extreme loading cases, such as $R\varepsilon_{21}$=0, the PID wasn't reactive enough and so the quality of the results was less accurate. Nevertheless, what was shown through these tests is that in the biaxial case, at least for the used sample, there was very little or no mean stress relaxation. This novel result is important and has not been observed so far. It will have to be taken into account in future studies, when the model will be used to perform structure computation for the whole sample.

Conclusion

Due to the increasing complexity of systems used in aeronautics, spatial, automotive industries, etc., the need for more sophisticated models to describe their behavior has grown in the past years. This implies that experiments manage to get as close as possible to the multiaxial loading states encountered in service. To improve the characterization and the design of their metallic parts, the propulsion systems manufacturer Safran Aircraft Engines (SAE) develops constitutive equations, damage laws and fatigue criteria that are more adapted to the real loading states.

The nickel-based superalloy Inco718DA is used for the manufacturing of the high-pressure turbine disks. It has been shown though that for Inco718, a material that softens cyclically, the inelastic analysis cannot be based solely on the stabilized cyclic behavior of the material [Chaboche and Cailletaud, 1986; Burlet and Cailletaud, 1986; Benallal and Marquis, 1987; Calloch and Marquis, 1997; Portier et al., 2000]. In order to have a precise characterization, both the monotonic (initial) behavior and the cyclic (softened) one should be introduced [Chaboche et al., 1991]. This is an important difficulty, given the slow transition between these two states especially at low strain levels in non-symmetrical loading.

The main goal of this thesis was to develop a plasticity model adapted to Inco718DA and capable of representing several loading conditions (monotonic, symmetrical and non-symmetrical cyclic loading). The identification of the model was possible thanks to a "rich" uniaxial campaign, favoring complex, innovative tests to numerous costly fatigue tests. We performed these tests both in the LMT lab and in the SAE facilities. Such tests include a monotonic test with elastic unloads, a multi-level $R_\varepsilon = -1$ test and two $R_\varepsilon = 0$ tests that could better quantify mean stress relaxation, or a test to analyze ratcheting. The cyclic behavior was identified using a kinematic hardening law derived from the one developed by Desmorat [2010b] with elements of memory surface inspired by Chaboche et al. [1979] and Delobelle et al. [1995]. This allowed us to obtain a very good description of the stabilized cyclic response in the R_ε=-1 regime. One of the challenges was to obtain sharp stabilized loops in a saturated cyclic plasticity regime, which was possible using parameter Γ evolving with respect to the maximum equivalent plastic strain, in the back-stress of the Desmorat [2010b] model. The uniaxial campaign, as well as the development and identification of the model, were described in chapter 2, with the closed form expressions for the 1D case being given in subsection 4.3.

A second difficulty appears in the description of complex phenomena such as mean

stress relaxation and ratcheting, which have a considerable impact on fatigue lifetime. Moreover, given that some failure criteria are not related to fatigue but to the maximum accumulated plastic strain, a precise description of these phenomena becomes crucial to a good estimation of component lifetime expectancy.

In chapter 3, a model was proposed for the description of the partial mean stress relaxation. One of the more original parts of the creation of the model is the idea that partial mean stress relaxation is a direct consequence of the difference between the loading and the unloading part of the hysteresis loop. By analyzing the parameters that could be responsible for this difference, we were able to find patterns that would indicate that there was indeed a considerable difference between what happens at the ascending and at the descending part of the loop. For reasons explained in chapter 3, section 3, the chosen parameter we used to describe this difference was the prefactor of the back-stress term Γ, for which the thermodynamics allows this liberty. We have shown in subsection 4.1 that $\Gamma \geq 0$ is a sufficient condition for the intrinsic dissipation to remain positive, whatever the loading. Its evolution was directly computed for all the cycles of the available tests and used in the description of the model.

When compared to confirmed kinematic hardening laws that model non-zero mean stress relaxation [Chaboche, 1991; Chaboche et al., 2012; Gustafsson et al., 2011], our model presents the advantage of using only one backstress, even if its description is more complex. Moreover, the model is incremental (written in a rate form in chapter 3, section 5) so it can take into account complex loadings such as increasing maximum strain tests, possibly random. Another important aspect when comparing our model to the confirmed non-linear kinematic hardening with thresholds developed by Chaboche et al. [1991] is that the description of the mean stress $\bar{\sigma}$ vs the strain amplitude $\frac{\Delta\varepsilon}{2}$ at a given strain ratio R_ε is continuous. It has no subsequent jumps in the response, as it happens with each deactivation of back-stresses.

Even if it was not the focus of this study, an interesting aspect that can also be represented with this dual Γ approach [2] is the asymmetry between tension and compression. It was shown in subsection 3.3 that with a minimal tuning of the parameters, this asymmetry can be very accurately represented.

In the last chapter of the thesis a vast biaxial campaign will be presented, along with developments to make Integrated-DIC (I-DIC) strain controlled tests. The initial goal of this study was to validate the plasticity model under the multiaxial conditions experienced by the engine components during normal use. Therefore, a biaxial campaign was performed using LASER sensors, mono and stereo full-field measurements using Digital Image Correlation (DIC). Moreover, for analyzing complex phenomena like mean stress relaxation, a reliable measurement and control method has to be developed for the high plastic strains occurring in the region of interest of the sample. By using adequate shape functions on one element and GPU computations using I-DIC, we were able to obtain measurement frequencies of 100 Hz with an accumulated response delay of 10 ms.

As was shown chapter 4, the I-DIC measurements are sufficiently precise to be used as

[2] dual meaning a different value of the parameter Γ for the ascending and descending loading states

a reliable "real-time" sensor for biaxial tests with a sufficiently homogeneous ROI. Moreover, with its precision and speed, I-DIC proved to be a suitable technique for controlling a biaxial hydraulic machine. It worked very well for the equi-biaxial strain control, up to very high levels of strain, superior to gauge capability. In the more extreme loading cases, such as $R\varepsilon_{21}$=0, the PID wasn't reactive enough and so the quality of the results was less accurate. Nevertheless, what was shown through these tests is that in the biaxial case, at least for the used sample, there was very little or no mean stress relaxation. This result is important and it will have to be taken into account in future studies, when the model will be used to perform structure computation for the whole sample.

Appendix A

Disk sampling plan

In this part, the preparations made for the machining of the uniaxial and biaxial samples will be presented. The main goal was to optimize the placement of samples in a forged circular block normally used to extract the high-pressure turbine disk. Given the complex thermo-mechanical process the block is submitted to before machining, it was very important to respect the micrographic charts and to ensure that the samples have their regions of interest as close as possible to the place where the disk is extracted.

With the dimensions of the disk partially known (*Fig. A.1*), we estimated that a maximum of 16 biaxial samples could be obtained (4 blocks containing 4 samples each). The rest of the usable space was occupied with a maximum number of uniaxial samples. The software CATIA was used to represent the block and position the samples inside it.

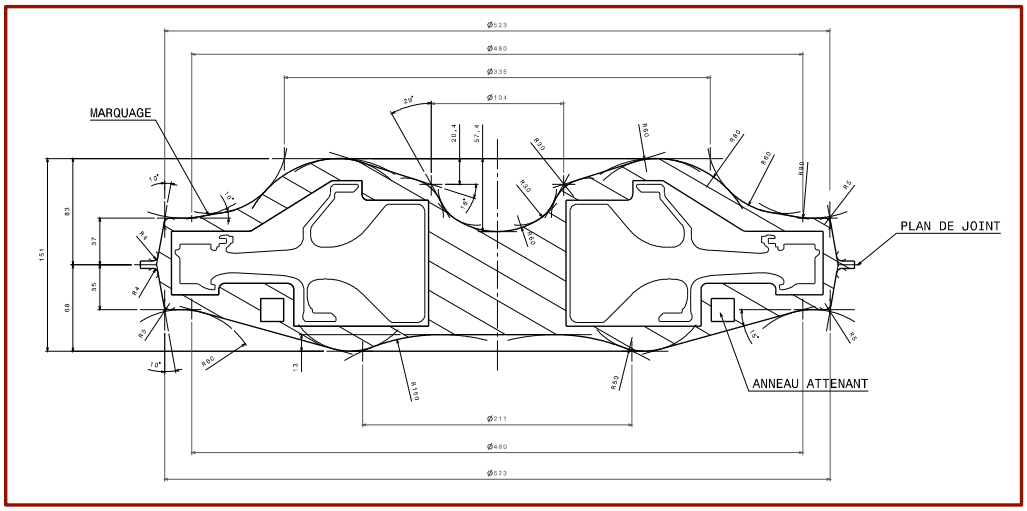

Figure A.1: Turbine disk block plan.

In sampling plans for similar studies the cross-shaped blocks were distributed symmetrically. Given the size of our blocks, such a distribution would make it impossible to have uniaxial samples at the same height and distance from the center as the biaxial ones. In order to correct this inconvenience, the distance between the cross blocks was reduced to 1 mm (the recommended minimum distance for the electric wirecut machine). Nevertheless, the blocks were chamfered, which serves on the one hand as a space saver and on the other to be able to identify the 4 cross-shaped blocks (*Fig. A.2*).

The final distribution in the sampling plan can be seen in *Fig. A.3* . The color coding used for the samples is: biaxial samples in red, tangential uniaxial in green, radial uniaxial in blue and vertical uniaxial in brown. Coded names have been attributed to each sample, in order to identify its precise position inside the plan. They are numbered starting from 0°clockwise, using the following rules:

1. Biaxial samples (Ex : **XA1..4**):

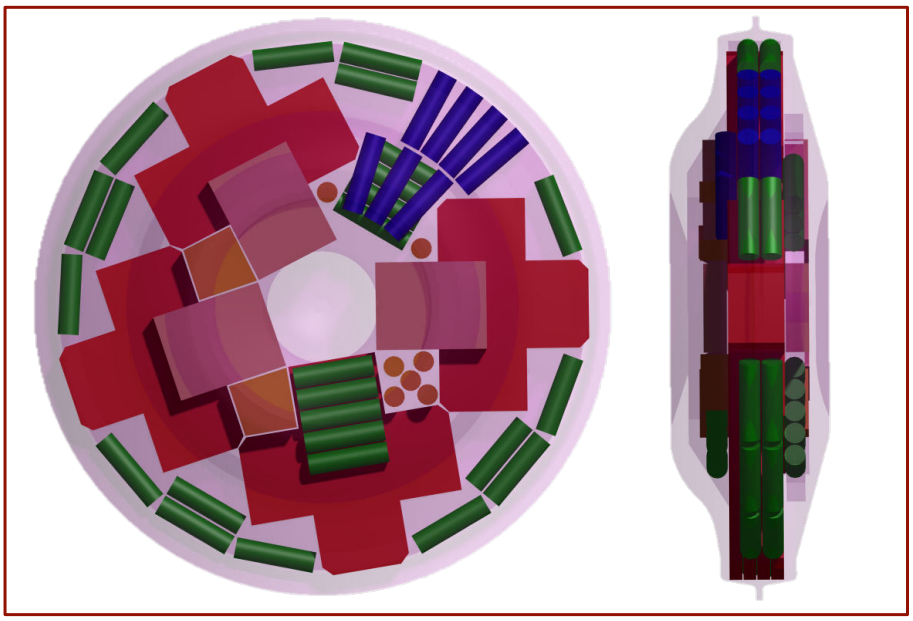

Figure A.2: 3D rendering of the position of the samples in the plan.

- sample type: X - cross;
- block identifier: block A to D;
- number: 1 - highest, 4 - lowest;

2. Uniaxial sample (Ex: **TEU1**):
   - sample type: T (tangential) or R (radial) ou V (vertical);
   - position with respect to the biaxial sample : U (up) or D (down);
   - number (to increment the samples with the same code);
3. Blocks:
   - Large cross-shaped blocks and parallelepiped ones (Ex: **BX**):
     - block code determining its position: (B, C ou D);
     - vertical position (X - cross shaped block, U - upper parallelepiped block (up), D - lower parallelepiped block (down));
   - Vertical blocks (Ex: **VB1..2**)

In *Fig. A.3* we also find the different types of chamfers (in black) marked on the view from above. The positioning of the cuts, necessary for a better understanding of delicate areas, may also be seen in this figure. The angles are to be used as guides, given that the real positioning of the blocks is defined by the minimum distance (1 mm) between them (detail M)

One of the most important cuts, cut A-A (*Fig. A.4*) shows the positioning of the first machined biaxial samples. The contour of the forged block (in purple) is not precise and has not been used as a reference. The wirecut will be based solely on the reference axis (vertical, in the center) and the reference plane (horizontal, perpendicular on the reference axis).

In *Fig. A.5* we may see the outline of the uniaxial sample and the limits left for machining. The name of each sample will be marked on the outline and again on the sample. Given that the sample is obtained through turning, a line marking the horizontal plane will be marked on each sample. The machining plan of the uniaxial sample can be seen in *Fig. A.6*.

In *Fig. A.7* we may see the outline of the biaxial sample. The name of each biaxial sample will be marked on the outline and engraved on each of the 4 arms, mentioning by a letter the direction (*e.g.*XA4-T, T for tangential and R for radial). The 4 arms are identical, other than the presence or absence of the chamfers $5\times45°$. The machining plan of the biaxial sample can be seen in *Fig. A.8*.

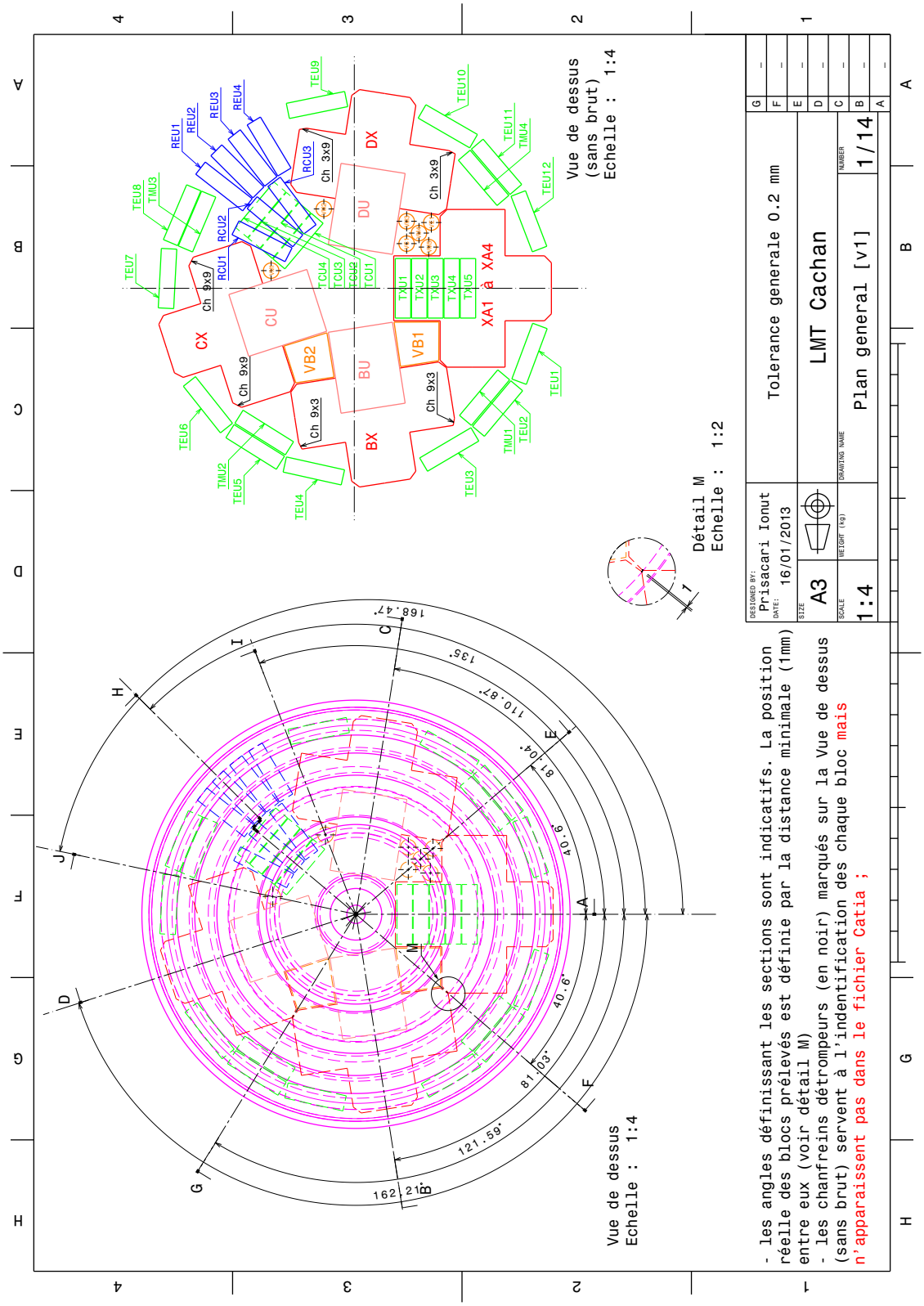

Figure A.3: Cuts distribution in the plan.

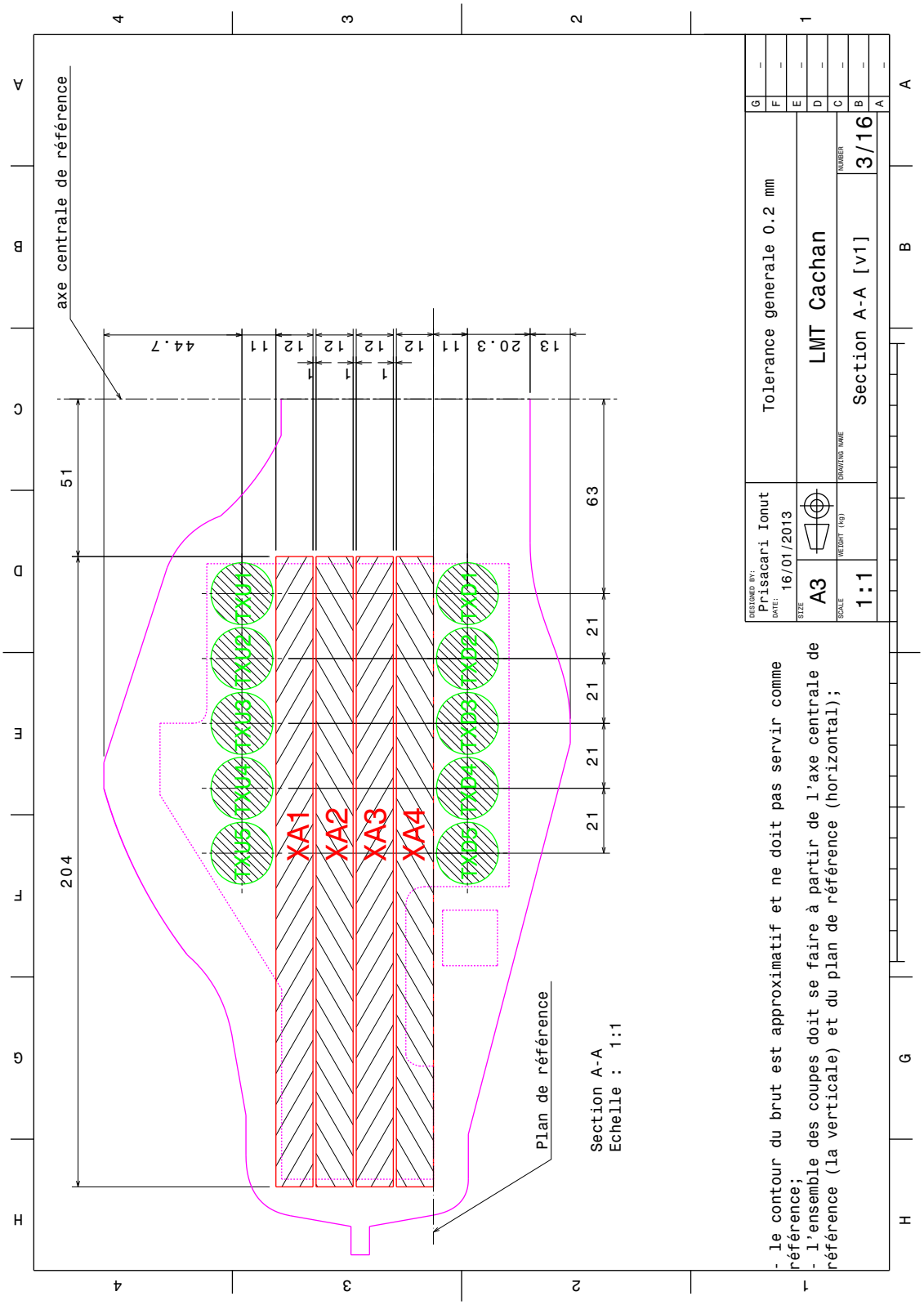

Figure A.4: Cut A-A.

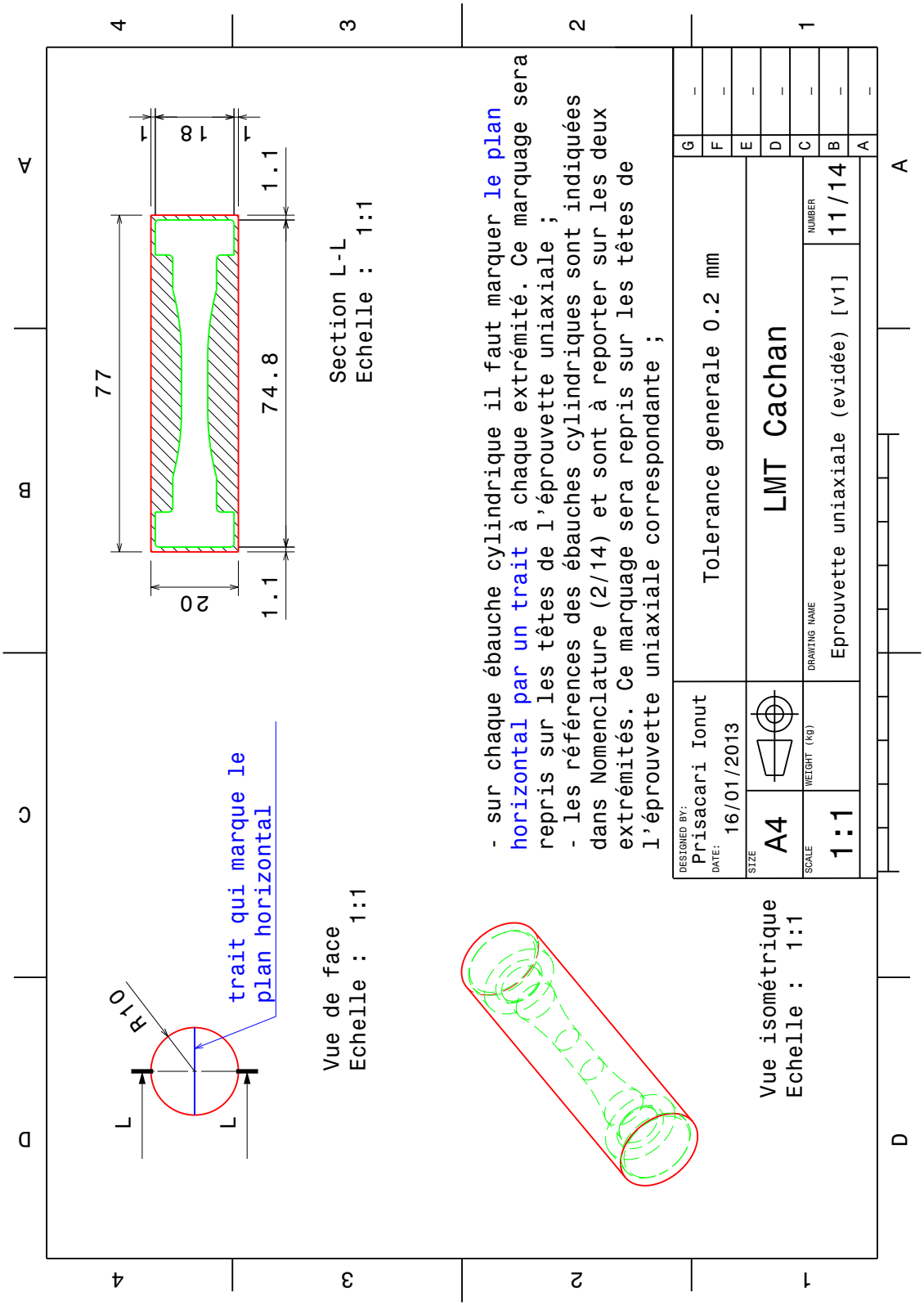

Figure A.5: Uniaxial sample outline.

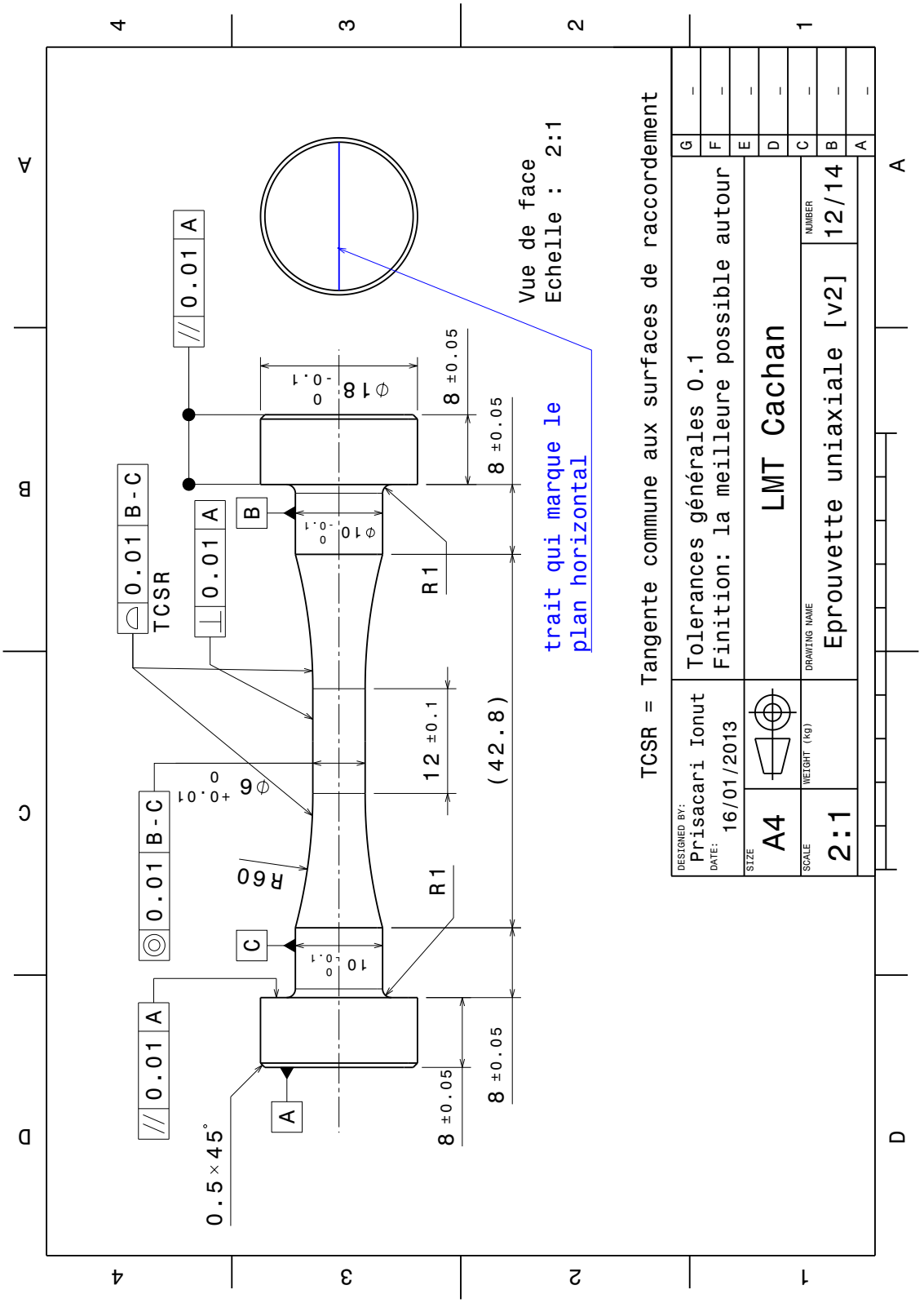

Figure A.6: Machining plan for the uniaxial sample.

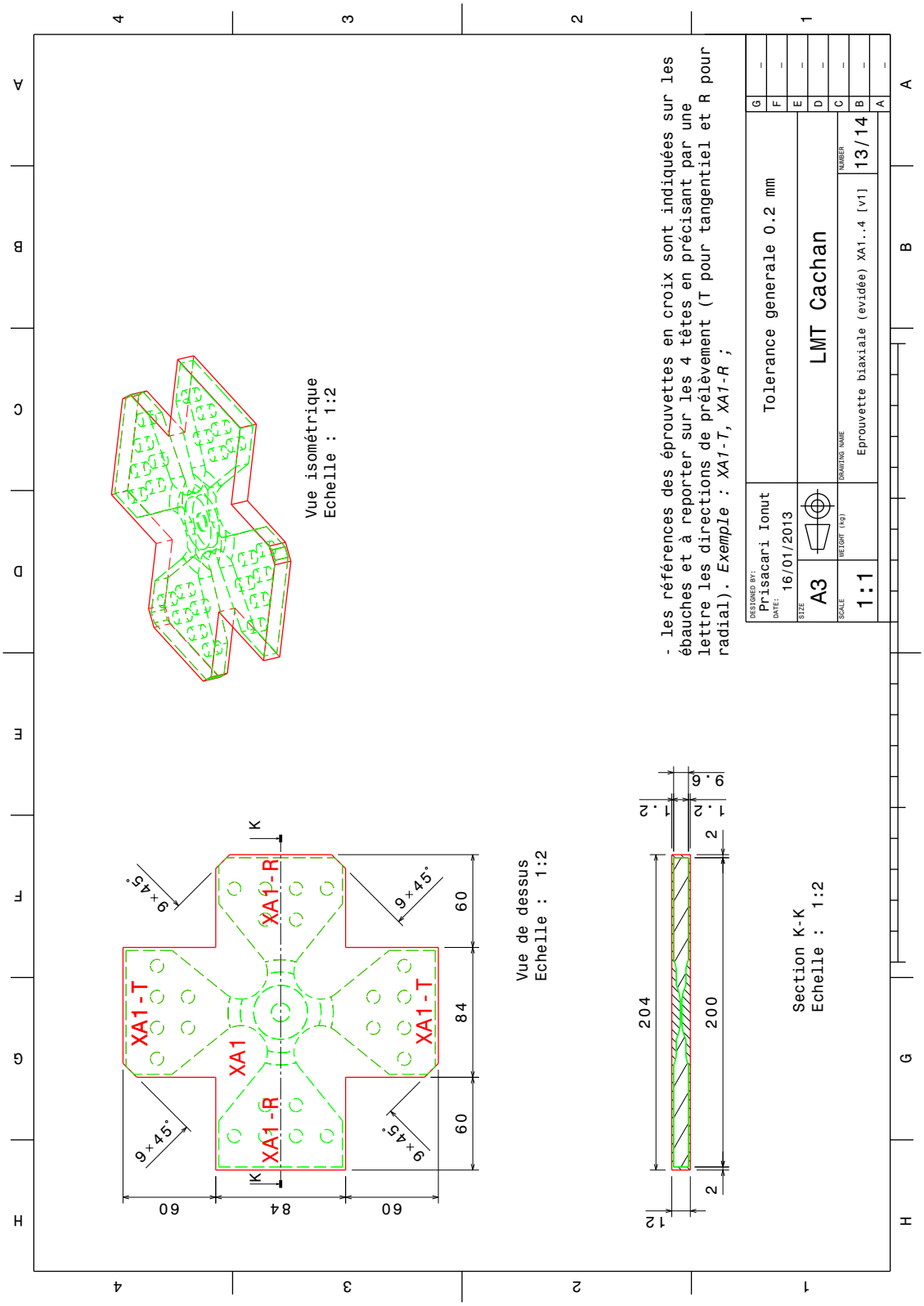

Figure A.7: Biaxial sample outline.

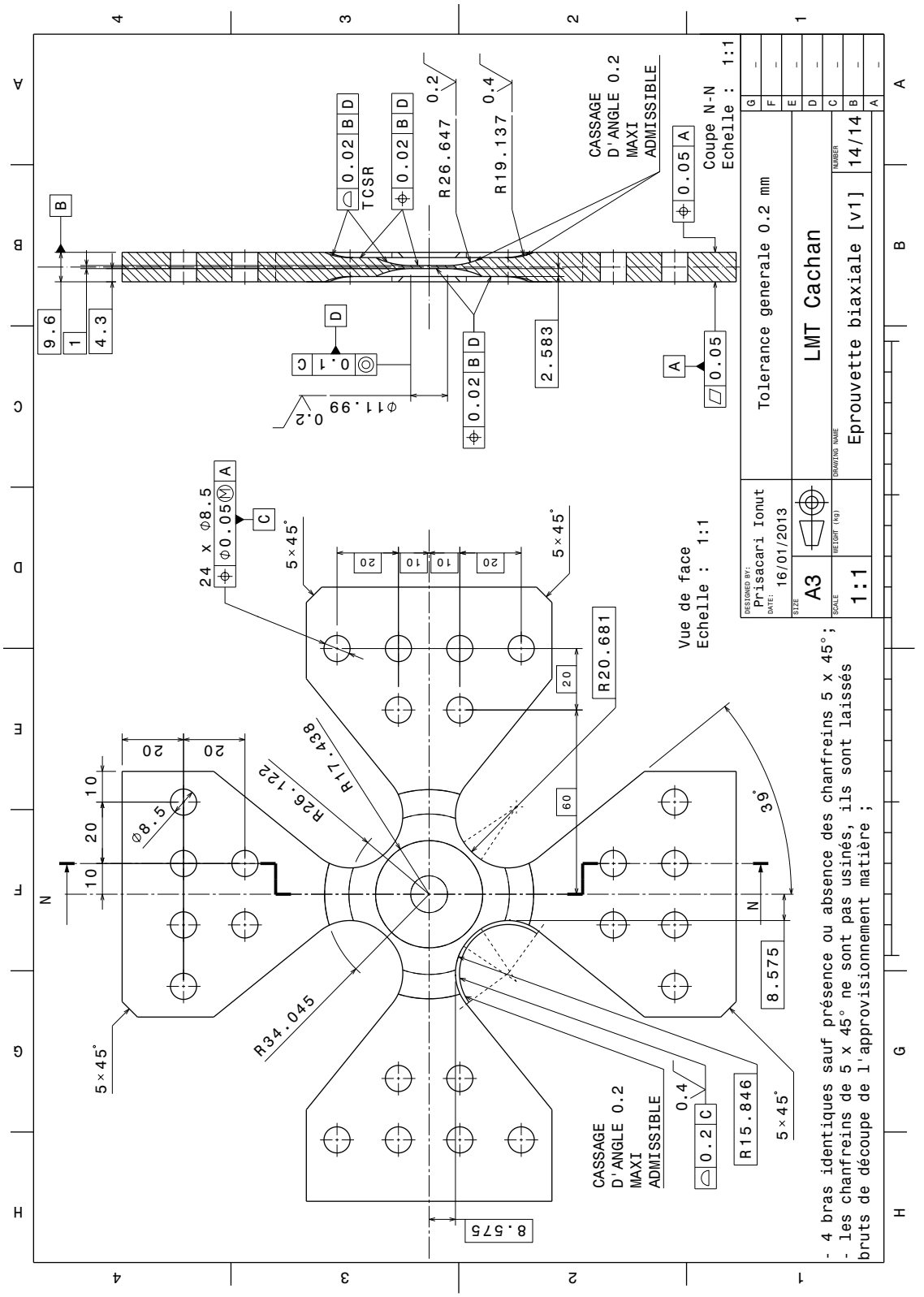

Figure A.8: Machining plan for the biaxial sample.

Appendix B

Monotonic test with elastic unloads identification

In the present appendix, the identification of the behavior of Inco718DA is performed based on the classic principle that a monotonic test with elastic discharges can give the decoupled evolution of both the isotropic hardening R and the kinematic hardening $\boldsymbol{X}$. Based on the assumption that each discharge gives the size of the elastic domain, we may detect the kinematic hardening $\boldsymbol{X}$ as being the ordinate of the middle of each discharge on the $\sigma(\varepsilon)$ curve. Thus, what is left is the yield stress σ_y and the isotropic hardening R (*Fig. B.2a*). This allowed to identify the hardening parameters using a classic method and follow their evolution in the monotonic case.

The evolution of the isotropic hardening using this method is a non-linearly decreasing one. Thus, as shown in *Fig. B.2b*, for the modeling of the isotropic hardening, an exponential law was used:

$$R = R_\infty \left(1 - e^{-bp}\right) \tag{B.1}$$

with the values identified for the isotropic hardening parameters are being:

σ_y [MPa]	R_∞ [MPa]	b
900	-540	18

One aspect that needs to be cleared is the differentiated modeling of the monotonic behavior with respect to the cyclic one. The cyclic plasticity curve is given by points obtained during the stabilized cycle when the isotropic hardening is considered to be saturated. Thus, if we plot the cyclic plasticity curve $\frac{\Delta\sigma}{2}(\frac{\Delta\varepsilon_p}{2})$ on the same graph with the monotonic curve $\sigma(\varepsilon^p)$, it will be lower due to cyclic softening (*Fig. B.1*). The general shape of the two distributions of points is also different, which implies the use of an evolution of the type $\Gamma = \Gamma(q)$ different for the two cases.

By following such an approach to the letter, it can be noticed that the value of σ_y will be precisely identified (*Fig. B.2b*) at quite a large value. Thus, in order to obtain the full monotonic behavior, the evolution of the kinematic hardening must also be well described.

The influence of the offset can be seen even more clearly in *Fig. B.3b* where using only a linear formulation ($\Gamma_0 = 0$) is insufficient in the description of the kinematic hardening and would cause an overshoot in the overall monotonic response (*Fig. B.4a*).

Thus, when using an affine evolution law for the kinematic hardening parameter Γ, the overall monotonic behavior is well described (*Fig. B.4b*), as well as the two types of hardenings, isotropic (*Fig. B.2b*) and kinematic (*Fig. B.3b*). The values found for the two parameters of the affine law Γ_0' and Γ_0, as identified on the computed Γ points (*Fig. B.3a*).

The kinematic hardening parameters found in this identification are given below, with the values that are the same as the official identification (chapter 3, section 6) in grey :

Other identifications were made based on the monotonic test with elastic discharges.

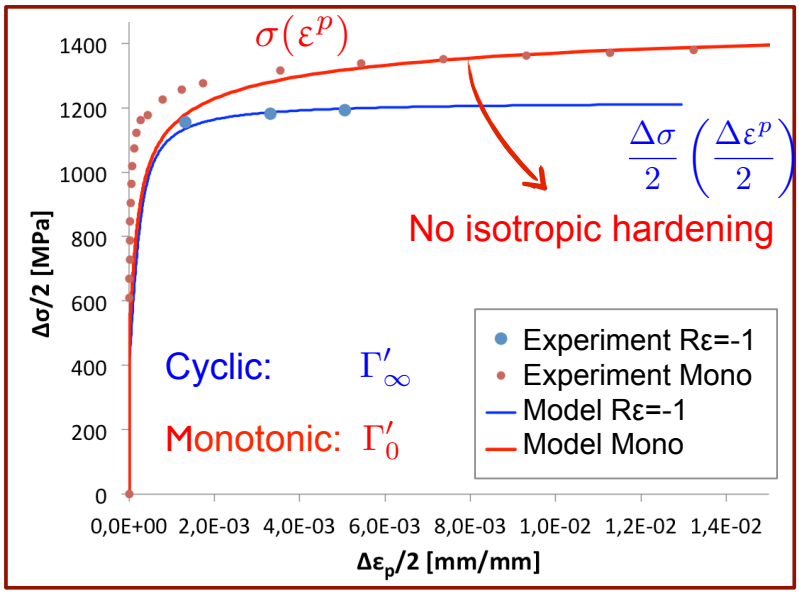

Figure B.1: Comparison between the monotonic and cyclic behavior.

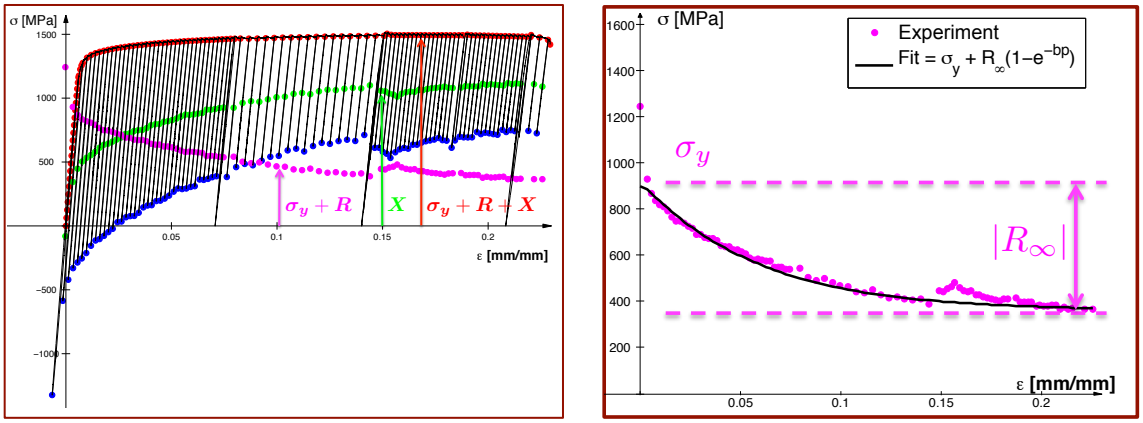

(a) (b)

Figure B.2: Model identification using monotonic test with elastic discharges: a) Component description b) Identification of the isotropic hardening.

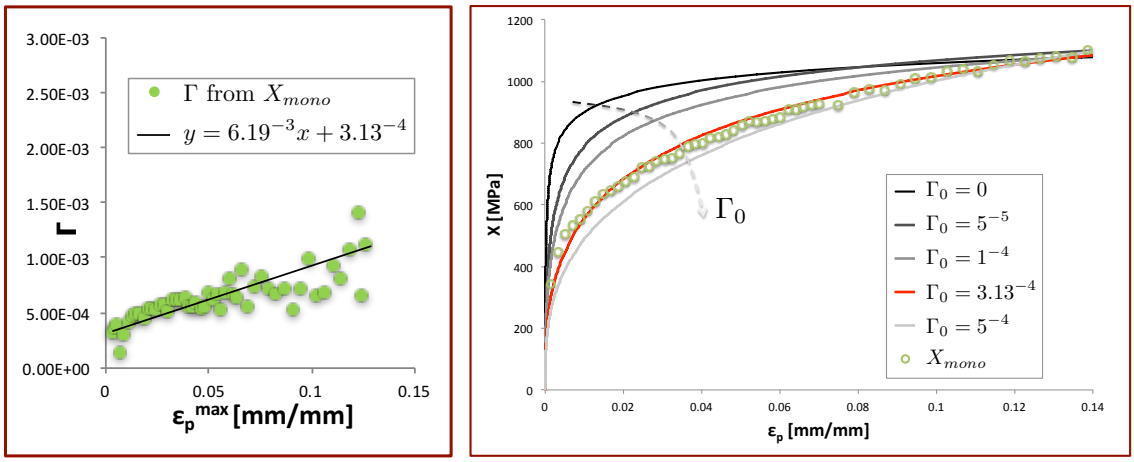

(a) (b)

Figure B.3: Distribution of kinematic hardening parameter Γ in the monotonic case: a) The affine distribution of Γ computed from measured X values b) The influence of the offset of the affine law Γ_0

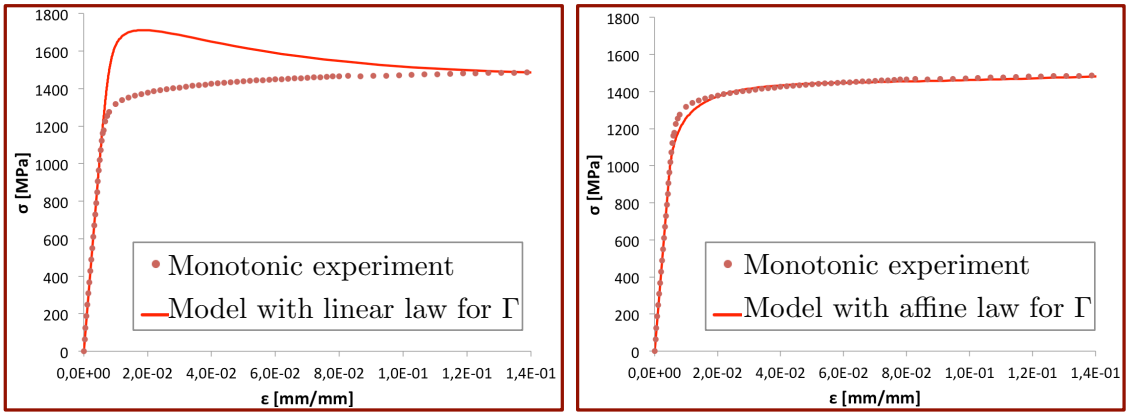

(a) (b)

Figure B.4: Identification of the monotonic behavior using: a) A linear evolution law $\Gamma(\varepsilon^p_{\max}) = \Gamma'_0 \cdot \varepsilon^p_{\max}$. b) An affine evolution law $\Gamma(\varepsilon^p_{\max}) = \Gamma'_0 \cdot \varepsilon^p_{\max} + \Gamma_0$.

E [GPa]	k [MPa]	M [MPa]	C [MPa]	Γ'_0 [MPa^{-2}]	Γ_0 [MPa^{-2}]
206	450	3	$2{\cdot}10^6$	$6.19 \cdot 10^{-3}$	$3.13 \cdot 10^{-4}$

Different types of isotropic hardenings were used in order to obtain an even better description of the monotonic behavior, such as the sum of two exponential formulations. The problem when following the isotropic hardening distribution given by the test was that with such a strong isotropic component (R_∞ =-540 MPa) even if it manages to represent well the monotonic case, the cyclic behavior is too far from the experiment. The isotropic hardening saturates very quickly, leading to cycles that are very different from what was obtained during experiments both for $R_\varepsilon = -1$ and $R_\varepsilon = 0$. This permitted us to conclude that such a combination of violent monotonic kinematic hardening and isotropic softening wasn't compatible with a model capable of accurately describing the transition from monotonic to saturated cyclic behavior. In 4.3, a different method was used, based only on the monotonic response without taking into account the results of the elastic discharges.

Appendix C

Ratcheting test

In the beginning of this study, when wanting to analyze the behavior of Inco718DA under load control, no data was found at 20°C in the SAE database. Thus, we decided to perform a multi-level load-controlled test. Before the actual test, 200 strain-controlled cycles were performed on the sample (0±0.007 [mm/mm]) in order to saturate the isotropic hardening, as shown by Chaboche et al. [1991]. This was done in order to analyze pure ratcheting and not a mix with phenomena like cyclic softening.

In order to analyze the evolution of the ratcheting step $\delta\varepsilon_p$ (the plastic strain increment over an hysteresis loop) with the rise in load level, we've used equivalent loading levels as those found for the strain-controlled multi-level test at R_ε=-1. For this, the load amplitude was kept constant and the mean load was incrementally increased. The first level was the symmetric equivalent of the strain-controlled test performed just before (0±0.007 [mm/mm]), for which we found a mean stress of $\bar{\sigma} = 0$ MPa and an amplitude of $\frac{\Delta\sigma}{2} \approx$ 1131 MPa. For the following levels, the mean stress was increased by ≈17.68 MPa at each level. The values are not round stress-wise because the stress is calculated from the actual load applied by the machine, which is chosen round. Therefore, the following set of stress levels were obtained $\bar{\sigma} \approx 0, 17, 35, 53, 70$ MPa and $\frac{\Delta\sigma}{2} \approx 1131$ MPa (which correspond to $\bar{F} = 0, 0.5, 1, 1.5, 2$ kN and $\frac{\Delta F}{2} = 32$ kN). For the first level, 500 cycles were performed, in order to make sure the method was accurate enough and for the others, 300 cycles per level. The last level finished in the fracture of the sample after 115 cycles (*Fig. C.1a*), for a total of 1515 cycles, without counting the initial 200 strain-controlled ones.

By analyzing the evolution of strain levels during the test, we can see that the ratcheting step is increasing with each level and is approximately constant per level, with the value $\delta\varepsilon_p$ marked in *Fig. C.1b*. Ratcheting becomes unstable during the last level, when complete fracture is approaching.

The modeling of the ratcheting was not performed using the final version of the model. As shown by Desmorat [2010a], the Frederick and Armstrong [1966] hardening rule has a larger ratcheting step then the equivalent hardening rule developed by Desmorat [2010a]. The ratcheting step for this model is constant per loading level, which is compatible with the behavior seen in our test. Nevertheless, the ratcheting step is more important than that seen in tests. The non-linear kinematic hardening model developed by Chaboche and Rousselier [1983] is composed of several Armstrong-Frederick back-stresses, often used for ratcheting applications because of it can be finely adapted, especially for low strain levels where ratcheting is the most delicate to model.

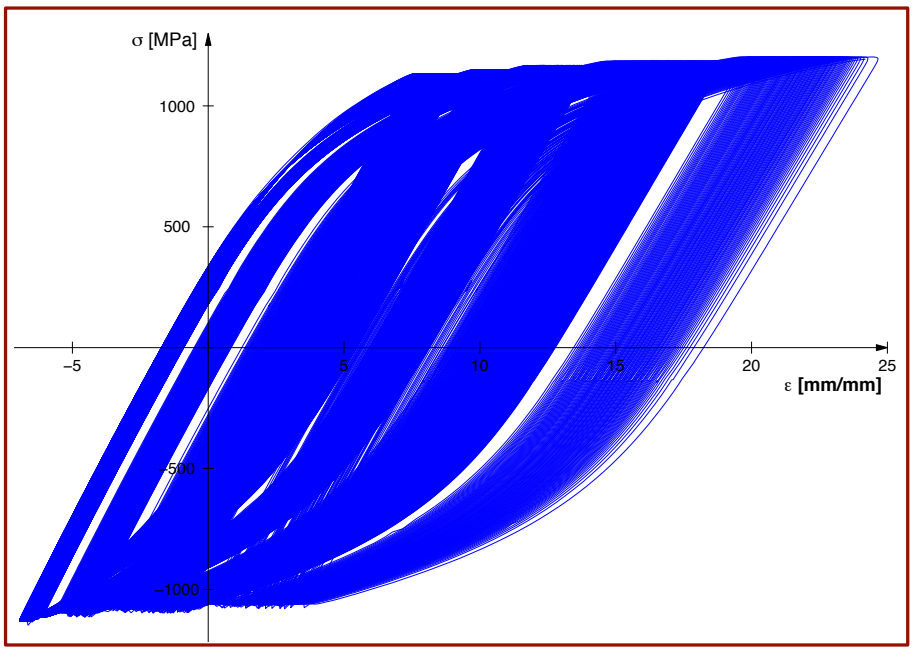

(a)

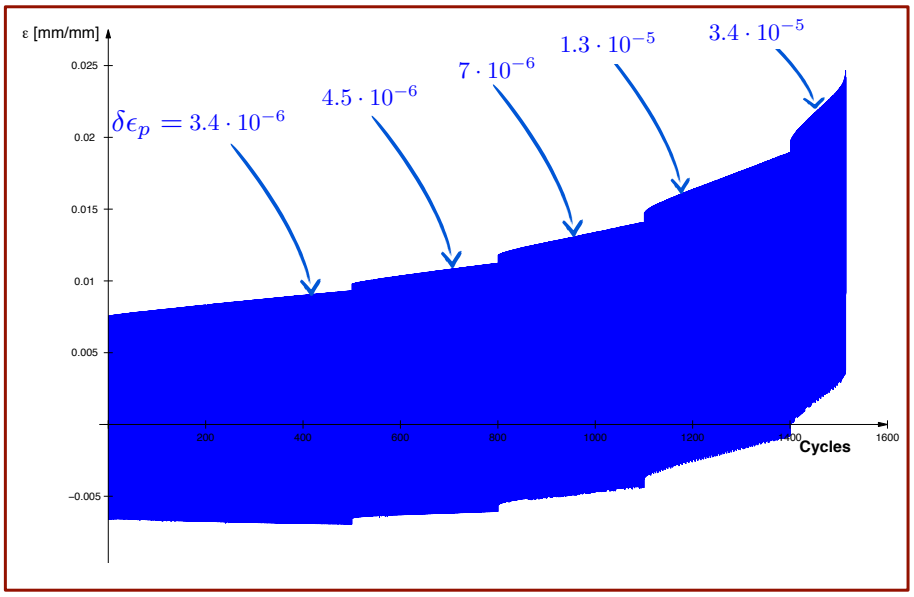

(b)

Figure C.1: Ratcheting test: a) Stress vs strain curves b) Evolution of ε with the increment of plastic strain marked for each loading level

Appendix D

Monotonic loading integration

Integration of the affine evolution of Γ starting from zero

$$\dot{\boldsymbol{X}} = \frac{2}{3}C\dot{\boldsymbol{\varepsilon}}^p - \Gamma X_{eq}^{M-2}\boldsymbol{X}\langle \dot{X}_{eq}\rangle - 3\mathrm{D}$$

$$\dot{X} = C\dot{\varepsilon}_p - (\Gamma_0 + \Gamma_0' q)X^{M-1}\dot{X} - 1\mathrm{D}$$

$$C\frac{d\varepsilon_p}{dX} - (\Gamma_0 + \Gamma_0' q)X^{M-1} = 1$$

$$C\frac{d\varepsilon_p}{dX} - \Gamma_0'\varepsilon_p X^{M-1} = 1 + \Gamma_0 X^{M-1}$$

$$C\frac{d\varepsilon_p}{dX} - \Gamma_0'\varepsilon_p X^{M-1} = 0 - \mathrm{ssm}$$

Variable change:

$$\varepsilon_p = Ae^{\left(\frac{X}{K_0'}\right)^M} \quad \text{where} \quad K_0' = \left(\frac{MC}{\Gamma_0'}\right)^{\frac{1}{M}}$$

$$\left[C\left(A\frac{MX^{M-1}}{K_0'^M} + \frac{dA}{dX}\right) - \Gamma_0' X^{M-1}A\right]e^{\left(\frac{X}{K_0'}\right)^M} =$$

$$= \left[\cancel{\Gamma_0' AX^{M-1}} + C\frac{dA}{dX} - \cancel{\Gamma_0' AX^{M-1}}\right]e^{\left(\frac{X}{K_0'}\right)^M} =$$

$$= C\frac{dA}{dX}e^{\left(\frac{X}{K_0'}\right)^M} = 1 + \Gamma_0 X^{M-1} - \mathrm{asm}$$

$$\frac{dA}{dX} = \left(\frac{1}{C} + \frac{M}{K_0^M}X^{M-1}\right)e^{\left[-\left(\frac{X}{K_0'}\right)^M\right]}$$

$$\frac{dA}{dX} = \frac{1}{C}e^{-\left(\frac{X}{K_0'}\right)^M} + \frac{M}{K_0^M}X^{M-1}e^{-\left(\frac{X}{K_0'}\right)^M}$$

Integration and solution:

$$A = \frac{1}{C}\int_0^X e^{-\left(\frac{X}{K_0'}\right)^M}dX + \frac{M}{K_0^M}\int_0^X X^{M-1}e^{-\left(\frac{X}{K_0'}\right)^M}dX$$

$$u = \left(\frac{X}{K_0'}\right)^M \quad X = K_0' u^{\frac{1}{M}} \quad dX = \frac{K_0'}{M}u^{\frac{1}{M}-1}du$$

$$A = \frac{K_0'}{MC}\int_0^{\left(\frac{X}{K_0'}\right)} u^{\frac{1}{M}-1}e^{-u}du + \left(\frac{K_0'}{K_0}\right)^M\int_0^{\left(\frac{X}{K_0'}\right)} e^{-u}du$$

$$A = \frac{K'_0}{MC}\Gamma^{inc}\left(\frac{1}{M},\left(\frac{X}{K'_0}\right)^M\right) + \frac{\Gamma_0}{\Gamma'_0}\left[-e^{-u}\right]_0^{\left(\frac{X}{K'_0}\right)^M}$$

where $\Gamma^{inc}(m,U) = \int_0^U u^{m-1}e^{-u}du$ – incomplete Gamma function

$$\varepsilon_p = \frac{K'_0}{MC}e^{\left(\frac{X}{K'_0}\right)^M}\Gamma^{inc}\left(\frac{1}{M},\left(\frac{X}{K'_0}\right)^M\right) + \frac{\Gamma_0}{\Gamma'_0}\left[e^{\left(\frac{X}{K'_0}\right)^M} - 1\right]$$

$$\varepsilon_p = \mathscr{E}_1^p(X) + \mathscr{E}_2^p(X)$$

Integration of the affine evolution of Γ from increment i to increment i+1

$\Gamma = \Gamma_0 + \Gamma'_0\varepsilon_p$

For $\Gamma = 0$ the limit value is:

$$\varepsilon_p^* = -\frac{\Gamma_0}{\Gamma'_0} \text{ — } X^* = C\varepsilon_p^*$$

Non linear part of the kinematic hardening

$$A = \frac{1}{C}\int_{X_i}^{X_{i+1}} e^{-\left(\frac{X^*}{K'_0}\right)^M}dX + \frac{M}{K_0^M}\int_{X_i}^{X_{i+1}} X^{M-1}e^{-\left(\frac{X}{K'_0}\right)^M}dX + Cst$$

$$u = \left(\frac{X}{K'_0}\right)^M \quad X = K'_0u^{\frac{1}{M}} \quad dX = \frac{K'_0}{M}u^{\frac{1}{M}-1}du$$

$$A = \frac{K'_0}{MC}\int_{\left(\frac{X_i}{K'_0}\right)}^{\left(\frac{X_{i+1}}{K'_0}\right)} u^{\frac{1}{M}-1}e^{-u}du + \left(\frac{K'_0}{K_0}\right)^M\int_{\left(\frac{X_i}{K'_0}\right)}^{\left(\frac{X_{i+1}}{K'_0}\right)} e^{-u}du + Cst$$

$$A = \frac{K'_0}{MC}\left[\Gamma^{inc}\left(\frac{1}{M},\left(\frac{X_{i+1}}{K'_0}\right)^M\right) - \Gamma^{inc}\left(\frac{1}{M},\left(\frac{X_i}{K'_0}\right)^M\right)\right] + \frac{\Gamma_0}{\Gamma'_0}\left[-e^{-u}\right]_{\left(\frac{X_i}{K'_0}\right)^M}^{\left(\frac{X_{i+1}}{K'_0}\right)^M} + Cst$$

Value of ε_p when integrating between X_i and X_{i+1}

$$\varepsilon_p^{i+1} = \frac{K'_0}{MC}e^{\left(\frac{X_{i+1}}{K'_0}\right)^M}\left[\Gamma^{inc}\left(\frac{1}{M},\left(\frac{X_{i+1}}{K'_0}\right)^M\right) - \Gamma^{inc}\left(\frac{1}{M},\left(\frac{X_i}{K'_0}\right)^M\right)\right] + \frac{\Gamma_0}{\Gamma'_0}\left[e^{\left[\left(\frac{X_{i+1}}{K'_0}\right)^M - \left(\frac{X_i}{K'_0}\right)^M\right]} - 1\right] + \varepsilon_p^i e^{\left[\left(\frac{X_{i+1}}{K'_0}\right)^M - \left(\frac{X_i}{K'_0}\right)^M\right]}$$

Value of ε_p when integrating between X^* and X

$$\varepsilon_p = \frac{K'_0}{MC}e^{\left(\frac{X}{K'_0}\right)^M}\left[\Gamma^{inc}\left(\frac{1}{M},\left(\frac{X}{K'_0}\right)^M\right) - \Gamma^{inc}\left(\frac{1}{M},\left(\frac{X^*}{K'_0}\right)^M\right)\right]$$

$$+\frac{\Gamma_0}{\Gamma_0'}\left[e^{\left[\left(\frac{X}{K_0'}\right)^M-\left(\frac{X^*}{K_0'}\right)^M\right]}-1\right]+\varepsilon_p^* e^{\left[\left(\frac{X}{K_0'}\right)^M-\left(\frac{X^*}{K_0'}\right)^M\right]}$$

$$\varepsilon_p=\frac{K_0'}{MC}e^{\left(\frac{X}{K_0'}\right)^M}\left[\Gamma^{inc}\left(\frac{1}{M},\left(\frac{X}{K_0'}\right)^M\right)-\Gamma^{inc}\left(\frac{1}{M},\left(\frac{C\varepsilon_p^*}{K_0'}\right)^M\right)\right]$$

$$+\frac{\Gamma_0}{\Gamma_0'}\left[e^{\left[\left(\frac{X}{K_0'}\right)^M-\left(\frac{X^*}{K_0'}\right)^M\right]}-1\right]-\frac{\Gamma_0}{\Gamma_0'}e^{\left[\left(\frac{X}{K_0'}\right)^M-\left(\frac{X^*}{K_0'}\right)^M\right]}$$

$$\varepsilon_p=\frac{K_0'}{MC}e^{\left(\frac{X}{K_0'}\right)^M}\left[\Gamma^{inc}\left(\frac{1}{M},\left(\frac{X}{K_0'}\right)^M\right)-\Gamma^{inc}\left(\frac{1}{M},\left(\frac{C\varepsilon_p^*}{K_0'}\right)^M\right)\right]+\varepsilon_p^*$$

Appendix E

New grips validation

The grips currently used in the triaxial machine Astree have been designed and tested by an LMT Cachan team, mainly because the grips previously used to perform biaxial tests on cross-shaped samples (*Fig. E.1*) wouldn't work for the sample type used during this thesis. These samples are shorter and thicker than what was usually used in the laboratory. One of the important aspects of these new grips is the possibility to perform a vertical alignment of the two axes using a system involving an oval hole. The complete study comprising the analysis of need, the design and validation were gathered in an internal LMT report [Poncelet et al., 2014]. Some elements of this report were part of the PhD work and will be briefly presented in the following.

1 Numerical validation

In order to quantify the gain in rigidity with respect to the previous grips, Abaqus simulations were made. The goal was to find the critical areas and to compare the manner in which the two systems distributed the applied loads. The loads weren't applied directly to the grips but on one forth of a sample, in order to get closer to the real behavior. For the clamping zone a perfect contact was used, and a gap was introduced between the lower (fixed) part and upper (mobile) part of the new grips in order to simulate an imperfect clamping. Thus, the transmission of loads between the fixed and the mobile part is done, in this case, via the 5 M12 screws and the sample.

The first simulation was in pure tension, the most common load type during testing. A force of 100 kN was applied, which is the maximum possible charge of a horizontal actuator. In *Fig. E.2* the represented stresses are limited to 150 MPa (superior values in gray), value that is still a lot smaller than the fatigue limit for the material used for the grips (X30Cr13 which is ≈600 MPa). After having optimized its geometry, the new grips are below this value, whereas the old grips surpass this limit in more than one area. The stresses in the critical areas are ≈2.5 times greater than in the case of the new grips. The gain in deflection is even greater, seeing a value 15 times larger for the extremity of the old grips (*Tab. 1*).

Secondly, accidental loads were studied. A load of 200 kN was applied in the plane of

	Measured value	Tension (100kN)	Shear (200kN)	Vertical (500kN)
Old grips	Deflection (mm)	0.3	-	-
	Maximum stress (MPa)	350	2000	10000
New grips	Deflection (mm)	0.02	-	-
	Maximum stress (MPa)	140	700	4000

Table E.1: Numerical simulations results

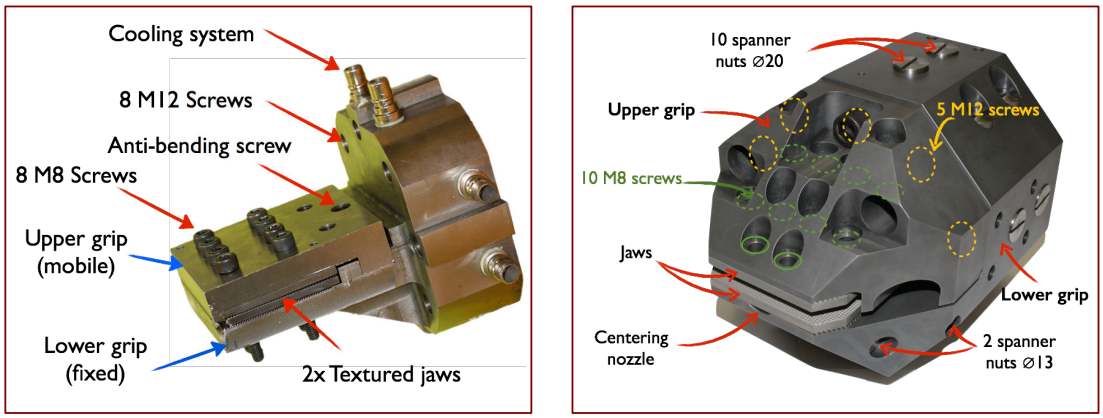

(a) (b)

Figure E.1: Component description: a) Former biaxial grips b) Current biaxial grips

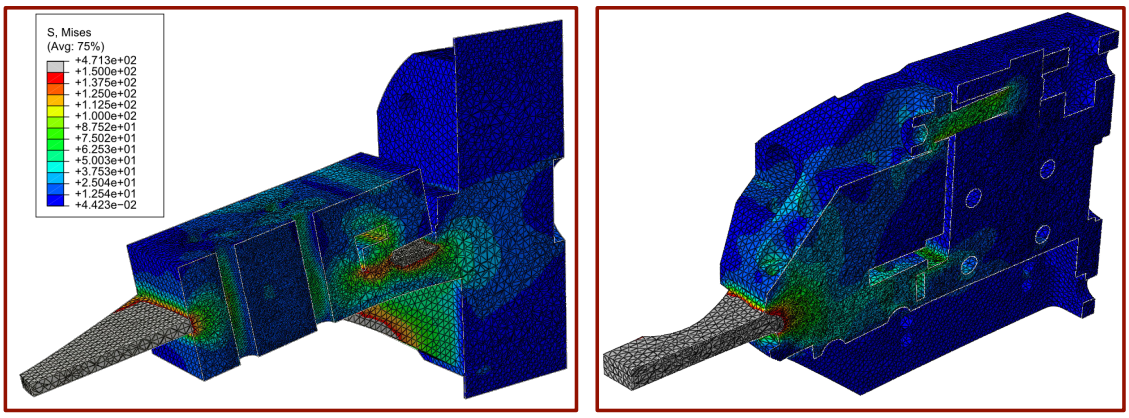

(a) (b)

Figure E.2: Axial tension simulations (100 kN) : a) Former biaxial grips b) Current biaxial grips

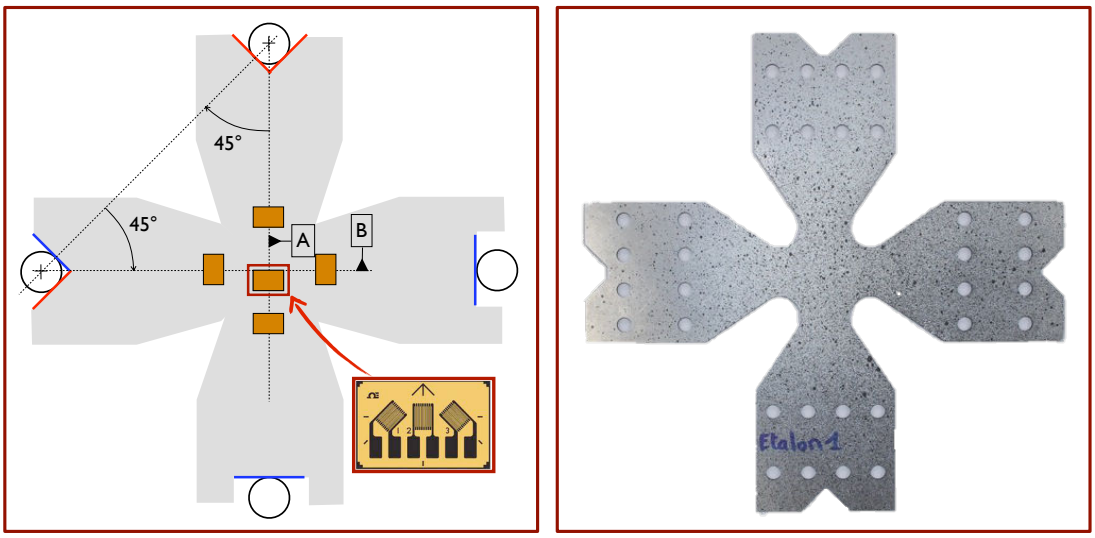

(a) (b)

Figure E.3: Test samples used for the experimental validation of the new grips a) Strain gauges b) Digital Image Correlation.

the sample, perpendicular to the axis of the grip. Even if the stresses are not realistic, they offer a qualitative comprehension of the gain in rigidity. Lastly, the systems were tested in the case of an accidental load perpendicular to the plane of the sample. A force of 500 kN was applied, representing the maximum effort of a pair of vertical actuators. This situation is unlikely to happen and is meant to show, as for the previous loading type, that the compact design and the compensation of the mobile part of the grips result in a better behavior of the grips. In the two accidental loading scenarios, the weakest link in the case of the new grips is the M12 screws and their corresponding nuts that are replaceable.

2 Experimental validation

The experimental validation consisted in a comparison between the behaviors of the two types of grips under common loads. Two test samples have been machined for these tests. The surface of the first sample was painted with a black and white speckle in order to post-treat the test results using digital image correlation (*Fig. E.3*). A second sample was equipped with 10 strain gauge rosettes (5 on each side) in order to obtain the mean strains on each arm and in the center of the sample. The term: ”flexural strain” used in the following is computed as the difference between the corresponding gauges on each side of the sample. Similarly, the term ”mean strain” is computed as the mean between the strains given by the corresponding gauge on each side. It also needs to be taken into consideration the fact that the thickness of the sample in the region of interest is 5 mm. LVDT sensors were also placed on the extremities of the grips, in order to directly verify their deflections.

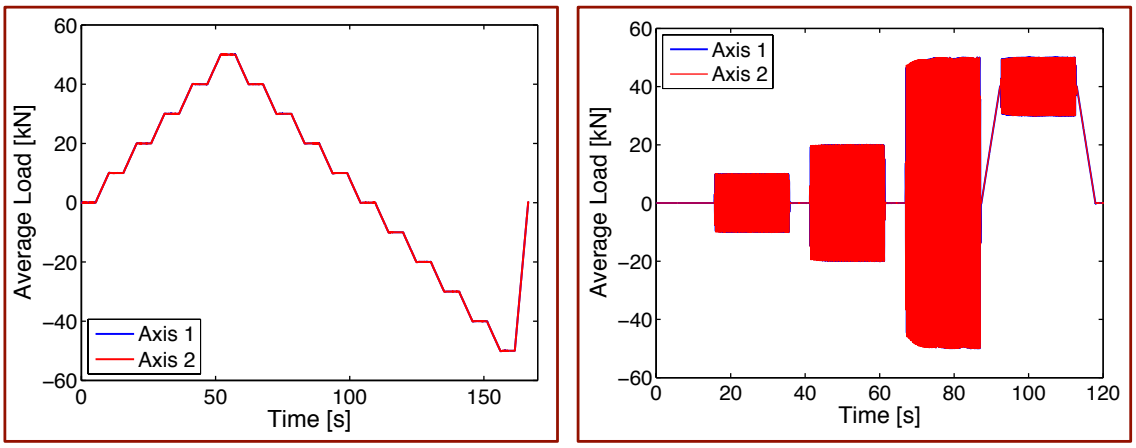

(a) (b)

Figure E.4: Loading types (a) Quasi-static (b) Cyclic loading at a given frequency (5 Hz).

In order to compare the behavior of the old and new grips and to analyze the influence of different loading parameters, the following tests were performed:

- Tightening / Untightening tests using the 3 measuring techniques: gauges, DIC & LVDT.
- Quasi-static tests (*Fig. E.4a*) at different load levels (10, 20, 50 kN)
- Cyclic tests (*Fig. E.4b*):
  - at different test ratios $R_F = \frac{F_{min}}{F_{max}}$:
    - $R_F = -1 : \pm 10, \pm 20, \pm 50$ kN
    - $R_F \neq -1 : 40 \pm 10$ kN
  - at different loading frequencies: 1, 5, 10, 20 Hz.

The main results of these influence studies are presented in the following.

2.1 Influence of the alignment on the static stress

The strains / static stresses introduced by the tightening and untightening of the sample have been studied. After performing a standard alignment, the influence of a cross-tightening of the 8 M8 screws has been studied on the old grips. *Fig. E.5* shows the amplitude of strains on the two sides of the sample during tightening (first on the left with M8 screws represented in green). The same procedure was applied to the new grips, first without the axial screws (5 M12 screws represented in orange in *Fig. E.5*). We obtain a value similar to that of the old grips, just slightly higher, given their increased rigidity. A second test was performed, where the axial screws were tightened in order to ensure the

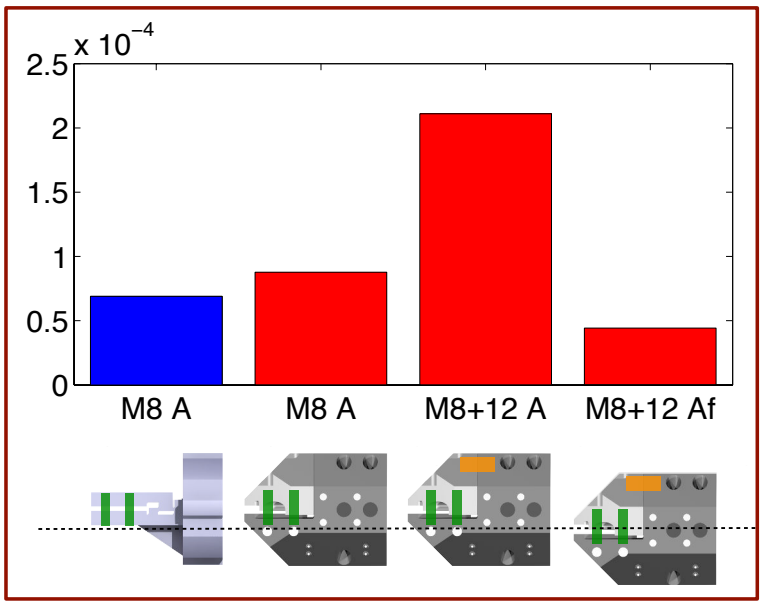

Figure E.5: Maximum flexural strains due to tightening, and depending on the alignment.

full rigidity of the new grip system. As expected, the result shows that a very rigid but poorly aligned system can have important static flexion effects on the sample. Finally, the case of a fine alignment (using the vertical positioning screws) followed by the tightening of the axial M12 screws was studied. It can be seen that this scenario (which is the one envisioned for the biaxial tests) causes less harm to the sample than the old grips while assuring *a priori* a higher rigidity.

2.2 Influence of the loading amplitude

By changing the loading amplitudes, quasi-proportional variations of the flexural strains and displacements are found. The values shown in *Fig. E.6* represent the mean value on all of the arms of the sample and the error bars show the dispersion of the measurement results of the gauges (*Fig. E.6a*) and the LVDTs respectively (*Fig. E.6b*). The improvement in the case of the new grips when compared to the old ones is clear both for the gauges and the LVDTs.

2.3 Influence of the loading frequency

The loading frequency doesn't show notable variations in the evolution of the mean strains. Nevertheless, the flexural strains vary during the validation test, without being able to see a clear tendency. These variations may seem important (up to $\approx$30%), but it needs to be noted that the flexural strains have very low values in the center of the sample (*Fig. E.7*) when using the new grips (less than 5% than the mean strain for $\pm$50 kN and less that 2.5% for $\pm$20 kN). Moreover, this sample has a thickness of 5 mm which makes

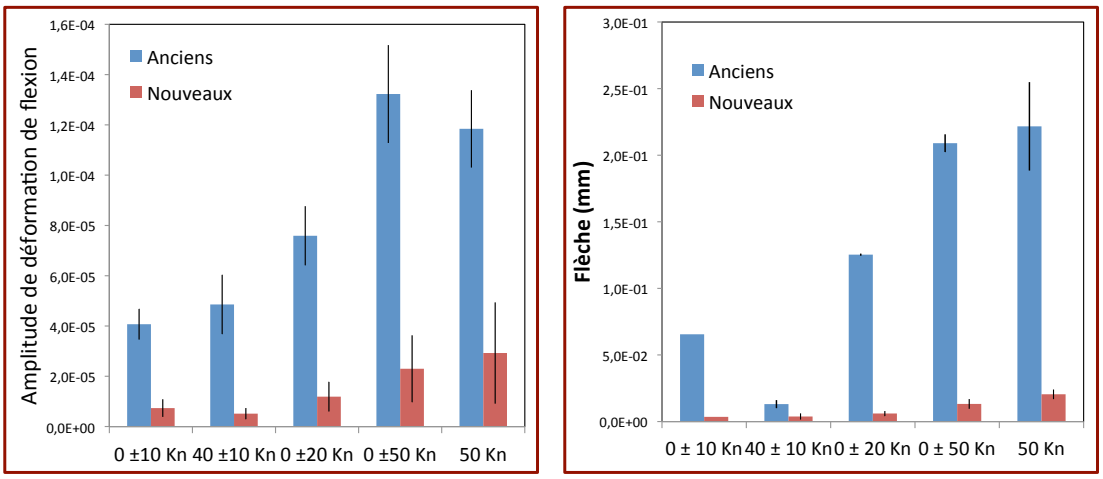

(a) (b)

Figure E.6: Influence of the loading amplitude (a) Gauges (b) LVDT.

this case all the more difficult to quantify, given that most biaxial samples tested in the machine have a thickness in the region of interest of 1 mm.

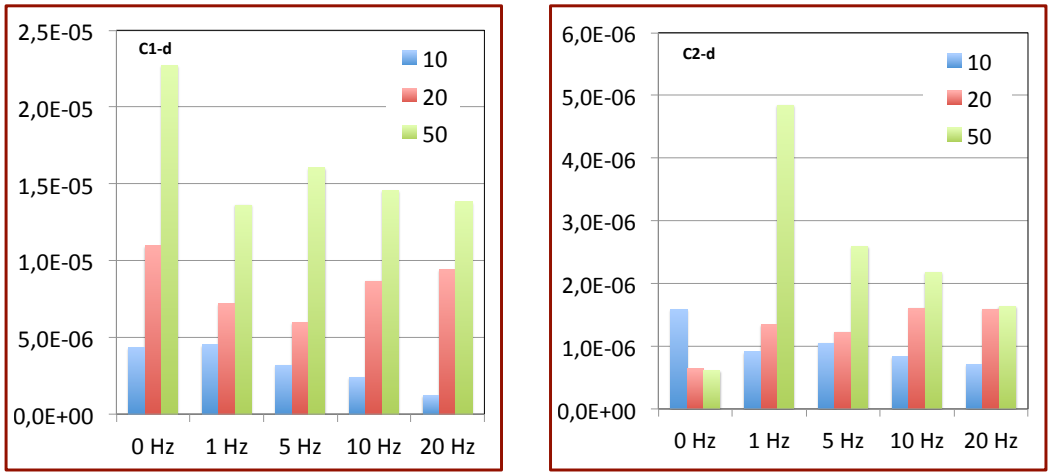

(a) (b)

Figure E.7: Influence of the loading frequency on the flexural strain in the center of the sample in direction: (a) 1 (b) 2.

Bibliography

Abdel-Karim, M. and Ohno, N. (2000). Kinematic hardening model suitable for ratchetting with steady-state. *International Journal of Plasticity*, 16(3):225–240.

Alexandre, F. (2004). *Aspects probabilistes et microstructuraux de l'amorçage des fissures de fatigue dans l'alliage INCO718*. PhD thesis, Ecole de Mines, Paris.

Allais, L., Bornert, M., Bretheau, T., and Caldemaison, D. (1994). Experimental characterization of the local strain field in a heterogeneous elastoplastic material. *Acta Metallurgica et materialia*, 42(11):3865–3880.

AMS (1965-2001). Aerospace material specification.

Andrews, J. and Ellison, E. (1973). A testing rig for cycling at high biaxial strains. 8:168–175.

Arcari, A. and Dowling, N. E. (2012). Modeling mean stress relaxation in variable amplitude loading for 7075-T6511 and 7249-T76511 high strength aluminum alloys. *International Journal of Fatigue*, 42(Supplement C):238–247.

Arcari, A., Vita, R. D., and Dowling, N. E. (2009). Mean stress relaxation during cyclic straining of high strength aluminum alloys. *International Journal of Fatigue*, 31(11):1742 – 1750. Fatigue Damage of Structural Materials VII.

Aubin, V. (2001). *Plasticité cyclique d'un acier inoxydable austeno-ferritique sous chargement biaxial non-proportionnel*. PhD thesis, Université des Sciences et Technologie de Lille.

Aubin, V., Quaegebeur, P., and Degallaix, S. (2003). Cyclic plasticity of a duplex stainless steel under non-proportional loading. *Materials Science and Engineering: A*, 346(1):208–215.

Augustins, L. (2014). *Dimensionnement à la fatigue thermomécanique de disques de frein automobiles en fonte à graphite lamellaire*. PhD thesis.

Avril, S., Bonnet, M., Bretelle, A.-S. S., Grédiac, M., Hild, F., Ienny, P., Latourte, F., Lemosse, D., Pagano, S., Pagnacco, E., and Pierron, F. (2008). Overview of Identification Methods of Mechanical Parameters Based on Full-field Measurements. *Experimental Mechanics*, 48(4):381–402.

Barbier, G. (2009). *Fatigue biaxiale à grand nombre de cycles : etude expérimentale et modèle d'endommagement à deux échelles probabiliste*. PhD thesis, EDSP.

Bari, S. and Hassan, T. (2001). Kinematic hardening rules in uncoupled modeling for multiaxial ratcheting simulation. *International Journal of Plasticity*, 17(7):885–905.

Barlat, F., Lege, D. J., and Brem, J. C. (1991). A six-component yield function for anisotropic materials. *International Journal of Plasticity*, 7(7):693 – 712.

Beaubier, B., Dufour, J. E., Hild, F., Roux, S., Lavernhe, S., and Lavernhe-Taillard, K. (2014). CAD-Based Calibration and Shape Measurement with StereoDIC - Principle and Application on Test and Industrial Parts. *Experimental Mechanics*, 54(3):329–341.

Becker, M. and Hackenberg, H.-P. (2011). A constitutive model for rate dependent and rate independent inelasticity. application to in718. *International Journal of Plasticity*, 27(4):596 – 619.

Bellett, D., Morel, F., Morel, A., and Lebrun, J.-L. (2011). A Biaxial Fatigue Specimen for Uniaxial Loading. *Strain*, 47(3):227–240.

Benallal, A. and Marquis, D. (1987). Constitutive equations for nonproportional cyclic elasto-viscoplasticity. *Journal of engineering materials and technology*, 109(4):326–336.

Berfield, T. A., Patel, J. K., Shimmin, R. G., Braun, P. V., Lambros, J., and Sottos, N. R. (2007). Micro- and Nanoscale Deformation Measurement of Surface and Internal Planes via Digital Image Correlation. *Experimental Mechanics*, 47(1):51–62.

Bergonnier, S., Hild, F., and Roux, S. (2007). Local anisotropy analysis for non-smooth images. *Pattern Recognition*, 40(2):544–556.

Besnard, G., Hild, F., and Roux, S. (2006a). "Finite-element" displacement fields analysis from digital images : Application to Portevin-Le Chatelier bands. *Experimental Mechanics*, 46(6):789–804.

Besnard, G., Hild, F., and Roux, S. (2006b). "Finite-Element" Displacement Fields Analysis from Digital Images: Application to Portevin-Le Châtelier Bands. *Experimental Mechanics*, 46(6):789–803.

Besson, J., Cailletaud, G., Chaboche, J.-L., and Forest, S. (2010). *Non-Linear Mechanics of Materials*, volume 33.

Boehler, J. P., Demmerle, S., and Koss, S. (1994). A new direct biaxial testing machine for anisotropic materials. *Experimental Mechanics*, 34(1):1–9.

Bonnand, V., Chaboche, J. L., Gomez, P., Kanouté, P., and Pacou, D. (2011). Investigation of multiaxial fatigue in the context of turboengine disc applications. *International Journal of Fatigue*, 33(8):1006–1016.

Bornert, M., Brémand, F., Doumalin, P., Dupré, J.-C., Fazzini, M., Grédiac, M., Hild, F., Mistou, S., Molimard, J., Orteu, J.-J., Robert, L., Surrel, Y., Vacher, P., and Wattrisse, B. (2009). Assessment of digital image correlation measurement errors: Methodology and results. *Experimental Mechanics*, 49(3):353–370.

Bouvet, C., Calloch, S., and Lexcellent, C. (2004). A phenomenological model for pseudoelasticity of shape memory alloys under multiaxial proportional and nonproportional loadings. *European Journal of Mechanics-A/Solids*, 23(1):37–61.

Broggiato, G. (2004). Adaptive image correlation technique for full-field strain measurement. pages 420–421.

Brown, M. W. and Miller, K. J. (1985). Mode i fatigue crack growth under biaxial stress at room and elevated temperature. In *Multiaxial fatigue*. ASTM International.

Buljac, A., Shakoor, M., Neggers, J., Bernacki, M., Bouchard, P.-O., Helfen, L., Morgeneyer, T. F., and Hild, F. (2017). Numerical validation framework for micromechanical simulations based on synchrotron 3d imaging. *Computational Mechanics*, 59(3):419–441.

Buljac, A., Taillandier-Thomas, T., Morgeneyer, T., Helfen, L., Roux, S., and Hild, F. (2015). Slant strained band development during flat to slant crack transition in aa 2198 t8 sheet: in situ 3d measurements. 200.

Burlet, H. and Cailletaud, G. (1986). Numerical techniques for cyclic plasticity at variable temperature. *Engineering Computations*, 3(2):143–153.

Burlet, H. and Cailletaud, G. (1987). Modeling of cyclic plasticity in finite element codes. *Int. Conf. on Constitutive Laws for Engineering Materials : Theory and Applications*, pages 1157–1164.

Calloch, S. (1997). *Essais triaxiaux non-proportionnels et ingénierie des modèles de plasticité cyclique*. LMT 1997 2. Laboratoire de mécanique et technologie, Cachan. Thèse de doctorat Mécanique, génie mécanique, génie civil Cachan, Ecole normale supérieure 1997.

Calloch, S., Dureisseix, D., and Hild, F. (2002). Identification de modèles de comportement de matériaux solides : utilisation d'essais et de calculs Identification de modèles de comportement de matériaux solides : utilisation d'essais et de calculs.

Calloch, S. and Marquis, D. (1997). Cyclic plasticity constitutive equations and triaxial tension experiments. In *Physics and Mechanics of Finite Plastic and Viscoplastic Deformation: Proceedings of Plasticity'97, the Sixth International Symposium on Plasticity and Its Current Applications*, page 343. Neat Press.

Calloch, S. and Marquis, D. (1999). Triaxial tension-compression tests for multiaxial cyclic plasticity. *International Journal of Plasticity*, 15(5):521–549.

Carpiuc, A. (2015). *Innovative tests for characterizing mixed-mode fracture of concrete: from pre-defined to interactive and hybrid tests*. PhD thesis, ENS-Cachan.

Cazacu, O. and Barlat, F. (2004). A criterion for description of anisotropy and yield differential effects in pressure-insensitive metals. *International Journal of Plasticity*, 20(11):2027–2045.

Chaboche, J. (1994). Modeling of ratchetting: evaluation of various approaches. *European journal of mechanics. A. Solids*, 13(4):501–518.

Chaboche, J. and Cailletaud, G. (1986). On the calculation of structures in cyclic plasticity or viscoplasticity. *Computers & Structures*, 23(1):23–31.

Chaboche, J., Dang Van, K., Cordier, G., and by Chaboche, J.L.; Dang Van, K.; Cordier, G. (1979). Modelization of the strain memory effect on the cyclic hardenning of 316 Stainless steel. *Structural mechanics in reactor technology*, L:13–17.

Chaboche, J. L. (1989a). A new constitutive framework to describe limited ratchetting effects. In *Plasticity'89, Tsu, Japan, A. S. Khan and M. Tokuda eds, Pergamon*, pages 211 – 214.

Chaboche, J. L. (1989b). Constitutive equations for cyclic plasticity and cyclic viscoplasticity. *International Journal of Plasticity*, 5(3):247–302.

Chaboche, J. L. (1989c). Un nouveau schéma d'écrouissage cinématique à surfaces mémoires discrètes. *Chatillon: ONERA*, pages 49–69.

Chaboche, J. L. (1991). On some modifications of kinematic hardening to improve the description of ratchetting effects. *International Journal of Plasticity*, 7(7):661–678.

Chaboche, J. L. (2008). A review of some plasticity and viscoplasticity constitutive theories. *International Journal of Plasticity*, 24(10):1642–1693.

Chaboche, J. L. and Jung, O. (1997). Application of a kinematic hardening viscoplasticity model with thresholds to the residual stress relaxation. *International Journal of Plasticity*, 13(10):785–807.

Chaboche, J.-L., Kanouté, P., and Azzouz, F. (2012). Cyclic inelastic constitutive equations and their impact on the fatigue life predictions. *International Journal of Plasticity*, 35:44–66.

Chaboche, J. L., Nouailhas, D., Pacou, D., and Paulmier, P. (1991). Modeling of the cyclic response and ratchetting effects on inconel-718 alloy. *European Journal of Mechanics - A/Solids*, 10(1):101–121.

Chaboche, J. L. and Rousselier, G. (1983). On the plastic and viscoplastic constitutive equations–part ii: Application of internal variable concepts to the 316 stainless steel. 105.

Charbal, A. (2017). Mesure de champs thermomécaniques pour l'étude de la fatigue par chocs thermiques.

Chen, D. J., Chiang, F. P., Tan, Y. S., and Don, H. S. (1993). Digital speckle-displacement measurement using a complex spectrum method. *Appl. Opt.*, 32(11):1839–1849.

Chu, T. C., Ranson, W. F., and Sutton, M. A. (1985). Applications of digital-image-correlation techniques to experimental mechanics. *Experimental Mechanics*, 25(3):232–244.

Clavel, M. (1980). *Fatigue plastique et fissuration de deux alliages durcis par des précipités cohérents. Etude comparative des mécanismes*. PhD thesis, Université de Poitiers UER-ENSMA.

Cleveland, R. M. and Ghosh, A. K. (2002). Inelastic effects on springback in metals. 18:769–785.

Cognard, J.-Y., Feuardent, V., and Virely, J.-M. (1997). *Optimisation of a Structure for Biaxial Mechanical Tests*, pages 495–504. Springer Netherlands, Dordrecht.

Connolley, T., Reed, P. A. S., and Starink, M. J. (2003). Short crack initiation and growth at 600°C in notched specimens of Inconel718. *Materials Science and Engineering: A*, 340(1–2):139–154.

Contesti, E. and Cailletaud, G. (1989). Description of creep-plasticity interaction with non-unified constitutive equations: application to an austenitic stainless steel. *Nuclear Engineering and Design*, 116(3):265–280.

Cozar, R. and Pineau, A. (1973). Morphology of γ' and γ'' precipitates and thermal stability of inconel 718 type alloys. *Metallurgical Transactions*, 4(1):47–59.

Davis, J. R. (2004). *Tensile Testing*. 2nd edition edition.

de Souza Campos, E. R. F., Desmorat, R., and Malcher, L. (2017). *Non saturating kinematic hardening law coupled with damage evolution for fatigue*.

Delahay, T. and Palinluc, T. (2006). Estimation of the fatigue strength distribution in high–cycle multiaxial fatigue taking into account the stress–strain gradient effect. *International Journal of Fatigue*, 28(5-6):474–484.

Delobelle, P., Robinet, P., and Bocher, L. (1995). Experimental study and phenomenological modelization of ratchet under uniaxial and biaxial loading on an austenitic stainless steel. *International Journal of Plasticity*, 11(4):295–330.

Demmerle, S. and Boehler, J. P. (1993). Optimal design of biaxial tensile cruciform specimens. *Journal of the Mechanics and Physics of Solids*, 41(1):143–181.

Desmars, B., Peres, P., Piron, E., Mistou, S., and Karama, M. (2004). Application de la méthode de stéréo-corrélation d'images à la caractérisation des élastomères en grandes déformations. *Photomécanique*, pages 217–224.

Desmorat, R. (2010a). Non-saturating nonlinear kinematic hardening laws. *Comptes Rendus Mécanique*, 338(3):146–151.

Desmorat, R. (2010b). Non-saturating nonlinear kinematic hardening laws. *Comptes Rendus Mécanique*, 338(3):146–151.

Diaz, F. A., Patterson, E. A., Tomlinson, R. A., and Yates, J. R. (2004). Measuring stress intensity factors during fatigue crack growth using thermoelasticity. *Fatigue and Fracture of Engineering Materials and Structures*, 27(7):571–583.

Dietmann, H., Bhongbhibhat, T., and Schmid, A. (1989). Multiaxial fatigue behaviour of steels under in-phase and out-of-phase loading including different wave forms and frequencies. In *ICBMFF3*.

Doudard, C., Poncelet, M., Calloch, S., Boue, C., Hild, F., and Galtier, A. (2007). Determination of an HCF criterion by thermal measurements under biaxial cyclic loading. *International Journal of Fatigue*, 29(4):748–757.

Dufour, J.-E. (2015). *Shape, displacement and mechanical properties from isogeometric stereo-correlation.* Theses, Université Paris-Saclay.

Dufour, J.-E., Beaubier, B., Hild, F., and Roux, S. (2015). Cad-based displacement measurements with stereo-dic. *Experimental Mechanics*, 55(9):1657–1668.

Fang, D. and Berkovits, A. (1994). Mean stress models for low-cycle fatigue of a nickel-base superalloy. *International Journal of Fatigue*, 16(6):429–437.

Fayman, Y. C. (1987). Microstructural characterization and elemental partitioning in a direct-aged superalloy (DA 718). *Materials Science and Engineering*, 92:159–171.

Fayolle, X., Calloch, S., and Hild, F. (2007). Controlling testing machines with digital image correlation. *Experimental Techniques*, 31(3):57–63. WOS.

Fayolle, X., Calloch, S., and Hild, F. (2008). Contrôler une machine d'essai avec une caméra. *Mécanique & Industries*, 9(5):447–457. WOS.

Fayolle, X. and Hild, F. (2014). Controlling Stress Intensity Factor Histories with Digital Images. *Experimental Mechanics*, 54(2):305–314.

Feyel, F., Calloch, S., Marquis, D., and Cailletaud, G. (1997). F.E. computation of a triaxial specimen using a polycrystalline model. *Computational Materials Science*, 9(1-2):141–157.

Fournier, D. (1977). *Etude du comportement en fatigue oligocyclique d'un alliage base nickel par des précipités déformables*. PhD thesis, Université de Poitiers.

Fournier, D. and Pineau, A. (1977). Low cycle fatigue behavior of inconel 718 at 298 K and 823 K. *Metallurgical Transactions A*, 8(7):1095–1105.

François, M. (2001). A plasticity model with yield surface distortion for non proportional loading. *International Journal of Plasticity*, 17(5):703–717. cited By 72.

Frederick, C. and Armstrong, P. (1966). A mathematical representation of the multiaxial Bauchinger effect.

Freed, A. D. and Walker, K. P. (1993). Viscoplasticity with creep and plasticity bounds. *International Journal of Plasticity*, 9(2):213–242.

Frémy, F. (2012). Fissuration par fatigue en mode mixte I+II+III non proportionnel dans l'acier 316L : approche expérimentale et modélisation des effets de la plasticité.

Gaborit, P. (2015). *Unification des modèles d'endommagement de type Lemaitre, pour la fatigue LCF/HCF, multiaxiale et aléatoire*. PhD thesis.

Gao, M., Harlow, G., P. Wei, R., and Chen, S. (1996). Preferential coarsening of γ'' precipitates in inconel 718 during creep. 27:3391–3398.

Geiger, M., Huß nätter, W., and Merklein, M. (2005). Specimen for a novel concept of the biaxial tension test. *Journal of Materials Processing Technology*, 167(2-3):177–183.

Gough, H. and Pollard, H. (1935). The strength of metals under combined alternating stresses. *Proceedings of the institution of mechanical engineers*, 131(1):3–103.

Grédiac, M. and Hild, F. (2012). *Full-Field Measurements and Identification in Solid Mechanics*. ISTE / Wiley.

Guery, A. (2014). *Développement d'une méthode de corrélation d'images numériques adaptée aux mesures cinématiques dans les polycristaux : application à l'identification de paramètres de lois de plasticité cristalline*. PhD thesis.

Gustafsson, D., Moverare, J. J., Simonsson, K., and Sjöström, S. (2011). Modeling of the Constitutive Behavior of Inconel 718 at Intermediate Temperatures. *Journal of Engineering for Gas Turbines and Power*, 133(9):094501.

Halilovič, M., Vrh, M., and Štok, B. (2008). Prediction of elastic strain recovery of a formed steel sheet considering stiffness degradation. *Meccanica*, 44(3):321.

Hannon, A. and Tiernan, P. (2008). A review of planar biaxial tensile test systems for sheet metal. *Journal of Materials Processing Technology*, 198(1-3):1–13.

Hassan, T. and Kyriakides, S. (1992). Ratcheting in cyclic plasticity, part I: Uniaxial behavior. *International Journal of Plasticity*, 8(1):91–116.

Hayhurst, D. (1973). A biaxial-tension creep-rupture testing machine. *Journal of Strain Analysis*, 8(2):119–123.

Helling, D. E., Miller, A. K., and Stout, M. G. (1986). An Experimental Investigation of the Yield Loci of 1100-0 Aluminum, 70:30 Brass, and an Overaged 2024 Aluminum Alloy After Various Prestrains. *Journal of Engineering Materials and Technology*, 108(4):313–320.

Hild, F. and Roux, S. (2006). Measuring stress intensity factors with a camera : integrated digital image correlation (I–DIC). *Comptes–Rendus Mécanique*, 334(1):8–12.

Hild, F. and Roux, S. (2012a). Comparison of local and global approaches to digital image correlation. *Experimental Mechanics*, 52(9):1503–1519.

Hild, F. and Roux, S. (2012b). *Optical Methods for Solid Mechanics. Section Digital Image Correlation.* Wiley-VCH, Berlin (Germany).

Hill, R. (1948). A theory of the yielding and plastic flow of anisotropic metals. *Proceedings of the Royal Society of London A: Mathematical, Physical and Engineering Sciences*, 193(1033):281–297.

Hill, R. (1956). *The Mathematical Theory of Plasticity*. Oxford engineering science series. Clarendon Press.

Hoffmann, K. (1989). An Introduction to Measurements using Strain Gages. *Hottinger Baldwin Messtechnik GmbH*, page 257.

Hopperstad, O. S., Langseth, M., and Remseth, S. (1995). Cyclic stress-strain behaviour of alloy AA6060, part I: Uniaxial experiments and modelling. *International Journal of Plasticity*, 11(6):725–739.

Hu, W. (2005). An orthotropic yield criterion in a 3-d general stress state. *International Journal of Plasticity*, 21(9):1771–1796.

Hu, W., Wang, C., and Barter, S. (1999). Analysis of cyclic mean stress relaxation and strain ratchetting behaviour of aluminium 7050. page 39.

Itoh, T., Sakane, M., and Ohnami, M. (1994). High temperature multiaxial low cycle fatigue of cruciform specimen. 116:90–96.

Iyer, S. K. and Lissenden, C. J. (2003). Multiaxial constitutive model accounting for the strength-differential in Inconel 718. *International Journal of Plasticity*, 19(12):2055–2081.

James, M. N., Pacey, M. N., Wei, L. W., and Patterson, E. A. (2003). Characterisation of plasticity-induced closure - crack flank contact force versus plastic enclave. *Engineering Fracture Mechanics*, 70(17):2473–2487.

Jhansale, H. and Topper, T. (1971). Engineering analysis of the inelastic stress response of a structural metal under variable cyclic strains. 519:246–270.

Kallmeyer, A. R., Krgo, A., and Kurath, P. (2002). Evaluation of Multiaxial Fatigue Life Prediction Methodologies for Ti-6Al-4V. *Journal of Engineering Materials and Technology*, 124(2):229.

Kang, G., Dong, Y., Wang, H., Liu, Y., and Cheng, X. (2010). Dislocation evolution in 316L stainless steel subjected to uniaxial ratchetting deformation. *Materials Science and Engineering: A*, 527(21):5952–5961.

Kelly, D. (1976). Problems in creep testing under biaxial stress systems. *The Journal of Strain Analysis for Engineering Design*, 11(1):1–6.

Köhn, A., Drexl, J., Ritter, F., König, M., and Peitgen, H. O. (2006). *GPU Accelerated Image Registration in Two and Three Dimensions*, pages 261–265. Springer Berlin Heidelberg, Berlin, Heidelberg.

Korth, G. E. (1991). Effects of various parameters on the fatigue life of Alloy 718. United States.

Koutiri, I. (2011). *Effet des fortes contraintes hydrostatiques sur la tenue en fatigue des matériaux métalliques*. PhD thesis, Arts et Métiers ParisTech.

Kulawinski, D., Ackermann, S., Glage, A., Henkel, S., and Biermann, H. (2011a). Biaxial Low Cycle Fatigue Behavior and Martensite Formation of a Metastable Austenitic Cast TRIP Steel Under Proportional Loading. *Steel research international*, 82(9):1141–1148.

Kulawinski, D., Nagel, K., Henkel, S., Hübner, P., Fischer, H., Kuna, M., and Biermann, H. (2011b). Characterization of stress–strain behavior of a cast TRIP steel under different biaxial planar load ratios. *Engineering Fracture Mechanics*, 78(8):1684–1695.

Lagoda, T., Macha, E., and Bedkowski, W. (1999). A critical plane approach based on energy concepts: application to biaxial random tension-compression high-cycle fatigue regime. *International Journal of Fatigue*, 21(5):431–443.

Landersheim, V., Bruder, T., and Hanselka, H. (2011). Approximation of mean stress relaxation by numerical simulation using the Jiang model and extrapolation of results. *Procedia Engineering*, 10:595–600.

Landgraf, R. W. and Chernenkoff, R. A. (1988). Residual stress effects on fatigue of surface processed steels. In *Analytical and experimental methods for residual stress effects in fatigue*. ASTM International.

Lasserre, S. and Froustey, C. (1992). Multiaxial fatigue of steel–testing out of phase and in blocks: validity and applicability of some criteria. *International Journal of Fatigue*, 14(2):113–120.

Le Flohic, J., Parpoil, V., Bouissou, S., Poncelet, M., and Leclerc, H. (2014). A 3D Displacement Control by Digital Image Correlation for the Multiaxial Testing of Materials with a Stewart Platform. *Experimental Mechanics*.

Leclerc, H. (2007). Plateforme metil : optimisations et facilités liées à la génération de code. In *8e Colloque National en Calcul des Structures.*

Leclerc, H., Périé, J., Roux, S., and Hild, F. (2009). Integrated Digital Image Correlation for the Identification of Mechanical Properties. *Computer Vision/Computer Graphics CollaborationTechniques*, 5496:161–171.

Lefebvre, D., Chebl, C., Thibodeau, L., and Khazzari, E. (1983). A high-strain biaxial-testing rig for thin-walled tubes under axial load and pressure. *Experimental Mechanics*, 23(4):384–392.

Lemaitre, J. and Chaboche, J. L. (1985). *Mechanics of Solid Materials*. Cambridge University Press.

Lemaitre, J., Chaboche, J.-L., Benallal, A., and Desmorat, R. (2009). Mécanique des matériaux solides-3eme édition.

Lemaitre, J. and Desmorat, R. (2005). *Engineering damage mechanics: ductile, creep, fatigue and brittle failures*. Springer Science & Business Media.

Lemaitre, J. and Dufailly, J. (1987). Damage measurements. *Engineering Fracture Mechanics*, 28(5-6):643–661.

Levieil, B. (2016). *Taking residual stresses into account using simplified methods in low cycle fatigue*. Theses, Université de Bretagne occidentale - Brest.

Li, E. B., Tieu, A. K., and Yuen, W. Y. D. (2003). Application of digital image correlation technique to dynamic measurement of the velocity field in the deformation zone in cold rolling. *Optics and Lasers in Engineering*, 39(4):479–488.

Lucas, B. D. and Kanade, T. (1981). An iterative image registration technique with an application to stereo vision.

Lukáš, P. and Kunz, L. (1989). Effect of mean stress on cyclic stress-strain response and high cycle fatigue life. *International Journal of Fatigue*, 11(1):55–58.

Makinde, A., Thibodeau, L., and Neale, K. W. (1992a). Development of an apparatus for biaxial testing using cruciform specimens. *Experimental Mechanics*, 32(2):138–144.

Makinde, A., Thibodeau, L., Neale, K. W., and Lefebvre, D. (1992b). Design of a biaxial extensometer for measuring strains in cruciform specimens. *Experimental Mechanics*, 32(2):132–137.

Makris, A., Vandenbergh, T., Ramault, C., Hemelrijck, D., Lamkanfi, E., and Van Paepegem, W. (2010). Shape optimisation of a biaxially loaded cruciform specimen. *Polymer Testing*, 29:216–223.

Manonukul, A., Dunne, F. P. E., Knowles, D., and Williams, S. (2005). Multiaxial creep and cyclic plasticity in nickel-base superalloy C263. *International Journal of Plasticity*, 21(1):1–20.

Marquis, D. (1989). *Phenomenologie et thermodynamique : couplages entre thermoelasticite, plasticite, vieillissement et endommagement*. PhD thesis.

Mathieu, F. (2013). *Analyse de la tenue mécanique d'un liner en titane : Apport des mesures de champs cinématiques*. PhD thesis, ENS Cachan.

Mathieu, F. and Hild, F. (2013). Analyse de l'amorçage de fissures dans une tôle fine en fatigue oligocyclique par mesures de champs cinématiques. pages 1–6.

McDiarmid, D. L. (1985). The effects of mean stress and stress concentration on fatigue under combined bending and twisting. *Fatigue & Fracture of Engineering Materials and Structures*, 8(1):1–12.

Mcdowell, D. L. (1995). STRESS STATE DEPENDENCE OF CYCLIC RATCHETTING BEHAVIOR OF TWO RAIL STEELS. I(4):397–421.

Mendiguren, J., Cortés, F., Galdos, L., and Berveiller, S. (2013). Strain path's influence on the elastic behaviour of the TRIP 700 steel. *Materials Science and Engineering: A*, 560:433–438.

Mises, R. v. (1913). Mechanik der festen körper im plastisch-deformablen zustand. *Nachrichten von der Gesellschaft der Wissenschaften zu Göttingen, Mathematisch-Physikalische Klasse*, 1913(4):582–592.

Moosbrugger, J. C. and McDowell, D. L. (1990). A rate-dependent bounding surface model with a generalized image point for cyclic nonproportional viscoplasticity. *Journal of the Mechanics and Physics of Solids*, 38(5):627–656.

Mróz, Z. (1967). On the description of anisotropic workhardening. *Journal of the Mechanics and Physics of Solids*, 15(3):163–175.

Mróz, Z. and Rodzik, P. (1996). On multisurface and integral description of anisotropic hardening evolution of metals. *European journal of mechanics. A. Solids*, 15(1):1–28.

Mücke, R. and Bernhardi, O.-E. (2006). On temperature rate terms for viscoplastic constitutive models with applications to high temperature materials. *Computer Methods in Applied Mechanics and Engineering*, 195(19):2411–2431.

Nierenberger, M., Poncelet, M., Pattofatto, S., Hamouche, A., Raka, B., and Virely, J. M. (2012). Multiaxial testing of materials using a stewart platform: Case study of the Nooru-Mohamed test. *Experimental Techniques*, 38(2):74–83.

Nouailhas, D. (1989). Unified modelling of cyclic viscoplasticity: Application to austenitic stainless steels. *International Journal of Plasticity*, 5(5):501–520.

Nouailhas, D., Cailletaud, G., Policella, H., Marquis, D., Dufailly, J., Lieurade, H., Ribes, A., and Bollinger, E. (1985). On the description of cyclic hardening and initial cold working. *Engineering Fracture Mechanics*, 21(4):887–895.

Nouailhas, D., Policella, H., and Kaczmarek, H. (1982). On the description of cyclic hardening under complex loading histories. pages 9–16.

Ohno, N. (1982). A Constitutive Model of Cyclic Plasticity With a Nonhardening Strain Region. *Journal of Applied Mechanics*, 49(4):721–727.

Ohno, N. (1990). Recent Topics in Constitutive Modeling of Cyclic Plasticity and Viscoplasticity. *Applied Mechanics Reviews*, 43(11):283–295.

Ohno, N. (1998). Constitutive modeling of cyclic plasticity with emphasis on ratchetting. *International Journal of Mechanical Sciences*, 40(2):251–261.

Ohno, N. and Abdel-Karim, M. (2000). Uniaxial Ratchetting of 316FR Steel at Room Temperature – Part II: Constitutive Modeling and Simulation. *Journal of Engineering Materials and Technology*, 122(1):35.

Ohno, N. and Kachi, Y. (1986). A constitutive model of cyclic plasticity for nonlinear hardening materials. *Journal of Applied Mechanics*, 53(2):395–403.

Ohno, N. and Wang, J. D. (1993a). Kinematic hardening rules with critical state of dynamic recovery, part I: formulation and basic features for ratchetting behavior. *International Journal of Plasticity*, 9(3):375–390.

Ohno, N. and Wang, J. D. (1993b). Kinematic hardening rules with critical state of dynamic recovery, part II: Application to experiments of ratchetting behavior. *International Journal of Plasticity*, 9(3):391–403.

Papadopoulos, I. V. (1987). *Fatigue polycyclique des métaux: une nouvelle approche*. PhD thesis, Ecole Nationale des Ponts et Chaussées.

Pascoe, K. and De Villiers, J. (1967). Low cycle fatigue of steels under biaxial straining. *Journal of Strain analysis*, 2(2):117–126.

Paul, S. K., Sivaprasad, S., Dhar, S., and Tarafder, S. (2010). True stress control asymmetric cyclic plastic behavior in SA333 C–Mn steel. *International Journal of Pressure Vessels and Piping*, 87(8):440–446.

Pelissier-Tanon, A., Bernard, J. L., Amzallag, C., and Rabbe, P. (1980). Evaluation of the resistance of type 316 stainless steel against progressive deformation. In *Low-Cycle Fatigue and Life Prediction. ASTM STP, vol 770*.

Périé, J.-N., Calloch, S., Cluzel, C., and Hild, F. (2002). Analysis of a multiaxial test on a C/C composite by using digital image correlation and a damage model. *Experimental Mechanics*, 42(3):318–328.

Périé, J. N., Leclerc, H., Roux, S., and Hild, F. (2009). Digital image correlation and biaxial test on composite material for anisotropic damage law identification. *International Journal of Solids and Structures*, 46(11–12):2388–2396.

Phillips, A. and Lee, C.-W. (1979). Yield surfaces and loading surfaces. Experiments and recommendations. *International Journal of Solids and Structures*, 15(9):715–729.

Piegl, L. and Tiller, W. (1997). *The NURBS Book. Monographs in Visual Communication.*, volume 335. Springer, 2nd edition edition.

Pierré, J.-E., Passieux, J.-C., and Périé, J.-N. (2017). Finite element stereo digital image correlation: Framework and mechanical regularization. *Experimental Mechanics*, 57(3):443–456.

Plenard, E. and Fromont, C. (1988). Some mechanical properties relevant to non-linear elasticity materials. In Yan, M., Zhang, S., and Zheng, Z., editors, *Mechanical Behaviour of Materials V*, pages 765 – 771. Pergamon, Oxford.

Poncelet, M., Barbier, G., Raka, B., Courtin, S., Desmorat, R., Le-Roux, J. C. C., and Vincent, L. (2010). Biaxial High Cycle Fatigue of a type 304L stainless steel: Cyclic strains and crack initiation detection by digital image correlation. *European Journal of Mechanics - A/Solids*, 29(5):810–825.

Poncelet, M., Gaborit, P., Prisacari, I., and Raka, B. (2014). Conception de mors de bitraction pour la machine Astree. Technical report, LMT-ENS Cachan, Cachan.

Ponnelle, S. (2001). *Propagation des fissures par fatigue a haute temperature dans l'inconel 718 : effets de microstructure et de chargements complexes*. PhD thesis.

Portier, L., Calloch, S., Marquis, D., and Geyer, P. (2000). Ratchetting under tension–torsion loadings: experiments and modelling. *International Journal of Plasticity*, 16(3):303–335.

Prager, W. (1949). Recent developments in the mathematical theory of plasticity. *Journal of Applied Physics*, 20(3):235–241.

Raghava, R., Caddell, R. M., and Yeh, G. S. (1973). The macroscopic yield behaviour of polymers. *Journal of Materials Science*, 8(2):225–232.

Réthoré, J., Roux, S., and Hild, F. (2007). From pictures to extended finite elements: extended digital image correlation (X-DIC). *Comptes Rendus Mécanique*, 335(3):131–137.

Revaud, M. (2013). *Optimisation métallurgique du superalliage à base de Nickel 718Plus*. PhD thesis.

Rezai-Aria, F., François, M., and Rémy, L. (1988). Thermal fatigue of MAR-M509 Superalloy – I. The influence of specimen geometry. *Fatigue & Fracture of Engineering Materials & Structures*, 11(4):277–289.

Rousset, M. (1985). *Surface seuil de plasticité: détermination automatique et modélisation*.

Ruggles, M. B. and Krempl, E. (1990). The interaction of cyclic hardening and ratchetting for AISI type 304 stainless steel at room temperature–I. Experiments. *Journal of the Mechanics and Physics of Solids*, 38(4):575–585.

Rupil, J. (2012). *Multifissuration en fatigue uniaxiale et biaxiale de l'acier inoxydable 304L*. PhD thesis, EDSP - ENS Cachan.

Sadriji, B., Raka, B., Brugier, F., Guilhem, Y., and Pommier, S. (2016). Effect of T-stress on a Nickel base superalloy under mode I fatigue crack propagation. International Conference on Fatigue Damage of Structural Materials XI (FATDXI). Poster.

Schreier, H. W., Braasch, J. R., and Sutton, M. A. (2000). Systematic errors in digital image correlation caused by intensity interpolation. *Optical engineering*, 39(11):2915–2921.

Schreier, H. W. and Sutton, M. A. (2002). Systematic errors in digital image correlation due to undermatched subset shape functions. *Experimental Mechanics*, 42(3):303–310.

Schwartz, J. (2012). Modélisation procédés de forge n IBGMM 00476. Technical report.

Selva, P., Lorrain, B., Alexis, J., Seror, A., Longuet, A., Mary, C., and Denard, F. (2017). Low cycle biaxial fatigue behavior of direct aged Nickel-based 718 superalloy.

Sermage, J. P. (1998). *Fatigue thermique multiaxiale à température variable*. LMT (Cachan). Laboratoire de m{é}canique et technologie.

Shenoy, M. M., McDowell, D. L., and Neu, R. W. (2006). Transversely isotropic viscoplasticity model for a directionally solidified Ni-base superalloy. *International Journal of Plasticity*, 22(12):2301–2326.

Shiratori, E. and Ikegami, K. (1968). Experimental study of the subsequent yield surface by using cross-shaped specimens. *Journal of the Mechanics and Physics of Solids*, 16(6):373–394.

Shiratori, E., Ikegami, K., and Yoshida, F. (1979). Analysis of stress-strain relations by use of an anisotropic hardening plastic potential. *Journal of the Mechanics and Physics of Solids*, 27(3):213–229.

Sines, G. (1961). The Prediction of Fatigue Fracture under Combined Stresses at Stress Concentrations. *Bulletin of JSME*, 4(15):443–453.

Singh, J., Sundararaman, M., Mukhopadhyay, P., and Prabhu, N. (2003). Effect of ternary nb additions on the stability of the d022 structure of the ni3v phase. *Scripta Materialia*, 48(3):261 – 267.

Soulé de Lafont, M.-F., Longuet, A., and Mary, C. (2015). Loi de Comportement et Critère de durée de vie pour l'Inconel 718. Technical report.

Sun, L. and Wagoner, R. (2011). Complex unloading behavior: Nature of the deformation and its consistent constitutive representation. *International Journal of Plasticity*, 27(7):1126–1144.

Sun, W. R., Guo, S. R., Lu, D. Z., and Hu, Z. Q. (1997). Effect of phosphorus on the microstructure and stress rupture properties in an fe-ni-cr base superalloy. *Metallurgical and Materials Transactions A*, 28(3):649–654.

Sutton, M., Wolters, W., Peters, W., Ranson, W., and McNeill, S. (1983a). Determination of displacements using an improved digital correlation method. *Image and Vision Computing*, 1(3):133–139.

Sutton, M. A., Orteu, J. J., and Schreier, H. W. (2009). *Image correlation for shape, motion and deformation measurements : Basic Concepts, Theory and Applications*. Springer.

Sutton, M. A., Wolters, W. J., Peters, W. H., Ranson, W. F., and McNeill, S. R. (1983b). Determination of displacements using an improved digital correlation method. *Image Vis. Comput.*, 1(3):133–139.

Taillandier-Thomas, T., Roux, S., Morgeneyer, T. F., and Hild, F. (2014). Localized strain field measurement on laminography data with mechanical regularization. *Nuclear Instruments and Methods in Physics Research Section B: Beam Interactions with Materials and Atoms*, 324(Supplement C):70 – 79. 1st International Conference on Tomography of Materials and Structures.

Taleb, L. and Hauet, A. (2009). Multiscale experimental investigations about the cyclic behavior of the 304L SS. *International Journal of Plasticity*, 25(7):1359–1385.

Tomicevic, Z. (2015). Identification of the mechanical properties of nodular graphite cast iron via multiaxial tests.

Tomicevic, Z., Hild, F., and Roux, S. (2013). Mechanincs-Aided Digital Image Correlation. *Journal of Strain Analysis for Engineering Design*, 48(1):330–343.

Tomičević, Z., Roux, S., and Hild, F. (2016). Evaluation of fatigue crack network growth in cast iron for different biaxial loading paths via full-field measurements. *International Journal of Fatigue*, 92(Part 1):281–303.

Tresca, H. (1864). Memoir on the flow of solid bodies under strong pressure. *Comptes Rendus Acad. Sci. Paris*, 59.

Triconnet, K., Derrien, K., Hild, F., and Baptiste, D. (2009). Parameter choice for optimized digital image correlation. *Optics and Lasers in Engineering*, 47(6):728 – 737.

Valanis, K. (1978). Fundamental consequences of a new intrinsic time measure. plasticity as a limit of the endochronic theory. 32:68.

Vincent, L., Calloch, S., and Marquis, D. (2004). A general cyclic plasticity model taking into account yield surface distortion for multiaxial ratchetting. *International Journal of Plasticity*, 20(10):1817–1850.

Watanabe, O. and Atluri, S. N. (1986). Constitutive modeling of cyclic plasticity and creep, using an internal time concept. *International Journal of Plasticity*, 2(2):107–134.

Wehner, T. and Fatemi, A. (1991). Effects of mean stress on fatigue behaviour of a hardened carbon steel. *International Journal of Fatigue*, 13(3):241 – 248.

Wilson, I. and White, D. (1971). Cruciform specimens for biaxial fatigue tests: An investigation using finite-element analysis and photoelastic-coating techniques. *Journal of Strain Analysis*, 6(1):27–37.

Worthem, D. W., Altstetter, C. J., Robertson, I. M., and Socie, D. F. (1989). Cyclic deformation and damage structure in inconel 718. In *ICBMFF2*.

Wu, H. C. and Yeh, W. C. (1991). On the experimental determination of yield surfaces and some results of annealed 304 stainless steel. *International Journal of Plasticity*, 7(8):803–826.

Xiao, L., Chen, D., and Chaturvedi, M. (2005). Shearing of γ' precipitates and formation of planar slip bands in inconel 718 during cyclic deformation. *Scripta Materialia*, 52(7):603 – 607.

Yu, M. (1961). General behaviour of isotropic yield function. *Scientific and technological research paper of Xi'an Jiaotong University*, pages 1–11.

Zener, C. (1948). *Elasticity and Anelasticity of Metals*. University of Chicago Press.

Zhou, L. X. and Baker, T. N. (1995). Effects on dynamic and metadynamic recrystallization on microstructures of wrought IN-718 due to hot deformation. *Materials Science and Engineering: A*, 196(1):89–95.

Zhuang, W. Z. and Halford, G. R. (2001). Investigation of residual stress relaxation under cyclic load. *International Journal of Fatigue*, 23:31–37.

université PARIS-SACLAY

ÉCOLE DOCTORALE
Sciences mécaniques et énergétiques, matériaux et géosciences (SMEMAG)

Titre : Modélisation de la relaxation partielle de la contrainte moyenne et essais biaxiaux sur l'Inco718DA
Mots clefs : Inco718DA, Multiaxial, I-CIN, Relaxation de la contrainte moyenne

Résumé : Pour améliorer la caractérisation et le dimensionnement des disques de turbines pour les moteurs d'avion, le motoriste Safran Aircraft Engines (SAE) développe des modèles de comportement, des lois d'endommagement et des critères de fatigue plus adaptés aux chargements réels. Pour aider à cette démarche, le but de cette étude est de développer un modèle de plasticité adapté à l'Inco718DA (un alliage à base nickel utilisé dans la fabrication des turbines haute pression), capable de représenter différents chargements (monotone, cyclique symétrique et non-symétrique). La proposition puis l'identification du modèle a été possible grâce à une campagne expérimentale favorisant des tests complexes et innovants aux essais de fatigue nombreux et coûteux. Les essais faits incluent un essai monotone avec décharges élastiques, un essai multi-niveau à R_ε=-1 et deux essais multi-niveau à R_ε=0 pour mieux caractériser la relaxation de la contrainte moyenne. Le comportement cyclique du matériau a été identifié en utilisant un écrouissage cinématique non saturant avec des éléments s'inspirant de la surface mémoire de Chaboche. Un des défis a été d'obtenir des boucles stabilisées "pointues" dans un régime de plasticité cyclique saturante, en utilisant une évolution du paramètre Γ en fonction de la déformation plastique équivalente maximale (prefacteur du terme de rappel de la loi d'écrouissage cinématique).
Une deuxième difficulté apparaît dans la description de la relaxation de la contrainte moyenne, phénomène complexe avec un impact considérable sur la durée de vie en fatigue. Dans le chapitre 3, un modèle est proposé pour la caractérisation de la relaxation partielle de la contrainte moyenne. Une originalité du modèle est l'idée que la relaxation incomplète est une conséquence directe de la différence entre la charge et la décharge de la boucle de hystérésis. Le paramètre choisi pour décrire cette différence a été le préfacteur du terme de rappel Γ, pour lequel la thermodynamique donne de la liberté. Par rapport à d'autres lois d'écrouissage confirmées, notre modèle présente l'avantage d'utiliser un seul terme de rappel, mais avec une formulation plus complexe. En plus, le modèle est incrémental (écrit en taux/en vitesse), il peut donc prendre en compte des chargements complexes tels que aléatoires ou plus simplement tels que dans les essais multi-niveaux pilotés en déformation.
Dans le dernier chapitre de la thèse, une campagne biaxiale vaste est présentée, avec les développements pour réaliser des essais biaxiaux pilotés en déformation. La campagne biaxiale a été réalisée sur des éprouvettes cruciformes en utilisant des capteurs LASER et des mesures de champs mono et stéréo analysées en utilisant la Corrélation d'Images Numeriques (CIN). Pour analyser la relaxation de la contrainte moyenne en biaxial un moyen de mesure et de contrôle fiable a dû être développé, adapté aux déformations plastiques élevées qui apparaissent dans la région d'intérêt de l'éprouvette. En utilisant la corrélation d'images intégrée (I-CIN) avec des fonctions de forme adaptées sur un seul élément et des calculs sur GPU, on a obtenu des fréquences de mesure de 100 Hz. En plus, avec sa précision et vitesse, I-CIN a été une technique adapté pour contrôler une machine d'essais multiaxiale hydraulique. Un résultat important obtenu quand on a réalisé des essais equi-biaxiaux pilotés en déformation a été l'observation d'une relaxation de la contrainte moyenne très faible par rapport au cas uniaxial. Ce résultat doit être pris en compte dans les études futures avec des calculs éléments finis sur l'éprouvette complète.

Title : Modeling of partial mean stress relaxation and biaxial mechanical testing of Inco718DA
Keywords : Inco718DA, Multiaxial, I-DIC, Mean stress relaxation

Abstract : To improve the characterization and design of aircraft engine turbine disks, the propulsion systems manufacturer Safran Aircraft Engines (SAE) develops constitutive equations, damage laws and fatigue criteria that are more adapted to real loadings. As part of this effort, the purpose of the current study is to develop a plasticity model for Inco718DA (a nickel-based alloy used in the manufacturing of high-pressure turbine disks), capable of representing several loading conditions (monotonic, symmetrical and non-symmetrical cyclic loading). The identification of the model was possible thanks to a uniaxial campaign, favoring a few but complex, innovative, tests to numerous costly fatigue tests. The tests we performed include a monotonic test with elastic discharges, a multi-level R_ε = -1 test and two multi-level R_ε = 0 tests that better quantify the mean stress relaxation. The cyclic behavior was identified using a non-saturating kinematic hardening law with elements of Chaboche's memory surface. One of the challenges was to obtain sharp stabilized loops in a saturated cyclic plasticity regime, which was possible using parameter Γ evolving with respect to the maximum equivalent plastic strain, in the back-stress of kinematic hardening rule.
A second difficulty appears in the description of mean stress relaxation, which has a considerable impact on fatigue lifetime. In chapter 3, a model is proposed for the description of the incomplete mean stress relaxation. One of the originalities is the idea that incomplete mean stress relaxation is a direct consequence of the difference between the loading and the unloading part of the hysteresis loop. The parameter we used to describe this difference, was the prefactor of the back-stress term Γ, for which the thermodynamics allows liberty. When compared to confirmed kinematic hardening laws that model non-zero mean stress relaxation, our model presents the advantage of using only one backstress, even if its description is more complex. Moreover, the model is incremental (written in a rate form in chapter 3 section 5) so it can take into account complex loadings such as multi-level strain-controlled tests.
In the last chapter of the thesis, a vast biaxial campaign is presented, along with developments to make biaxial strain-controlled tests. The biaxial campaign was performed on cross-shaped samples using LASER sensors, mono and stereo full-field measurements using Digital Image Correlation (DIC). In order to analyze biaxial mean stress relaxation, a reliable measurement and control method had to be developed for the high plastic strains occurring in the region of interest of the sample. By using an Integrated-DIC (I-DIC) algorithm with adequate shape functions on one element and GPU computations we were able to obtain measurement frequencies of 100 Hz. Moreover, with its precision and speed, I-DIC proved to be a suitable technique for controlling a biaxial hydraulic machine. An important result obtained when performing equi-biaxial I-DIC strain-controlled tests was that there was very little biaxial mean stress relaxation, with respect to the uniaxial case. This result will have to be taken into account in future studies when performing finite element computations of the whole sample.

Université Paris-Saclay
Espace Technologique / Immeuble Discovery
Route de l'Orme aux Merisiers RD 128 / 91190 Saint-Aubin, France